Experimental Modeling of Ice Cover Effects on the Secondary Flow Formation in Meander Bend

Samaneh Ebrahimi

Thesis submitted to the University of Ottawa
in partial fulfillment of the requirements for the
Doctorate in Philosophy in Environmental Engineering

Department of Civil Engineering
Faculty of Engineering
University of Ottawa

© Samaneh Ebrahimi, Ottawa, Canada, 2026

"*Water is the driving force of all nature.*"

– Leonardo da Vinci (1452–1519)

Acknowledgements

The preparation of this thesis took a few years of work, shaped by different experiences along the way. As this PhD journey is coming to completion, I reflect on a period of change and growth. I am deeply grateful to those who supported me throughout this journey. My foremost respectful thanks are to my supervisors, Prof. Mohammadian and Prof. Rennie, for their continued confidence, support, the liberty they gave me, and introducing me to an academic field in which I have always wished to work in.

Although conducting a PhD is by definition an individual work, its success reflects the efforts and contributions of many individuals. Such work would not have been possible without the support from many people in my life, my husband and my two young children who stood with me as we grew together. I owe a special gratitude to my parents, and my siblings, though I could not be with them as much as I wished. They gave me the strength that I needed to complete this journey, even as they were navigating some of life's most difficult moments.

The experimental part of this PhD relied on the high-tech particle image velocimetry, developed in our new laboratory specifically designed PIV room. I am grateful to my supervisors for their support in using this technique. I also thank my friend, Katie Schreiner, whose experiments preceded mine. Owing to some link between our studies, she helped address some of my initial experimental challenges and aided in continued discussions and cooperation. I thank the staff at the hydraulic lab, the machine shop, and the summer students for their kind support at different times in the setup and testing for this study.

Last but not least, I would like to thank the Natural Sciences and Engineering Research Council of Canada (NSERC) for having funded this research.

Abstract

When a river surfaces freezes, the ice cover introduces a rigid upper boundary that alters flow structure. In straight reaches, this results in a two-layer system governed by shear at both the bed and the ice-water interface. In bends, the combined effects of channel curvature and the ice boundary generate counter-rotating secondary circulation cells near the bed and the ice underside. These processes remain poorly understood due to limited observations under ice-covered conditions, and because many existing models assume an idealized open-channel condition with negligible surface shear, thereby neglecting ice-induced roughness and resistance. This study investigates the mechanisms governing secondary flow in ice-covered bends, hypothesizing that the observed flow structure arises from the interaction between channel curvature and the rigid ice boundary, although the underlying dynamics are not yet fully resolved.

The central focus of this thesis is advancing the understanding of how these circulation cells form and develop under varying flow and roughness conditions. The effects of flow rate, flow depth, and the ice cover surface roughness on the flow structure in a simulated ice-covered bend are systematically examined. A comprehensive set of experimental investigations was conducted using uOttawa's laboratory bend flume, where Particle Image Velocimetry (PIV) technology was applied to capture 3D velocity components. The data was used to carry a detailed examination of flow characteristics under ice-covered conditions. These measurements provided unique insights into the spatial variations of velocity, turbulence, and secondary flow circulations in ice-covered confined channel bends where the flow displays strong three-dimensional characteristics.

In particular, it was found that variations in flow rate (i.e., Froude number) distinctly influenced turbulence distribution patterns beneath the ice cover in the channel bend. As discharge decreased, the normalized mean kinetic energy increased, indicating more structured flow and greater relative turbulence at lower flow rates. Results related to increasing ice-cover roughness revealed a reduction in total secondary circulation within the ice layer, while circulation near the bed was enhanced. The three-dimensional momentum response

under varying roughness conditions was also examined, revealing directional sensitivity differences: vertical and cross-stream momentum exhibited greater sensitivity to ice roughness than streamwise momentum, leading to a reshaping of the secondary vortex structure under increased roughness. The aspect ratio variation under the ice cover additionally showed a marked change in the spatial configuration and strength of secondary circulation vortices. Clear variations in the height of maximum velocity were observed along the channel, a related but distinct trend driven by local turbulence as the aspect ratio changed. Such data are rare (if not entirely absent) in existing experimental studies, especially for meander bend river channels. These findings provide new insights into the influence of ice cover on turbulent flow fields in meandering rivers and offer valuable guidance for hydraulic engineers and researchers working in cold-region water systems.

Contents

Acknowledgements **iii**

Abstract **iv**

Glossary **xxii**

Symbols **xxiii**

1 Introduction **1**

1.1 Cold Regions and River Channels 2

1.1.1 Seasonal Ice Formation and River Freeze-Up 4

1.1.2 Secondary Flow in Meander River Channels 5

1.2 Fluid Dynamics and Turbulence Theory 8

1.2.1 Turbulent Flows 8

1.2.2 Velocity Distribution in Open and Closed Channels 9

1.2.3 Shear Stress and Flow Resistance Relationship 10

1.2.4 Turbulence Scales 14

2 Background Literature Review **17**

2.1 Free-surface Channel Studies 18

2.2 Ice-Covered Channel Studies 24

3 Scope, Objectives, and Novelty **31**

3.1 Research Motivation 31

3.2 Objectives and Novelty 32
3.3 Thesis Structure 36

4 Methodology and Data **38**
4.1 River Channel Meander 38
4.2 Physical Model of Bend Channel 39
4.2.1 Physical Model of the Ice Cover 41
4.2.2 Verification of Fully Developed Flow 43
4.3 Flow Conditions Scaling 45
4.4 Velocity Data Measurement 48
4.4.1 Calibration for Stereoscopic PIV 51
4.4.2 Planar Self-Calibration and Disparity Analysis 52
4.4.3 Temporal Resolution of Velocity Measurements 54

5 Secondary Flow and Froude Number Variation **56**
Secondary flow dynamics and turbulence in an ice-covered sharp bend channel at different subcritical Froude numbers 56
5.1 Abstract 56
5.2 Introduction 57
5.3 Methods 60
5.3.1 Velocity Scaling of Flow 61
5.3.2 Ice Cover and Roughness Scale 62
5.3.3 PIV Data Processing 63
5.3.4 Spatial and Temporal Resolution of Measurements 64
5.3.5 Vortex Identification Algorithm 65
5.4 Results 66
5.4.1 Secondary flow vortices under ice-cover 66
5.4.2 Mean Flow Distribution 69
5.4.3 Mean and turbulent kinetic energy variation 70

5.4.4 Reynolds stresses configuration 72
5.4.5 Turbulent structure parameter 74
5.5 Discussion 75
5.6 Conclusions 82

Appendices **84**
A.1 Wall shear and friction partitioning 84
A.2 Non-normalized TKE distribution 86

6 Secondary Flow and Ice-cover Roughness Impact **87**
Roughness influence on secondary circulation and momentum distribution in an ice-covered river bend 87
6.1 Abstract 87
6.2 Introduction 88
6.3 Methods 93
6.3.1 Physical model of the ice-cover 94
6.3.2 Hydrodynamic entrance length of the flow 95
6.3.3 Stereo-PIV configuration and data acquisition 96
6.3.4 Spatial and temporal resolution of the PIV data 97
6.3.5 Planar Self-Calibration and Spatial Disparity Evaluation 98
6.3.6 Temporal Continuity Validation via Discharge Constancy 98
6.3.7 Estimation of Velocity Uncertainty from Sub-pixel Errors 100
6.3.8 Estimation of Near-boundary Uncertainty 101
6.4 Results 102
6.4.1 Effect of ice roughness on secondary vortex structure and circulation 102
6.4.2 Directional influence of roughness on secondary flow and momentum distribution 109
6.4.3 Statistical significance of momentum changes 112
6.4.4 Roughness-induced patterns of momentum changes 114
6.5 Discussion 118

6.6 Conclusions 125

7 Secondary Flow and Aspect Ratio Change **127**

Influence of Channel Aspect Ratio on Secondary Flow Circulation and Turbulence in an Ice Covered Rectangular Bend Channel 127

7.1 Abstract 127

7.2 Introduction 128

7.3 Methodology 130

7.3.1 Physical bend channel model 130

7.3.2 Simulated ice-cover 131

7.3.3 Flow conditions and scaling 131

7.3.4 Velocity measurement technique 133

7.3.5 Vortex identification algorithm 134

7.4 Results 135

7.4.1 Statistical difference across the AR configurations 135

7.4.2 Effect of aspect ratio on secondary flow structure 138

7.4.3 Analysis of some transverse velocity profiles 141

7.4.4 Streamwise velocity and energy structure 142

7.4.5 Secondary-flow kinetic energy 145

7.4.6 Reynolds shear stress distributions 148

7.5 Discussion 151

7.6 Conclusion 159

Appendices **161**

A.1 Statistical difference across the AR configurations 161

A.1.1 Kruskal–Wallis H-test 161

A.1.2 Post-hoc pairwise comparisons 163

A.1.3 Pairwise effect size comparisons 165

A.1.4 Brown–Forsythe variance test 167

8 Conclusions and Future Works **171**

8.1 Study Summary and Remarks 171

8.2 Key Findings 174

8.2.1 Effect of Flow Rate (Froude Number) 174

8.2.2 Effect of Ice Roughness (Boundary Conditions) 176

8.2.3 Effect of Aspect Ratio (flow width-to-hight) 179

8.3 Recommendations for Future Work 181

Bibliography **182**

List of Figures

1.1 Global distribution of seasonal river ice derived from Landsat satellite observations between 1984 and 2018. The map shows the average fraction of river length covered by ice during the winter season (December–February in the Northern Hemisphere and June–August in the Southern Hemisphere). The accompanying bar chart presents the monthly global extent of river ice, while the percentages in parentheses indicate the proportion of rivers successfully observed by Landsat for each month [163]. 2

1.2 Monthly temperature and precipitation patterns in some Canadian cities, as reported in the 1991–2020 Canadian Climate Normals. In each subplot, the red line with square markers represents the daily maximum temperature ($^{\circ}\mathrm{C}$), the black line with circular markers indicates the daily average temperature ($^{\circ}\mathrm{C}$), and the blue line with triangular markers shows the daily minimum temperature ($^{\circ}\mathrm{C}$). The green bars represent the monthly precipitation (mm). Temperature and precipitation data are published by *Environment and Natural Resources Canada* (1991–2020 Canadian Climate Normals). 3

1.3 Conceptual schematic of the simplified main phases of river ice freeze-up, showing the progression from open water (top left) with frazil ice to ice pan formation, upstream ice cover advancement, and a stabilized ice cover (bottom right) (modified after [145]). 4

1.4 Schematic illustration of the cross-sectional Secondary flow sketch in an open curved channel [17]. The coordinate system is denoted by s, n, and z, representing the streamwise, cross-stream, and vertical directions, respectively. 6

1.5 Schematic illustration of the cross-sectional force balance and secondary circulation structure in a curved channel under free-surface and ice-covered conditions. Note that depending on channel geometry a free-surface or ice-covered curved channel flow may include a co-rotating inner bank cell and/or a counter-rotating outer bank cell. Solid grey arrows indicate the secondary flow direction, while the patterned straight arrow denotes the main flow direction. Subplots and arrows are not drawn to scale. The conceptual framework in this figure is adapted and extended from [145]. 7

1.6 Schematic representation comparing laminar and turbulent velocity profiles in steady, uniform flow for an open-channel (left) and a closed-channel (right). The notation L (in black) denotes laminar flow, and T (in blue) denotes turbulent flow (Adapted from [134]). 10

1.7 Schematic comparison of velocity and shear stress distributions in steady, uniform flow for open- and closed-channel configurations. Panels (a) and (b) illustrate representative streamwise velocity profiles for open-channel and closed-channel flow, respectively. Panels (c) and (d) show the corresponding shear stress (τ) distributions. The dashed line in the closed-channel profiles denotes the channel centerline. The schematics are not drawn to scale (modified after [145]). 12

1.8 Schematic representation of Reynolds decomposition showing the instantaneous velocity u_i, mean velocity U_i, and turbulent fluctuation u_i' as a function of time t (Modified after [42]). 16

4.1 The 135° bend channel with transparent plexiglass walls and a rectangular bed. In the figure, the adjustable gate used to regulate the flow depth is indicated by letter *A*, the outlet tank by *B*, the inlet tank by *C*, and the measurement section located at the bend apex by *D*. 40

4.2 Application of a black adhesive vinyl mat on the ice cover to improve the optical conditions of the experiments. 41

4.3 Schematic of the 135° bend physical model for rough ice-cover configuration and the arrangement of roughness elements used for the PIV experiments. The x, y, and z directions represent the streamwise, cross-stream, and vertical directions of the flow, respectively (Credit: Julien Pierrat) . . . 43

4.4 Schematic layout of the stereo-PIV system and experimental flow setup, showing the cameras positions and the laser sheet introduced from underside of the channel (credit: Julien Pierrat). The streamwise flow direction is indicated by the blue arrow. The turquoise solid line within the bend denotes the bend apex (90° cross-section), where the velocity measurements were conducted. 50

4.5 Two level calibration plate (From LaVision System Components, Calibration Plates) 51

4.6 Calibration plates: (a) the plate provided with the standard LaVision system, and (b) a 3D-printed plate with the same marker pattern and 3d-geometry. In panel (a), region 'A' denotes the portion of the channel width covered by the plate, while region 'B' indicates the uncovered portion. In panel (b), region 'C' represents the full channel width covered by the 3D-printed calibration plate. 52

5.1 Schematic of the bend flume and stereo-PIV setup (Credit: Julien Pierrat). A vertical laser sheet (green line) aligned to illuminate the 90° cross-sectional plane from the bottom wall. The two cameras recording stereo image pairs were positioned on either side of the measurement section. The coordinate origin (0°), indicated by the dashed blue line at the junction where the straight inflow section meets the curved bend, marks the start of the meander. 63

5.2 Mean flow streamlines illustrating secondary flow vortices under (a) high flow rate, (b) medium flow rate, and (c) low flow rate. Colored rectangles indicate the identified vortex regions, while white arrows denote the flow directions within the upper and lower boundary layers, intersecting approximately at mid-depth. The vertical axis represents the flow depth (0–0.06 m, from the bed to the ice cover), and the horizontal axis represents the channel width (0–0.20 m, from the inner bank to the outer bank). 67

5.3 Mean streamwise velocity showing high-velocity core regions exceeding the 90th percentile of local velocity for (a) high, (b) medium, and (c) low flow rates. 69

5.4 Normalized mean flow kinetic energy (KE/$\frac{1}{2}U_{\text{bulk}}^2$) in (a–c) and turbulent kinetic energy (TKE/$\frac{1}{2}U_{\text{bulk}}^2$) in (d–f) under high (1.44 L/s), medium (1.08 L/s), and low (0.48 L/s) flow conditions. Each MKE plot includes a highlighted yellow isoline (value labeled in black) indicating the 90^{th}-percentile energy level for the respective flow scenario. Note the higher colorbar range in plot (f) compared to plot (d) and (e). The vertical and horizontal axes of each plot represent the flow domain's height and width, respectively. 71

5.5 Normalized Reynolds shear stresses τ_{uw} (a–c), and τ_{vw} (d–f) for high (1.44 L/s), medium (1.08 L/s), and low (0.48 L/s) flow conditions. All plotted values are multiplied by 10^2 to improve visual clarity. Note the higher colorbar range in plot (c) compared to (a) and (b), and in plot (f) compared to (d) and (e). White bands along the edges of the plots represent masking applied to exclude near-wall data. 73

5.6 Turbulent structure parameter a_1 for (a) high, (b) medium, and (c) low flow conditions. White bands along the edges of the plots represent masking applied to exclude near-wall data. 75

A.1 Non normalized TKE distribution for high (1.44 L/s), medium (1.08 L/s), and low (0.48 L/s) flow conditions. White bands along the edges of the plots represent masking applied to exclude near-wall data. 86

6.1 Schematic illustration of the cross-sectional force balance and secondary circulation structure in a curved channel under free-surface and ice-covered conditions. Note that depending on channel geometry a free-surface or ice-covered curved channel flow may include a co-rotating inner bank cell and/or a counter-rotating outer bank cell. Solid grey arrows indicate the secondary flow direction, while the patterned straight arrow denotes the main flow direction. Subplots and arrows are not drawn to scale. 89

6.2 Schematic of the 135-degree bend physical model of rough ice cover, showing the configuration of surface roughness elements used in the PIV experiments (Credit: Julien Pierrat). 94

6.3 Schematic layout of the stereo-PIV system and experimental flow setup (credit: Julien Pierrat). The coordinate axes x, y, and z denote the streamwise, cross-stream, and vertical directions, respectively. The red line indicates the bend apex (90° cross-section) where the PIV measurements were conducted. The angle θ represents the angle between the optical axes of the cameras. 96

6.4 Time series of instantaneous discharge $Q(t)$ calculated from the PIV velocity fields over the full 600-second measurement length. The mean discharge $\bar{Q}$ is shown as a dashed black line, and the $\pm 2\sigma$ bounds are indicated by red dashed lines. 99

6.5 Mean flow streamlines illustrating secondary flow vortices under (a) smooth and (b) rough ice covers. Colored rectangles indicate identified vortex regions, while blue arrows denote flow directions within the ice (top) and bed (bottom) boundary layers, intersecting approximately at mid-depth. The vertical axis represents flow depth (0-0.06 m, from bed to ice cover), and the horizontal axis represents channel width (0-0.20 m, from inner bank to outer bank). 103

6.6 Vertical profiles of cross-stream velocity (V) at selected lateral positions across the channel width, ranging from 10% near the inner bank to 95% near the outer bank, under smooth (circle markers) and rough (triangle markers) ice cover conditions. Each subplot is labeled with the corresponding normalized lateral position, where y is the lateral distance from the inner bank and y_{max} is the total channel width. The vertical axis represents the dimensionless height z/z_{max}, where z_{max} denotes the flow depth. No velocity filtering was applied. An asterisk (*) indicates profiles where near-bed data points were excluded due to high velocity uncertainty. 107

6.7 Vector fields of transverse circulation under (a) smooth and (b) rough ice covers, where arrows indicate the direction of secondary flow, and their lengths reflect local velocity magnitudes. The horizontal and vertical axes are normalized by the channel width and flow depth, respectively, where y denotes the lateral position, y_{max} the total channel width, z the vertical position, and z_{max} the total flow depth. White bands at the top and bottom of each panel represent masking applied to exclude near-ice and bed data. . . . 108

6.8 Momentum distribution for (a–c) smooth ice and (d–f) rough ice cover in the streamwise (a,d), cross-stream (b,e), and vertical (c,f) directions. All momentum components shown are time-averaged. The colorbar shows momentum magnitude and direction. The white areas near the edges indicate masked data. 110

6.9 Distribution of rough to smooth momentum ratios in (a) streamwise, (b) cross-stream, and (c) vertical components. Note the lower colorbar range in plot (a) compared to plot (b) and (c). The white areas near the edges indicate masked data. 116

6.10 Lateral distribution of depth-averaged secondary flow magnitude (top panel) and total velocity magnitude (bottom panel) under smooth ($\circ$) and rough ($\triangle$) ice-covered conditions. Profiles adjacent to the sidewalls are excluded due to PIV data obscured in those regions. 120

6.11 Comparison of normalized turbulent kinetic energy fields under (a) smooth and (b) rough ice conditions, and (c) their difference. The vertical axis represents flow depth (0-0.06 m, from bed to ice cover), and the horizontal axis represents channel width (0-0.20 m, from inner bank to outer bank. Note the lower colorbar range in plot (c) compared to plot (a) and (b). The white areas near the edges indicate masked data. 122

6.12 Mean streamwise velocity component under smooth and rough-ice conditions. 124

7.1 Schematic of the 135° bend physical model, including the dimensions of the main components expressed in metres. The blue arrow in the straight entrance indicates the flow direction, and the blue line in the curve shows the 90° measurement section in the bend. 131

7.2 Schematic representation of the stereo-PIV system and experimental configuration (credit: Julien Pierrat). The coordinate axes (x, y, z) correspond to the streamwise, cross-stream, and vertical directions, respectively. 133

7.3 Secondary-flow vortex structures for different aspect ratios beneath a smooth ice cover. Colored rectangles shows the identified the detected vortices, and blue arrows indicate the direction of secondary flow. The horizontal axis represents the normalized channel width, $x/x_{\max}$, where $x_{\max} = 0.20$ m; $x/x_{\max} = 0$ and 1 correspond to the inner and outer banks, respectively. The vertical axis represents the normalized flow depth for (a) 0.05 m, (b) 0.07 m, and (c) 0.08 m, where 0 and 1 correspond to the channel bed and ice cover, respectively. 139

7.4 Normalized cross-stream velocity profiles at different width locations (10-90% from the inner bank) for three aspect-ratio cases. The horizontal axis shows the normalized cross-stream velocity component v/v_{ref}, where v_{ref} is the maximum absolute cross-stream velocity for each case. The vertical axis shows the normalized flow depth z/H, where z is the vertical location and H is the flow depth. The legend in all subplots is the same as in subplot (a). 141

7.5 Time-averaged streamwise velocity distribution for (a) $AR = 4.0$, (b) $AR = 2.9$, and (c) $AR = 2.5$. The horizontal axis represents normalized channel width ($x/x_{\max}$), where 0 corresponds to inner bank and 1 to outer bank, while the vertical axis represents normalized flow depth ($z/z_{\max}$). 143

7.6 Mean flow kinetic energy (MKE) in (a–c) and turbulent kinetic energy (TKE) in (d–f) under high (AR4.0), medium (AR2.9), and low (AR2.5) aspect ratios. The yellow contour outlines the region corresponding to the upper 10% of mean kinetic energy values for each case.The vertical and horizontal axes of each plot represent the flow domain's normalized height and width, respectively. 144

7.7 The normalized secondary flow kinetic energy under high (AR4.0), medium (AR2.9), and low (AR2.5) aspect ratios. The vertical and horizontal axes of each plot represent the flow domain's normalized height and width, respectively. 147

7.8 Spatial distributions of Reynolds shear stress components τ_{uw}, τ_{vw}, and τ_{uv}, for the three aspect-ratio configurations (AR4.0, AR2.9, AR2.5). Positive and negative values indicate the direction of turbulent momentum transfer between velocity components. The values are scaled by the order of magnitude indicated in the legend for visual enhancement. 149

7.9 Spatial distributions of streamwise vorticity ω_s for the three aspect-ratio configurations: (a) AR4.0, (b) AR2.9, and (c) AR2.5. The horizontal direction extends from the inner bank (left) to the outer bank (right), and the vertical direction extends from the bed to the ice cover. 154

7.10 Spatial distributions of the normalized secondary-flow velocity magnitude, U^*_{sec}, for the three aspect-ratio configurations: (a) AR = 4.0, (b) AR = 2.9, and (c) AR = 2.5. The corresponding cross-sectionally averaged values, U^*_{sec}, are reported for each case. The lateral and vertical coordinates are normalized by the channel width, B, and flow depth, H, respectively. 156

List of Tables

4.1 Surface materials and corresponding roughness parameters used in the experiments 42

4.2 Summary of experimental flow conditions and corresponding hydraulic parameters. Here, k_s is the roughness height (mm), H is the flow depth (cm), B/H is the aspect ratio with constant channel width $B = 20$ cm, U_b is the bulk velocity (m/s), Q is the discharge (L/s), $m = \frac{Q^2}{gA^3}$ is the momentum function, $Fr = \frac{U_b}{\sqrt{gH}}$ is the Froude number, and $Re = \frac{U_b D_h}{\nu}$ is the Reynolds number based on the hydraulic diameter $D_h = \frac{4A}{P}$. 47

4.3 Specifications of the LaVision cameras used in the stereo-PIV system. . . . 49

4.4 Specifications of the Nd:YAG laser used for illumination in the stereo-PIV system. 49

4.5 Specifications of the programmable timing unit (PTU) used for synchronization. 50

5.1 Summary of boundary materials and roughness parameters. 62

5.2 Properties of vortices identified at different flow rates. 68

A.1 Summary of mean flow mid-channel hydraulic properties across three flow conditions. 85

6.1 Surface materials and roughness parameters used in the experiments 95

6.2 Properties of vortices identified under different ice covers. 104

6.3 Layered momentum comparison: M_x, M_y^+, M_y^-, M_z^+, M_z^-, and M_t represent streamwise, outward cross-stream, inward cross-stream, upward vertical, downward vertical, and total momentum sums, respectively. Units are in $\times 10^5$ kg·m/s. 111

6.4 Results of the Mann–Whitney $\boldsymbol{U}$ test for momentum under smooth and rough ice conditions. 114

7.1 Summary of test conditions and their hydraulic characteristics. In this table, H is the flow depth (cm), B/H is the aspect ratio for a constant channel width of $B = 20$ cm, U_b is the bulk velocity (m/s), Q is the discharge (L/s), $m = \frac{Q^2}{gA^3}$ is the momentum function, $Fr = \frac{U_b}{\sqrt{gH}}$ is the Froude number, and $Re = \frac{U_b D_h}{\nu}$ is the Reynolds number based on the hydraulic diameter $D_h = \frac{4A}{P}$. 132

7.2 Integrated summary of statistical outcomes for velocity components across aspect ratios based on the normalized-coordinate analysis. Results synthesize the distributional differences (Kruskal–Wallis and Kolmogorov–Smirnov tests), pairwise comparisons, effect sizes (Cliff's δ), and variance-based responses (Brown–Forsythe test). 136

7.3 Properties of secondary-flow vortices identified at different aspect ratios. "AR" denotes the flow aspect ratio, and the vortex IDs correspond to the vortex labels shown in Figure 7.3. 140

A.1 Kruskal–Wallis tests for each velocity component across aspect ratios (AR4, AR2.9, AR2.5), and post hoc pairwise comparisons. Omnibus KW reports χ^2 statistic, p, and call at $\alpha = 0.001$; pairwise tests report Dunn–Šidák (DS), Holm-adjusted Wilcoxon (H), and Kolmogorov–Smirnov (KS) p-values. "S" denotes significant and "NS" denotes non-significant. 164

A.2 Effect sizes for pairwise comparisons across aspect ratios, reported as Cliff's δ, which indicates the direction and magnitude of stochastic dominance between the compared groups, and the median difference $\Delta\tilde{x}$, reported in physical units. 166

A.3 Brown–Forsythe variance test results for velocity components across aspect ratios (AR4, AR2.9, AR2.5). Reported are omnibus p-values and pairwise F-statistics with raw and Holm-adjusted p-values. Significance is evaluated at $\alpha = 0.001$. "S" denotes significant and "NS" denotes non-significant. . . 169

Glossary

ADCP	acoustic Doppler current profiler
ADV	acoustic Doppler velocimeter
AR	aspect ratio
DNS	direct numerical simulations
FOV	field of view
GPR	ground-penetrating radar
HVC	high-velocity core
IBC	inner bank cell
IDM	iterative deformation method
LDA	laser Doppler anemometry
LES	large eddy simulation
MKE	mean kinetic energy
OBC	outer bank cell
PC-ADP	pulse coherent acoustic Doppler profiler
RANS	Reynolds averaged Navier Stokes
RMS	root mean squared
RMSE	root mean squared error
PIV	particle image velocimetry
PTU	programmable timing unit
ROI	region of interest
SF	secondary flow
stereo-PIV	stereoscopic particle image velocimetry
TKE	turbulent kinetic energy
USGS	United States Geological Survey
3C	three-component
3D	three-dimensional

Symbols

Roman Symbols

A	domain area	cm^2
a_1	turbulent structure parameter	–
B	channel width	m
C_r	curvature ratio	–
CV_Q	coefficient of variation of discharge	–
D_e	Dean number	–
D_h	hydraulic diameter	m
d_avg	average disparity	px
f	Darcy–Weisbach friction factor	–
f_{Nyquist}	Nyquist frequency	s^{-1} (Hz)
f_s	sampling frequency	s^{-1} (Hz)
Fr	Froude number	–
g	gravitational acceleration	$\mathrm{m\,s}^{-2}$
h	water depth	m
H_m	model flow height	m
H_p	prototype flow height	m
k	turbulent kinetic energy	$\mathrm{m}^2\,\mathrm{s}^{-2}$
k_s	roughness element height	mm
L	characteristic length scale	m
M_x	streamwise momentum	$\mathrm{kg\,m\,s}^{-1}$
M_y	cross-stream momentum	$\mathrm{kg\,m\,s}^{-1}$
M_z	vertical momentum	$\mathrm{kg\,m\,s}^{-1}$
N	number of independent time samples	–
N_x	number of vectors in width direction	–
N_z	number of vectors in height direction	–
n	transverse coordinate	m
p	pressure	Pa

Q	flow rate	$\mathrm{m^3\,s^{-1}}$
$Q(t)$	instantaneous discharge	$\mathrm{m^3\,s^{-1}}$
R	channel radius of curvature	m
R_h	hydraulic radius	m
Re	Reynolds number	–
S	energy slope	–
s	streamwise coordinate	m
s_x	image horizontal scale factor	–
s_y	image vertical scale factor	–
$T_{\min}$	minimum resolvable time scale	s
$T_{\max}$	total acquisition time	s
t	time	s
U	characteristic velocity	$\mathrm{m\,s^{-1}}$
U_b	bulk velocity	$\mathrm{m\,s^{-1}}$
U_i	time-averaged velocity component	$\mathrm{m\,s^{-1}}$
U_m	model velocity	$\mathrm{m\,s^{-1}}$
U_p	prototype velocity	$\mathrm{m\,s^{-1}}$
u	streamwise velocity component	$\mathrm{m\,s^{-1}}$
u_i	instantaneous velocity component	$\mathrm{m\,s^{-1}}$
u_i'	turbulent velocity fluctuation	$\mathrm{m\,s^{-1}}$
u_*	shear velocity	$\mathrm{m\,s^{-1}}$
u^+	dimensionless velocity	–
$\overline{u'v'}$	Reynolds shear stress (streamwise–transverse)	$\mathrm{m^2\,s^{-2}}$
$\overline{u'w'}$	Reynolds shear stress (streamwise–vertical)	$\mathrm{m^2\,s^{-2}}$
v	cross-stream velocity component	$\mathrm{m\,s^{-1}}$
$\overline{v'w'}$	Reynolds shear stress (transverse–vertical)	$\mathrm{m^2\,s^{-2}}$
W	interrogation window size	px
w	vertical velocity component	$\mathrm{m\,s^{-1}}$
x	streamwise coordinate	m
y	transverse coordinate	m
y^+	dimensionless wall distance	–
z	vertical coordinate	m

Statistical Analysis Symbols

α	significance level	–
δ	Cliff's effect size measure	–
$\Delta\tilde{x}$	difference in group medians	$\mathrm{m\,s^{-1}}$
χ^2	Kruskal–Wallis test statistic	–
H	Kruskal–Wallis test statistic	–
H_0	null hypothesis	–
k	number of groups	–
N	total sample size	–
n_1	sample size (sample 1)	–
n_2	sample size (sample 2)	–
n_i	sample size (group i)	–
$n_>$	pairwise counts where sample 1 $>$ sample 2	–
$n_<$	pairwise counts where sample 1 $<$ sample 2	–
p	p-value	–
p_{BF}	Brown–Forsythe test p-value	–
R_1	sum of ranks (sample 1)	–
R_2	sum of ranks (sample 2)	–
R_i	sum of ranks (group i)	–
U	Mann–Whitney test statistic	–
U_1	Mann–Whitney statistic (sample 1)	–
U_2	Mann–Whitney statistic (sample 2)	–
z	standardized test statistic (z-score)	–
Z_{ik}	Brown–Forsythe transformed variable	–
μ_U	expected value of U under H_0	–
σ_U	standard deviation of U	–
σ^2	variance	–
$\tilde{x}$	sample median	$\mathrm{m\,s^{-1}}$

Greek Symbols

Δavg	physical disparity	mm
Δx	transverse spatial grid resolution	mm
Δz	vertical spatial grid resolution	mm
ε	turbulent dissipation rate	$\mathrm{m^2\,s^{-3}}$
Γ_1	vortex identification parameter (center)	–
Γ_2	vortex identification parameter (area)	–
κ	von Kármán constant	–
λ_2	vortex core identification criterion	–
λ_H	depth scale	–
λ_U	velocity scale	–
μ	dynamic viscosity	$\mathrm{kg\,m^{-1}\,s^{-1}}$
ν	kinematic viscosity	$\mathrm{m^2\,s^{-1}}$
ρ	fluid density	$\mathrm{kg\,m^{-3}}$
σ_Q	standard deviation of discharge	–
σ_U	uncertainty in streamwise velocity	$\mathrm{m\,s^{-1}}$
σ_{disp}	sub-pixel displacement error	px
τ_0	bed shear stress	Pa
τ_{uv}	Reynolds shear stress	Pa
τ_{uw}	Reynolds shear stress	Pa
τ_{vw}	Reynolds shear stress	Pa
ω	vorticity	$\mathrm{s^{-1}}$
Ω	antisymmetric velocity gradient tensor	$\mathrm{s^{-1}}$

Chapter 1

Introduction

Ice is a fundamental component of the hydrologic cycle across high-latitude and high-elevation regions, and river systems in these environments are strongly influenced by the presence of snow and ice. Globally, more than one-third of Earth's land surface is drained by rivers that freeze seasonally [163]. As a result, a large fraction of river networks is subject to ice-related processes for part of the year, during which ice can dominate fluvial behavior. Seasonal river ice alters flow structure, turbulence, and secondary circulation, and therefore plays a key role in shaping hydraulic and geomorphic processes in these environments. Beyond hydraulics, river ice affects sediment transport, ecological connectivity, flood risk, navigation, and transportation, and influences river ecology through changes in water quality, flora, and fauna, as well as geomorphology through impacts on bank stability and channel form. These effects extend to river hydrology by modifying winter discharge and conveyance capacity, making river ice a critical factor in the functioning of cold-region river corridors and human activities.

The significant socio-economic impacts of river ice in northern countries, including Canada, have driven major advances in river ice engineering and hydrology research. River ice studies began to appear in the scientific literature in the early 20th century, with notable contributions from Canada, Norway, and Russia [6]. In addition, atmospheric fluxes and the temporal and spatial trends of river ice can serve as indicators of climate [61, 110], as they control the various forms of river ice and the associated physical processes. A brief review

on cold-region climates and the conditions that promote seasonal river ice development is introduced next.

1.1 Cold Regions and River Channels

Almost 25% of the land mass, or 29% of the total river length, in the Northern Hemisphere lies within climates where mean annual air temperatures approach or fall below freezing [12]. As a result, many rivers develop seasonal ice cover during winter. River ice strongly influences river hydraulics, channel morphology, sediment transport, and aquatic ecosystems, making it an important component of cold-region river systems. Figure 1.1 illustrates the global distribution of river ice occurrence based on satellite observations [163], highlighting its widespread seasonal presence across northern high-latitude regions.

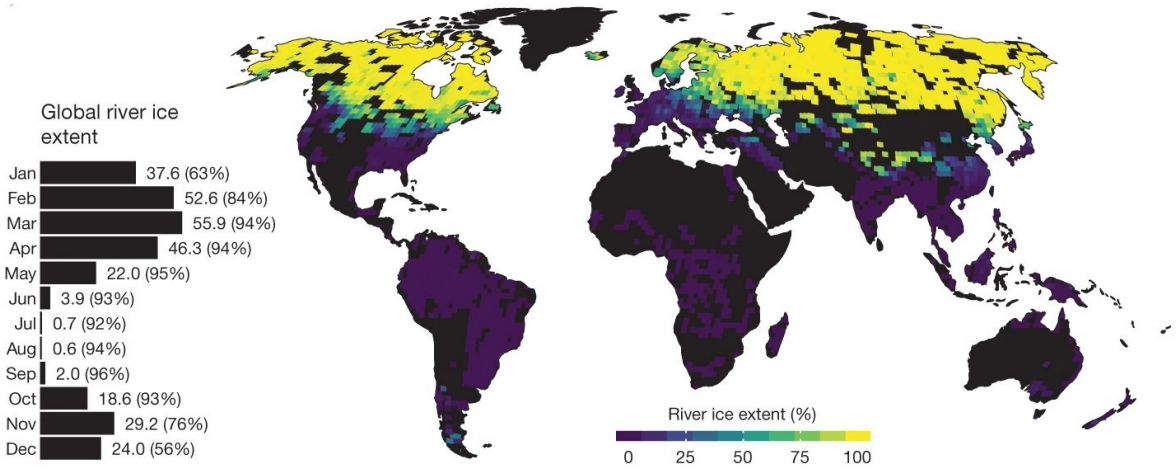
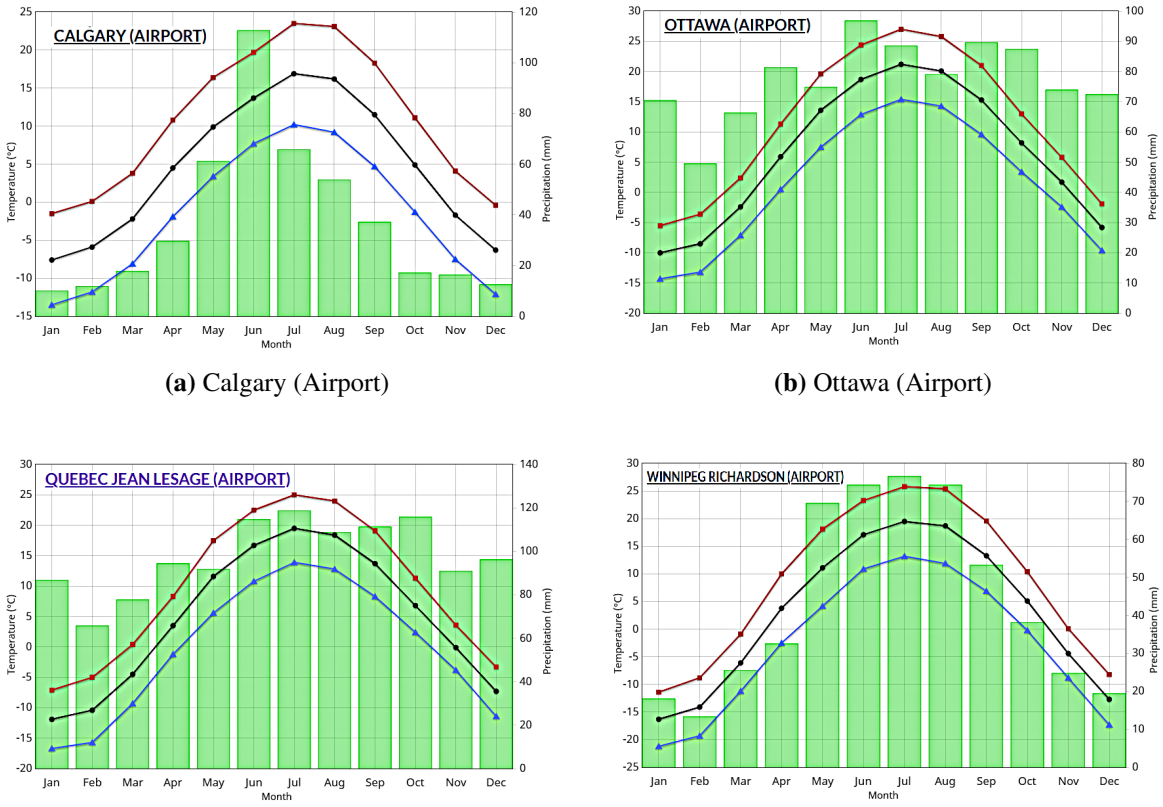


Figure 1.1. Global distribution of seasonal river ice derived from Landsat satellite observations between 1984 and 2018. The map shows the average fraction of river length covered by ice during the winter season (December–February in the Northern Hemisphere and June–August in the Southern Hemisphere). The accompanying bar chart presents the monthly global extent of river ice, while the percentages in parentheses indicate the proportion of rivers successfully observed by Landsat for each month [163].

In Canada, climatic conditions vary greatly across the country due to regional geographic and atmospheric factors, resulting in cold winters and generally cool to moderate summers. During winter, air temperatures frequently remain below the freezing point for extended periods, particularly in inland and northern regions. These prolonged freezing conditions promote the formation of river ice covers, which can persist for several months depending on local climate and hydrological conditions. Figure 1.2 illustrates the 1991–2020 Canadian Climate Normals for selected cities, based on meteorological data recorded at major airport weather stations.



(a) Calgary (Airport)

(b) Ottawa (Airport)

(c) Québec (Jean Lesage Airport)

(d) Winnipeg (Richardson Airport)

Figure 1.2. Monthly temperature and precipitation patterns in some Canadian cities, as reported in the 1991–2020 Canadian Climate Normals. In each subplot, the red line with square markers represents the daily maximum temperature (°C), the black line with circular markers indicates the daily average temperature (°C), and the blue line with triangular markers shows the daily minimum temperature (°C). The green bars represent the monthly precipitation (mm). Temperature and precipitation data are published by *Environment and Natural Resources Canada* (1991–2020 Canadian Climate Normals).

These data highlight the pronounced seasonal variations in air temperature and precipitation across the country, where cold winters are characterized by reduced precipitation and subzero temperatures. Figure 1.2 shows these climatic conditions promote the formation, growth, and persistence of river ice for approximately half of the year, influencing river hydraulics, channel morphology, sediment transport, and aquatic ecosystems.

1.1.1 Seasonal Ice Formation and River Freeze-Up

River ice formation is a dynamic process governed by both hydraulic and thermal conditions. Freeze-up generally begins with the formation of frazil ice and progresses through several distinct stages, ultimately leading to the development of a continuous ice cover. Figure 1.3 illustrates the simplified sequence of river freeze-up, from open water to a stabilized ice cover.

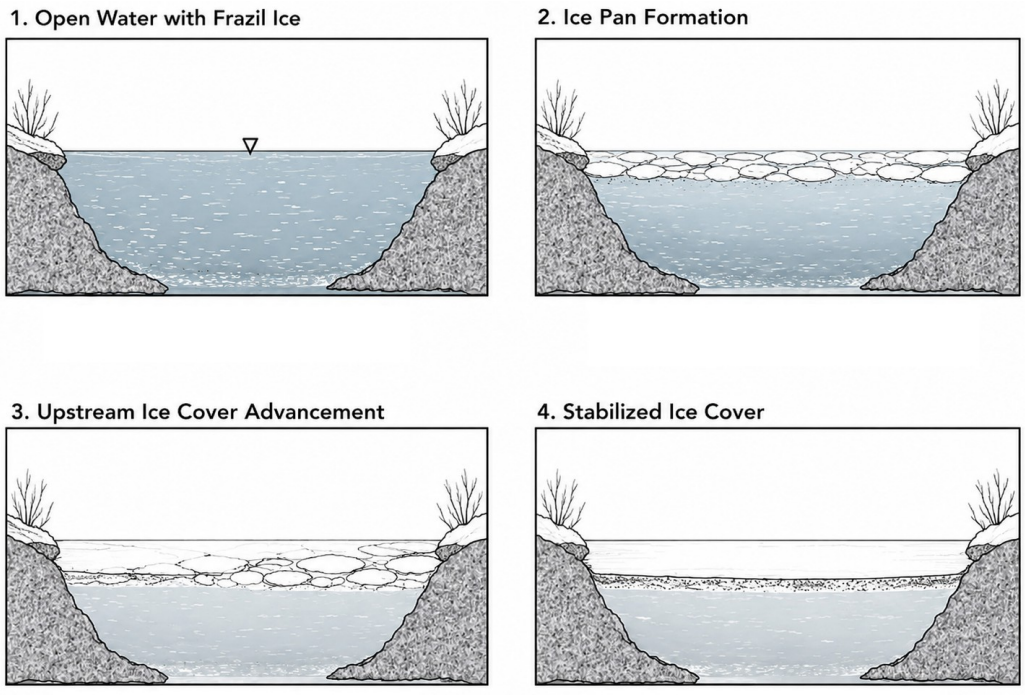


Figure 1.3. Conceptual schematic of the simplified main phases of river ice freeze-up, showing the progression from open water (top left) with frazil ice to ice pan formation, upstream ice cover advancement, and a stabilized ice cover (bottom right) (modified after [145]).

Cold water first becomes supercooled, promoting the formation of frazil ice crystals throughout the water column. As frazil ice rises to the surface, the crystals aggregate into floating ice pans, while border ice, which is stationary ice attached to the riverbanks, begins to form along the channel margins. During this stage, the central portion of the channel often remains open. As the ice pans consolidate and become lodged against the border ice or other obstructions, a continuous ice cover develops and progressively advances upstream. The advancing ice cover increases flow resistance and displaces water, resulting in greater flow depth and reduced flow velocity upstream. These hydraulic changes promote additional ice formation in regions where flow conditions were previously too energetic to sustain ice, further accelerating upstream ice cover development. The final ice-cover thickness depends on hydraulic and thermal conditions, including flow velocity, water depth, and heat exchange between the water and the atmosphere. Once the ice cover has stabilized, its underside reflects the freeze-up mechanism: thermally grown ice typically develops a relatively smooth underside, whereas ice covers formed from consolidated frazil pans or freeze-up ice jams generally exhibit much greater roughness. With time, thermal ice covers may become rougher because of ice accretion and deformation. Ultimately, the ice cover breaks up following the winter season as increasing thermal and hydraulic forcing weaken and mobilize the ice [11].

1.1.2 Secondary Flow in Meander River Channels

The meandering of rivers results from the interplay of various factors such as the movement of water around bends, the wearing away of riverbanks, and the transport of sediment. It is a complex phenomenon that has been the subject of much research. The presence of bends in river channels causes non-uniform cross sections and alters the velocity fields due to the influence of centrifugal acceleration. The velocity field in a river channel is commonly described in terms of primary and secondary flow components to account for the three-dimensional nature of fluid motion in river channels. The primary flow represents the main downstream (longitudinal) movement of fluid, while secondary circulation refers to the transverse and vertical flow superimposed on the primary streamwise motion. In turbulent flows, secondary currents are formally categorized by Prandtl [106] into two types: secondary currents of the first kind, driven by centrifugal forces and pressure gradients due to flow curvature (e.g., meander bends); and secondary currents of the second kind, which are weaker and arise from turbulent stress anisotropy near wall boundaries.

The first type of Prandtl's secondary currents, also known as the center region cell, is common in meandering river bends and is a result of vortex stretching that enhances the mean streamwise velocity [89]. The second type of Prandtl's secondary currents, also called corner flows, originate from turbulence anisotropy at the channel boundary, where the roughness of the wall and bed alters the relative strength of vortices. These weaker outer bank cells, with velocities on the order of 5% of the mean streamwise velocity, play an important role in protecting steep outer banks from erosion [22]. However, experimental studies often focus on the center region cell, which is far from the bank, and their relatively low accuracy and coarse grid failed to provide sufficient understanding for the underlying mechanisms of the two cells [18]. The imbalance between centrifugal force and pressure gradient at the channel's bend is responsible for generating the center region's secondary flow (as illustrated schematically in Figure 1.5, leftside). The centrifugal acceleration directs the flow towards the outer bank, increasing the water surface and resulting in a super-elevation effect, while the pressure difference acts in the opposite direction. The centrifugal acceleration force has a greater influence on the high-speed velocities at the water surface than the low-speed flow near the channel bend, where the pressure gradient force is greater. The smaller effect of centrifugal acceleration at the slow bottom layer results in flow moving towards the inner bank on the bed, leading to a single-cell secondary flow circulation [20, 38].

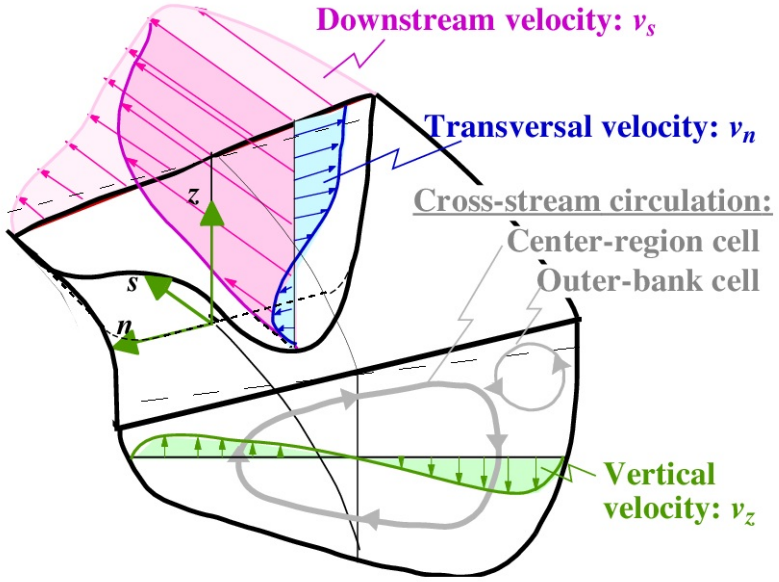


Figure 1.4. Schematic illustration of the cross-sectional Secondary flow sketch in an open curved channel [17]. The coordinate system is denoted by s, n, and z, representing the streamwise, cross-stream, and vertical directions, respectively.

In a curved open channel, secondary circulation causes the flow momentum to move laterally, shaping the spatial distribution of velocity and boundary shear stresses [22]. As a result, the classical helical motion covers most of the channel cross section, and is referred to as the centre-region cell. Additionally, there is a weaker counter rotating cell that is often present near the outer bank [18]. They explain that the downstream vorticity balance reveals the mechanisms governing the two circulation cells, where the dominant factors are the centrifugal force and the turbulent stresses across the stream. However, the confirmation of this finding through experiments has been hindered due to limited available data on these turbulent stresses that occur perpendicular to the flow direction. The illustration in Figure 1.4 shows the two circulation cells present in a bend section of an open channel, where the coordinate system is defined according to the direction of channel flow.

The flow dynamics in an ice-covered river differ from those in an open channel due to the presence of ice cover as an upper boundary. This results in two distinct flow layers, associated with the ice-water interface and the bed (Figure 1.5, right). In studies of lateral velocity components in highly curved ice-covered river bends using flumes, two stacked counter-rotating helical cell motions were observed [146, 166], as illustrated in Figure 1.5.

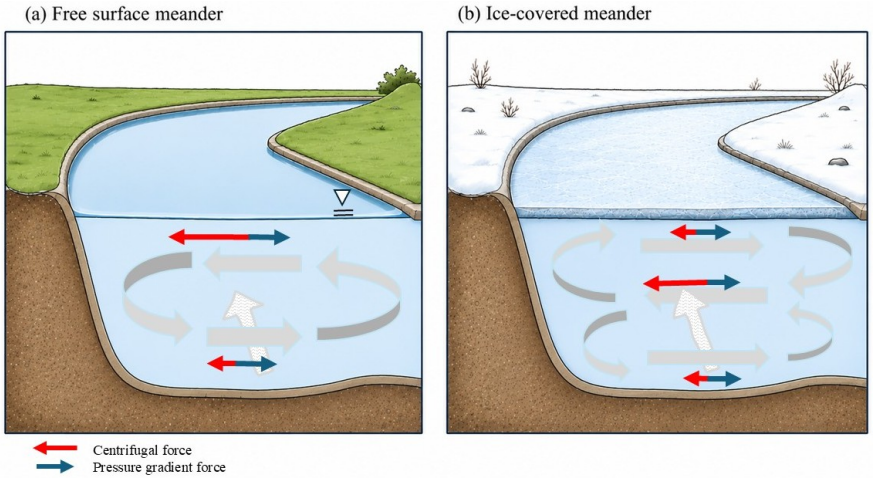


Figure 1.5. Schematic illustration of the cross-sectional force balance and secondary circulation structure in a curved channel under free-surface and ice-covered conditions. Note that depending on channel geometry a free-surface or ice-covered curved channel flow may include a co-rotating inner bank cell and/or a counter-rotating outer bank cell. Solid grey arrows indicate the secondary flow direction, while the patterned straight arrow denotes the main flow direction. Subplots and arrows are not drawn to scale. The conceptual framework in this figure is adapted and extended from [145].

It was found that the maximum velocity flow around the middle of the water column is directed towards the outer bank by centrifugal acceleration. The flow near the ice-cover and channel bed boundaries deflects towards the bend's inner bank. Together these mechanisms result into the two counter-rotating helical cell pattern [38]. This approach, called two-layer hypothesis, is generally adopted in ice-covered flow analysis, where two counter-rotating top and bottom cells are formed [145].

Despite decades of research demonstrating the fundamental role of secondary circulation in river processes, many aspects of its physical origin and dynamic behavior remain incompletely resolved. The mechanisms governing the generation, maintenance, and interaction of secondary cells with the mean flow and turbulence structure remain complex, particularly in curved channels where centrifugal effects, pressure gradients, boundary roughness, and anisotropic Reynolds stresses act simultaneously. Thus, secondary flows remain a central topic in fluvial hydraulics, drawing continued attention from hydraulic engineers, geomorphologists, hydrologists, and ecohydraulic researchers. The extensive body of literature on open- and closed-channel flow, including numerous review studies, reflects both the progress achieved in understanding these complex three-dimensional structures and the persistent open questions regarding their scaling, turbulence interactions, and implications for natural river systems.

1.2 Fluid Dynamics and Turbulence Theory

1.2.1 Turbulent Flows

Although turbulence does not have a single universally accepted definition, several key features are consistently observed in turbulent motions. Turbulent flow is characterized by irregular three-dimensional fluid motion. Turbulence is commonly found in natural systems and strongly influences geomorphic and hydraulic processes, including river morphodynamics, sediment transport, and channel evolution.

The systematic study of turbulence was advanced by Osborne Reynolds in 1883, who demonstrated through controlled pipe-flow experiments that fluid motion transitions between laminar and turbulent regimes depending on flow conditions. This transition is

commonly characterized using the Reynolds number, a dimensionless parameter defined as the ratio of inertial forces to viscous forces within a flow. The Reynolds number can be expressed as:

$$Re = \frac{\rho U L}{\mu} = \frac{U L}{\nu}, \tag{1.1}$$

where ρ is fluid density ($\mathrm{kg\,m^{-3}}$), U is a characteristic velocity ($\mathrm{m\,s^{-1}}$), L is a characteristic length scale (m) (e.g., flow depth or hydraulic radius), μ is dynamic viscosity ($\mathrm{kg\,m^{-1}\,s^{-1}}$ or Pa s), and $\nu = \mu/\rho$ is kinematic viscosity ($\mathrm{m^2\,s^{-1}}$). When inertial effects dominate over viscous damping (i.e., at sufficiently high Reynolds numbers), disturbances amplify and the flow becomes unstable, ultimately developing into turbulence. For example, in closed channel flow, values of $Re \leq 2000$ are generally associated with laminar flow, values of $Re \geq 4000$ with fully turbulent flow, and the intermediate range corresponds to transitional conditions.

1.2.2 Velocity Distribution in Open and Closed Channels

Open-channel flows are flows whose boundaries are in contact with another fluid or with the atmosphere (i.e., they possess a free surface), such as rivers or canals. Closed-channel flows, on the other hand, are flows that are entirely enclosed by rigid boundaries, such as conduits, pipes, ducts, or fully ice-covered (frozen) river channels. The flow characteristics change from an open-channel cross section to a closed-channel cross section, revealing several fundamental aspects of more complex flow behavior. Figure 1.6 presents a comparison of velocity profiles in open-channel and closed-channel flows, highlighting the differences between laminar and turbulent conditions for the same discharge. In both channel types, the laminar velocity profile is strongly curved, with significant variation in velocity across the flow depth. In contrast, the turbulent velocity profile is much more uniform over most of the flow cross section, but exhibits a much steeper velocity gradient near the solid boundaries.

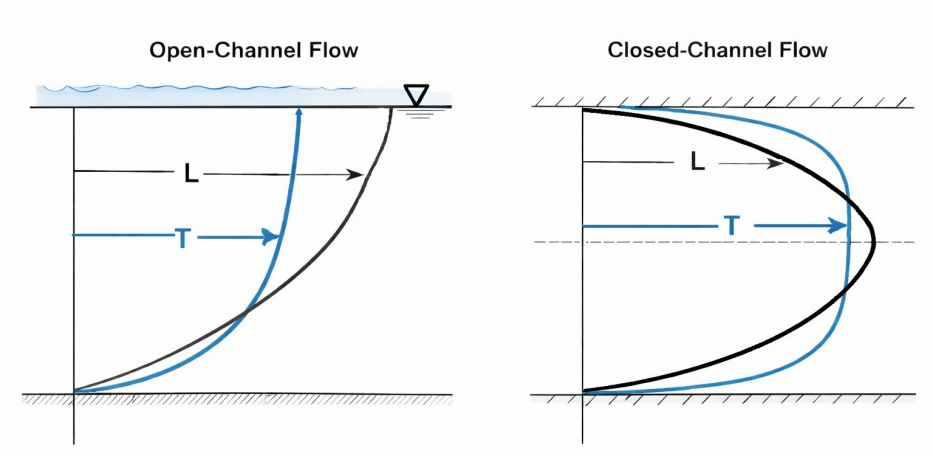


Figure 1.6. Schematic representation comparing laminar and turbulent velocity profiles in steady, uniform flow for an open-channel (left) and a closed-channel (right). The notation L (in black) denotes laminar flow, and T (in blue) denotes turbulent flow (Adapted from [134]).

This behavior can be explained by the different mechanisms of momentum transfer in laminar and turbulent flows. In laminar flow, momentum exchange occurs primarily through molecular diffusion, which is relatively weak and acts over very small distances. As a result, velocity differences across the flow persist, due to flow resistance at the boundary, leading to a pronounced curvature in the velocity profile [50]. In turbulent flow, however, momentum is transported not only by molecular motion but also by turbulent eddies, larger fluid parcels that move across layers of different mean velocity. These eddies enhance momentum mixing and reduce velocity differences across much of the flow depth, producing a flatter velocity distribution [104, 92].

Near the boundary, the no-slip condition requires the velocity to be zero at the wall. In turbulent flow, the wall restricts the normal motion of eddies, reducing their ability to transfer momentum close to the boundary. Consequently, the velocity gradient becomes very steep in this near-wall region, forming what is commonly referred to as the viscous sublayer and buffer region [104].

1.2.3 Shear Stress and Flow Resistance Relationship

Shear stress, τ, acting as the force per unit area, is the viscous resistance to fluid movement. It governs the velocity gradient near solid boundaries and directly controls energy dissipation, flow resistance, and head loss. In open-channel flows, the velocity gra-

dients between the fluid and the solid boundary imposed by the no-slip condition, where $u_{\text{fluid}}(y = 0) = u_{\text{wall}}$ and for a stationary wall $u_{\text{wall}} = 0$, determining the bed stability and sediment entrainment. Physically, shear stress represents the mechanism by which momentum is transferred between adjacent fluid layers and between the fluid and the boundary [104].The viscous component of the shear stress is given by

$$\tau_v = \mu \frac{du}{dy}, \tag{1.2}$$

where μ is the dynamic viscosity ($\mathrm{kg\,m^{-1}\,s^{-1}}$ or $\mathrm{Pa\,s}$), u is the streamwise velocity ($\mathrm{m\,s^{-1}}$), and y is the coordinate normal to the boundary (m). In turbulent flows, which are the focus of this study, the total shear stress consists of both the viscous shear stress and the Reynolds (turbulent) shear stress arising from velocity fluctuations. The total shear stress can therefore be written as

$$\tau = \mu \frac{du}{dy} - \rho\overline{u'v'}, \tag{1.3}$$

where $-\rho\overline{u'v'}$ represents the Reynolds shear stress ($\mathrm{N\,m^{-2}}$ or Pa) associated with turbulent momentum transport [104, 92].

The shear stress distribution differs between open-channel and closed-channel flows (Figure 1.7). In steady, uniform open-channel flow, shear stress decreases approximately linearly from a maximum at the bed to zero at the free surface, where it becomes negligible due to the absence of tangential resistance at the air-water interface [92]. In fully developed turbulent pipe flow, shear stress is greatest at the wall and decreases linearly toward the centerline, where it equals zero [145].

Energy losses associated with boundary roughness occur primarily through two physical mechanisms: viscous (skin) friction and turbulence generated by flow separation. Skin friction arises from molecular interactions between the fluid and the boundary under the no-slip condition. Its magnitude therefore depends on the total wetted surface area over which frictional forces act. Turbulence-related losses primarily arise from flow separation around roughness elements that protrude into the flow, generating recirculation zones and turbu-

lent wakes. The height and geometry of these roughness elements influence the size and intensity of the wake region, thereby affecting the magnitude of turbulent energy dissipation. Relative roughness, defined as the ratio of roughness height to flow depth, is therefore an important parameter because it indicates the proportion of the flow that is influenced by wake turbulence.

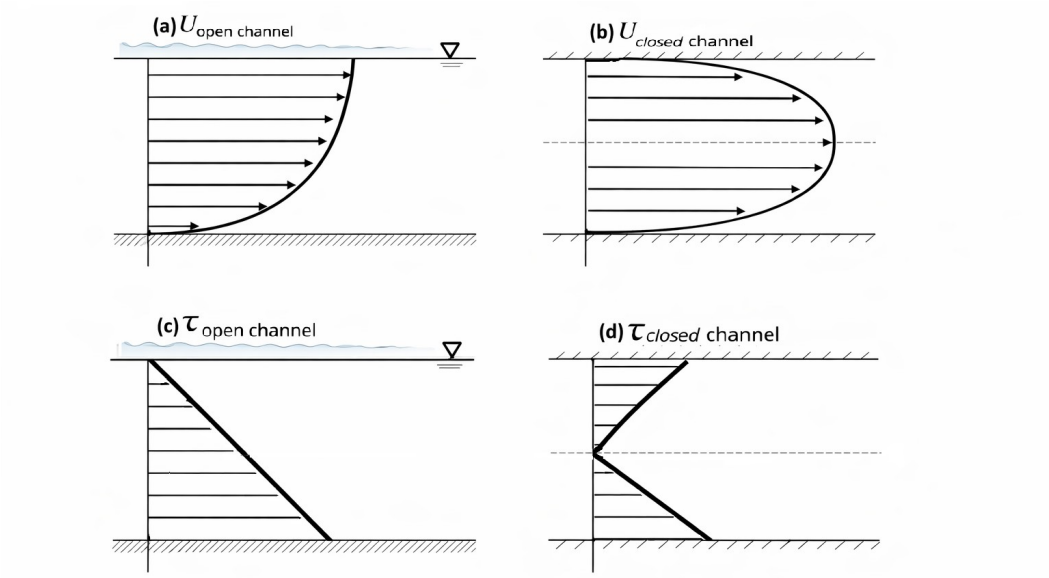


Figure 1.7. Schematic comparison of velocity and shear stress distributions in steady, uniform flow for open- and closed-channel configurations. Panels (a) and (b) illustrate representative streamwise velocity profiles for open-channel and closed-channel flow, respectively. Panels (c) and (d) show the corresponding shear stress (τ) distributions. The dashed line in the closed-channel profiles denotes the channel centerline. The schematics are not drawn to scale (modified after [145]).

In natural rivers, hydraulic resistance is commonly divided into two primary components: grain resistance and form resistance. Grain resistance is associated with the interaction between the flow and individual sediment particles on the bed surface, including both viscous skin friction and small-scale wake formation behind grains. Form resistance, on the other hand, arises from larger-scale bed and channel features such as dunes, bars, channel curvature, vegetation, and large woody debris. These morphological features induce additional flow separation and turbulence, which increase energy losses beyond those associated with grain-scale roughness alone. As the prominence of bedforms, channel irregularities, and instream obstacles increases, the contribution of form resistance typically becomes more significant.

Hydraulic resistance in open-channel flow is commonly quantified using the Darcy–Weisbach friction factor, f, a dimensionless coefficient relating flow velocity to energy losses caused by boundary friction. For steady, uniform flow, the friction factor can be expressed as

$$f = \frac{8gRS}{U^2}, \tag{1.4}$$

where g is the gravitational acceleration ($\mathrm{m\,s^{-2}}$), R is the hydraulic radius (m), S is the energy slope (-), and U is the cross-sectionally averaged flow velocity ($\mathrm{m\,s^{-1}}$). This formulation links hydraulic resistance directly to measurable flow parameters. The friction factor can also be expressed as a function of relative roughness [27]:

$$\frac{1}{\sqrt{f}} = \frac{U}{\sqrt{8gR_hS}} = 2.03\log\left(\frac{R_h}{k_s}\right) + 2.21, \tag{1.5}$$

where k_s is the equivalent roughness height (m). Rearranging gives

$$f = \left[2.03\log\left(\frac{12.2R_h}{k_s}\right)\right]^{-2}. \tag{1.6}$$

In natural channels, the total boundary shear stress, τ_0, can be partitioned into grain shear stress and form shear stress. Correspondingly, the Darcy–Weisbach friction factor may be partitioned into grain, f_g, and form,f_f, components [49]. Since the bed shear stress may also be written as

$$\tau_0 = C_d\rho U^2, \tag{1.7}$$

the friction factor can be related to shear stress as

$$f = \frac{8\tau_0}{\rho U^2}. \tag{1.8}$$

Therefore, both grain resistance from sediment particles and channel roughness elements (which are larger in scale) contribute to the total boundary shear stress and the resulting friction factor of the flow.

1.2.4 Turbulence Scales

The multiscale nature of turbulence was clearly described by Richardson (1922), who stated: "Big whorls have little whorls, which feed on their velocity; and little whorls have lesser whorls, and so on to viscosity." This description introduced the concept of the energy cascade, which remains central to modern turbulence theory.

In turbulent flows, kinetic energy is unevenly distributed in space and time due to the interaction between inertial and viscous forces. When inertial forces dominate (i.e., at high Reynolds numbers), velocity and pressure fluctuations develop, forming rotating flow structures known as eddies. These eddies exist over a wide range of spatial and temporal scales. The largest eddies are typically of the order of the characteristic flow dimension (e.g., flow depth or hydraulic radius) and contain most of the turbulent kinetic energy. Through nonlinear interactions governed by the Navier–Stokes equations, energy is transferred progressively from larger eddies to smaller ones. This process continues until the smallest scales are reached, where viscous effects dominate and kinetic energy is dissipated into heat. This mechanism is known as the Richardson–Kolmogorov energy cascade [67, 135, 149].

Turbulent flows are therefore characterized by a hierarchy of length and time scales. The integral length scale L represents the size of the largest energy-containing eddies. A practical estimate of this large-eddy length scale is given by:

$$L \approx \frac{k^{3/2}}{\varepsilon}, \tag{1.9}$$

where k is the turbulent kinetic energy ($\mathrm{m^2\,s^{-2}}$) and ε is the turbulent kinetic energy dissipation rate ($\mathrm{m^2\,s^{-3}}$) [104, 149].

The turbulent kinetic energy k represents the mean kinetic energy per unit mass associated with velocity fluctuations. It is defined as:

$$k = \frac{1}{2}\left(\overline{u'^2} + \overline{v'^2} + \overline{w'^2}\right), \tag{1.10}$$

where u', v', and w' are the fluctuating velocity components in the x, y, and z directions ($\mathrm{m\,s^{-1}}$), and the overbar denotes time averaging. The turbulent kinetic energy k has units of $\mathrm{m^2\,s^{-2}}$.

In turbulence analysis, the instantaneous velocity is commonly decomposed using Reynolds decomposition into a mean and a fluctuating component. The instantaneous velocity component u_i can be written as:

$$u_i = U_i + u_i', \tag{1.11}$$

where u_i is the instantaneous velocity component ($\mathrm{m\,s^{-1}}$), U_i is the mean (time-averaged) velocity component ($\mathrm{m\,s^{-1}}$), and u_i' is the turbulent velocity fluctuation ($\mathrm{m\,s^{-1}}$). The fluctuation u_i' represents the random, time-varying part of the velocity caused by turbulence. It oscillates around the mean velocity U_i, and its time average is zero:

$$\overline{u_i'} = 0. \tag{1.12}$$

A schematic illustration of this decomposition is shown in Figure 1.8.

The dissipation rate ε represents the rate at which turbulent kinetic energy is converted into heat by viscous action at small scales. It controls the transfer of energy through the cascade and links the large energy-containing eddies to the smallest dissipative scales. In general form, it is defined as [104]:

$$\varepsilon = 2\nu\overline{S_{ij}S_{ij}}, \tag{1.13}$$

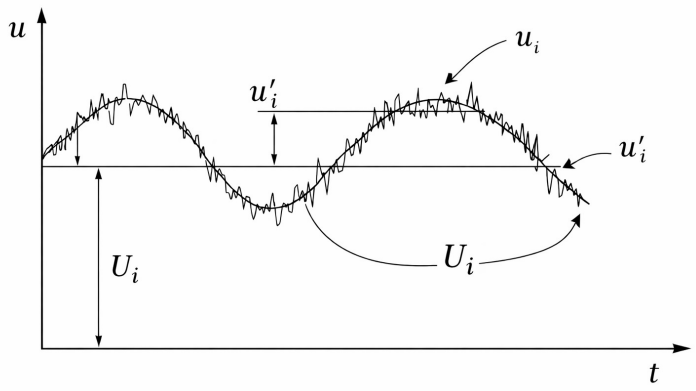


Figure 1.8. Schematic representation of Reynolds decomposition showing the instantaneous velocity u_i, mean velocity U_i, and turbulent fluctuation u'_i as a function of time t (Modified after [42]).

where ν is the kinematic viscosity ($m^2\ s^{-1}$) and S_{ij} is the fluctuating strain-rate tensor (s^{-1}). The dissipation rate ε has units of $m^2\ s^{-3}$.

The corresponding integral time scale T represents the characteristic lifetime of the large energy-containing eddies and can be expressed as:

$$T = \frac{L}{U}, \tag{1.14}$$

where U is a characteristic mean velocity ($m\,s^{-1}$). Together, these scales describe how energy is transferred across different sizes of motion in turbulent flows.

Chapter 2

Background Literature Review

The transverse circulation, commonly referred to as secondary flow or helical flow, is an important feature of river channels, defining the hydraulic dynamics and affecting sediment transport and channel morphodynamics. In 1877, experiments by James Thomson showed that a helical flow is obtained in a curved stream of water, with inward motion near the bed and outward motion near the surface. A major advancement came with Dean's study [37], which provided the analytical solution for laminar, fully developed flow in a curved pipe (or conduit), introducing the concept of Dean vortices. They showed that in curved pipe flow, the primary streamwise motion is accompanied by a secondary circulation that shifts the region of maximum streamwise velocity toward the outer wall and reduces the overall flow rate for a given pressure gradient. Although derived for pipes, this work established the mathematical framework for curvature-induced secondary flow applicable to river bends.

In the early 20th century, Prandtl [106] provided a physical explanation by classifying secondary flow into first kind (curvature-driven) and second kind (turbulence-driven), and laid the theoretical framework for understanding cross-stream circulation in rivers. Many subsequent studies extended these concepts to river-channel flows, leading to the development of modern field-based, experimental, and numerical investigations of secondary circulation in meandering rivers. Although numerous studies exist, particularly for open-channel conditions, only a selective review of key contributions is presented here, progressing from foundational to more recent work. Given the extensive and continually expanding

body of literature, it is beyond the scope of this chapter to provide a comprehensive review; instead, emphasis is placed on studies most relevant to meandering rivers, turbulence and secondary flow.

2.1 Free-surface Channel Studies

In 1944, Quraishy [111] showed via controlled flume experiments that small-scale bed perturbations ("skew scales") arose from localized scour driven by flow instability and sediment transport gradients near channel margins. These evolved into skew shoals that altered near-bed flow and induced transverse velocity gradients. Once a critical morphology was reached, secondary circulation developed, with outward surface flow and inward near-bed sediment transport, promoting bank erosion and point-bar deposition and initiating channel bends. In 1957, Leopold and Wolman interpreted meander evolution as a flow–morphology feedback governed by secondary (helical) circulation [161, 73]. They showed that channel curvature induces transverse velocity gradients, producing centrifugal acceleration, leading to water-surface superelevation and elevated shear stress at the concave bank. This drives outer-bank erosion and inner-bank deposition via near-bed return flow, promoting point-bar growth and lateral accretion. Increasing curvature amplifies these processes, sustaining bend migration, while overbank flows redistribute sediment across the floodplain.

Yokosi (1967), through field measurements [164], demonstrated that energy is transferred from large-scale eddies, generated by flow instability and channel boundaries, to smaller scales via a cascade process consistent with Kolmogorov theory. Importantly, interactions between the free surface, bed, and sidewalls produced anisotropic turbulence and strong velocity gradients, particularly in corner and near-boundary regions, leading to the formation of secondary currents. These circulatory motions redistributed momentum and sediment laterally and vertically, thereby modifying the mean flow structure beyond classical boundary-layer assumptions. Townsend (1968) investigated turbulence in an asymmetrical compound channel and showed that flow interaction between the main channel and adjacent floodplain generated strong shear layers at their interface [144]. These shear layers produced vortex sheets and a mixing zone characterized by intense turbulence and lateral momentum exchange. This momentum transfer redistributed flow energy, distorted veloc-

ity fields, and enhanced transverse gradients, promoting secondary circulation and lateral mixing in non-uniform channels.

Hey (1976), in a study on the geometric controls of river meanders [56], showed macroturbulent flow structures (including both single-cell and more realistic twin-cell secondary flow patterns) generate alternating zones of acceleration and deceleration along the channel, producing periodic lateral shear and flow asymmetry. These flow instabilities drive erosion at outer banks and deposition at inner banks, thereby controlling meander wavelength and curvature. By relating bend length directly to channel width, the study demonstrated how turbulence-driven flow organization regulates planform geometry through feedbacks between flow structure and sediment transport.

De Vriend (1981) showed that secondary circulation dominated velocity redistribution in curved rectangular pipe channels, with helical flow shifting high velocities toward the outer bank and lower velocities toward the inner bank [36]. This redistribution was governed primarily by convective momentum transport associated with the secondary flow, rather than by diffusion alone, and resulted in both horizontal skewing and vertical flattening of the velocity profile. They showed that radial and vertical components of secondary flow played distinct roles, with vertical convection driving local velocity changes and radial convection enabling cross-sectional redistribution. At higher curvature, these interactions led to strong non-uniformity, and even the emergence of additional secondary vortices near the outer bank. Davies and Sutherland (1983) re-evaluated extremal hypotheses for river behavior and showed that turbulent flows are governed by nonlinear feedback mechanisms rather than energy minimization principles [35]. They demonstrated that turbulence generates coherent, organized flow structures that enhance momentum transfer and energy dissipation, particularly through interactions between flow, boundary roughness, and sediment transport. These processes promote channel adjustment toward states of increased friction factor, reflecting enhanced resistance and turbulence intensity, rather than minimized energy expenditure. This hypothesis was more consistent with observed turbulent flow and sediment transport. Utami and Ueno (1984) used flow visualization and image processing to resolve the three-dimensional structure of turbulent open-channel flow [147], showing that turbulence organizes into coherent structures driven by boundary interactions. These structures generated spatial gradients in velocity, rotation, and divergence, driving vertical and lateral momentum exchange. In particular, ejections transported low-momentum fluid away from the bed, while sweeps conveyed high-momentum fluid downward, collec-

tively redistributing energy and shaping the mean flow structure. This demonstrated that turbulence-induced coherent motions are key mechanisms governing the flow. Webel and Schatzmann (1984) investigated transverse mixing in open-channel flow using tracer experiments [156]. They showed that the mixing coefficient reflects combined contributions from turbulent diffusion, secondary flow, and velocity non-uniformity, with turbulent diffusion dominating under typical river conditions. Secondary flow was significant mainly near channel boundaries or in low aspect-ratio flows. For large aspect ratios and fully developed turbulence, mixing was largely independent of channel width and controlled by flow resistance and bed roughness. Variations in mixing were linked to turbulence intensity and eddy scale, with smoother beds promoting larger energy-containing structures and enhanced mixing. Prinos et al. (1985) showed that velocity contrasts in compound channels generate strong shear layers at the main channel-floodplain interface, producing intense turbulence and vortical structures [108]. These drive lateral momentum transfer and elevated apparent shear stress, redistributing velocity and turbulence across the section, particularly under narrow-channel conditions where mixing extends throughout the flow. The study demonstrated that turbulence levels were sensitive to relative depth and roughness, increasing with greater roughness and decreasing floodplain depth.

Kotsovinos (1988), in a theoretical analysis of the origin of secondary currents in straight, wide rectangular channels, showed that they arise from hydrodynamic instability driven by Reynolds normal stress anisotropy [68]. A balance between destabilizing normal stresses, which drive fluid away from boundaries, and stabilizing viscous effects leads to a marginal stability state that generates organized cellular secondary flows. These circulatory cells induce transverse momentum transport and redistribute velocity across the channel, with characteristic scales governed by flow depth, consistent with experimental observations.

Early studies largely reported bulk turbulence characteristics in compound channels without resolving the mechanisms by which overbank flow modifies them. Knight and Shiono (1990) addressed that gap by providing detailed measurements of velocity, turbulent intensities, and Reynolds stresses within the shear layer, demonstrating that the introduction of a floodplain generated strong lateral shear, secondary currents, and large-scale eddies that altered momentum transfer processes. These mechanisms produced non-linear Reynolds stress distributions, enhanced turbulent kinetic energy near the interface, and spatially variable eddy viscosity and friction, fundamentally modifying flow structure com-

pared to single-channel conditions [65]. They extended their previous work by explicitly incorporating the physical processes that alter flow structure in compound channels, namely the interaction between bed-generated turbulence, lateral shear-layer turbulence, and secondary flows [129]. Using analytical development and large scale experimental data, it was shown that strong lateral depth variation modify momentum exchange through enhanced Reynolds stresses and secondary-flow-induced shear, which significantly redistribute velocity and boundary shear stress across the channel. The results demonstrated that these processes widen the shear layer, alter eddy viscosity, and must be included to accurately predict depth-averaged velocity and shear stress distributions [129].

Blanckaert and Graf (2001) experimentally studied flow and turbulence in a 120° curved open-channel bend with a mobile sand bed. They found a complex two-cell secondary circulation, consisting of a main helical cell and a weaker outer-bank counter-rotating cell near the surface, which shifts peak velocity toward the channel inner bank. The three-dimensional turbulence was reduced near the outer bank, showed significant spatial variability, and differed markedly from that in straight channels. These patterns influenced momentum exchange and shear stress distribution, with the outer-bank cell and lower turbulence found to have a protective effect on the outer bank by reducing local shear stress [25]. Blanckaert and De Vriend (2004) investigated the dynamics of secondary circulation in curved open-channel flow using detailed experiments and analysis of the vorticity balance and energy transfer. They showed that the centre-region cell was primarily driven by centrifugal forces, while turbulence mainly contributed to dissipation, with limited feedback to the mean flow. In contrast, the outer-bank cell resulted from the combined effects of centrifugal forcing and turbulence anisotropy induced by boundary proximity, where gradients in cross-stream turbulent stresses generated additional vorticity . The study further demonstrated that turbulence was not purely dissipative but could locally transfer kinetic energy back to the mean flow, influencing circulation strength. They showed that boundary changes controlled turbulence, circulation, and shear [18].

Van Balen et al. (2010) conducted a combined experimental and numerical investigation of turbulent flow in a strongly curved rectangular-section open-channel flume with constant curvature, and three flow depths. It was shown that the strength and structure of the curvature-induced secondary circulation, including the centre-region helical cell, outer-bank cell, and inner-bank shear layer, were strongly dependent on turbulence dynamics, particularly near the banks. Large-scale turbulent motions were found to interact with and

sustain the secondary flow structures, whereas small-scale turbulence acted primarily as a dissipative mechanism with limited influence on the mean flow pattern. The results revealed that large eddy simulation (LES) successfully reproduced experimentally observed features such as boundary layer detachment, internal shear layers, and the outer-bank secondary cell, while Reynolds-Averaged Navier-Stokes (RANS) models failed to capture these phenomena and significantly overestimated bed shear stresses. Turbulence was shown to regulate the magnitude and spatial distribution of shear stresses and energy losses [148].

Kashyap et al. (2012) extended previous research by investigating flow behavior in a rectangular curved flume, based on three experimental flow conditions and a series of numerical simulations. The primary parameters studied were curvature ratio, aspect ratio, and bed configuration (flat and deformed). Their results indicated that decreasing either curvature or aspect ratio in flat-bed cases led to a substantial increase in the strength of the primary cross-stream circulation, along with higher maximum bed shear stress and a greater contribution of transverse shear to the overall stress magnitude. Furthermore, at low curvature ratios, the primary circulation cell divided into two clockwise-rotating cells, with the inner-bank cell generating strong vorticity ejections. In contrast, higher curvature ratios promoted the formation of a counter-rotating cell near the outer bank. A similar splitting of the primary cell was also observed under lower aspect ratios. The study demonstrated how bend geometry controlled the distribution and intensity of bed shear stress and velocity [64].

The study by Yang et al. (2012) demonstrated that secondary currents originated in the near-boundary region due to lateral gradients in streamwise velocity, which generated transverse shear and initiated circulation. These near-boundary motions propagated into the main flow, forming organized secondary cells confined within regions bounded by zero shear stress. The authors further showed that secondary currents systematically developed from zones of lower velocity or boundary shear stress toward regions of higher values, with the strongest circulation occurring where near-bed velocity changed abruptly, such as at transitions between flow regions. In contrast, secondary currents were negligible where lateral velocity gradients were absent. Boundary conditions, especially bed variations, were identified as the primary drivers of secondary circulation [162].

Jamieson et al. (2013) experimentally investigated the turbulent flow structure, vorticity, and sediment dynamics in a laboratory channel bend under equilibrium clear-water scour conditions, both with and without stream barbs (submerged groyne-like struc-

tures). Using detailed acoustic Doppler velocimeter (ADV) measurements, they calculated Reynolds shear stresses, turbulent kinetic energy (TKE), turbulence scales, and vorticity fields, and related these to observed patterns of scour and deposition. The regions of increased scour were consistently associated with elevated nonprincipal Reynolds stresses, higher TKE, and strong vertical (z-) vorticity. In particular, outer-bank scour zones corresponded to enhanced streamwise–cross-stream Reynolds stress and significant velocity gradients. The presence of stream barbs altered the flow field by increasing turbulence and secondary circulation; however, their effectiveness depended strongly on stream barb size and configuration. Large barbs generated excessive turbulence between structures, leading to increased erosion, whereas smaller barbs more effectively redirected flow while limiting adverse turbulence effects. The study demonstrated that local scour in channel bends is governed by complex interactions between turbulence, vorticity, and flow structure, and showed the importance of optimizing barb design to balance flow redirection and turbulence generation [62].

The study by Blanckaert (2015) showed that flow separation at the inner bank of channel bends was driven by the interaction between streamline curvature and turbulence-induced secondary circulation, rather than geometry alone. A distinct shear layer formed at the boundary of the separation zone, characterized by strong velocity gradients, elevated turbulent kinetic energy, and intensified Reynolds shear stresses. These features were associated with a reversal of streamwise vorticity and vertical velocity. The authors demonstrated that the extent and structure of the separation zone were controlled by the production of turbulent kinetic energy, which depended on the accurate description of Reynolds stresses [16]. Wei et al. (2016) investigated the mechanisms controlling curvature-induced secondary flow in a laboratory flume by varying curvature ratio, Froude number, and bed roughness. The results showed that the commonly assumed linear increase of normalized secondary flow strength with curvature applied only to mildly curved channels, while stronger curvature led to nonlinear growth and eventual saturation due to interactions between primary and secondary flows. Bed roughness further modified these interactions, enhancing secondary flow over rough beds, whereas the Froude number had negligible influence[157].

Schreiner et al. (2023) linked time-averaged secondary circulation to the dynamics of instantaneous coherent flow structures using a vortex clustering approach applied to validate LES data in a curved open channel. This study demonstrated that secondary circulation cells emerged from the spatial organization and evolution of instantaneous vortices. The

results identified distinct sub-cells within the overall secondary flow, including inner-bank and center-region structures, each exhibiting different development patterns governed by their location and vorticity generation mechanisms. The study showed that weaker and transient circulation features, often obscured in mean flow analysis, played a significant role in shaping the overall flow structure and persisted farther downstream than previously recognized [121]. The study by Mei (et al 2026) tracked how turbulence structures change along the flow direction in a streight open channel as the water slows down and depth increases. It showed that turbulence becomes more connected over long distances (more coherent) and maintains its structure better downstream. It also found that although the flow slows, the turbulent energy actually increases and spreads differently, shifting toward intermediate scales and extending from near the bed toward the whole water depth. This helps explain how mixing, sediment movement, and flow behavior change in non-uniform river conditions. [84].

The scope and extent of experimental and numerical investigations into turbulent flow and its characteristics have expanded significantly in the 21st century, particularly with the advancement of high-precision measurement techniques such as particle image velocimetry (PIV) and laser Doppler anemometry (LDA). Given the vast and rapidly growing body of literature, this section presents only a selective overview of existing studies. Nevertheless, it provides a structured overview of the dominant research directions and highlights the key areas of focus that have shaped the present understanding of turbulent flow processes.

2.2 Ice-Covered Channel Studies

The effects of ice on river flows have been investigated under a wide range of ice conditions in river channels. Depending on geographical setting, study objectives, and socio-economic or hazard-related concerns, research has addressed a wide range of ice processes, including ice formation, breakup, ice jams, frazil and slush transport, as well as complete ice cover. Moreover, the logistical difficulties and measurement challenges in cold environments have historically limited the number of ice-covered flow studies compared to those on open-channel hydraulics. In this section, selected studies from the early 20th century to more recent contributions are reviewed to provide an overview of the development of this field.

An early USGS report (1913) systematically examined the effects of surface, frazil, and anchor ice on streamflow using field observations and analyses of climatic and hydraulic controls. It showed that ice disrupted the stage-discharge relationship by increasing flow resistance, altering velocity distributions, and inducing backwater effects, complicating winter flow estimation. They also showed that ice reduced discharge for a given stage, stored water within the channel, and could significantly diminish flow in low-gradient systems. It also demonstrated that winter discharge was strongly temperature-dependent, with freezing suppressing runoff and warming, even below $0^{\circ}\mathrm{C}$, enhancing flow through release of stored water [58]. The study by Barnes (1929) presented an early conceptual framework for understanding river ice processes in the emerging field of ice engineering, combining physical theory and field observations to explain the formation and behavior of frazil, anchor, and surface ice. They suggested that ice formation in rivers results from the rapid aggregation of pre-existing microscopic ice-like structures within supercooled water. This explained the sudden onset of frazil ice and its sensitivity to small temperature changes, and highlighted the reliance of effective ice jam control on physical mechanisms [7]. Frazier (1934) provided an early field-based investigation of the influence of ice processes on river discharge. It showed that winter discharge fluctuated systematically with air temperature, driven by the formation and decay of frazil-ice jams rather than changes in upstream inflow. During cooling, frazil ice accumulated into jams that obstructed flow and caused temporary upstream storage (e.g., Lake St. Croix), whereas warming led to jam breakup and increased discharge. The study further demonstrated that natural reservoirs enhanced and regulated these fluctuations, indicating that winter flow was governed by a coupled thermo-hydraulic mechanism involving ice formation, backwater effects, and storage [51].

Carstens (1968) examined river ice hydraulics by treating frazil/slush transport as a two-phase flow analogous to sediment transport, combining theory and laboratory studies. It extended suspension theory to buoyant particles, showing that their transport and vertical distribution follow modified diffusion-settling behavior. The results highlighted the roles of turbulence, buoyancy, and particle clustering in controlling concentration profiles, and introduced the concept of surface load transport, demonstrating that floating ice can dominate transport capacity near the free surface [29]. Michel and Ramseier (1971) developed a comprehensive classification of river and lake ice based on the combined consideration of ice formation history, structural layering, and crystal texture. Unlike earlier studies that focused primarily on isolated ice types or descriptive observations, this work introduced a systematic framework linking primary, secondary, and superimposed ice layers to their governing

meteorological and hydrodynamic conditions. They showed that ice mechanical properties provide a basis for predicting ice behavior in engineering applications [85]. Ashton (1978) reviewed river ice processes and showed its behavior is governed by highly dynamic interactions among fluid flow, heat transfer, and ice mechanics. The study highlighted the central role of frazil ice in initiating ice cover formation and controlling flow resistance, and identified ice jams as a critical and least understood phenomenon in river ice hydraulics. Ice cover was shown to significantly alter hydraulic characteristics (e.g. resistance and stage-discharge relationships), and emphasized the importance of thermal processes and turbulence in ice growth and decay [5]. Engmann experimentally investigated turbulent transverse diffusion in a straight rectangular channel under ice-covered conditions using tracer techniques. The results showed that ice cover alters flow structure, producing asymmetric velocity profiles with the maximum velocity shifted toward the smoother ice boundary. The transverse diffusion coefficient was reduced by about 50% compared to open-channel conditions, indicating a substantially decreased mixing efficiency due to suppression of large turbulent eddies by the surface cover. However, when normalized by shear velocity and hydraulic radius, the diffusion coefficient was comparable to open-water values, suggesting similar scaling behavior [46].

Beltaos (1984) developed a conceptual hydraulic model of river ice breakup to improve prediction of breakup onset and flooding. Using field data, they showed that breakup is controlled by the interaction of rising water levels, ice properties, and channel geometry, and occurs when the water stage exceeds the maximum stable freeze-up level, causing transverse cracking of the ice cover. It further demonstrated that breakup progression depends on the available flow width relative to ice sheet size, and introduced the concept of an "ice-clearing" discharge, a certain flow threshold above which the ice cover becomes unstable and is rapidly removed [8]. Shen and Yapa (1986) developed an empirical, time-dependent model to estimate the hydraulic resistance of river ice covers using an effective Manning's coefficient. Field data from the St. Lawrence River showed that ice-cover resistance varies systematically throughout the season, decreasing from high values after freeze-up due to smoothing of the ice underside and increasing again prior to breakup due to the formation of relief features and ice accumulations. The resistance was modeled as the sum of three components: a seasonal term, a melting-period term related to underside roughness, and a fluctuation term driven by frazil ice transport from upstream open water. The resistance was mainly controlled by flow velocity, air temperature, and open-water extent, with good agreement between modeled and observed data [128].

Ettema and Huang (1990) investigated ice formation in frequently transited navigation channels using experiments, field data, and numerical modeling. They showed that repeated vessel transits modify flow patterns and enhance ice accumulation by generating open-water tracks that refreeze into brash ice, forming thick porous layers that hinder navigation. Ice formation was controlled by transit frequency, vessel characteristics, channel geometry, flow conditions, and thermal effects, and a predictive model was developed to estimate ice growth and distribution [48]. Teal et al. (1994) evaluated methods for estimating mean velocity in ice-covered straight channels using point measurements. A two-power law model was used to represent vertical velocity profiles and validated with field and laboratory data. The study quantified measurement bias under varying bed and ice roughness and showed that the standard two-point method (0.2 and 0.8 depth) yields low bias (2%)consistently, and applying a correction factor (0.98) reduces this bias to near zero. Single-point methods showed larger and more variable errors depending on flow and roughness conditions. They provided a framework linking velocity-profile structure to measurement accuracy [140].

The study by Tsai and Ettema (1994) analyzed the influence of ice cover on flow structure, sediment transport, and transverse bed slopes in a 180° curved alluvial channel using laboratory experiments and an adapted theoretical model. A curved flume with a mobile sand bed was tested under open-water and simulated ice-covered conditions to quantify changes in flow and morphology. Ice cover modified flow distribution and secondary circulation, leading to a transition from a single to a double helical flow structure. While transverse bed slopes were only slightly reduced (about 15–20%), bedload transport was significantly decreased, indicating a strong impact on sediment dynamics. Additional factors such as increased underside roughness and lower water temperature further reduced transverse bed slopes. Although ice cover altered both flow structure and sediment transport in bends, its effect on transport was more pronounced than on bed morphology [145].

Smith and Ettema (1997) studied flow resistance in a straight ice-covered alluvial channel and developed a semi-empirical model. Ice cover increased flow depth and reduced bulk velocity, while modifying bed morphology by increasing dune length and decreasing dune steepness. Hence, bed-load transport rates were significantly reduced (to about 25% of open-water values). While bed-form resistance decreased, cover resistance increased, altering total resistance. They showed that open-water transport relations remain applicable with robust estimation of bed shear stress and proposed a framework for predicting resistance and

depth–discharge relationships [130]. Sukhodolov et al. (1999) examined turbulence structure in a straight, ice-covered sand-bed river using ADV measurements. Ice cover increased flow nonuniformity and three-dimensionality due to variations in cover roughness and bed morphology. Mean velocity and Reynolds stresses generally followed two-layer models in the core region but deviated near boundaries. Vertical turbulence exchange was reduced due to stable stratification, and coherent structures (ejections and sweeps) exhibited scales on the order of flow depth. The results highlight limitations of two-dimensional models for ice-covered river flows [138].

Muste et al. (2000) examined flow structure and sediment transport in a straight ice-covered alluvial channel using a discriminator laser-doppler velocimeter to simultaneously measure water and sediment velocities, allowing detailed analysis of two-phase flow behavior. Ice cover increased flow depth and reduced bulk velocity, leading to significant reductions in both suspended and bed-load transport rates. It also altered turbulence structure and Reynolds shear stress distribution, producing asymmetric flow due to differing roughness at the bed and cover. A velocity lag between water and sediment was observed, with sediment moving slower than the fluid, especially near the bed. Increasing ice-cover roughness further reduced sediment transport and enhanced turbulence near the ice, highlighting coupled interactions among turbulence, sediment transport, and ice-cover roughness [87]. Later, Ettema (2002) presented a comprehensive review of how river ice influences alluvial-channel hydraulics, sediment transport, and morphology, highlighting the importance of relative length and time scales and noting that many processes remain poorly quantified [47]. Prowse and Beltaos (2002) reviewed the hydrological role of river ice and its climatic controls, showing that ice cover increases hydraulic resistance and water levels, inducing ice-jam flooding that can exceed open-water events, while freeze-up processes reduce winter discharge through storage and flow obstruction. They showed that long-term climatic trends generally delay freeze-up and advance break-up, shortening the ice season, and that changes in temperature, precipitation, and snowmelt can alter both the timing and severity of ice processes. They showed river ice is a critical control on hydrology, governed by coupled hydraulic, thermal, and meteorological interactions [109].

The study by Demers et al. (2011) examined secondary flow structure in a natural ice-covered meander using PC-ADP measurements. The primary flow was deflected toward the outer bend, while secondary flows formed helical patterns with magnitudes about one order smaller than the main flow. Two stacked counter-rotating helical cells were ob-

served at the bend entrance, but this pattern evolved downstream into a single cell rotating opposite to typical open-channel flows. Flow structure varied with bed morphology, ice roughness, and flow redistribution, and frazil ice did not prevent helical motion. The study highlighted the complexity and spatial variability of secondary circulation in ice-covered bends and limitations of simplified two-cell models [38]. Aghaji Zare et al. (2016) analyzed hydraulic resistance in ice-covered alluvial rivers using 4 months of field measurements (ADCP and sonar). A new method was developed to estimate composite resistance directly from measured velocity profiles by separating ice and bed zones and applying log-law analysis. Results showed that ice cover increases resistance and alters velocity distribution, with dynamically varying under-ice roughness. The proposed method improved agreement with measured resistance compared to existing approaches [3]. Peters et al. (2017) experimentally examined flow beneath partial ice cover in a straight flume using 3D ADV measurements. Partial cover redistributed flow, reducing velocities beneath the ice and increasing them in the open region. The flow was divided into open, covered, and transitional zones, with a consistent transition width. Shear stress beneath the ice exhibited a three-zone structure, while increasing Froude number enhanced flow redistribution and reduced the transition zone [101].

Kämäri et al. (2017) used ground-penetrating radar (GPR) surveys and borehole measurements across multiple cross-sections, complemented by vertically averaged flow velocities from ADCP and concurrent bathymetric observations in the meandering sand-bed Pulmanki River in northern Finland, providing one of the first high-resolution cross-sectional datasets of ice thickness in a multi-bend river reach. Ice thickness was highly heterogeneous, with cross-sectional differences of up to approximately 32 cm and pronounced intra-section variability. Thinner ice consistently occurred in regions of higher flow velocity, particularly near outer banks and bend apices, whereas thicker ice was associated with shallow, low-velocity regions such as inner banks and point bars. They indicated that hydrodynamic processes, especially flow velocity and turbulence, exert a primary control on ice thickness by enhancing turbulent heat flux from the water to the ice underside, thereby suppressing ice growth. GPR was demonstrated to be an effective tool for mapping river-ice thickness with high accuracy (approximately ±3 cm), while also enabling reliable discrimination between floating and bottom-fast ice. Although the observed mean ice thickness agreed reasonably well with classical thermal growth formulations (e.g., Stefan's equation), such models were unable to reproduce the strong spatial variability induced by flow dynamics and channel morphology [63].

Koyuncu and Le (2022) examined the effects of ice cover on velocity profiles and bed shear stress in a natural meandering bend using ADCP field measurements under open-water and ice-covered conditions. Ice cover altered the vertical velocity structure, producing asymmetric profiles that deviated from the classical logarithmic law, while a quartic velocity distribution better represented the flow under full ice cover. Ice effects were most pronounced near the banks, where velocity and shear stresses were strongly modified by turbulence, curvature, and ice roughness. Ice cover also changed secondary flow patterns and redistributed shear stress toward the banks, with implications for sediment transport and channel morphology, particularly during transitional conditions such as breakup [69]. Li et al. (2025) studied the hydrodynamic behavior of flow in pools with submerged rigid leafless vegetation under ice-covered conditions using combined large-scale straight (rectangular) flume experiments and 3D numerical simulations. The vegetation significantly altered velocity structure, transforming vertical profiles from logarithmic to quasi-S shapes and reducing velocities within the vegetated zone while increasing them in the shear layer above. Vegetation also generated strong disturbances in lateral and vertical velocities, promoting secondary currents and enhanced 3D flow. Under ice-covered conditions, turbulence characteristics were further modified, with increased turbulent kinetic energy near the surface and altered velocity distributions resembling pipe-like flow [75].

The growing attention to winter flow management in recent years highlights the need for improved understanding of flow and transport processes under ice cover. This need has become more pronounced in regulated systems where winter discharges exceed pre-regulation conditions, requiring more reliable predictions of flow stage, sediment transport, and channel adjustments [47]. Despite the extensive body of literature on alluvial-channel hydraulics, the effects of ice-covered conditions on these processes remain insufficiently addressed, and most analyses of ice-covered flows have not incorporated key complexities, such as channel curvature, full ice cover, and ice-cover roughness. This study built upon previous research to examine ice-cover influences on flow hydraulics. However, although sediment plays a critical role in channel behavior, sediment processes were not addressed here due to PIV measurement limitations under fully ice-covered conditions and remain an important direction for future research. Further details on the research motivation and objectives are provided in the next chapter.

Chapter 3

Scope, Objectives, and Novelty

3.1 Research Motivation

Rivers in cold regions are frequently covered by seasonal ice during winter, which alters the hydraulic and turbulent structure of the flow. The presence of an ice cover transforms the river from an open-channel system with a free surface into a closed-channel flow bounded by rigid surfaces at both the bed and the ice underside. This change significantly modifies the turbulence structure, momentum transfer mechanisms, and the development of secondary circulation in curved channels. Despite the importance of these processes, the hydrodynamics of ice-covered river bends remain insufficiently understood.

In natural meandering rivers, channel curvature generates secondary circulation that redistributes momentum across the cross-section. These secondary motions play a fundamental role in sediment transport, bank erosion, and channel morphology. While the dynamics of secondary flow in open-channel bends have been extensively studied, relatively few experimental investigations have addressed how these mechanisms change when the free surface is replaced by an ice cover. The presence of a rigid upper boundary modifies velocity gradients, turbulence production, and the interaction between bed-generated and surface-generated turbulence. As a result, the structure, strength, and spatial distribution of secondary circulation in ice-covered bends may differ significantly from those observed in

open-channel conditions.

Existing studies of ice-covered rivers have investigated a wide range of hydraulic processes, including flow resistance, stage–discharge relationships, velocity distributions, and turbulence characteristics. Experimental measurements using techniques such as acoustic Doppler velocimetry (ADV) and particle image velocimetry (PIV) have significantly improved the understanding of flow behaviour beneath ice covers. However, most of these studies have focused on straight channels or simple flow configurations. In contrast, detailed investigations of three-dimensional flow structure, turbulence, and secondary circulation in ice-covered meander bends remain limited. High-resolution experimental datasets addressing these complex flow features are scarce, restricting both the physical understanding of flow dynamics in curved ice-covered channels and the validation of numerical models.

The growing interest in resource development, infrastructure expansion, and environmental management in northern regions further emphasizes the need for improved understanding of ice-covered river hydraulics. Reliable knowledge of flow behaviour under ice is essential for predicting sediment transport, contaminant dispersion, and hydraulic resistance in cold-region rivers. Consequently, addressing the lack of detailed experimental observations of turbulent flow behaviour in ice-covered river bends represents a critical research need.

This research therefore aims to provide a systematic experimental investigation of turbulent flow structures and secondary circulation in an ice-covered meandering channel. By combining high-resolution velocity measurements with detailed analysis of turbulence statistics, this study seeks to identify the governing physical mechanisms controlling flow behaviour in ice-covered bends and to provide datasets that support the development and validation of future numerical models.

3.2 Objectives and Novelty

The primary objective of this research is to improve the understanding of how an ice-covered surface influences the hydraulic and turbulent characteristics of flow in a curved channel. In particular, the study investigates the development of secondary circulation, tur-

bulence structure, and momentum redistribution in an ice-covered river bend. Although previous studies have demonstrated that the presence of a rigid upper boundary significantly modifies turbulence and velocity distributions, the detailed mechanisms governing these changes remain incompletely understood for a curved channel.

To address these knowledge gaps, this research combines high-resolution experimental measurements with detailed turbulence analysis to investigate the interaction between channel curvature, ice-cover surface and roughness, and turbulent flow structures. The main objective of the study is therefore divided into several specific research objectives, which are outlined below.

Objective 1: Characterization of three-dimensional flow structure in a bend section

The first objective is to obtain detailed measurements of three-dimensional velocity components and turbulence characteristics within the cross-section of a fully developed flow in an ice-covered channel bend. Particle Image Velocimetry (PIV) is used to capture spatially dense velocity fields with high temporal resolution.

The novelty of this dataset lies in several aspects. First, it represents one of the first detailed experimental investigations using PIV to examine secondary circulation and turbulence structures beneath an ice cover in a curved channel. Second, the measurements provide a spatially dense representation of the three velocity components across the entire cross-section. Third, the experiments are conducted in a sharp ($135°$) channel bend, allowing the influence of strong curvature and secondary flow development to be examined under ice-covered conditions.

The resulting velocity dataset also provides a valuable benchmark for the calibration and validation of future numerical simulations of ice-covered river bends.

Objective 2: Analysis of turbulence structure and turbulence kinetic energy

The second objective is to examine the spatial distribution and dynamics of turbulence within the cross-section of an ice-covered channel bend. In particular, the structure and distribution of turbulence kinetic energy (TKE) are investigated in detail.

Previous studies, such as Blanckaert and de Vriend (2005), have examined turbulence behaviour in open-channel bends and demonstrated that turbulence activity varies significantly between the inner and outer banks. However, the influence of an ice cover on these turbulence structures remains poorly understood due to the limited number of studies on ice-covered channel bends.

By analysing the turbulence statistics obtained from the PIV measurements, this objective seeks to quantify how the presence of an ice cover alters turbulence production, redistribution, and dissipation mechanisms within the cross-section.

Objective 3: Investigation of momentum redistribution due to secondary circulation

The third objective is to investigate how secondary circulation influences the redistribution of momentum and shear stresses within the cross-section of an ice-covered channel bend. In curved channels, centrifugal forces generate transverse pressure gradients that drive counter-rotating secondary cells. These motions redistribute streamwise momentum and significantly influence bed shear stress distribution.

Understanding how these mechanisms change in the presence of an ice cover is important because the rigid upper boundary modifies velocity gradients and turbulence production. Through detailed analysis of velocity fields and Reynolds stresses, this objective seeks to clarify the mechanisms responsible for the formation and evolution of the dual counter-rotating secondary cells commonly observed in curved channels.

Objective 4: Influence of surface roughness on flow structure in a curved channel

The fourth objective is to evaluate how boundary roughness, particularly the roughness of the ice cover, influences the flow structure in an ice-covered channel bend. In ice-covered channels, friction is generated by both boundaries, and the relative roughness of the bed and ice surfaces can significantly influence velocity distributions and turbulence production.

This objective investigates the relationship between velocity distribution, roughness characteristics, and resistance parameters such as friction factors. Existing resistance re-

lationships are examined to assess whether modifications are required to account for the influence of channel curvature and the presence of an ice cover.

Objective 5: Influence of discharge on flow structure

The fifth objective is to investigate the influence of discharge on the hydraulic and turbulent characteristics of flow in an ice-covered channel bend. Changes in discharge modify the bulk flow velocity and Reynolds number, thereby altering the relative importance of inertial and turbulent forces within the bend. This objective examines how increasing or decreasing discharge affects the overall flow field, turbulence structure, and momentum transport under ice-covered conditions.

Objective 6: Influence of aspect ratio on flow structure

The sixth objective is to evaluate the influence of the channel aspect ratio (flow width-to-depth ratio) on the flow structure within an ice-covered channel bend. The aspect ratio governs the geometric confinement of the flow and influences the interaction between the bed and ice-cover boundary layers. This objective investigates how variations in channel geometry modify the organization of secondary circulation, the distribution of streamwise velocity, and the locations of high- and low-momentum regions within the channel cross-section.

Using the experimental PIV dataset, this study examines how changes in hydraulic conditions modify the intensity and location of secondary circulation and turbulence structures across the channel.

Research Contributions

The results obtained from the objectives outlined above provide a comprehensive experimental dataset and a detailed analysis of turbulent flow behaviour in ice-covered river bends. The study offers direct observations of secondary circulation, momentum redistribution, and turbulence structures beneath an ice cover.

These findings contribute to improved understanding of flow behaviour in cold-region rivers and provide valuable data for the development and validation of numerical models. Ultimately, the research contributes to advancing predictive capabilities for hydraulic processes in ice-covered rivers, which is important for engineering applications such as sediment transport prediction, environmental assessment, and river management in cold climates.

3.3 Thesis Structure

This thesis presents a detailed experimental investigation of turbulent flow behaviour and the influence of key hydraulic variables on the development of secondary circulation in an ice-covered river bend. The study provides high-resolution measurements of three-dimensional velocity fields and turbulence statistics across the full cross-section of a curved channel under ice-covered conditions. These measurements offer valuable insight into the mechanisms governing momentum redistribution, turbulence structure, and secondary flow development in closed-channel bends. The resulting dataset can serve as a reliable benchmark for the calibration and validation of future numerical simulations of ice-covered river bends.

Chapter 4 describes the experimental methodology used to collect the velocity and turbulence data analysed in this study. This chapter introduces the laboratory flume and the curved channel section used for the measurements and provides a description of the Particle Image Velocimetry (PIV) technique employed to obtain three-dimensional velocity components across the entire cross-section. In addition, the chapter discusses the experimental setup, measurement procedures, and data processing methods. The challenges associated with performing PIV measurements beneath a simulated ice cover, as well as the solutions implemented to ensure accurate and reliable velocity measurements are also explained in this section.

Chapter 5 presents a detailed investigation of the influence of discharge (flow rate) on the turbulent flow structure within the ice-covered bend. The chapter examines how variations in flow rate affect velocity distributions, turbulence characteristics, and the development of secondary circulation. Relevant datasets used for the analysis are introduced and

discussed. Furthermore, previous studies investigating flow behaviour in both open-channel and closed-channel bends are reviewed to provide context for the experimental observations obtained in this work. **This chapter has been published in full as: Ebrahimi, S., Rennie, C. D., Mohammadian, A., and Schreiner, H. K. (2026),** ***Secondary flow dynamics and turbulence in an ice-covered sharp bend channel at different subcritical Froude numbers*****, Environmental Fluid Mechanics, 26(2), 13.**

Chapter 6 investigates the influence of ice-cover roughness on momentum redistribution in an ice-covered channel bend. In particular, the chapter examines how variations in ice-cover roughness modify the distribution of momentum components and the associated turbulence structure. The results provide insight into the interaction between ice-generated and bed-generated turbulence and their combined influence on the overall flow structure. **This chapter has been published in full as: Ebrahimi, S., Mohammadian, A., and Rennie, C. D. (2026),** ***Roughness influence on secondary circulation and momentum distribution in an ice-covered river bend*****, Physics of Fluids, 38(2).**

Chapter 7 examines the influence of the flow aspect ratio (width-to-depth ratio) on the development and strength of secondary circulation in the ice-covered bend. By comparing different hydraulic conditions, this chapter evaluates how variations in channel geometry and flow depth modify the spatial structure of secondary vortices and the associated turbulence characteristics within the cross-section. **This chapter has been drafted as a journal paper for submission entitled:** ***Influence of Channel Aspect Ratio on Secondary Flow Circulation and Turbulence in an Ice Covered Rectangular Bend Channel*****.**

Finally, Chapter 8 summarizes the key findings of the thesis and highlights the main contributions of this research to the understanding of turbulent flow behaviour in ice-covered river bends. The chapter also outlines the implications of the results for hydraulic modelling and suggests directions for future research.

Chapter 4

Methodology and Data

4.1 River Channel Meander

River meanders represent a fundamental geomorphological feature of many alluvial rivers. Extensive scientific literature indicates that meandering develops as rivers adjust their flow energy while transporting water and sediment across relatively low-gradient landscapes. When a river flows through unconstrained terrain, variations in velocity and shear stress cause erosion along the outer bank of bends and sediment deposition along the inner bank. These processes gradually shift the river channel laterally and create the characteristic curved planform of meandering rivers [74, 99].

Meandering rivers play an important role in shaping landscapes and sustaining diverse ecological environments. The hydraulic and geomorphological processes occurring within river bends create a variety of habitats, including shallow point bars, deeper pools, and vegetated floodplain areas. Such heterogeneity supports a wide range of aquatic organisms, riparian vegetation, and terrestrial wildlife [155, 54]. The ecological diversity associated with meandering channels is therefore closely linked to the dynamic interaction between flow processes and sediment deposition.

Meandering rivers also contribute to the development and maintenance of flood-

plains. During periods of high discharge, rivers may overflow their banks and deposit sediment across adjacent floodplain areas. This overbank sedimentation enriches soils with nutrients and supports riparian ecosystems while simultaneously influencing the long-term evolution of valley landscapes [97, 160]. Over time, the lateral migration of meanders can create complex floodplain topography characterized by scroll bars, abandoned channels, and floodplain wetlands.

From a hydraulic perspective, river bends are of particular interest in river engineering and fluvial geomorphology because flow characteristics change significantly in curved channels. Velocity distribution becomes asymmetrical, secondary circulation develops, and sediment transport processes are altered. These factors influence channel stability, erosion patterns, and the long-term morphology of river systems [45, 60]. Understanding these hydraulic mechanisms is essential for predicting channel migration, managing flood risks, and designing infrastructure such as bridges, levees, and river training works.

Furthermore, recognizing the natural tendency of rivers to meander is important for sustainable land and water resource management. Allowing sufficient space for river migration and avoiding development within active floodplains can reduce the risks associated with bank erosion and flooding. Consequently, river meanders provide valuable information about historical channel movement and play a key role in guiding environmental management and river restoration strategies [26, 160].

4.2 Physical Model of Bend Channel

Obtaining detailed 3D velocity measurements in natural rivers, particularly under ice-covered conditions, is extremely challenging due to logistical constraints, safety considerations, and the spatial and temporal variability of natural flows. Full cross sectional measurements of velocity fields in such environments are therefore rarely achievable. For this reason, laboratory physical modeling is widely used in hydraulic research to investigate complex flow processes under controlled conditions. Physical models allow researchers to isolate the influence of individual parameters while minimizing the effects of environmental variability that are commonly encountered in field measurements [24, 141]. The use of a laboratory-scale physical model therefore provides valuable insights into the 3D flow struc-

tures and hydraulic processes that occur in river bends, which are often difficult to observe directly in natural river systems [98, 105].

Laboratory flumes provide a controlled experimental environment in which hydraulic conditions such as discharge, flow depth, channel geometry, and boundary conditions can be systematically varied. This approach enables repeatable experiments and detailed observation of flow structures, including secondary circulation, turbulence, and velocity redistribution within channel bends. Numerous studies have demonstrated that physical models of curved channels can successfully reproduce the essential hydraulic processes observed in natural meandering rivers, including the development of helical secondary flow and the associated redistribution of momentum and bed shear stress across the channel cross section [157, 136].

In this study, a physical model representing a sharp curved river channel was used in the Hydraulics Laboratory at the University of Ottawa. The experimental setup and the bend flume used in this study are shown in Figure 4.1.

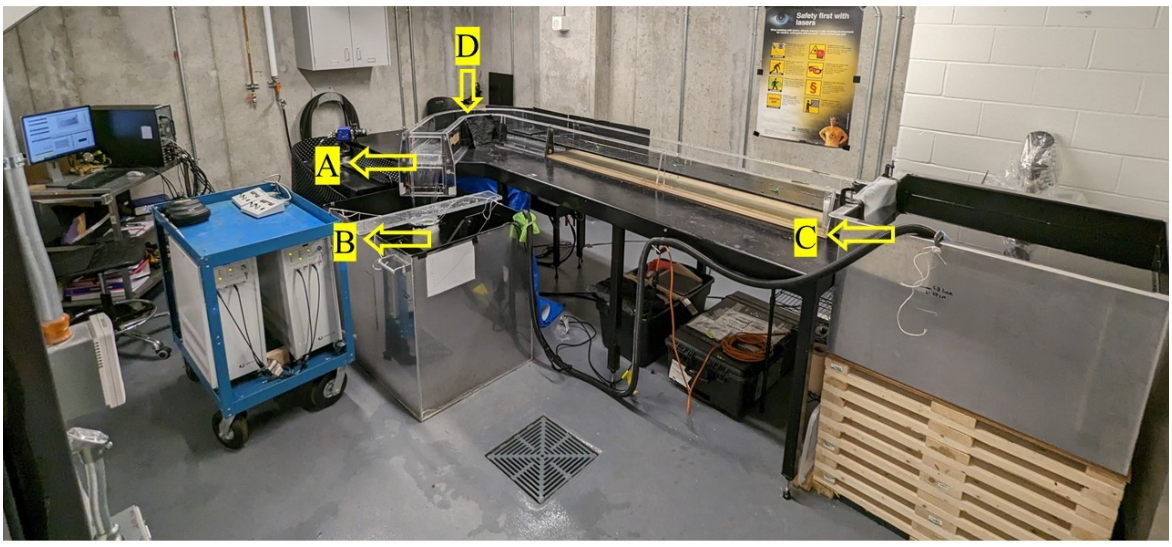


Figure 4.1. The 135° bend channel with transparent plexiglass walls and a rectangular bed. In the figure, the adjustable gate used to regulate the flow depth is indicated by letter *A*, the outlet tank by *B*, the inlet tank by *C*, and the measurement section located at the bend apex by *D*.

The experiments were conducted in a laboratory bend flume within a dedicated PIV laboratory with controlled lighting and surroundings to provide the optical conditions necessary for PIV measurements. The flume allows controlled adjustment of flow conditions, enabling multiple experiments to be performed within the same geometric configuration. This ensures consistency across experimental runs and allows the influence of selected variables to be examined independently.

All experimental cases in this research were conducted using the same flume configuration to ensure comparable hydraulic conditions throughout the study. This approach enabled a systematic analysis of the flow behavior within the bend channel. Parameters such as discharge, water depth, and wall roughness conditions were carefully controlled during each experimental run.

4.2.1 Physical Model of the Ice Cover

To reproduce the presence of an ice cover at the free surface of the flow, a rigid cover made of marine-grade mahogany plywood was used. This material was selected because it provides a flat and structurally stable surface that maintains its shape when exposed to moisture and repeated contact with water. To improve the optical conditions required for flow measurements, the underside of the wooden panel was covered with a layer of matte black adhesive vinyl (see Figure 4.2).



Figure 4.2. Application of a black adhesive vinyl mat on the ice cover to improve the optical conditions of the experiments.

This treatment reduces reflections and light scattering from the surface, thereby minimizing glare and improving image quality during optical measurements.

In addition, the vinyl coating provides a smooth and uniform boundary that approximates the hydraulically smooth underside of natural river ice. The resulting composite surface exhibits a very small equivalent roughness height ($k_s \approx 0.1\,\text{mm}$) compared with the flow depth ($H = 0.06\,\text{m}$), corresponding to a relative roughness of $k_s/H \approx 1.7 \times 10^{-4}$. Under these conditions, the boundary can be considered hydraulically smooth.

Table 4.1. Surface materials and corresponding roughness parameters used in the experiments

Surface	**Material**	$\mathbf{k_s}$ **(mm)**	$\mathbf{k_s/H}$
Top wall (smooth cover)	Vinyl-covered wood	0.1	1.7×10^{-4}
Top wall (rough cover)	Vinyl-covered wood with screws	5.0	0.083
Bottom wall	Plexiglass	0.003	5.0×10^{-5}
Side walls	Plexiglass	0.003	5.0×10^{-5}

To represent rough ice-cover conditions, uniformly distributed roughness elements were installed on the vinyl-covered surface. Black wood screws with a head height of approximately $5\,\text{mm}$ were attached to the underside of the cover at a spacing of about $4.5\,\text{cm}$. These screws provide rigid and repeatable roughness elements that remain fixed during the experiments. The black coloration of the screws also preserves the optical contrast required for Particle Image Velocimetry (PIV) measurements. This configuration produced an effective roughness height of approximately $k_s = 0.005\,\text{m}$, resulting in a relative roughness of $k_s/H \approx 0.083$. A schematic representation of the rough ice-cover configuration is shown in Figure 4.3, where the x, y, and z directions correspond to the streamwise, cross-stream, and vertical directions of the flow, respectively. Note that the cross-stream direction is also denoted by n in Chapter 5; thus, y and n are used interchangeably.

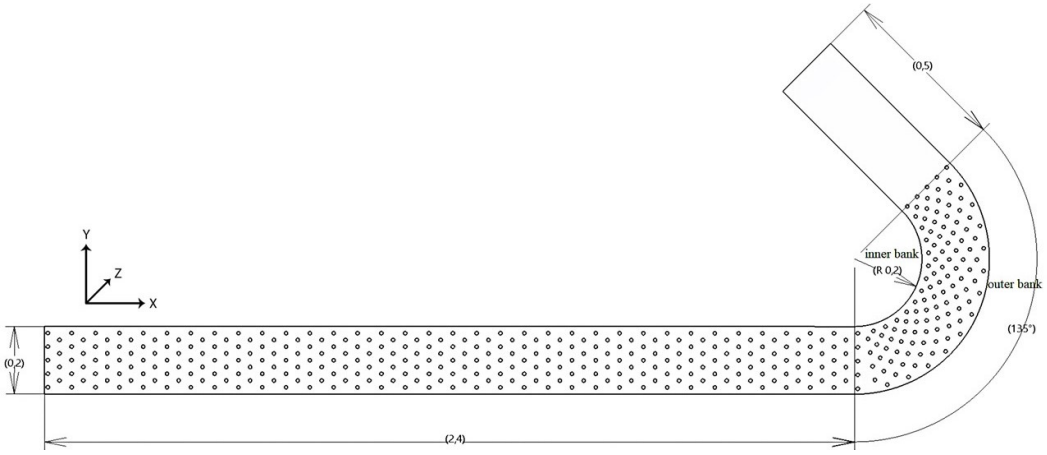


Figure 4.3. Schematic of the 135° bend physical model for rough ice-cover configuration and the arrangement of roughness elements used for the PIV experiments. The x, y, and z directions represent the streamwise, cross-stream, and vertical directions of the flow, respectively (Credit: Julien Pierrat)

In this study, the hydraulic resistance of the ice cover is described using the relative roughness parameter (k_s/H), because it provides a direct and physically meaningful representation of the interaction between the flow depth and the size of the roughness elements. Unlike empirical resistance coefficients such as Manning's n, which integrate multiple sources of resistance into a single calibrated parameter, the use of relative roughness allows the effects of the ice-cover boundary to be isolated and systematically evaluated under controlled laboratory conditions. This approach is particularly suitable for the present experimental configuration, where the geometry and roughness characteristics of each boundary are explicitly defined.

4.2.2 Verification of Fully Developed Flow

To ensure that velocity measurements were obtained under fully developed flow conditions, the required hydrodynamic entrance length was estimated using a standard empirical correlation for turbulent internal flows. Although some previous studies have assessed flow development by visually examining measured velocity profiles [151], the present study adopts an analytical approach based on the hydrodynamic entrance length to provide an objective and repeatable assessment. The experimental flume has a rectangular cross-section with all four boundaries wetted.

The cross-sectional area of the flume is $A = 0.012\,\mathrm{m}^2$, and the wetted perimeter is $P = 0.52\,\mathrm{m}$. The hydraulic diameter is therefore calculated as $D_h = \frac{4A}{P} = \frac{4(0.012)}{0.52} = 0.0923\,\mathrm{m}$. Using the bulk flow velocity of $U_b = 0.12\,\mathrm{m\,s^{-1}}$ and the kinematic viscosity of water at approximately $20\,^\circ\mathrm{C}$, $\nu = 1.0 \times 10^{-6}\,\mathrm{m^2\,s^{-1}}$, the Reynolds number is calculated as $\mathrm{Re} = \frac{U_b D_h}{\nu} \approx 1.1 \times 10^4$, confirming that the flow is fully turbulent.

For turbulent flow in ducts, the hydrodynamic entrance length can be estimated using the empirical relationship [78]

$$\frac{L_e}{D_h} \approx 4.4\,\mathrm{Re}^{1/6}, \tag{4.1}$$

where L_e is the hydrodynamic entrance length. Substituting the calculated Reynolds number into Eq. (6.2) gives $L_e = 4.4\,\mathrm{Re}^{1/6} D_h \approx 1.92\,\mathrm{m}$, which corresponds to approximately $\frac{L_e}{D_h} \approx 21$.

The available straight inlet section upstream of the bend is

$$L_{\mathrm{inlet}} = 2.40\,\mathrm{m},$$

or approximately

$$\frac{L_{\mathrm{inlet}}}{D_h} \approx 26.$$

Since the available inlet length exceeds the required hydrodynamic entrance length, the flow can be considered fully developed before entering the bend and the measurement section.

4.3 Flow Conditions Scaling

Dimensionless parameters were employed to characterize the flow conditions and to enable comparison between laboratory-scale experiments and real-world hydraulic systems. Such parameters express the relative magnitude of dominant forces acting within a fluid and are therefore essential for establishing dynamic similarity between model and prototype flows. In incompressible channel flows, the flow dynamics are primarily governed by the interaction between inertial, viscous, and gravitational forces. Among the available similarity criteria, the Reynolds number (Re) and the Froude number (Fr) are most commonly used in studies of river hydraulics. The Reynolds number represents the ratio of inertial to viscous forces and is typically used to characterize the flow regime (laminar, transitional, or turbulent). In contrast, the Froude number represents the ratio of inertial to gravitational forces and governs the hydraulic regime, determining whether the flow is subcritical, critical, or supercritical.

In the present experiments, full Reynolds number similarity could not be achieved due to geometric constraints imposed by the laboratory flume. Achieving Reynolds similarity would have required either unrealistically high flow velocities or significantly larger model dimensions, which were not feasible in the experiments laboratory conditions. Instead, all experiments were conducted at sufficiently high Reynolds numbers ($Re \gtrsim 4{,}000$), ensuring fully turbulent flow conditions. Under such conditions, previous studies have demonstrated that the flow structure becomes largely independent of Reynolds number, and viscous effects are confined to near-wall regions [80, 4]. Additionally, the experimental setup was constrained by the requirements of Particle Image Velocimetry (PIV) measurements, which necessitated sufficient flow depth to avoid optical interference near both the bed and the free surface.

Consequently, Froude similarity was adopted as the primary scaling criterion. This approach ensured that the ratio between inertial and gravitational forces was preserved, which is essential for reproducing flow depth characteristics typical of natural channels [94]. Moreover, Froude similarity is more readily achievable in laboratory flumes, as it only requires that the Froude number be preserved between model and prototype ($Fr_m = Fr_p$). This condition yields

$$\lambda_U = \frac{U_m}{U_p} = \sqrt{\frac{H_m}{H_p}} \tag{4.2}$$

where λ_U denotes the velocity scale, H_m is the model flow depth, and H_p is the prototype channel mean depth. From Froude similarity, the velocity scaling relationship is expressed as $\lambda_U = \sqrt{\lambda_H}$, where $\lambda_H = H_m/H_p$ is the geometric (depth) scale, noting that the depth scale is equal to the characteristic geometric scale only for an undistorted model. This relationship indicates that the velocity scale is proportional to the square root of the characteristic length scale, making Froude-based scaling particularly suitable for modeling river-channel flows [55].

While maintaining a more realistic natural width-to-depth aspect ratio of approximately 10 would imply a flow depth of about 2 cm for the given channel width, such shallow flows were not suitable for reliable velocity measurements due to experimental limitations. Therefore, the investigated flow depths were selected in the range of 5 to 8 cm. Experiments were conducted at depths of 5, 6, 7, and 8 cm, with a representative depth of 6 cm adopted for the majority of the tests. This range allowed for the systematic evaluation of the effects of flow rate, boundary roughness conditions, and aspect ratio variations on 3D flow structure, as summarized in Table 4.2.

Applying Eq. 5.3 for the representative flow depth of $H_m = 0.06\,\mathrm{m}$ used in this study, and considering the Rideau River in Ottawa as the prototype, the characteristic flow conditions were defined by a mean depth of $H_p = 5\,\mathrm{m}$, a channel width of $B_p = 100\,\mathrm{m}$, and an average velocity of $U_p = 1\,\mathrm{m/s}$. The corresponding laboratory model dimensions were $B_m = 0.20\,\mathrm{m}$ and $H_m = 0.06\,\mathrm{m}$.

The geometric (depth) scale was therefore calculated as

$$\lambda_H = \frac{H_m}{H_p} = \frac{0.06}{5} = 0.012 = 1.2 \times 10^{-2}. \tag{4.3}$$

Based on Froude similarity, the velocity scale follows as

$$\lambda_U = \sqrt{\lambda_H} = \sqrt{0.012} \approx 0.11. \tag{4.4}$$

These results indicate that the model velocity is approximately 11% of the prototype velocity. Accordingly, the prototype velocity corresponding to a given model velocity U_m may be expressed as

$$U_p = \frac{U_m}{\lambda_U}. \tag{4.5}$$

For the present experiments, model velocities ranging from $U_m = 0.04$ to $0.13\,\mathrm{m/s}$ correspond to prototype velocities of approximately 0.36 to $1.18\,\mathrm{m/s}$, respectively. The corresponding laboratory Froude numbers ranged from approximately 0.05 to 0.17.

Table 4.2. Summary of experimental flow conditions and corresponding hydraulic parameters. Here, k_s is the roughness height (mm), H is the flow depth (cm), B/H is the aspect ratio with constant channel width $B = 20$ cm, U_b is the bulk velocity (m/s), Q is the discharge (L/s), $m = \frac{Q^2}{gA^3}$ is the momentum function, $Fr = \frac{U_b}{\sqrt{gH}}$ is the Froude number, and $Re = \frac{U_b D_h}{\nu}$ is the Reynolds number based on the hydraulic diameter $D_h = \frac{4A}{P}$.

Case	k_s (mm)	H (cm)	B/H (-)	U_b (m/s)	Q (L/s)	m (-)	Fr (-)	Re (-)
1	0.1	6	3.3	0.12	1.44	0.122	0.15	11000
2	0.1	6	3.3	0.09	1.08	0.069	0.12	8300
3	0.1	6	3.3	0.04	0.48	0.014	0.05	3700
4	0.1	6	3.3	0.13	1.44	0.122	0.16	11000
5	5	6	3.3	0.13	1.44	0.122	0.16	11000
6	0.1	5	4.0	0.10	1.00	0.102	0.14	8000
7	0.1	7	2.9	0.10	1.40	0.073	0.12	10400
8	0.1	8	2.5	0.10	1.60	0.064	0.11	11400

This range includes the estimated prototype value for the Rideau River ($Fr \approx 0.14$), indicating that the selected laboratory conditions reproduced subcritical prototype flow conditions with reasonable dynamic similarity. This agreement indicates that the selected laboratory conditions adequately reproduce the subcritical flow regime of the prototype, thereby satisfying the requirements of dynamic similarity under Froude scaling. Furthermore, the range of tested flow conditions was selected to represent typical hydraulic states observed in natural rivers, particularly during periods of stable ice cover and moderate discharge. These values are consistent with field measurements reported in previous studies (e.g., [6], [9]), and were chosen to span a range of flow regimes. As a result, the selected flow cases enable a systematic investigation of variations in secondary flow structures and their behavior under ice-covered conditions.

Although the exact geometric similarity, particularly with respect to the width-to-depth aspect ratio, could not be strictly maintained as the commonest natural dimensions, this approach allowed a balance to be achieved between hydraulic similarity requirements and experimental measurement constraints, while still capturing the primary flow characteristics of interest. The adopted scaling strategy ensured that the dominant physical processes were appropriately represented, with Froude number similarity preserving riverine dynamics and sufficiently high Reynolds numbers maintaining turbulent flow conditions.

4.4 Velocity Data Measurement

PIV is a non-intrusive optical measurement technique widely used for investigation of fluid flow fields. It enables the characterization of instantaneous velocity distributions by tracking the motion of tracer particles seeded in the flow. These particles follow the fluid motion, allowing the local velocity vectors to be inferred from their displacement over a known time interval [1, 113]. In a PIV setup, the flow is illuminated by a pulsed laser sheet, and successive images of the seeded particles are captured using one or more cameras. The displacement of particle patterns between consecutive image pairs is determined using cross-correlation algorithms, which provide velocity vectors over a grid of interrogation regions. This approach allows for high-resolution, planar measurements of complex flow structures while preserving the spatial and temporal characteristics of the flow [158, 113].

In stereo-PIV, two cameras are positioned at different viewing angles relative to the measurement plane. Through the calibration and image reconstruction, all three components of the velocity vector (two in-plane and one out-of-plane) can be resolved in the planar measurement domain [107, 118]. This capability is particularly important for investigating 3C-2D flow features, such as secondary circulation and vortical structures; accordingly, experimental measurements in this study were conducted using a two-camera stereo-PIV system. Table 4.3 presents the specifications of the cameras used in the experimental setup.

Table 4.3. Specifications of the LaVision cameras used in the stereo-PIV system.

Parameter	Value
Camera model	LaVision Imager sCMOS
Sensor type	Scientific CMOS (sCMOS)
Resolution	2560×2160 pixels
Bit depth	16-bit
Maximum frame rate	50 fps
Interframe time	120 ns
Readout noise	$< 3e^-$
Lens mount	Nikon F-mount; 50 mm lens

The specifications of the laser and timing unit employed in the present experimental setup are summarized in Tables 4.4 and 4.5.

Table 4.4. Specifications of the Nd:YAG laser used for illumination in the stereo-PIV system.

Parameter	Value
Laser type	Dual-cavity Nd:YAG
Model	Litron Nano L100-50
Wavelength	532 nm
Pulse energy	up to 100 mJ per cavity
Repetition rate	50 Hz
Laser operation	Double-pulse
Trigger control	Q-switch and flash lamp triggering

Table 4.5. Specifications of the programmable timing unit (PTU) used for synchronization.

Parameter	Value
Device	LaVision Programmable Timing Unit (PTU X)
Timing resolution	10 ns
Function	Synchronization of cameras and laser
Control	Software-controlled triggering (DaVis)

Figure 4.4 illustrates a schematic of the PIV setup, highlighting the camera positions, laser-sheet orientation, and the alignment of the field of view with the channel bend geometry.

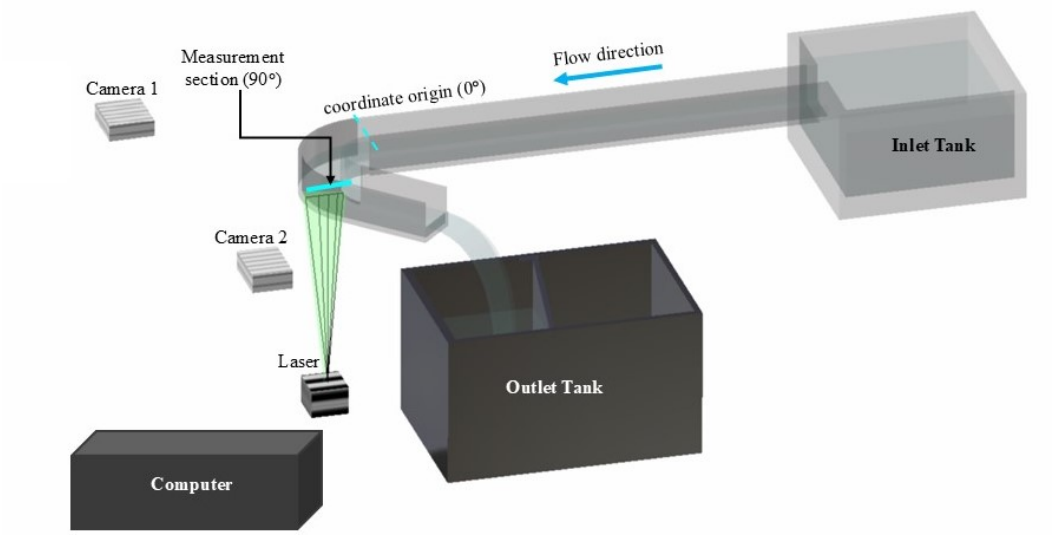


Figure 4.4. Schematic layout of the stereo-PIV system and experimental flow setup, showing the cameras positions and the laser sheet introduced from underside of the channel (credit: Julien Pierrat). The streamwise flow direction is indicated by the blue arrow. The turquoise solid line within the bend denotes the bend apex (90° cross-section), where the velocity measurements were conducted.

This measurement system enabled detailed characterization of the flow structure, including the development and variation of secondary currents under different boundary and flow configurations.

4.4.1 Calibration for Stereoscopic PIV

Accurate calibration is an important component of stereo-PIV, as the measurement relies on combining particle image information acquired from two cameras viewing the flow field from different angles. Due to this angular arrangement, each camera introduces geometric distortions and perspective differences between the image plane and the measurement plane. Therefore, a calibration procedure is required to map image coordinates to physical space and to correct for optical distortions [107, 113]. In stereo-PIV, the reconstruction of 3D velocity components is achieved by combining two independent projections of particle displacements obtained from different viewing directions. Through geometric calibration, a mapping function is established between the image coordinates of each camera and the physical measurement domain. This mapping is typically determined using a calibration target consisting of a grid of markers with known spatial locations.

For three-component (3C) velocity measurements, a two-level calibration plate with a known separation distance (Figure 4.5) is commonly employed to enable accurate reconstruction of the out-of-plane velocity component [118]. In this study, a two-level calibration approach was adopted to obtain 3D velocity reconstruction. The stereoscopic camera configuration followed a forward–forward (or backward–backward) scattering arrangement, in which both cameras were positioned on opposite sides of the laser sheet. This configuration provides improved sensitivity to the out-of-plane velocity component but requires careful calibration using a two-level target with markers visible from both viewing directions.

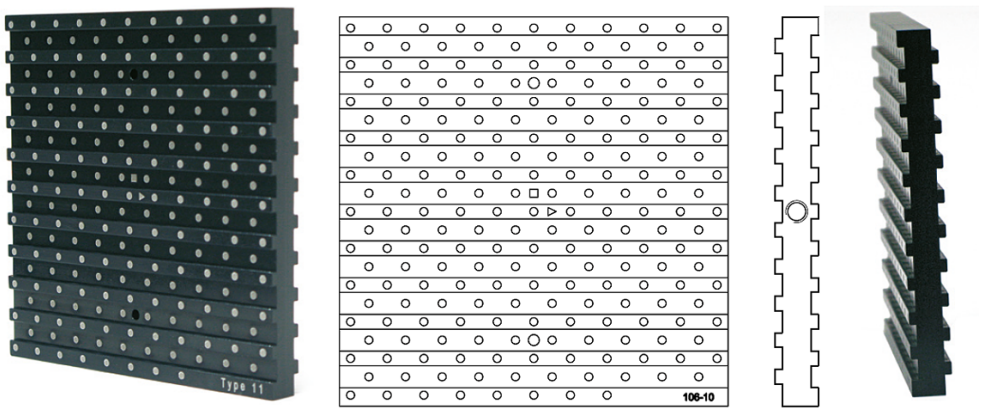


Figure 4.5. Two level calibration plate (From LaVision System Components, Calibration Plates)

Although the calibration plates provided by LaVision are commonly used, the standard plate dimensions (10 cm $\times$ 10 cm) were insufficient to cover the full channel width in this study. To overcome this limitation and avoid potential errors associated with mosaic calibration, a custom two-level calibration plate (10 cm $\times$ 20 cm) with identical marker (dot) patterns was designed and 3D-printed (see Figure 4.6). This ensured full spatial coverage of the measurement domain and improved calibration consistency across the entire field of view.

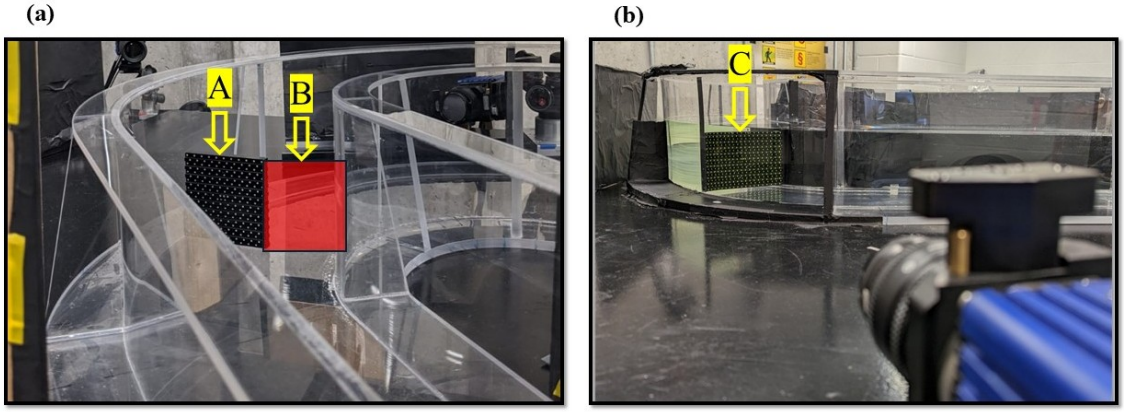


Figure 4.6. Calibration plates: (a) the plate provided with the standard LaVision system, and (b) a 3D-printed plate with the same marker pattern and 3d-geometry. In panel (a), region 'A' denotes the portion of the channel width covered by the plate, while region 'B' indicates the uncovered portion. In panel (b), region 'C' represents the full channel width covered by the 3D-printed calibration plate.

To minimize alignment errors during calibration, the calibration plate was fixed in position using a dense foam support, spanning the channel width (not shown in Figure 4.6). This prevented unintended movement during image acquisition, which is a known source of calibration inaccuracies. Maintaining a stable calibration target is essential for achieving reliable mapping functions and reducing systematic errors in velocity reconstruction [113].

4.4.2 Planar Self-Calibration and Disparity Analysis

Here planar self-calibration was performed using the DaVis (v10.2) software. This procedure refines the mapping by minimizing the disparity (i.e., the difference in the position of corresponding particle images between the two camera views) between corresponding

particle images from the two cameras. The calibration quality was assessed using the mean disparity error from the dewarped image size.

The average disparity obtained from the planar self-calibration was converted from pixels to physical units using the dewarped image scale. Based on the dewarped image dimensions, the scale factor was determined independently in the horizontal and vertical directions as

$$s_x = \frac{281.5\ \mathrm{mm}}{3992\ \mathrm{px}} = 0.0705\ \mathrm{mm/px}, \tag{4.6}$$

$$s_y = \frac{151.8\ \mathrm{mm}}{2152\ \mathrm{px}} = 0.0705\ \mathrm{mm/px}. \tag{4.7}$$

Since both values were essentially identical, the dewarped image scale was taken as $s = 0.0705\,\mathrm{mm/px}$. Using the average disparity reported by DaVis, $d_{\mathrm{avg}} = 4.358$ px, the corresponding physical disparity was calculated as

$$\Delta_{\mathrm{avg}} = d_{\mathrm{avg}} \times s = 4.358\ \mathrm{px} \times 0.0705\ \mathrm{mm/px} = 0.307\ \mathrm{mm}. \tag{4.8}$$

Accordingly, the average disparity of 4.358 pixels corresponded to a physical displacement of approximately $0.307\ \mathrm{mm}$. When expressed relative to the measurement domain dimensions (200 mm width and 60 mm depth), this corresponds to $\frac{0.307}{200} \times 100 \approx 0.15\%$ (width) and $\frac{0.307}{60} \times 100 \approx 0.50\%$ (depth). Thus, the disparity represents approximately 0.15% of the channel width and 0.50% of the flow depth.

These low disparity values indicate excellent geometric agreement between the two camera views and confirm that residual calibration errors are negligible. Consequently, the stereo reconstruction is considered reliable, and the measured three-dimensional velocity fields are expected to accurately represent the underlying flow structures.

4.4.3 Temporal Resolution of Velocity Measurements

The temporal resolution of the velocity measurements was determined as a function of the sampling frequency and total acquisition duration, following the Nyquist sampling criterion. In time-resolved or sequential PIV measurements, the sampling frequency must be sufficiently high to capture the relevant temporal scales of turbulent fluctuations, while the total record length determines the lowest resolvable frequencies [1, 158, 13].

The resolvable frequency range (temporal resolution range) of the measurements was calculated using the Nyquist frequency, defined as

$$f_{\mathrm{Nyquist}} = \frac{f_s}{2}, \tag{4.9}$$

where f_s is the sampling frequency. The Nyquist frequency represents the upper limit of resolvable frequencies in the measured signal, beyond which aliasing effects may occur. The corresponding minimum resolvable time scale is given by

$$T_{\mathrm{min}} = \frac{1}{f_{\mathrm{Nyquist}}}. \tag{4.10}$$

In addition to the high-frequency limit, the finite duration of the measurement imposes a lower bound on the resolvable frequencies. This limit is defined as

$$f_{\mathrm{min}} = \frac{1}{T_{\mathrm{max}}}, \tag{4.11}$$

where T_{max} is the total acquisition time. The corresponding maximum resolvable time scale is therefore equal to the record length,

$$T_{\mathrm{max}} = T_{\mathrm{record}}. \tag{4.12}$$

For the present experiments, a sampling frequency of $f_s = 10\,\mathrm{Hz}$ and a total measurement duration of $T_{\mathrm{record}} = 600\,\mathrm{s}$ were employed. Substituting these values yields

$$f_{\mathrm{Nyquist}} = 5\,\mathrm{Hz}, \quad T_{\mathrm{min}} = 0.2\,\mathrm{s}, \tag{4.13}$$

and

$$f_{\min} = 1.67 \times 10^{-3}\,\mathrm{Hz}, \quad T_{\max} = 600\,\mathrm{s}. \tag{4.14}$$

These results indicate that the measurements resolve flow fluctuations with characteristic time scales ranging from $0.2\,\mathrm{s}$ to $600\,\mathrm{s}$, spanning more than three orders of magnitude. Although the lowest frequency corresponds to the full record length, long-period oscillations are not expected in this flume setup, and the chosen duration is sufficient to capture the relevant flow behaviour. This temporal range is sufficient to capture the dominant large-scale and low-frequency turbulent structures typically observed in open-channel and ice-covered flows, where coherent motions and secondary circulation evolve over relatively long time scales [94, 10].

It is noted that higher-frequency turbulent fluctuations with time scales smaller than $T_{\min}$ are not fully resolved due to the limitations imposed by the sampling frequency. However, for the present study, the focus is on the mean flow structure and large-scale secondary motions, for which the selected temporal resolution is considered adequate. Furthermore, previous studies have demonstrated that, for such flows, the dominant energy-containing structures occur at relatively low frequencies that are well within the resolved temporal range [1, 13].

Chapter 5

Secondary Flow and Froude Number Variation

Secondary flow dynamics and turbulence in an ice-covered sharp bend channel at different subcritical Froude numbers

This chapter has been published in full as: Ebrahimi, S., Rennie, C. D., Mohammadian, A., and Schreiner, H. K. (2026), *Secondary flow dynamics and turbulence in an ice-covered sharp bend channel at different subcritical Froude numbers*, Environmental Fluid Mechanics, 26(2), 13.

5.1 Abstract

This study examines ice cover effects on secondary flow and turbulence in a sharp bend with curvature ratio $R/B = 1.5$, where R is the channel's centerline radius and B the width. Three flow rates (1.44, 1.08, and 0.48 L/s) with Froude numbers 0.15, 0.12, and 0.05 were measured. Unlike previous ice-covered bend studies that often report ice- and bed-layer primary cells, here two distinct circulation cells developed in the upper layer: one

near the inner bank and another near the channel center, while a circulation cell formed near the outer bank in the bed layer. Circulation was strongest at high flow and declined with decreasing discharge. Turbulent kinetic energy (TKE) increased with flow rate, but normalized TKE decreased, suggesting that turbulence was maintained at low flows by stronger relative shear beneath the ice. The turbulent structure parameter (a_1) showed that turbulence at high flow was more uniformly distributed with reduced localized stress dominance, while low flow exhibited enhanced shear stress effects, forming localized regions of high turbulence. At lower flow, vertical shear stress (τ_{uw}) became greater relative to lateral-vertical shear stress (τ_{vw}), reflecting enhanced velocity gradient effects under reduced discharge. These results provide insights into how ice cover alters flow structures by intensifying mean turbulence beneath the ice and creating distinct secondary circulation and turbulence dynamics compared to open or partially covered channels.

Keywords: Secondary flow, Ice-covered river bend, Turbulence

Key Points

- A consistent three-cell structure was observed across all flow conditions: two vortices in the ice layer and one near the outer bank at the bed.
- Normalized mean kinetic energy increased as discharge decreased, indicating more structured flow and increased relative turbulence at lower flow rates.
- Variations in the Froude number distinctly influenced turbulence distribution patterns beneath the ice cover.

5.2 Introduction

Secondary flow refers to a cross-stream circulation superimposed on the primary streamwise flow that develops in meander bends. In a curved channel, the centrifugal acceleration force drives the flow toward the outer bank, while the resulting pressure gradient acts in the opposite direction. In open-channel bends, secondary flow forms a single helical cell (center-region vortex) that often includes a weaker counter-rotating cell near the outer bank [19]. In contrast, under ice-covered conditions, the flow is bounded by both the bed and the ice surface, which alters boundary shear, velocity distribution, and turbulence structure.

The rigid upper boundary introduces an additional shear layer at the ice-water interface, resulting in two vertically stacked counter-rotating helical cells, a bed-driven lower cell and an ice-driven upper cell, as reported in previous studies [146, 166, 38, 145]. This two-layer secondary flow structure represents a fundamental departure from the single-layer behavior of open-channel flows and is central to understanding momentum exchange and mixing in ice-covered river bends.

These characteristic secondary flow motions along curved channels are responsible for the complex morphodynamic processes in meandering rivers and estuaries [132]. However, the influence of a solid ice cover on sub-ice flow and turbulence remains poorly understood. Turbulent flow dynamics beneath ice are difficult to characterize, largely because field measurements in meandering rivers are inherently challenging under open-surface conditions and become even more constrained by safety and accuracy limitations when ice is present [14, 95, 69]. As a result, numerous studies have focused on developing physical models to better represent turbulent flow processes.

Curvature-induced secondary flow turbulence in open channels has been widely studied through both laboratory experiments and numerical simulations. In a detailed breakdown of turbulence dynamics in curved open-channel flows, [19] demonstrated that turbulence activity tends to diminish toward the outer bank. This reduction is attributed to the increasing diagonal dominance of the Reynolds stress tensor, which in turn reduces the efficiency of shear production and the generation of turbulent kinetic energy. Recent investigations into narrow and sharply curved open-channel bends have revealed more complex flow patterns than previously recognized. Notably, [59] and [120] reported the presence of an additional circulation cell near the inner bank, coexisting with the conventional single or bi-cellular secondary flow structure.

Further complexity arises under ice-covered conditions, where the vertical velocity structure is significantly altered, particularly in meandering rivers. Tsai and Ettema [145], using a 180-degree curved flume with a trapezoidal bed, showed that the presence of an ice cover induced a double helical secondary flow pattern, with near-bed and near-surface flows directed toward the inner bank. The upper helical cell, although weaker than previously reported [146, 166], arises from the added boundary at the ice underside, which enhances vertical confinement, modifies velocity gradients, and redistributes shear and turbulence. Peters et al. [101], through controlled flume experiments of partial and full ice-covered

flow, demonstrated that a simulated partial ice cover, as an upper boundary layer, increased the overall flow resistance, thereby redistributing both minimum and maximum velocities laterally and vertically across the channel cross-section. Nyantekyi-Kwakye et al. [95] studied how partial ice cover affects turbulent flow in a straight channel. They found that a 25% increase in ice coverage raised the freestream velocity by about 8%.

Ice-covered bend flows have also recently been studied in the field. Koyuncu and Le [69] examined flow profiles in a river bend using an Acoustic Doppler Current Profiler (ADCP). Their study highlighted that ice cover significantly increases the complexity of secondary flow patterns, yet they observed a single vortex near the outer bank in one of the cross sections. Their findings did not support the persistent existence of a stacked double layer structure across all cross-sections, as reported in other field measurements [38]. Smith et al. [131] investigated the effects of ice cover on velocity and shear stress in a river reach. They observed that ice presence often changed the mainstream flow direction, with maximum velocity consistently found closer to the bed and higher bed shear stress values under ice-covered conditions. Koyuncu and Le [70] modeled the distribution of bed shear stresses in ice-covered meandering rivers and demonstrated a significant increase in bed shear stress near both banks, concluding that the distance from the bank significantly affects velocity profiles and secondary flow patterns. Studying a river confluence as opposed to a river bend, Biron et al. [14] compared the flow structures in the mixing zone under ice-covered versus ice-free conditions to identify the role of Kelvin-Helmholtz (KH) structures. They found a shift of the highest velocity toward the center of velocity profiles and also observed significant turbulent structures in both the streamwise and lateral velocity components. They found a strong correlation between these components, indicating KH vortices are the dominant coherent structures in the mixing zone.

Previous studies on ice-covered river channels exhibit several limitations, including the use of partially ice-covered setups, limited experimental capacities for capturing detailed flow structures, and a reliance on straight flumes that do not represent the curvature typical of natural channels. Therefore, a comprehensive investigations into the combined effects of varying flow rates and Froude numbers on turbulence and secondary circulation in fully ice-covered, sharply curved channels remain lacking. This study addresses that gap by examining how variations in flow rate influence secondary flow behaviour and the redistribution of turbulent kinetic energy across the apex of a laboratory-scale meandering channel under full ice cover.

5.3 Methods

A river bend is typically classified as sharp when the ratio (R/B) of centerline radius of curvature (R) to channel width (B) falls below a certain threshold, cited as less than 3 [64] or around 2 [20]. Here, ice-covered experiments are conducted in a sharp bend channel with $R/B = 1.5$ ([64]). The physical model of the river channel used here is a transparent plexiglass walled flume, with a rectangular, located in the PIV room of the University of Ottawa's Hydraulics Laboratory. While we acknowledge that natural rivers often exhibit compound or sloped banks that can enhance or suppress certain secondary flow cells, the use of a rectangular cross-section in this study allows for simplified boundary condition control, clearer interpretation of the velocity field, and direct comparison with previous laboratory studies of meander flows. The flume includes a 2.4 m long, 0.2 m wide straight inlet, a 135° bend with a 0.3 m centerline radius, and a straight outlet section. The flume has a self-contained recirculating system comprising inlet and outlet tanks connected by a pump, ensuring consistent water quality for PIV measurements. The flow depth was maintained using the downstream gate, while keeping the bed slope constant. Three different flow rates were measured under a constant flow depth ($H = 6\,\text{cm}$) in all the experiments. The key dimensionless parameters (e.g., Reynolds and Froude numbers) were matched to subcritical turbulent flow conditions of ice-covered rivers, preserving dynamical similarity. The high flow rate, which was the maximum achievable with the pump used in the experimental setup ($U_b = 0.12\,\text{m/s}$), started at 1.44 L/s, decreased by 25% to 1.08 L/s, and then dropped an additional 55% to 0.48 L/s. The Froude number was then calculated as

$$Fr = \frac{U}{\sqrt{gR_h}} \tag{5.1}$$

resulting in values of 0.15, 0.12, and 0.05, which indicate subcritical flow conditions. Similarly, the Reynolds number was determined using

$$Re = \frac{UR_h}{\nu} \tag{5.2}$$

where $1.004 \times 10^{-6}\,\frac{\text{m}^2}{\text{s}}$. The resulting values were 11,000 for the high-flow case

($U_b = 0.12$ m/s), 8,300 for the medium-flow case ($U_b = 0.09$ m/s), and 3,700 for the low-flow case ($U_b = 0.04$ m/s).

5.3.1 Velocity Scaling of Flow

Full Reynolds number similarity could not be achieved due to the geometric scale limitations of the laboratory model. However, all experimental flows were maintained in the turbulent regime ($Re_{\text{pipe}} \gtrsim 4{,}000$), to reproduce the main secondary flow structures and boundary layer behavior. The experiments followed Froude similarity to ensure dynamic similarity between the model and natural river conditions, where both gravitational and inertial forces govern the flow behavior. Model (or experimental) quantities are denoted by the subscript "m" and prototype (real) quantities by "p". To ensure dynamic similarity between the laboratory model and the river prototype, the Froude numbers must be equal ($Fr_m = Fr_p$); hence, the velocity scale is given by:

$$\lambda = \frac{U_m}{U_p} = \sqrt{\frac{H_m}{H_p}} \tag{5.3}$$

For the prototypical Rideau River in Ottawa, the approximate flow parameters used were a mean depth H_p of $5\,\mathrm{m}$, channel width B_p of $100\,\mathrm{m}$, and an average velocity $U_p = 1\,\mathrm{m/s}$. With the laboratory model, $H_m = 0.06\,\mathrm{m}$ and $B_m = 0.20\,\mathrm{m}$. The corresponding scaling ratios are obtained as $\lambda_H = 1.2 \times 10^{-3}$ and $\lambda_U \approx 0.11$, where λ_H and λ_U represent the depth scale and velocity (Froude) scale. Accordingly, the prototype velocity corresponding to a given model velocity U_m is $U_p = U_m/\lambda_U$. For the present experiments, $U_m = 0.12, 0.09,$ and $0.04\,\mathrm{m/s}$ correspond to prototype velocities of approximately $1.08, 0.81,$ and $0.36\,\mathrm{m/s}$, respectively.

The associated laboratory Froude numbers are $0.15, 0.12,$ and 0.05, which compare closely with the prototypical river ($Fr \approx 0.14$). This demonstrates that the selected laboratory flow conditions reproduce the subcritical flow conditions in the prototype (Rideau River) Froude number with reasonable accuracy, providing appropriate dynamic similarity. The selected flow scenarios are representative of many natural rivers during periods of stable ice cover and moderate discharge. These values were chosen based on field observations

reported in prior studies (e.g., Ashton, 1986; Beltaos, 2008), and represent distinct flow regimes to capture variation in secondary circulation strength under ice-covered conditions.

5.3.2 Ice Cover and Roughness Scale

To simulate the ice-cover surface on top of the flow, marine-grade mahogany plywood was employed. This material was selected for its flatness, dimensional stability, and resistance to warping under high humidity. Its density ($\approx 800\ \mathrm{kg/m^3}$) closely matches that of natural freshwater ice ($917\ \mathrm{kg/m^3}$), providing a realistic stress condition at the ice–water interface without requiring additional external pressure. Matte black adhesive vinyl was applied to the entire bottom surface of the ice cover to minimize light scattering from the wood surface. No additional mechanical pressure was applied to the cover, and therefore the pressure at the lid remained atmospheric in all experiments.

The channel bottom and side walls were constructed from smooth plexiglass ($k_s = 0.003\,\mathrm{mm}$), with an effective roughness of approximately ($k_s/H = 5 \times 10^{-5}$). The roughness of the vinyl-covered wood ($\sim\ 0.001\,\mathrm{mm}$) was selected to approximate the smooth basal surface of natural sheet ice, as observed in many riverine environments during stable ice-cover conditions (e.g., solid ice without frazil or anchor ice and without mechanical thickening). The combined wood-vinyl surface exhibits negligible roughness ($k_s = 0.1\,\mathrm{mm}$) relative to the flow depth ($H = 0.06\,\mathrm{m}$), resulting in a hydraulically smooth boundary condition ($k_s/H = 1.7 \times 10^{-4}$). A summary of the materials and corresponding roughness properties of the channel boundaries used in the experiments is provided in Table 5.1.

Table 5.1. Summary of boundary materials and roughness parameters.

Surface	Material	$k_s\,(\mathrm{mm})$	k_s/H
Top wall (smooth cover)	Vinyl-covered wood	0.1	1.7×10^{-4}
Bottom wall	Plexiglass	0.003	5.0×10^{-5}
Side walls	Plexiglass	0.003	5.0×10^{-5}

This configuration ensured controlled boundary conditions and reproducible optical quality for PIV measurements, while maintaining consistency with ice-covered flow scenarios. While natural ice covers can exhibit large spatial variability in roughness, particularly in the presence of frazil or anchor ice formation, the present experiments were designed to investigate flow dynamics under a smooth ice regime, thereby isolating the influence of the rigid-lid boundary on flow behavior.

5.3.3 PIV Data Processing

A stereo-PIV system comprising a dual-head laser (model: NANO L100-50), two high-frequency iDS sCMOS cameras, and a LaVision PTU X standard model (USB interface, 10 ns time resolution), synchronized through DaVis 10.2 software, was used. PIV seeding particles consisted of 10 μm diameter hollow glass spheres with a slurry concentration of approximately 5 ml. Velocity measurements were obtained by illuminating the seeded flow from below the bottom wall using pulsed laser sheet illumination. Figure 5.1 shows a schematic of the flume geometry and the PIV system.

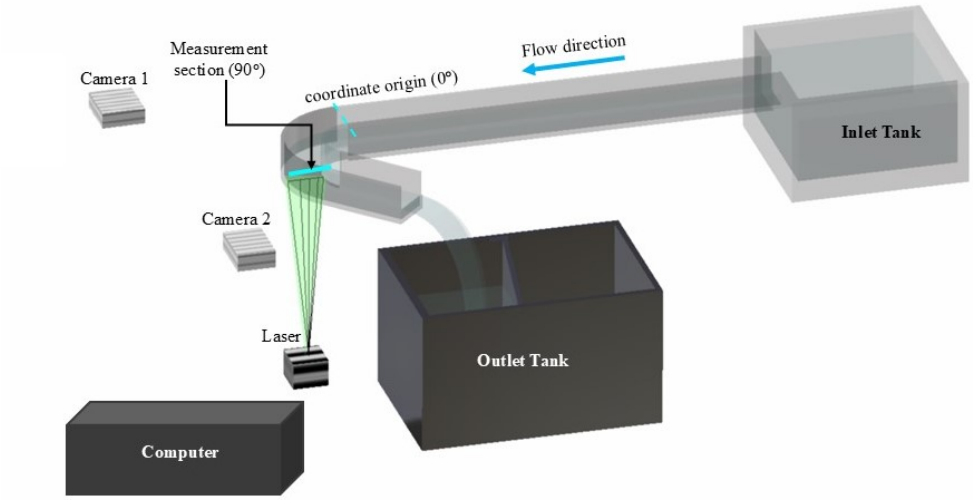


Figure 5.1. Schematic of the bend flume and stereo-PIV setup (Credit: Julien Pierrat). A vertical laser sheet (green line) aligned to illuminate the 90° cross-sectional plane from the bottom wall. The two cameras recording stereo image pairs were positioned on either side of the measurement section. The coordinate origin (0°), indicated by the dashed blue line at the junction where the straight inflow section meets the curved bend, marks the start of the meander.

Following image acquisition, the PIV data were post-processed in DaVis to obtain velocity vector fields and derived flow quantities. Planar self-calibration was first performed to correct geometric misalignments between the cameras and the calibration target. A geometric mask was applied to define the region of interest (ROI) corresponding to the valid flow area. This mask excluded outside regions such as channel walls, the ice cover, and zones where reflections could produce spurious vectors. Next, image pre-processing filter was used to enhance the quality of raw PIV images. This included background subtraction to remove static reflections or illumination gradients, intensity normalization to ensure uniform particle brightness, and contrast enhancement or filtering to sharpen particle edges and reduce noise. Then, the image reconstruction procedure transformed the 2D particle images from each camera into a 3D representation of the flow field, forming a common, dewarped coordinate system derived from the refined calibration mapping functions. Finally, the *Vector Statistics: Vector Field Results* operation was used to compute statistical quantities from the time series of velocity fields. This step combined all instantaneous velocity maps into ensemble-averaged fields and calculated derived quantities such as mean velocity components, which were then exported for further analysis.

5.3.4 Spatial and Temporal Resolution of Measurements

From the calibration results, the dewarped image dimensions were $3992 \times 2152\,\text{px}$. The interrogation window size was set to $W = 64\,\text{px}$ with 75% overlap, resulting in an effective step size of $S = W(1 - \text{overlap}) = 16\,\text{px}$. The number of vectors along each direction was estimated using the conventional sliding-window formulation [83, 82]:

$$N_x = 1 + \frac{N_{px} - W}{S}, \tag{5.4}$$

This produced $N_x = 246$ (width) and $N_z = 132$ (height), giving a total, N_{vectors}, of $32{,}472$ vectors per frame. With a calibrated field of view (FOV) of $282\,\text{mm} \times 152\,\text{mm}$, the spatial grid resolution was $\Delta x = 1.146\,\text{mm}$ and $\Delta z = 1.152\,\text{mm}$, corresponding to vector grid dimensions of 246×132. The resulting mean resolution of approximately $1.15\,\text{mm}$ allowed detailed capture of velocity gradients across the channel cross-section.

The temporal bandwidth was assessed using the Nyquist frequency (f_{Nyquist}), the

minimum resolvable period ($T_{\min}$), the lower frequency bound given by the record length ($f_{\min}$), and the maximum resolvable period ($T_{\max}$), expressed as

$$f_{\text{Nyquist}} = \frac{f_s}{2}, \quad T_{\min} = \frac{1}{f_{\text{Nyquist}}}, \quad f_{\min} = \frac{1}{T}, \quad T_{\max} = T. \tag{5.5}$$

For a sampling frequency, f_s, of $10\,\text{Hz}$, this yields $f_{\text{Nyquist}} = 5\,\text{Hz}$ and $T_{\min} = 0.2\,\text{s}$. The record-length lower limit is $f_{\min} = 1.67 \times 10^{-3}\,\text{Hz}$, with a corresponding maximum period of $T_{\max} = 600\,\text{s}$. Thus, the dataset resolves fluctuations with characteristic timescales ranging from $0.2\,\text{s}$ to $600\,\text{s}$, spanning over three orders of magnitude and covering the dominant macroturbulent timescales under ice-covered flow conditions.

5.3.5 Vortex Identification Algorithm

In the post-processing of PIV data, the vortex identification algorithm developed by Graftieaux et al. (2001) was employed to detect coherent vortical structures in turbulent flows. This method introduces two dimensionless scalar functions, Γ_1 and Γ_2, derived from the local geometric arrangement of velocity vectors. The scalar function Γ_1 identifies the vortex center. For a given point P within the flow field and a surrounding area S, Γ_1 is defined in its continuous form as:

$$\Gamma_1(P) = \frac{1}{S}\int_{M\in S} \frac{(\vec{PM} \times \vec{U}_M)\cdot\vec{z}}{|\vec{PM}|\cdot|\vec{U}_M|}, dS = \frac{1}{S}\int_S \sin(\theta_M), dS \tag{5.6}$$

where $\vec{PM}$ is the position vector from P to M, $\vec{U}_M$ is the velocity at point M, $\vec{z}$ is the unit vector normal to the measurement plane, and θ_M is the angle between $\vec{PM}$ and $\vec{U}_M$. The scalar Γ_1 ranges between -1 and 1, with $|\Gamma_1| \approx 1$ indicating a likely vortex center. To delineate the vortex boundary (core), the scalar function Γ_2 is defined in its continuous form as:

$$\Gamma_2(P) = \frac{1}{S}\int_{M\in S} \frac{\left[\vec{PM} \times (\vec{U}_M - \tilde{\vec{U}}_P)\right]\cdot\vec{z}}{\|\vec{PM}\|\cdot\|\vec{U}_M - \tilde{\vec{U}}_P\|} dS \tag{5.7}$$

where $\tilde{\vec{U}}_P$ is the average velocity within the neighborhood S around point P. A threshold of $|\Gamma_2| \approx 0.636$ (i.e., $2/\pi$) is typically used to identify the boundary of the vortex core. In this study, a slightly higher value of 0.69, still within the commonly accepted range of 0.6-0.7, was applied to further suppress background noise. The vortex center is located at the point of maximum Γ_1, while the contour where $\Gamma_2 = 2/\pi$ marks the core boundary. These functions were computed at each grid point in the flow field using MATLAB. Their independence from velocity magnitude makes them robust in noisy conditions. Combined with their computational simplicity, these properties supported their application to time-averaged data to extract persistent vortex features.

5.4 Results

Velocity measurements for all flow rates in this study are examined at the 90° cross-section of the bend. Figure 5.2 illustrates the time-averaged secondary circulation for three different flow conditions: high flow at 1.44 L/s (subplot a), medium flow at 1.08 L/s (subplot b), and low flow at 0.72 L/s (subplot c). In this figure and all the following figures, the left end of the horizontal axis represents the inner bank, and the right end represents the outer bank of the channel.

To compare the impact of ice cover on circulation cells at different flow rates, vortex cores detected using the algorithm of Graftieaux *et al.* were overlaid onto the velocity field, marked as colored rectangles, with a number assigned in the rectangle for clearer referencing in further analysis. The results across all datasets demonstrate good consistency in the identified locations of cell centers within both the ice and bed layers.

5.4.1 Secondary flow vortices under ice-cover

A distinct two-layer structure, with the top layer linked to the ice cover and the bottom layer associated with the bed, is evident under all flow conditions. The directional pattern of the secondary circulation moves from the inner to the outer bank at mid-depth, and in the opposite direction near the top and bottom walls, as indicated by the bright blue arrows in Figure 5.2.

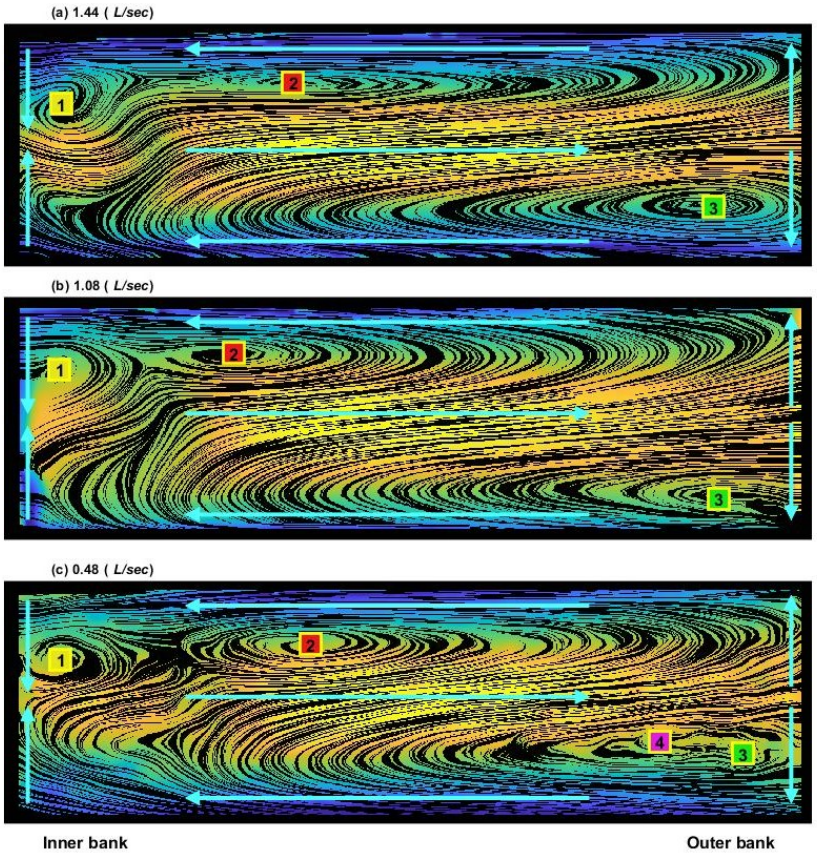


Figure 5.2. Mean flow streamlines illustrating secondary flow vortices under (a) high flow rate, (b) medium flow rate, and (c) low flow rate. Colored rectangles indicate the identified vortex regions, while white arrows denote the flow directions within the upper and lower boundary layers, intersecting approximately at mid-depth. The vertical axis represents the flow depth (0–0.06 m, from the bed to the ice cover), and the horizontal axis represents the channel width (0–0.20 m, from the inner bank to the outer bank).

The two primary counter-rotating cells, driven by the centrifugal force of bend curvature, are clearly visible across all tested flow rates. In the ice layer, the vortex pattern consistently includes a primary vortex and an inner wall cell splitting from it near the convex bank, while in the bed layer, circulation consistently forms near the outer bank. At high and medium flow rates, a main cell dominates the flow. However, at the lowest flow rate, where the flow drops by more than half, the reduced circulation intensity changes the near-bed flow structure, causing the near-bed cell to divide into two vortices. Table 5.2 summarizes the circulation properties of the vortices identified under various flow rates, with vortex IDs corresponding to the vortex numbers presented in Figure 5.2.

Table 5.2. Properties of vortices identified at different flow rates.

Flow Type	Vortex ID	Circulation ($\times 10^3$ mm^2/s)	x Location (m)	y Location (m)
High	1	1.99	0.01	0.02
High	2	1.67	0.07	0.01
High	3	-2.32	0.18	0.05
Medium	1	0.92	0.01	0.02
Medium	2	1.68	0.06	0.01
Medium	3	-0.43	0.18	0.05
Low	1	0.29	0.01	0.02
Low	2	0.47	0.08	0.02
Low	3	-0.14	0.18	0.04
Low	4	-0.04	0.16	0.04

At the highest flow rate, the bed layer circulation (-2.32×10^3 mm^2/s) is the strongest vortex in the cross-section and also the strongest bed layer circulation across all three flow rates. In the ice layer, the two vortices have similar strengths, with the inner bank vortex (1.99×10^3 mm^2/s) being stronger than the center vortex (1.67×10^3 mm^2/s).

At the medium flow rate, where the flow drops by 25%, the bed layer circulation (-0.43×10^3 mm^2/s) weakens significantly, decreasing by more than 80%. In the ice layer, the inner bank circulation (0.92×10^3 mm^2/s) also reduces by over 50%, while the main cell circulation (1.68×10^3 mm^2/s) remains as strong as its counterpart (1.67×10^3 mm^2/s) at the highest flow rate and becomes the strongest vortex in this scenario.

With a Froude number reduction of over 50% at the lowest flow rate, the total bed layer circulation (-0.18×10^3 mm^2/s) weakens further by more than 58%, and a very weak secondary vortex (-0.04×10^3 mm^2/s) begins to separate from the main bed layer circulation. In this low-flow condition, the inner bank and main vortices in the ice layer show major strength reductions of 68% and 72%, respectively, with the main cell circulation (0.47×10^3 mm^2/s) becoming stronger than the inner bank vortex (0.29×10^3 mm^2/s) in

the ice layer.

5.4.2 Mean Flow Distribution

We identified the high-velocity core (HVC) through analysis of the time-averaged streamwise velocity field, employing a weighted-centroid method applied to regions exceeding the 90th percentile of local velocity magnitudes (Figure 5.3). This methodology enables the physically consistent and reliable identification of HVCs, even in cases where the core is elongated or exhibits deformation across different flow conditions.

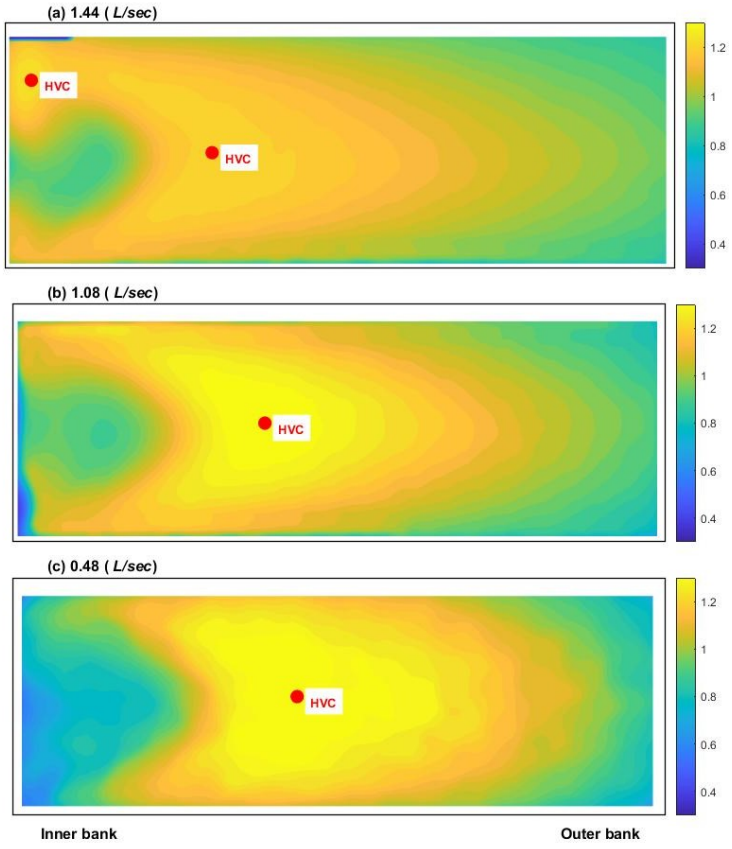


Figure 5.3. Mean streamwise velocity showing high-velocity core regions exceeding the 90th percentile of local velocity for (a) high, (b) medium, and (c) low flow rates.

Both the number and spatial distribution of HVCs are observed to vary in response

to changes in the secondary flow circulation patterns. Under high-flow conditions, two distinct HVCs are observed: one located in the ice layer along the inner bank, corresponding spatially to the inner-bank secondary circulation cell, and a second HVC positioned at approximately mid-height of the flow, near the channel's mid-width. Notably, both HVCs are co-located with regions of elevated mean kinetic energy (KE) rather than the centers of vortex circulation.

The mid-height HVC appears across all flow rates and consistently coincides with the region of peak mean flow KE. However, the lateral position of the mid-height HVC shifts systematically with discharge magnitude. As the discharge decreases, the inner-bank cell weakens, and the HVC reverts to a more centralized location along the channel width. Thus, while the HVCs do not align precisely with the vortex centers of the secondary flow structures, their positions are modulated by the strength and configuration of these circulations. This behavior indicates that the spatial distribution of high streamwise velocity across the channel width is primarily governed by the bulk flow rate, with the secondary flow's influence more evident in the number of HVCs.

5.4.3 Mean and turbulent kinetic energy variation

To explain the variations in vortex strength and location across vertical layers and flow rates, we analyzed the mean kinetic energy (MKE), normalized by the bulk velocity specific to each flow condition. For instance, in Figures 5.4a–c, the MKE is normalized using the high-, medium-, and low-flow energy ($\frac{1}{2}U_{\text{bulk}}^2$), respectively. This normalization converts the plots to a dimensionless form and facilitates the comparison of turbulence patterns across cases. A two-dimensional median filter (medfilt2) was applied in MATLAB to effectively remove random noise and velocity outliers from the measured data. The data in regions near the channel boundaries, where velocity measurements are obscured by laser reflections (indicated by the white mask along the borders), were excluded from the analysis.

The normalized mean kinetic energy (MKE), evaluated as the 90^{th}-percentile (upper 10%) values for each flow scenario (Figures 5.4a–c), increases from the high- to the low-flow cases, with peak decile values of $\mathrm{MKE} = 1.7$ in the high-flow case and $\mathrm{MKE} = 2.72$ in the low-flow case. (Note that individual normalized MKE values exceed these upper decile thresholds; they represent the lower bound of the highest 10% of observations, not

the absolute maxima.) In the high-flow case (Figure 5.4a), the region of the highest decile of mean kinetic energy extends from near the inner bank in the ice layer toward the central region, spanning both the ice and bed layers. In contrast, in the medium- and low-flow cases, the high energy regions are more confined to the central region.

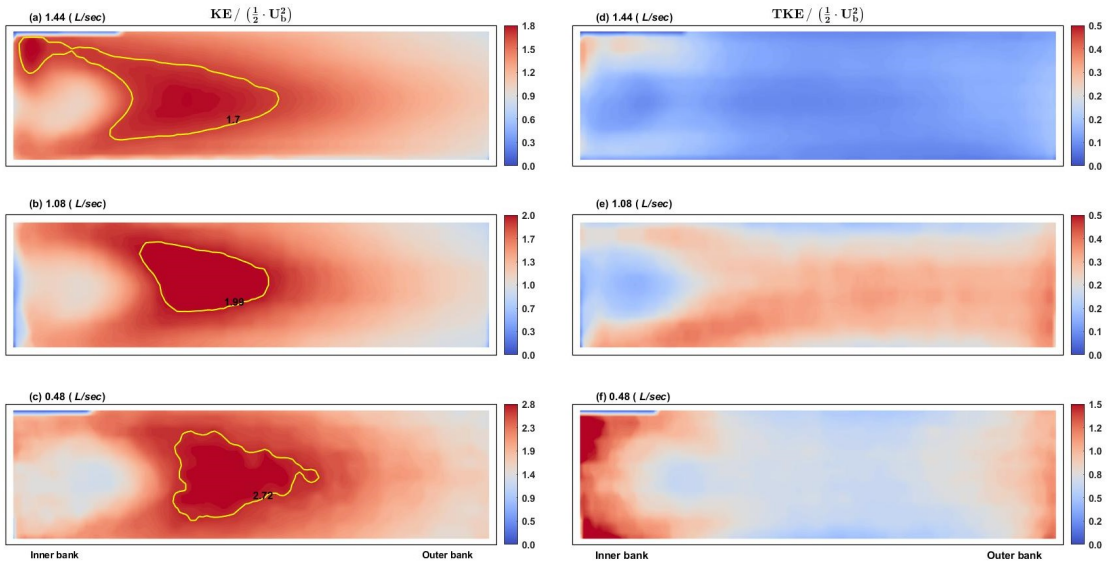


Figure 5.4. Normalized mean flow kinetic energy (KE/$\frac{1}{2}U_{\text{bulk}}^2$) in (a–c) and turbulent kinetic energy (TKE/$\frac{1}{2}U_{\text{bulk}}^2$) in (d–f) under high (1.44 L/s), medium (1.08 L/s), and low (0.48 L/s) flow conditions. Each MKE plot includes a highlighted yellow isoline (value labeled in black) indicating the 90$^{\text{th}}$-percentile energy level for the respective flow scenario. Note the higher colorbar range in plot (f) compared to plot (d) and (e). The vertical and horizontal axes of each plot represent the flow domain's height and width, respectively.

Similarly, despite having the lowest absolute turbulent kinetic energy (TKE), the low-flow case shows the highest relative TKE throughout the cross-section among the three cases (Figures 5.4d–f), an outcome that, to our knowledge, has not been explicitly identified in previous studies of flow under river ice. The TKE distributions show distinct spatial patterns for each flow condition. Regions of elevated TKE generally coincide with areas of high mean kinetic energy (MKE), particularly near the inner bank in the top layer where the secondary vortices accelerate with increasing flow, suggesting that increased mean flow velocities contribute to heightened turbulence levels. However, this correspondence between MKE and TKE is less straightforward in the medium-flow case, indicating that local tur-

bulence dynamics modulate the variation in this pattern. The underlying mechanisms are further examined through analysis of Reynolds shear stress and the turbulent structure parameter.

5.4.4 Reynolds stresses configuration

The distribution of Reynolds stresses represents the momentum transfer associated with turbulent velocity fluctuations and plays a critical role in shaping turbulence structure, circulation strength, and energy distribution within the channel cross-section. These stresses arise from the decomposition of instantaneous velocity into mean and fluctuating components using Reynolds decomposition:

$$u_i = \overline{u_i} + u_i' \tag{5.8}$$

where u_i is the instantaneous velocity component, $\overline{u_i}$ is the time-averaged (mean) velocity, and u_i' is the fluctuating component. In this study, the flow domain cross-section is aligned along the x–z (normal-vertical) plane, i.e., across the width and depth of the channel and perpendicular to the main (streamwise) flow direction. To examine turbulent momentum transport in this plane, the Reynolds shear stresses τ_{uw} and τ_{vw} are evaluated. These are defined by:

$$\tau_{ij} = -\rho\,\overline{u_i' u_j'} \tag{5.9}$$

where ρ is the fluid density and $\overline{u_i' u_j'}$ is the time-averaged product of velocity fluctuations. These stresses are used to assess vertical momentum exchange and the influence of secondary circulation near the bend apex (Figure 5.5).

The Reynolds stress values at each flow rate show notable differences between the ice and bed layers. The corresponding mid-line shear velocities at the upper and lower boundaries are also provided in Appendix A. Both τ_{uw} and τ_{vw} exhibit positive and negative values, indicating vertical momentum flux in both upward (toward the ice) and downward (toward the bed) directions, depending on local turbulence structure and flow energy dis-

tribution. In particular, τ_{uw} in the bed layer shows consistently high and positive values, indicating upward momentum transfer away from the bed toward the ice cover, while the ice layer exhibits weaker, often negative values, reflecting a downward flux. This pattern is observed consistently across all flow rates examined.

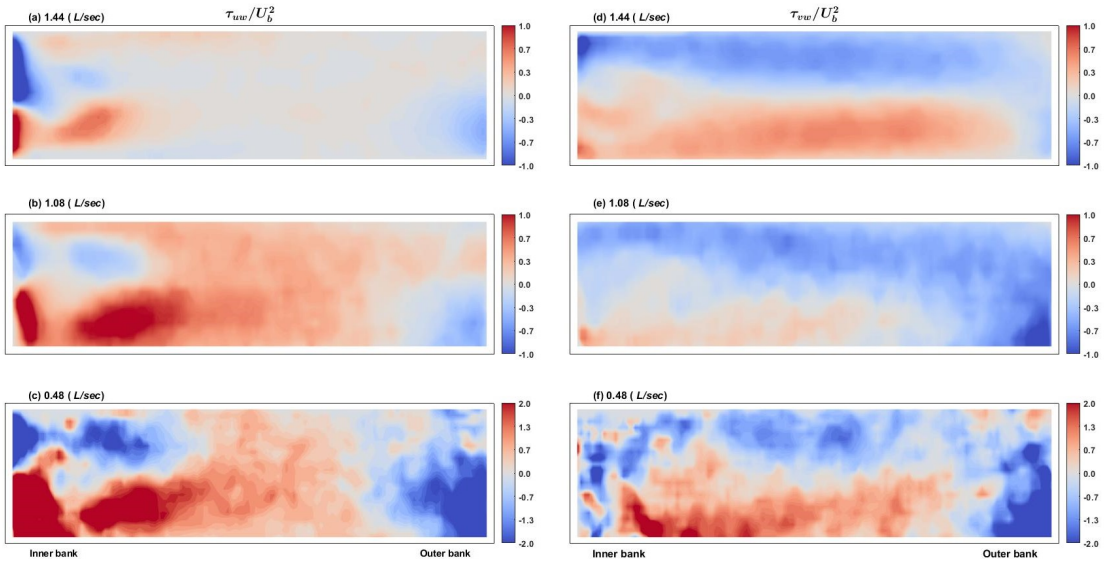


Figure 5.5. Normalized Reynolds shear stresses τ_{uw} (a–c), and τ_{vw} (d–f) for high (1.44 L/s), medium (1.08 L/s), and low (0.48 L/s) flow conditions. All plotted values are multiplied by 10^2 to improve visual clarity. Note the higher colorbar range in plot (c) compared to (a) and (b), and in plot (f) compared to (d) and (e). White bands along the edges of the plots represent masking applied to exclude near-wall data.

The distribution of τ_{vw} across the flow rates in Figure 5.5 reveals an expansion of regions with negative (downward) lateral-vertical momentum flux, suggesting increased downward transfer of lateral momentum from the ice layer to the bed as flow rate decreases. This trend implies that at lower flow rates, the weaker circulation in the bed layer is less effective at transporting upward momentum in the transverse direction.

The tendency of the Reynolds stresses to concentrate near the inner bank is a direct consequence of the specific flow structure observed in this system. As illustrated in the high-velocity core (HVC) contours, the core regions tend to remain skewed toward the channel center or slightly toward the inner bank, particularly under higher flow conditions.

This asymmetric distribution promotes localized turbulent production near the inner bank, thereby reinforcing the observed pattern in the Reynolds stress fields.

5.4.5 Turbulent structure parameter

The turbulent structure parameter, a_1, is the ratio of Reynolds shear stress to turbulent kinetic energy. It is a dimensionless metric indicating how turbulent eddies with a given energy level generate shear [123, 19], calculated as:

$$a_1 = \frac{\sqrt{\overline{u'w'}^2 + \overline{v'w'}^2}}{2k} \tag{5.10}$$

where $\overline{u'w'}$ and $\overline{v'w'}$ are components of the Reynolds stress tensor, and k is the turbulent kinetic energy [19]. The parameter a_1 thus represents the normalized intensity of turbulent fluctuations contributing to shear.

Figure 5.6a–c presents the distribution of a_1 across different flows. The high-flow case exhibits the highest turbulent structure parameter based on the 90$^{\text{th}}$ percentile level ($a_1 = 5$), which closely corresponds to regions of elevated τ_{vw} in both the ice and bed layers. As the flow rate decreases, the 90$^{\text{th}}$ percentile value of a_1 declines in both magnitude and spatial extent across the measurement plane. Interestingly, the 90$^{\text{th}}$ percentile value of a_1 in the medium-flow case ($a_1 = 3$) is lower than in the low-flow case ($a_1 = 4$), and is confined to areas with higher τ_{uw} near the ice and bed layers. The relatively higher a_1 observed in the low-flow case is attributed to its lower TKE compared to the other two cases, as shown in Figures 5.4d–f.

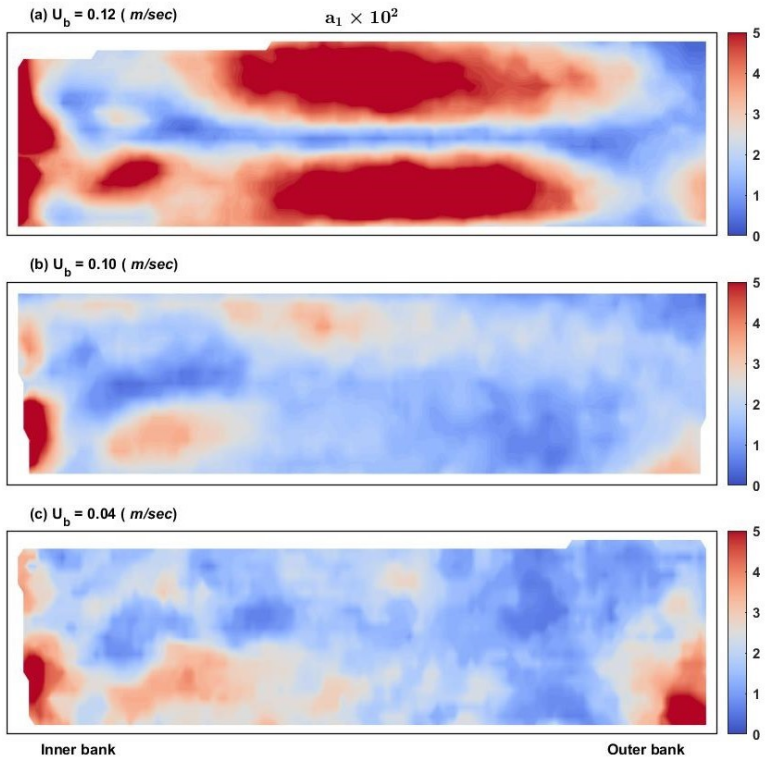


Figure 5.6. Turbulent structure parameter a_1 for (a) high, (b) medium, and (c) low flow conditions. White bands along the edges of the plots represent masking applied to exclude near-wall data.

5.5 Discussion

From the above results, it is evident that the mechanisms governing the formation of secondary circulation cells are not limited to one controlling factor. A systematic analysis of turbulence characteristics provides a more coherent explanation of the secondary flow behavior under ice-covered conditions.

Under open-channel conditions, centrifugal acceleration and cross-stream pressure gradients generate a vertically coherent helical cell [145], or in some cases, multiple cells within the same layer [19, 121]. In contrast, when an upper boundary is introduced, as in ice-covered channels, the flow experiences vertical confinement and shear partitioning between the bed and ice. This promotes the development of two-layer secondary circulation, either weak [145, 69] or pronounced [38], depending on the flow and measurement conditions. The ice cover thus alters the distribution of Reynolds stresses and modifies the balance between centrifugal and frictional forces, resulting in a fundamentally different secondary

flow structure.

The consistent formation of two distinct and coherent vortices in the upper layer of the 90° cross-section was reported under the low Reynolds number condition in the duct plane of [77], but not at medium or high Reynolds numbers (see Fig. 6 in [77]). In the present study, however, this double-cell structure appears across all flow rates. In addition, a persistent inner-bank cell in the upper half of the flow, present across all flow rates in this study, has not been previously documented under comparable ice-covered conditions. Without the ice cover, the flow in the same curvature showed corner cells on both sides of the main cell in the open channel [121]. However, the concave half of the ice-covered flow did not develop a cell at the ice layer, whereas the bed layer cell was positioned closer to the outer bank. The comparison of circulation intensity among the identified vortices (Figure 5.2) indicates a systematic reduction in bed-layer circulation strength with decreasing Froude number and a concurrent shift in dominance toward the main-cell circulation over the inner-bank circulation within the ice layer at lower flow rates. The strengthening of the main circulation cell under ice-covered conditions parallels the trend reported for open-channel flows in the same flume [120]. Nevertheless, the turbulence characteristics of a free-surface open channel do not translate to ice-covered conditions, where the layered flow structure reshapes momentum exchange processes and alters turbulence dynamics. Therefore, the question arises: how can the secondary flow patterns observed in the present study be explained?

This difference is not due to vortex identification techniques but arises from altered turbulence dynamics and shear-induced instabilities introduced by the rigid ice cover. As illustrated in Figure 5.4, the turbulent kinetic energy (TKE) increases near the ice surface, where elevated velocity gradients enhance local instabilities, consistently producing and sustaining two separate vortical structures. These instabilities are further modulated by flow rate and boundary effects. At the lowest flow rate, a smaller two-cell vortex forms near the bed layer, resembling secondary flow patterns observed by [77] at lower Reynolds numbers. In such conditions, the significantly reduced inertia intensifies the influence of friction and shear near the bed while diminishing the overall flow energy, promoting the fragmentation or subdivision of the circulation structure. This demonstrates how ice-induced changes in energy partitioning fundamentally reshape flow near the banks and in both surface and bed layers.

Our observations of energy dynamics from the 90° cross-section revealed a distinct pattern in kinetic energy partitioning across varying flow rates. As discharge decreases, the normalized mean kinetic energy (MKE) increases. This indicates that at lower flow rates, a greater proportion of the total kinetic energy remains in the mean flow rather than being dissipated through turbulent fluctuations. Physically, this trend suggests that under reduced discharge conditions, the flow structure becomes more organized, exhibiting lower turbulence intensity.

A similar observation was reported by Blanckaert and de Vriend [19] in their open-channel experiments. They documented a notable spatial redistribution of TKE and MKE influenced by curvature-induced secondary flows. Specifically, they observed a reduction in TKE near the outer bank due to a modified turbulence structure arising from streamline curvature effects. This curvature-induced phenomenon leads to a form of pressure-driven stratification, suppressing turbulence generation and reducing the efficiency of turbulence production via shear stresses. Consequently, the MKE became predominantly concentrated near the outer bank region, enhancing the organization of the mean flow and further diminishing turbulence activity [19, Fig. 3].

The asymmetrical circulation patterns observed under ice-covered conditions likely result from the combined influence of channel curvature, pressure-gradient-induced stratification, and subtle variations in wall-boundary properties. Channel curvature disrupts flow symmetry by generating outward centrifugal forces and inward pressure gradients, which shift circulation cells laterally, particularly toward the outer bank [20, 157]. While both the top and bottom boundaries were treated as hydraulically smooth, minor differences in material composition (vinyl-covered wood on the top wall vs. plexiglass on the bed) and surface roughness ($\sim$0.001 mm vs. $\sim$0.0003 mm) may have influenced near-wall turbulence and boundary layer development. These small inconsistencies, although controlled for, could contribute to near-surface asymmetries in flow structure.

Beyond boundary roughness effects, the continuous ice cover introduces stratification dynamics that substantially modify energy distribution and momentum exchange across the water column. In particular, the ice suppresses vertical turbulent mixing and enhances shear-induced layering, especially under intermediate flow conditions. For example, at a Froude number of $Fr = 0.12$, a distinct band of elevated turbulent kinetic energy (TKE) was present at mid-depth (Figure 5.4e), coinciding with elevated Reynolds shear stress and

indicating strong momentum exchange between the upper and lower circulation cells. This interlayer shear zone was far less pronounced in the high- and low-flow cases, suggesting that intermediate flows most effectively promote interaction between stratified layers. These findings highlight that the presence of ice alters not only the near-wall turbulence due to roughness and material properties but also introduces layered flow regimes driven by pressure gradients and suppressed vertical mixing.

Our analysis of normalized Reynolds stresses across varying flow rates reveals distinct changes in turbulent momentum transfer due to the presence of the ice cover. The consistently high and positive values of τ_{uw} in the bed layer indicate upward momentum transport, driven by bottom-induced shear. In contrast, the often negative τ_{uw} values in the ice layer signify a downward flux of momentum, reflecting the dampening role of the rigid ice boundary on near-surface turbulence. This suppression limits vertical momentum exchange and enhances flow stratification, particularly under low-flow conditions. The distribution of τ_{vw} further underscores how the ice cover modulates transverse-vertical interactions. At lower discharges, the reduction in regions of positive τ_{vw} suggests increased downward flux from the upper layer, weakening the near-bed vortex and diminishing the capacity for upward lateral momentum transfer. These trends demonstrate that the ice cover reinforces a more stratified and stable mean flow structure by constraining momentum redistribution and suppressing turbulent mixing. Importantly, these mechanisms are specific to ice-covered conditions and cannot be inferred from structural changes observed in free-surface flows.

These results align with previous observations by Koyuncu and Le [69], who reported elevated shear stresses near channel banks under ice-covered conditions, even at relatively low discharges. Their study attributed this to enhanced transverse momentum exchange near boundaries induced by the presence of ice. Extending their findings, our results not only confirm increased downward transverse-vertical momentum transfer (negative τ_{vw}) under low-flow conditions, but also demonstrate how ice cover modifies the structure of secondary flows by constraining vertical momentum pathways and promoting stratified shear layers. Specifically, our analysis of normalized Reynolds stress distributions reveals that although both τ_{uw} and τ_{vw} decrease with declining flow rate, the relative reduction in τ_{uw} is more pronounced. This indicates a shift in dominant turbulent transport mechanisms: under lower flow conditions, upward momentum exchange becomes increasingly suppressed by the ice (i.e. more dominant τ_{uw}), while at higher discharges, transverse momentum transfer plays a more significant role in redistributing energy across the flow depth. This role of

turbulent momentum pathways evolving with changing flow conditions underscore particular dynamics of Reynolds stresses under the ice-covered regimes, that were not previously captured in earlier studies.

A comparison of Figures 5.6a–c for the turbulent structure parameter (a_1) shows that a_1 reaches its highest value in the high-flow scenario, clearly indicating regions of efficient turbulence production. These high a_1 values closely match areas with strong Reynolds shear stress (τ_{vw}), found in both the ice and bed layers. This result indicates that at higher flow rates, a substantial portion of turbulence energy converts into shear stress, which supports strong secondary circulation (Figure 5.2a) and effective vertical mixing. Comparing this finding with the open-channel study of Blanckaert and De Vriend [19] suggests that high a_1 values consistently identify areas of enhanced turbulence and secondary circulation, regardless of whether the channel is open or ice-covered.

However, the spatial pattern of a_1 in the current ice-covered study differs notably from open-channel conditions. While Blanckaert and De Vriend [19] observed high turbulent efficiency mainly in the central region of the flow (noting that values near bed boundaries were likely overestimated due to velocity measurement limits), the present study identifies high turbulence efficiency at both the ice and bed boundaries in the high-flow case, while at medium and low flows these high-a_1 regions become smaller and more scattered.

Moreover, the ice cover introduces a vertically layered flow regime, driving distinct turbulence patterns, especially at lower discharges. The observed reduction in both magnitude and spatial extent of peak a_1 at lower flows (Figures 5.6b–c) indicates decreased turbulence efficiency. The lower peak a_1 value in the medium-flow scenario (compared to the low-flow scenario) is confined to areas with higher vertical momentum flux (τ_{uw}), suggesting a transitional turbulence pattern dominated by vertical momentum transport rather than lateral. Conversely, the slightly higher peak a_1 in the low-flow scenario indicates a relatively greater contribution from turbulent kinetic energy (TKE). Despite overall lower turbulence levels at low flow, the relatively high a_1 demonstrates efficient conversion of available turbulence into shear stress, likely driven by increased friction and shear at the ice boundary. The distribution of high a_1 values, in conjunction with Reynolds stress patterns, specifically lateral-vertical shear stress (τ_{vw}) at higher flows and the increased role of vertical momentum transport (τ_{uw}) at lower flows, highlights the complex dynamics of turbulence structure introduced by the ice cover. Although a_1 is not yet widely adopted in

river hydraulics studies, it provides valuable insights into turbulence structure changes, with practical implications for predicting momentum exchange, mixing efficiency, and sediment transport dynamics in ice-covered rivers.

[157] examined curvature-induced secondary flow structures in a 193° open channel and found no clear relationship between Froude number (Fr) and circulation strength. In contrast, [120] reported in a 135° open channel that the strength of the center circulation cell increased as Fr decreased, but only down to a threshold of $Fr = 0.12$. Beyond this point, circulation strength plateaued, and a separate trend emerged, wherein inner-bank circulation intensified with increasing Fr. This suggests that the Fr-dependence observed by Wei et al. primarily pertains to the central circulation cell, while the inner-bank dynamics follow a different regime.

In our experiments across three flow conditions, we observed distinct modifications in turbulence structure and secondary circulation induced by the ice cover. While all flow cases exhibited elevated turbulence near the outer bank, the intensity and vertical extent of this zone varied with Fr, likely from the evolving interaction between ice-induced shear and curvature-driven secondary flows. As illustrated in Figure 5.2, overall circulation intensity decreased with decreasing Fr in both the ice and bed layers. Notably, the ice-layer vortex near the inner bank exhibited a strong peak at high flow but diminished sharply at lower Fr, allowing the central circulation cell to dominate. This differs from open-channel observations where flow separation effects maintain stronger inner-bank circulation at lower discharges [120, 16, 72]. These findings demonstrate that the addition of an ice cover is not a minor boundary modification but a transformative condition that reshapes flow symmetry, turbulence pathways, and circulation pattern in different regimes. While the current results reveal key trends, extending the analysis to a broader range of flow rates would refine our understanding of how Froude number influences turbulence structure and secondary flow under ice cover.

The findings of this study hold important implications for river engineering and management in cold regions, particularly in meander bends. While this study analysis centers on a single cross-section for each of the three flow conditions, specifically at the 90° bend apex, this focus represents a trade-off. The bend apex is hydraulically significant, as it typically exhibits the well-developed helical flow structures in curved channels, though their strength and position depend on flow and channel characteristics [24]. This focus enabled high-

resolution analysis of turbulence and secondary flows at a representative location. Due to field-of-view limitations of the PIV system under full ice cover, extending detailed three-dimensional turbulence measurements to multiple downstream sections was not feasible without compromising spatial resolution or data quality. To preserve measurement fidelity, the analysis was constrained to the apex section.

The distinct responses of normalized mean kinetic energy (MKE) and turbulent kinetic energy (TKE) across varying flow conditions highlight the critical role of turbulence-induced energy loss and boundary friction, effects that become increasingly important under low-flow scenarios. If unaccounted for, these dynamics may lead to underestimation of flow resistance and water surface elevation during winter periods [69]. Moreover, the spatial distribution of MKE and TKE suggests distinct sediment transport and localized erosion patterns, especially near the inner bank. The presence of high-shear zones beneath the ice along both banks, as also reported by [69], indicates that conventional assumptions about bank stability and sediment dynamics may not hold under ice-covered conditions.

It is important to note that the rectangular channel cross-section used in this study, while advantageous for measurement and experimental control, represents only one type of bed condition. As such, it may not capture the full complexity of flow structures present in natural meandering rivers, particularly those with compound or laterally sloped bathymetry. Previous studies (e.g., [143]) have demonstrated that lateral slope can influence the formation and intensity of secondary (helical) flow cells. In our experiments, the flow structures were primarily governed by channel curvature, the imposed upper boundary condition (rigid lid vs. free surface), and frictional asymmetry, allowing us to isolate and analyze these effects independently of slope-induced influences. This controlled setup enabled clearer attribution of the observed flow behavior to ice cover and curvature. Nevertheless, we acknowledge that incorporating more naturalistic geometries in future studies would be valuable for assessing the combined influence of lateral slope, curvature, and ice cover on secondary flow development.

Furthermore, the controlled nature of our experimental setup allows us to isolate the effects of ice cover from the more complex variables typically present in the field. The observations of localized dominance in vertical versus lateral momentum fluxes offer a detailed mechanism explanation for field-reported phenomena such as enhanced near-surface shear, stratified velocity profiles, and asymmetric bank erosion under ice-covered condi-

tions. Although laboratory models inevitably involve geometric and dynamic scaling, their reduced complexity enables clearer attribution of observed flow behaviors to ice-induced changes. Therefore, the turbulence mechanisms identified here hold relevance for improving predictive understanding of flow resistance, sediment transport, and erosion processes in seasonally ice-covered river bends.

In one of the field surveys conducted by Demers et al. [38], substantial frazil ice accumulation was reported, compared to approximately one-third of that amount in the second year of their study. Yet, two counter-rotating helical cells were also observed immediately downstream of the frazil accumulation zone. The persistence of this fundamental feature, even under frazil-impacted conditions, may suggest some degree of similarity with the simpler ice-covered flow structures. However, any potential correspondence should be interpreted with caution. The presence of frazil ice substantially alters the ice-water interface roughness, which in turn modify flow profiles and vertical energy distribution in ways not replicated in our experimental setup. As such, extrapolating the present findings to natural systems influenced by frazil ice should be approached with care.

Future research should explore the effects of ice thickness, channel geometry, and additional flow rates to further understand the interactions between ice-induced velocity gradients, turbulence, and secondary flows. This will ultimately enhance predictive models and help river management practices in cold regions.

5.6 Conclusions

This study investigated the influence of ice cover on the secondary flow circulation and turbulence at the apex of a sharp bend, which commonly exhibits well-developed helical flow structures. This makes the results produced distinct and offer valuable insights into the flow dynamics of comparable natural systems. The turbulence behavior was attributed to the presence of solid boundaries at both the top and bottom, which constrained and redistributed energy, consistent with the concept of flow confinement in wall-bounded flows. High spatial and temporal resolution measurements allowed analysing some key features of ice-covered flows.

The results revealed a clear and consistent two-layer secondary circulation structure, characterized by two distinct vortices in the ice layer and a vortex near the outer bank in the bed layer, accross the varying Froude numbers. This pattern differs from previous ice-covered river channel studies, which often reported two primary cells, one in the ice layer and one in the bed layer, or, in some cases, did not observe a well-defined double-stacked circulation under the ice cover. Notably, unlike in open-channel studies, increasing the Froude number was found to enhance circulation strength in both the ice- and bed-layers.

As Froude number increased, secondary circulation became more pronounced in both layers due to the greater mean flow energy. At the highest flow rate, large areas of elevated mean kinetic energy (MKE) occurred, especially in the ice layer, facilitating strong momentum transfer. This led to a prominent inner-bank vortex in the ice layer and strong circulation near the outer bank in the bed layer. In contrast, at medium flow, both circulation intensity and turbulence decreased significantly. Lower velocity gradients and reduced energy levels limited turbulence production, weakening interactions between the ice and bed layers.

While the variations in secondary flow and mean flow energy were relatively similar across the three experiments, the turbulent stresses exhibit asymmetric responses to changes in flow rate. The analysis of Reynolds stresses (τ_{uw} and τ_{vw}) and the turbulent structure parameter (a_1) provided deeper insights into turbulence mechanisms under the ice surface. As flow rates decreased, Reynolds shear stresses, particularly in the lateral-vertical plane (τ_{vw}), decreased, dampening momentum exchanges between layers, and contributing to the weakest circulation intensity at low flow. Additionally, distributions of τ_{uw} and τ_{vw} revealed substantial vertical asymmetry in Reynolds stresses. These observations suggest a nonlinear and coupled response to ice cover in a sharply curved channel. A wider range of ice-cover conditions would further enhance the applicability and generalization of the results.

Appendices

A.1 Wall shear and friction partitioning

The bed-side and ice-side friction velocities (u^*_{bed} and u^*_{ice}) were determined from mid-channel vertical velocity profiles by fitting the near-wall data to the logarithmic law of the wall:

$$U(z) = \frac{u^*}{\kappa} \ln\left(\frac{z}{z_0}\right),$$

where $\kappa = 0.41$ is the von Kármán constant. Recognizing that secondary flows influence the profile of streamwise velocity [22], and consistent with the expected semi-log linear portion of the profile, only the near-surface portion of each profile was utilized for the fit. A linear regression of U versus $\ln z$ was performed over the range $z/H = 0.01$–0.15 to obtain the slope m and intercept γ. The friction velocity and hydrodynamic roughness length were then computed as $u^* = \kappa m$ and $z_0 = \exp(-\gamma/m)$, respectively.

Considering the overall shear stress balance between the two walls, the total friction velocity was derived as $u^*_{\text{total}} = \sqrt{(u^*_{\text{bed}})^2 + (u^*_{\text{ice}})^2}$, while the shear partitioning between boundaries was quantified using the wall shear ratio, defined as $u^*_{\text{wall ratio}} = \frac{(u^*_{\text{bed}})^2}{(u^*_{\text{ice}})^2}$. Table 1 summarizes the results for the three discharges.

The calculated friction velocities increase with bulk velocity, ranging from $u^*_{\text{bed}} = 0.0033\ \text{m/s}$ at low flow to $0.0099\ \text{m/s}$ at high flow. The corresponding total values ($u^*_{\text{total}} = 0.0042$–$0.0111\ \text{m/s}$) indicate that both boundaries contribute appreciably to overall momentum loss. The u^*_{ratio} values show that bed shear generally dominates, though at the medium discharge the shear partitioning between bed and ice becomes nearly equal ($u^*_{\text{ratio}} \approx 1$).

Table A.1. Summary of mean flow mid-channel hydraulic properties across three flow conditions.

Flow	**Layer**	u^* **[m/s]**	z_0 **[m]**	z_0^+	k_s^+
High	Ice	0.00507	0.0000001	0.0005	0.2537
High	Bed	0.00987	0.0000190	0.1872	0.0987
Med	Ice	0.00794	0.0000256	0.2033	0.3969
Med	Bed	0.00806	0.0000277	0.2232	0.0806
Low	Ice	0.00250	0.0000013	0.0033	0.1249
Low	Bed	0.00334	0.0000106	0.0355	0.0334

Flow	U_b **[m/s]**	$u^*_{\textbf{total}}$ **[m/s]**	$u^*_{\textbf{ratio}}$ **[-]**
High	0.13	0.0111	3.79
Med	0.10	0.0113	1.03
Low	0.04	0.0042	1.78

This intermediate behavior corresponds to the enhanced near-ice shear observed in the Reynolds-stress fields (Figure 4b) and the intensified main-cell circulation relative to the inner-bank vortex (Figure 2, Table 1). The higher u^*_{ice} at medium flow likely results from stronger secondary-flow impingement and turbulence exchange near the upper boundary. Conversely, at low flow, the smaller u^*_{ice} values indicate weaker near-ice turbulence and diminished mixing across the core region.

Overall, larger bed friction velocities imply a more developed logarithmic layer and stronger wall-shear production, whereas smaller near-ice values reflect suppressed turbulence generation under the smooth ice cover. The resulting total u^* values thus provide a representative measure of the combined resistance in the ice-covered bend flow.

A.2 Non-normalized TKE distribution

To further clarify the distinct behavior of the normalized TKE distribution, especially at the highest flow rate (1.44 L/sec), this appendix includes non-normalized TKE plots. Because normalized TKE is scaled by the square of the bulk velocity $\left(\frac{1}{2}U_b^2\right)$, which increases substantially with discharge, this scaling can suppress normalized values even when absolute turbulence remains high. The non-normalized fields (Figure A.1) reveal comparable or greater turbulence magnitudes near the banks at 1.44 L/sec, highlighting a shift toward boundary-concentrated turbulence at high flow, in contrast to the more centrally distributed pattern observed at medium flow.

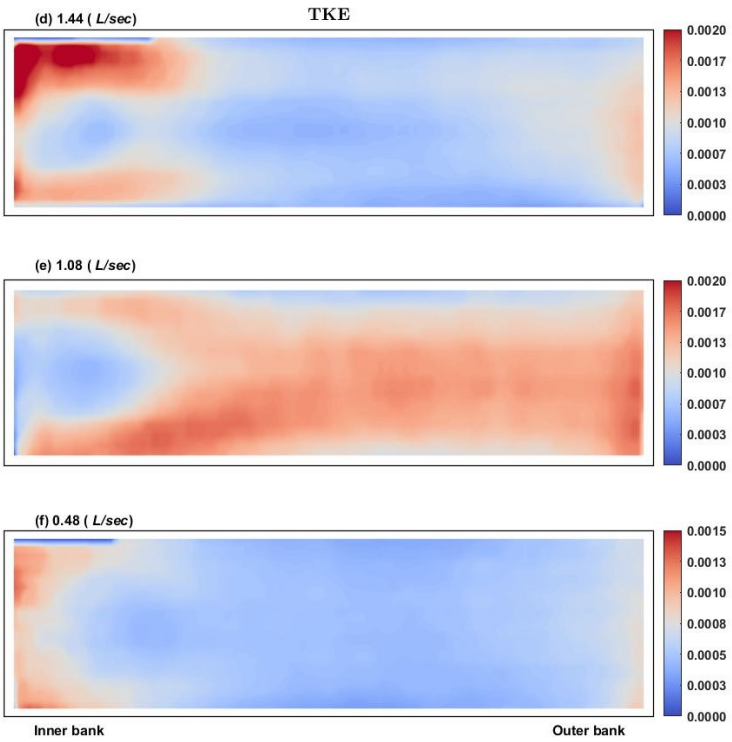


Figure A.1. Non normalized TKE distribution for high (1.44 L/s), medium (1.08 L/s), and low (0.48 L/s) flow conditions. White bands along the edges of the plots represent masking applied to exclude near-wall data.

While normalized TKE is used in the main analysis for consistency and comparability across flow rates, we acknowledge that normalization may obscure key spatial features. This supplemental plot are therefore provided to aid in interpreting the observed trends.

Chapter 6

Secondary Flow and Ice-cover Roughness Impact

Roughness influence on secondary circulation and momentum distribution in an ice-covered river bend

This chapter has been published in full as: Ebrahimi, S., Mohammadian, A., and Rennie, C. D. (2026), *Roughness influence on secondary circulation and momentum distribution in an ice-covered river bend*, Physics of Fluids, 38(2).

6.1 Abstract

Ice-cover roughness perturbs velocity and momentum distributions, leading to secondary flow redistribution within river channels. Particle Image Velocimetry (PIV) measurements examined ice roughness effects on secondary flow at the apex of a 135° bend under two different simulated ice covers. Both flows produced a two-layer flow structure, with roughness strongly influencing cell position and intensity. Under rough ice, the top layer inner-bank cell (IBC) observed in the smooth ice case merged with the primary vortex,

forming a single dominant vortex that was shifted towards the inner bank. While the total circulation in the ice-layer decreased, the bottom-layer vortex circulation increased with roughness. A three-dimensional (3D) momentum analysis showed vertical momentum with intensified downward flux from the ice layer and enhanced upward flux from the bed. Cross-stream momentum was characterized by concentrated high-intensity zones near the inner bank, indicating roughness-induced lateral redistribution. Roughness had a greater effect on the vertical and cross-stream components of momentum than the streamwise momentum. The rough ice cover induced greater turbulence across the cross-section from outer to inner bank, with a localized decrease near the bed layer adjacent to the inner bank. Increased turbulence under rough ice facilitated the observed merging in the ice layer of the IBC with the primary circulation cell. Momentum and turbulence responses suggest that IBC formation and stability are shaped by boundary morphology and, under rough ice, involve structural reorganization and integration into the primary circulation.

6.2 Introduction

The velocity field in a river channel is commonly described in terms of primary and secondary flow components to account for the three-dimensional nature of fluid motion in river channels. The primary flow represents the main downstream (longitudinal) movement of fluid, while secondary circulation refers to the transverse and vertical flow superimposed on the primary streamwise motion. In turbulent flows, secondary currents are formally categorized by Prandtl [106] into two types: secondary currents of the first kind, driven by centrifugal forces and pressure gradients due to flow curvature (e.g., meander bends, as illustrated schematically in Figure 6.1); and secondary currents of the second kind, which are weaker and arise from turbulent stress anisotropy near wall boundaries. In duct and corner flows, similar vortices have been observed and explained through analysis of simulated Reynolds stress tensors and vorticity production terms. The interplay between turbulence anisotropy and flow inhomogeneity near corners or curved boundaries results in the generation of these secondary flows [100, 119]. The term “corner flow” is also used in the literature [119, 90] to describe smaller secondary circulations that develop near geometric boundaries.

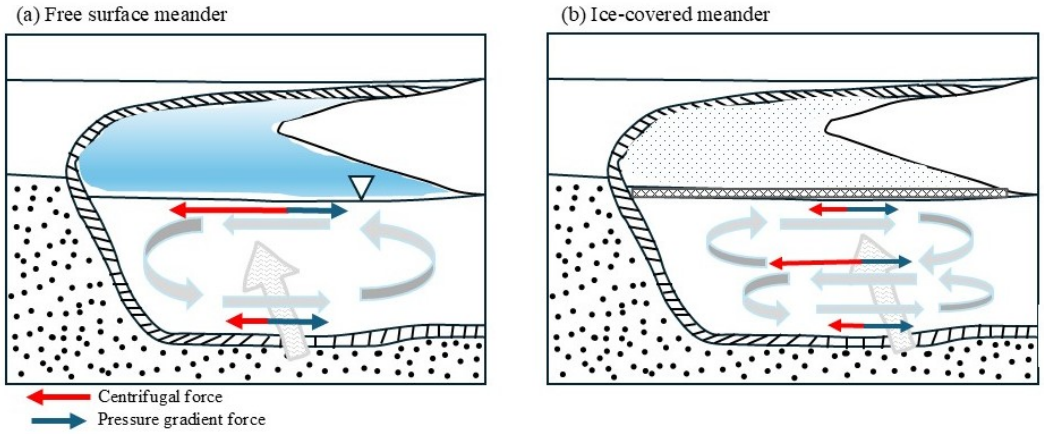


Figure 6.1. Schematic illustration of the cross-sectional force balance and secondary circulation structure in a curved channel under free-surface and ice-covered conditions. Note that depending on channel geometry a free-surface or ice-covered curved channel flow may include a co-rotating inner bank cell and/or a counter-rotating outer bank cell. Solid grey arrows indicate the secondary flow direction, while the patterned straight arrow denotes the main flow direction. Subplots and arrows are not drawn to scale.

Flow in an ice-covered channel is typically fully developed, turbulent, and asymmetric due to the differing hydraulic roughnesses of the ice cover and the channel bed [88]. While the importance of ice roughness effects on flow structure in ice-covered rivers has been recognized for several decades, studies on these inter-relations remain fragmented, with significant gaps in our understanding of how roughness conditions interact. Previous experimental investigations of ice-covered flow have primarily been conducted in straight channels, employing various combinations of bed and ice surface roughness, either differing in material or composed of the same roughness elements.

Teal and Ettema [140] showed that in an ice-covered straight channel, two boundary layers, at the bed and ice underside, produce a mid-depth velocity maximum. Their result indicated that differences in bed and ice roughness shift the velocity maximum upward/downward when the bed/ice is rougher, altering the vertical gradient. Using two-layer and composite models, the authors showed that boundary roughness jointly controls mean velocity and shear. Smith and Ettema [130] investigated flow resistance and velocity profiles in a straight laboratory flume with a movable alluvial bed and simulated ice covers of varying underside roughness. They observed the typical two-boundary-layer velocity structure in ice-covered channels, with the velocity maximum shifted depending on the relative

roughness of the boundaries, moving closer to the smoother surface.

Sukhodolov et al. [138] found that ice-cover roughness substantially increased near-bank roughness, leading to skewed distributions of turbulence characteristics and flow asymmetry across a straight reach of an ice-covered, sand-bed river channel. These skewed patterns, together with the vertical distribution of the transverse Reynolds stress component (Figure 2b in the paper), suggest the presence of asymmetric turbulence and secondary flow structures as a result of spatial variability in the morphology of the ice cover. Wang et al. [152] investigated both full and symmetrical shore ice conditions in straight trapezoidal compound channels. Their results showed the formation of distinct secondary circulation cells, with counter-rotating structures emerging between the main-channel side slope and the floodplain. The rotational direction of secondary flows was found to reverse between the full ice cover and shore ice cases in their study. The typical double-layered velocity profile in ice-covered straight channels has also been reported in several other studies (e.g.,[138, 57, 153, 34, 76, 115, 3, 102, 165]), all of which confirm the influence of both the bed and ice boundaries.

Additionally, some past studies in ice-covered bend channel flow have documented stacked counter-rotating secondary circulation cells. Urroz and Ettema [146], using a laboratory flume with a 90-degree bend, a rough sand bed, and a smooth simulated ice cover, identified the characteristic two-layered flow feature in ice-covered bends, with one cell forming near the bed and a mirror-image cell near the underside of the ice. Tsai and Ettema [145] also conducted experiments in a 90-degree curved alluvial flume with a movable sand bed and a smooth simulated ice cover, and observed the presence of a pair of stacked counter-rotating secondary circulation cells, with one near the bed and the other near the underside of the ice.

Sui et al. [137] investigated frazil ice accumulation in a curved river bend using both field measurements and laboratory flume experiments under ice-covered conditions. The laboratory setup featured a 180° bend with a radius of curvature of 1.5 m. Field observations revealed the presence of stacked counter-rotating secondary circulation cells, characterized by near-surface and near-bed flows moving toward the inner convex bank and mid-depth flow directed toward the outer concave bank. This flow structure played a key role in the lateral transport and deposition of frazil ice, contributing to ice jam formation along the inner bank.

In a natural river, the flow processes under ice are not always similar, due to roughness differences between ice-water and bed-water interfaces. Using a submersible optical camera, Demerse *et al.* [38] visually inspected the undercover roughness of an ice cover in a small 134° meandering reach in Quebec, Canada during the winters of 2007 and 2008, and classified ice roughness into three categories: smooth, smooth-rough, and rough ice. They observed two stacked helical cell motions between the 30° and 51° cross-sections, with the pattern rapidly modified further downstream. At the meander apex (65° cross-section), Demerse *et al.* [38] observed strong secondary flow forming a single helical cell (though near-bed secondary flows were not clearly apparent), with near-surface flow directed toward the inner bank and near-bed flow toward the outer bank. This counterclockwise rotation was opposite to the expected rotation under open-channel conditions [38], where the typical single-cell bend flow has near-surface flow directed toward the outer bank.

Koyuncu and Le [69] examined secondary flow structures in a natural curved river bend with a distinct inner and outer bank (suggesting a moderate curvature) under both open-water and ice-covered conditions. Their results revealed complex patterns, including multiple secondary circulation cells, and demonstrated how ice cover modifies these structures. While signatures of vertically stacked counter-rotating vortices were occasionally observed under ice-covered conditions, the authors note that such features were not consistently present; instead, the field data showed localized variations and isolated vortices near specific cross-sections.

Wang et al. [154] conducted laboratory experiments in a meandering flume consisting of two consecutive channel bends, each with a centerline radius of curvature of 1.5 m and a channel width of 0.3 m (i.e., $w/R = 0.2$), indicating strong curvature. Artificial roughness elements were introduced on both the bed and under the simulated ice cover to mimic natural boundary resistance. Using both experiments and 3D numerical modeling, the study identified stacked, counter-rotating secondary circulation cells beneath the ice, a flow structure characteristic of ice-covered river bends.

Sediqi *et al.* [125] investigated the turbulence characteristics of ice-covered flow in a large-scale outdoor 180° bend flume, accounting for the combined effects of submerged vegetation, ice cover, and bed sediment. The channel featured asymmetric boundary roughness, with a rough bed and a smooth ice cover. Their results revealed a dual-cell pattern of stacked counter-rotating secondary circulation cells, typical of ice-covered bends: an up-

per cell formed near the smooth ice cover and rotated in one direction, while a lower cell developed near the rough bed and rotated in the opposite direction. They also calculated the composite Manning's roughness coefficient under different conditions for an empirical model for total flow resistance [125].

Blanckaert *et al.* [21] investigated the influence of outer bank roughness variation in a 193° curved open channel. A reversed outer-bank cell formed alongside the curvature-induced center cell, transporting momentum away from the bank, reducing streamwise velocity near the cell region, and advecting near-surface high-momentum fluid to lower depths. Increased roughness along the outer bank was shown to strengthen this secondary cell and broaden the associated boundary layer. Similar effects near the bank enhanced sediment transport capacity in the mid-channel. Overall, increased outer-bank roughness intensified all dominant secondary flow mechanisms while keeping their relative importance. The findings of Blanckaert *et al.* [21] provided a valuable foundation for exploring the controlling mechanisms of flow in an ice-covered, closed-channel bend, as examined in the present study.

Despite the significance of roughness elements in influencing turbulence and velocity distributions, the relationship between directly measured roughness conditions and observed secondary flow remains understudied. Measuring roughness in natural environments is particularly challenging, especially in sub-zero conditions. Previous studies on ice-covered river channels present several key limitations: incomplete ice coverage, restricted experimental capabilities for capturing detailed flow structures, reliance on indirect estimates (e.g., inferred friction coefficients) to characterize the measured roughness interaction between the ice cover and channel bed, and a predominant reliance on straight flumes that fail to represent the geometric complexity of naturally curved channels. The present study addresses this gap by elucidating the impact of controlled variations in roughness element height on velocity and momentum distributions at a cross-section of a sharply curved laboratory flume with a 135° bend angle, representative of typical river bends [33]. This is achieved by means of high-resolution PIV measurements in a laboratory ice-covered bend channel with both a smooth and a rough ice surface of known roughness.

6.3 Methods

This paper employs both smooth and rough ice-covered turbulent flow experiments to assess the influence of ice-cover roughness on flow behavior in a closed bend channel plane. The physical model of the river channel used for these experiments is a transparent plexiglass-walled bend flume with a rectangular cross-section. The flume has a 2.4 m long straight entrance section, a 135° bend with a curvature radius (R) of 0.3 m at the centerline, and a straight exit section. The flow rate was set to 144 mL/s with a flow depth (H) of 6 cm in both experiments. The flume width (B) is uniformly 0.2 m in the straight and bend sections, giving an aspect ratio (H/B) of 3.3 throughout the channel. This results in a Froude number of 0.16, indicating subcritical flow, and with a Reynolds number of 11,000, the flow was fully turbulent. The Froude number is calculated using:

$$Fr = \frac{U_b}{\sqrt{gR_h}} \tag{6.1}$$

where U_b is bulk velocity, g is the acceleration due to gravity, and R_h is the hydraulic radius ($R_h = A/P$, where A is the cross-sectional area and P is the wetted perimeter).

The flume is located in the PIV room of the hydraulics laboratory at the University of Ottawa. This flume is equipped with an independent, self-contained recirculating water system that includes inlet and outlet tanks connected by a pump, enabling the maintenance of the required water quality standards for PIV measurements. A custom-made 3D-printed calibration plate, measuring 10 cm by 20 cm, was used to cover the entire width of the flume during calibration. Using the gate at the exit section of the flume, the desired flow depth was achieved at the constant flat bed slope.

Reproducing near-freezing temperature conditions in the laboratory led to persistent bubble formation, which degraded PIV measurement quality remarkably. Warmer water ($\approx$ 20 °C) reduces gas solubility [66], thereby minimizing bubble interference [79] and enabling high signal quality. Importantly, key dimensionless parameters (e.g., Reynolds and Froude numbers) were matched to subcritical turbulent flow conditions of ice-covered rivers, preserving dynamical similarity despite thermal differences.

6.3.1 Physical model of the ice-cover

To simulate an ice-covered surface at the top of the flow, marine-grade mahogany plywood was employed. This material provides a flat, dimensionally stable surface that resists warping when exposed to water and humidity. To minimize light scattering from the wood surface, matte black adhesive vinyl was applied to its entire underside. This vinyl covering ensures optical uniformity, reduces glare, and mimics the hydraulically smooth underside of natural ice. The combined wood–vinyl surface exhibits negligible roughness ($k_s \sim 0.1\,\text{mm}$) relative to the flow depth ($H = 0.06\,\text{m}$), resulting in a hydraulically smooth boundary condition ($k_s/H \sim 1.7 \times 10^{-4}$).

For the rough ice-cover condition, black wood screws with a head height of $5\,\text{mm}$ were uniformly attached (at approximately $4.5\,\text{cm}$ spacing) to the vinyl-covered wood surface. These screws act as repeatable, rigid, non-deformable roughness elements. Their black color maintains the optical quality required for Particle Image Velocimetry (PIV) measurements. This configuration yielded a representative roughness height of $k_s = 0.005\,\text{m}$, corresponding to a relative roughness of $k_s/H \approx 0.083$. A schematic of the rough ice-cover geometry is shown in Figure 6.2.

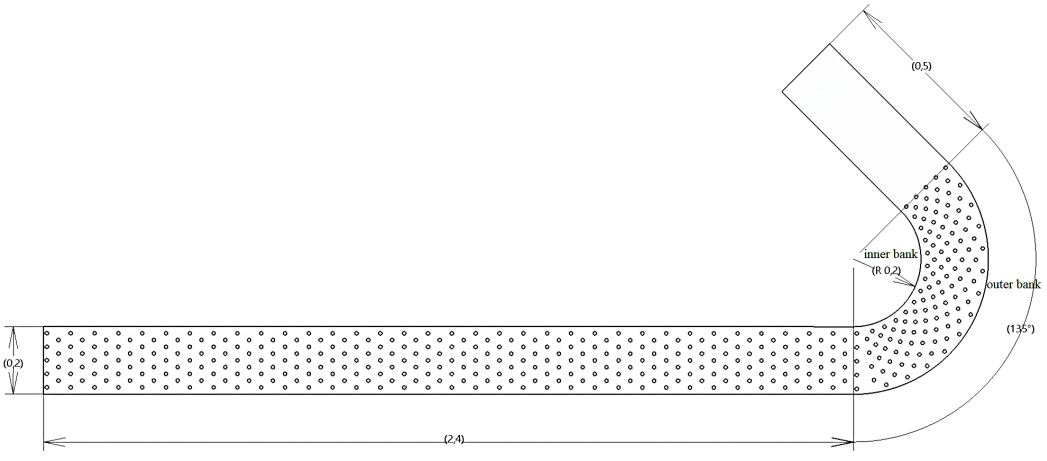


Figure 6.2. Schematic of the 135-degree bend physical model of rough ice cover, showing the configuration of surface roughness elements used in the PIV experiments (Credit: Julien Pierrat).

Table 6.1. Surface materials and roughness parameters used in the experiments

Surface	**Material**	$\mathbf{k_s}$ **(mm)**	$\mathbf{k_s/H}$
Top wall (smooth cover)	Vinyl-covered wood	0.1	1.7×10^{-4}
Top wall (rough cover)	Vinyl-covered wood + screws	5.0	0.083
Bottom wall	Plexiglass	0.003	5.0×10^{-5}
Side walls	Plexiglass	0.003	5.0×10^{-5}

The channel bottom and side walls were constructed from smooth plexiglass, with an effective roughness of approximately $k_s \sim 0.003\,\text{mm}$ ($k_s/H \sim 5 \times 10^{-5}$). The selected screw geometry resembles centimeter-scale roughness features such as rubble commonly observed under natural ice covers, while the plexiglass surfaces serve to establish a clear hydraulic contrast between rough and smooth boundaries. This configuration (Table 6.1) ensured controlled boundary conditions and reproducible optical quality for PIV measurements, consistent with methodologies used in prior flume studies of ice-covered flows.

6.3.2 Hydrodynamic entrance length of the flow

To assess whether the flow was fully developed prior to the measurement section at the bend, the hydrodynamic entrance length was estimated using standard correlations for turbulent internal flows. While some studies determine flow development based on visual assessment of velocity profiles [151], the present study employs a hydrodynamic entrance length calculation due to its physical basis and preference for methodological repeatability. The flume cross-section is rectangular, with all four walls wetted.

Given the flume dimensions, the cross-sectional area was $A = 0.012\,\text{m}^2$, and the wetted perimeter was $P = 0.52\,\text{m}$. The hydraulic diameter is calculated as $D_h = \frac{4A}{P} = 0.0923\,\text{m}$. Using the bulk velocity of $U_b = 0.12\,\text{m/s}$ and with kinematic viscosity $\nu \approx 1.0 \times 10^{-6}\,\text{m}^2/\text{s}$ (approximately 20 °C water), the Reynolds number was $\text{Re} \approx 1.1 \times 10^4$, indicating turbulent flow. The entrance length was then estimated using the empirical correlation [78]:

$$\frac{L_e}{D_h} \approx 4.4\,\mathrm{Re}^{1/6} \tag{6.2}$$

Substituting the values gives $L_e \approx 1.92\,\mathrm{m}$. The available straight section upstream of the bend is $L_{\text{inlet}} = 2.4\,\mathrm{m}$, corresponding to $\approx 26D_h$, which exceeds the estimated entrance length requirement ($\approx 21D_h$), thus indicating that fully developed flow conditions had been reached prior to the measurement section.

6.3.3 Stereo-PIV configuration and data acquisition

A stereo-PIV system including a laser, two high-frequency iDS cameras, a programmable timing unit, and a computer was used in this work. The size of the PIV seeding particles is recommended to be on the order of the light's wavelength to benefit from Mie scattering for measuring flow velocities. Here, $10\,\mu$m diameter hollow glass spheres were used as seeding particles, with approximately 5 ml of concentrated slury added to the tank. Figure 6.3 shows a schematic of the stereo-PIV optical setup, highlighting camera locations, laser-sheet orientation, and field-of-view (FOV) alignment with the bend geometry.

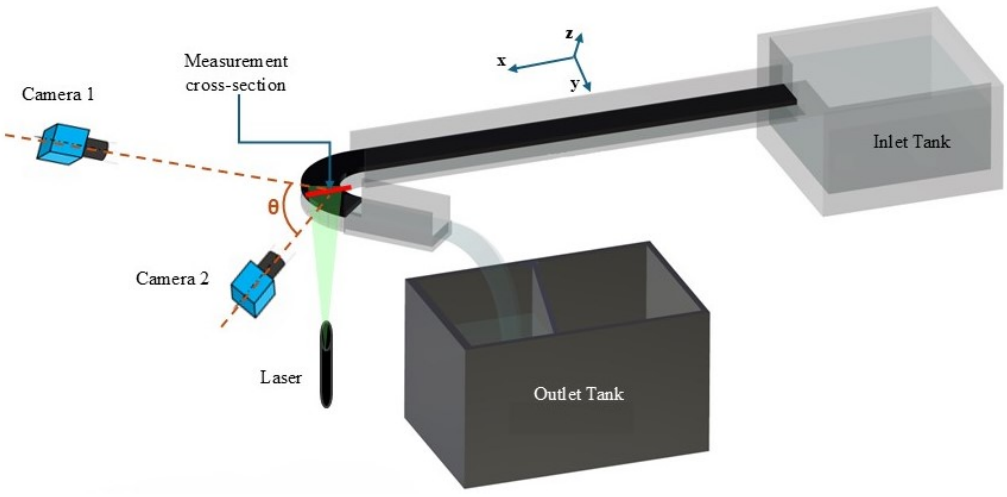


Figure 6.3. Schematic layout of the stereo-PIV system and experimental flow setup (credit: Julien Pierrat). The coordinate axes x, y, and z denote the streamwise, cross-stream, and vertical directions, respectively. The red line indicates the bend apex (90° cross-section) where the PIV measurements were conducted. The angle θ represents the angle between the optical axes of the cameras.

The laser light sheet was positioned beneath the bend; the beam was introduced vertically from below and aligned normal (90°) to the local cross-section to minimize out-of-plane misalignment. Two high-resolution PIV cameras, each fitted with Scheimpflug adapters to maintain focus across tilted image planes, were mounted on opposite sides of the bend. Their optical axes subtended approximately 75° and converged at the measurement plane at the 90° bend section. This configuration provided a practical compromise between spatial coverage and calibration accuracy, given laboratory and flume-geometry constraints.

6.3.4 Spatial and temporal resolution of the PIV data

The spatial resolution was calculated from the measurement image size and calibration settings. The dewarped image size was 3992 px $\times$ 2152 px (or 282 mm $\times$ 152 mm) in the transverse and vertical directions, respectively. The interrogation window, square in shape, was set to $W = 64$ px with a 75% overlap, resulting in a step size of $S = W(1 - \text{overlap}) = 16$ px. The number of vectors in the transverse (N_y) and vertical (N_z) directions was computed using the standard sliding-window approach [83, 82]:

$$N_y = 1 + \frac{N_{py} - W}{S}, \text{ and } N_z = 1 + \frac{N_{pz} - W}{S}. \tag{6.3}$$

Thus, N_y was equal to 246 (width) and N_z to 132 (height), giving a total count of N_{vectors} of 32,472 vectors per frame. With a calibrated field of view of $\text{FOV}_y = 282$ mm and $\text{FOV}_z = 152$ mm, the spatial resolutions in each directions were calculated using $\Delta y = \text{FOV}_y/N_y$ and $\Delta z = \text{FOV}_z/N_z$, giving $\Delta y = 1.146$ mm and $\Delta z = 1.152$ mm. This resolution, averaging approximately 1.15 mm across the directions, enabled detailed capture of velocity gradients in the channel cross-section.

The temporal bandwidth was evaluated using the Nyquist frequency, f_{Nyquist} [118], based on a measurement length of $600\,\text{s}$ and a sampling frequency of $f_s = 10\,\text{Hz}$ in the experiments. The minimum resolvable period ($T_{\min}$), the lower frequency bound imposed by the record length ($f_{\min}$), and the maximum resolvable period ($T_{\max}$) are expressed as:

$$f_{\text{Nyquist}} = \frac{f_s}{2}, \quad T_{\min} = \frac{1}{f_{\text{Nyquist}}}, \quad f_{\min} = \frac{1}{T_{\max}}. \tag{6.4}$$

For a sampling frequency of $f_s = 10\,\text{Hz}$, this yields $f_{\text{Nyquist}} = 5\,\text{Hz}$ and $T_{\min} = 0.2\,\text{s}$. The record-length lower limit is $f_{\min} = 1.67 \times 10^{-3}\,\text{Hz}$, with a corresponding maximum period of $T_{\max} = 600\,\text{s}$. Thus, the dataset resolves fluctuations with characteristic periods ranging from $0.2\,\text{s}$ to $600\,\text{s}$, spanning over three orders of magnitude and covering the relevant larger turbulent time scales under an ice-cover.

6.3.5 Planar Self-Calibration and Spatial Disparity Evaluation

To ensure geometric consistency and assess spatial uncertainty, first planar self-calibration quality was evaluated using the average disparity reported by DaVis. For the present measurements, the average disparity was 4.36 px, corresponding to a physical offset of 0.305 mm based on the calibration scaling. Relative to the measurement domain dimensions of 200 mm (width) and 60 mm (height), this offset corresponds to only 0.15% and 0.50%, respectively. Thus, the mean disparity corresponds to less than 0.2% of the cross-section width and 0.5% of the flow depth. These values indicate a very low level of residual geometric disparity between camera views, confirming a high-quality alignment achieved through planar self-calibration. The resulting disparity is minimal relative to the measurement domain, indicating that disparity-related errors are negligible and that the reconstruction is geometrically consistent.

6.3.6 Temporal Continuity Validation via Discharge Constancy

To validate the internal consistency of the velocity fields over time, the instantaneous discharge $Q(t)$ was computed at each time step by integrating the streamwise velocity over the measurement domain. This approach is based on the principle of discharge continuity and has been employed across different velocimetry measurement techniques to assess temporal coherence and adherence to physical conservation laws [114, 52, 39, 133, 40]. The method is fundamentally sensor-independent and serves as a robust validation criterion for optical flow measurements. The discharge was estimated as:

$$Q(t) = \sum_{i=1}^{N_y} \sum_{j=1}^{N_z} u_{ij}(t) \cdot \Delta y \cdot \Delta z \tag{6.5}$$

Here, $u_{ij}(t)$ denotes the instantaneous streamwise velocity component measured at the (i, j)-th grid point in the lateral and vertical directions at time t. The values $\Delta y = 1.146$ mm and $\Delta z = 1.152$ mm are the spatial resolutions in the vertical and lateral directions respectively. The temporal variability of $Q(t)$ was assessed (Figure 6.4) using the coefficient of variation (CV_Q):

$$\mathrm{CV}_Q = \frac{\sigma_Q}{|\bar{Q}|} \times 100\% \tag{6.6}$$

Here, σ_Q denotes the standard deviation of the discharge time series, $|\bar{Q}|$ is the absolute value of the time-averaged discharge, and the factor $\times 100\%$ is included to express the coefficient of variation as a percentage.

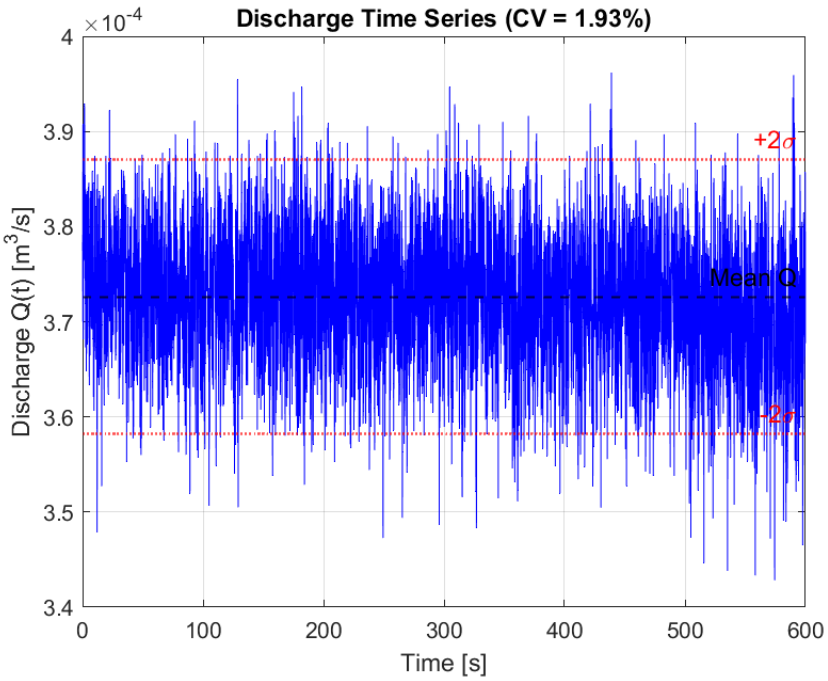


Figure 6.4. Time series of instantaneous discharge $Q(t)$ calculated from the PIV velocity fields over the full 600-second measurement length. The mean discharge $\bar{Q}$ is shown as a dashed black line, and the $\pm 2\sigma$ bounds are indicated by red dashed lines.

A low value of $\mathrm{CV}_Q = 1.93\%$ was obtained, indicating high temporal stability of the velocity measurements and minimal presence of spurious fluctuations. Song et al. [133] employed the coefficient of variation as a dimensionless measure to evaluate the repeatability of velocity and discharge time series. In their study, CV values below 0.1 (i.e., 10%) were interpreted as indicative of high repeatability. While their data source was acoustic in nature, the coefficient of variation is a general statistical tool that is independent of the sensing method. It quantifies relative temporal variability and is equally applicable to optical velocimetry data. Using the same interpretive framework, the low CV_Q value obtained in this study demonstrates that the PIV-derived discharge remained temporally consistent. This result confirms compliance with physical continuity principles and substantiates the validity of the velocity fields for further analysis of turbulent flow structures.

6.3.7 Estimation of Velocity Uncertainty from Sub-pixel Errors

The uncertainty in velocity magnitude was estimated using sub-pixel displacement error theory, a commonly adopted approach for quantifying measurement precision in PIV systems [112]. Using sub-pixel displacement error of 0.1 pixels, the resulting uncertainty in streamwise velocity, σ_U, was computed as:

$$\sigma_U = \frac{\sigma_{\text{disp}} \cdot C}{\Delta t} \tag{6.7}$$

where $\sigma_{\text{disp}} = 0.1$ pixels is the assumed sub-pixel displacement error, $C = 0.013$ m/pixel is the physical scaling factor (conversion from pixels to meters), and $\Delta t = 0.1$ s is the time separation between correlated image pairs (i.e., the inverse of the 10 Hz acquisition rate). Substituting these values yielded $\sigma_U = 0.013$ m/s, which corresponds to approximately 3.5% of the bulk velocity and represents the uncertainty associated with the instantaneous velocity measurements due to sub-pixel resolution limits.

The uncertainty in the root-mean-square (RMS) velocity fluctuations, denoted $\sigma_{u'_{\text{rms}}}$, refers to the uncertainty in the estimation of the standard deviation of the velocity signal, a metric used to quantify turbulent fluctuations in the flow. Assuming that measurement errors are random and uncorrelated, the standard error of the RMS velocity fluctuations was estimated as:

$$\sigma_{u'_{\text{rms}}} = \frac{\sigma_U}{\sqrt{2(N-1)}} \tag{6.8}$$

where σ_U is the uncertainty in individual velocity measurements (as computed above), and N is the number of independent time samples used to compute the RMS velocity fluctuations [124]. This yielded an uncertainty in the RMS fluctuations of $\sigma_{u'_{\text{rms}}} \approx 1.18 \times 10^{-4}$ m/s.

6.3.8 Estimation of Near-boundary Uncertainty

Accurate velocity measurement near solid boundaries remains a persistent challenge in PIV due to steep velocity gradients and reduced spatial resolution. The Iterative Deformation Method (IDM) PIV algorithm, which has been found to offer advantages over conventional cross-correlation approaches, decomposes measurement error into related subcomponents [28]. Among the sources of uncertainty in this algorithm, the gradient-related contribution is particularly significant in near-boundary regions, where steep velocity gradients coincide with limited spatial resolution δ. This contribution arises from unresolved subgrid velocity variations within the interrogation region and is derived analytically through the variance of the unresolved displacement field. In the present cross-sectional measurements, direct evaluation of $\partial u/\partial x$ was not possible. Instead, the magnitude of the in-plane velocity gradient was used as a proxy:

$$|\nabla u| = \sqrt{\left(\frac{\partial u}{\partial y}\right)^2 + \left(\frac{\partial u}{\partial z}\right)^2}, \tag{6.9}$$

and the effective unresolved length scale, δ, was taken as the vector spacing of the processed PIV field, $\delta = \min(\Delta y, \Delta z)$, rather than the full interrogation window width. This length scale was selected because it corresponds to the effective spatial resolution of the processed vector field, which defines the smallest resolvable velocity gradient in the dataset. Since velocity gradients are approximated using central differences between adjacent vector points, the vector spacing inherently limits the observable spatial variation and thus serves as the physically meaningful unresolved length scale in the gradient error formulation.

To quantify the influence of spatial velocity gradients on local measurement er-

ror arising from the finite spatial resolution of the PIV measurement, a simplified finite-resolution (Taylor-series–based) formulation was adopted. The gradient-induced finite-resolution error at each grid point was estimated as:

$$\sigma_{\text{grad}} = C\,|\nabla u|\,\delta, \tag{6.10}$$

where C is a proportionality constant derived from a Taylor-series–based finite-resolution truncation. Under symmetric spatial averaging, this leads to a coefficient, C, of $1/\sqrt{12}$. This estimate is used here to quantify the potential influence of finite spatial resolution on local velocity statistics, providing a physics-based diagnostic that serves as an alternative to calibration-based uncertainty assessments. The expression was evaluated locally across the domain, with the in-plane velocity gradient magnitude characterizing gradient strength and the vector spacing taken as the effective unresolved scale.

Using this formulation, a gradient-amplification indicator σ_{grad} was computed over the full dataset. The resulting median and 95th-percentile values were $\sigma_{\text{grad,med}} = 4.9 \times 10^{-3}$ m/s and $\sigma_{\text{grad,95}} = 1.9 \times 10^{-2}$ m/s, respectively. These correspond to approximately 3.8% (median) and 14% (95th percentile) of the bulk flow velocity indicating that gradient-induced uncertainties contribute modestly to the overall velocity uncertainty in most of the domain. To further reduce the influence of high-uncertainty regions near the walls, the outermost rows and columns of the velocity field were excluded from the analysis. This masking strategy was employed to eliminate zones most affected by known PIV limitations, including optical distortions, light reflections, poor particle image quality, and steep velocity gradients that are challenging to resolve accurately during post-processing.

6.4 Results

6.4.1 Effect of ice roughness on secondary vortex structure and circulation

Figure 6.5 presents a comparison of PIV results for two ice-cover wall roughness conditions at the same flow rate. All results presented are based on time-averaged (unless specified) measurements obtained at the 90° cross-section of the channel bend. In all figures,

the horizontal axis is oriented with the channel's inner bank on the left and the outer bank on the right. The data in regions near the channel boundaries, where velocity measurements are obscured by laser reflections (indicated by the black or white mask along the borders), were excluded from the analysis. The vortex identification method of Graftieaux *et al.* [53] was used to quantify the secondary circulation patterns observed in ice-covered river bends (Figure 6.5a–b), extending beyond earlier studies. This method involves the calculation of two dimensionless scalar fields, Γ_1 and Γ_2, for each point in the velocity field to identify vortex centers and delineate vortex cores.

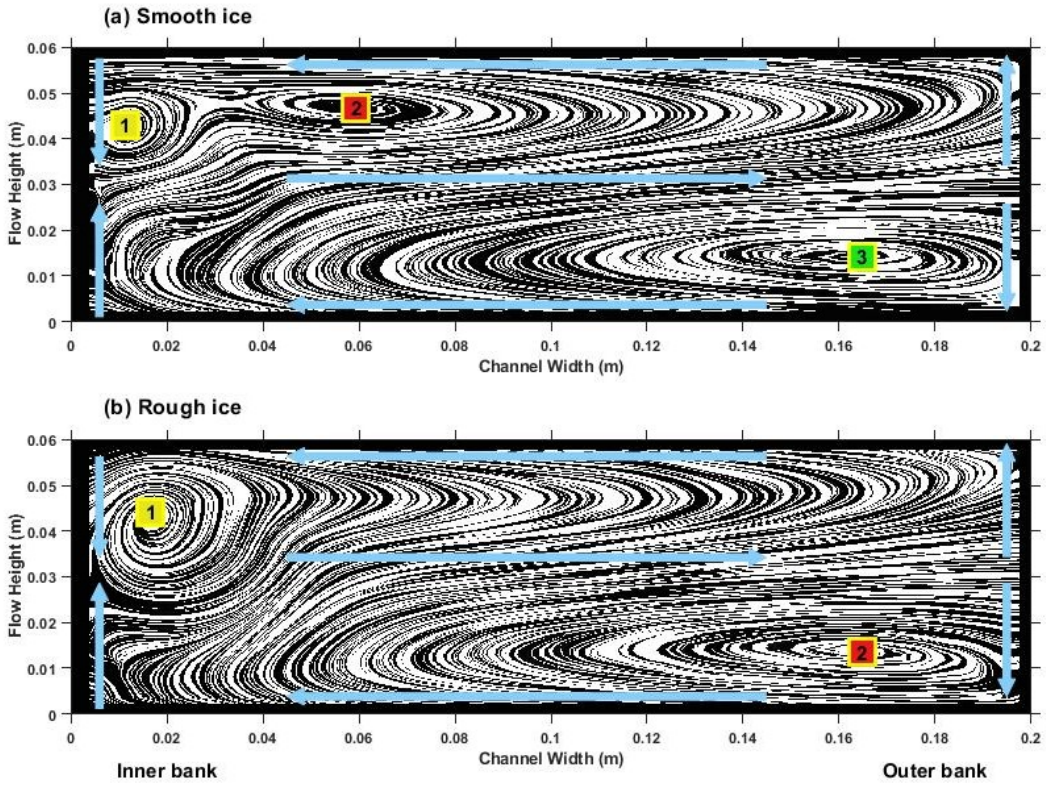


Figure 6.5. Mean flow streamlines illustrating secondary flow vortices under (a) smooth and (b) rough ice covers. Colored rectangles indicate identified vortex regions, while blue arrows denote flow directions within the ice (top) and bed (bottom) boundary layers, intersecting approximately at mid-depth. The vertical axis represents flow depth (0-0.06 m, from bed to ice cover), and the horizontal axis represents channel width (0-0.20 m, from inner bank to outer bank).

The circulation (Γ) of each vortex was obtained by integrating the mean spanwise vorticity (Ω_z) over the vortex core region, defined by the $\Gamma_2 = 0.69$ contour:

$$\Gamma = \iint \Omega_z \, \mathrm{d}A \tag{6.11}$$

where Ω_z denotes the out-of-plane vorticity calculated from the mean velocity field. The integration domain corresponds to the closed contour enclosing the coherent vortex core, ensuring that only the circulation associated with the vortex structure is included, excluding background shear or noise.

Table 6.2 summarizes the circulation magnitudes for the vortices identified under both smooth and rough ice covers, with vortex IDs corresponding to those shown in Figure 6.5.

Table 6.2. Properties of vortices identified under different ice covers.

Ice Cover Type	Vortex ID	Circulation ($\times 10^3$ mm^2/s)	y Location (m)	z Location (m)
Smooth Ice	1	1.64	0.01	0.02
Smooth Ice	2	3.19	0.06	0.01
Smooth Ice	3	-0.72	0.16	0.05
Rough Ice	1	2.78	0.02	0.02
Rough Ice	2	-1.13	0.16	0.05

In both cases, a distinct two-layer structure develops; however, the number, strength, and distribution of vortices change depending on the roughness of the ice surface. Under the smooth ice cover, two vortices form in the upper layer: a primary vortex (vortex 2 in Figure 6.5a) and a smaller inner bank cell. The inner-bank cell (IBC) refers to a small, coherent secondary flow vortex that develops near the inner (concave) bank of a sharply curved open-channel flow and is commonly associated with flow separation at the inner bank [64, 23, 16, 121, 122]. The rotation direction of the IBC is typically the same as the primary central cell. The development of the IBC is thus associated with meander bend flow,

but given its position as a corner cell near the inner wall its generation is also influenced by turbulence anisotropy.

To determine the variation in flow resistance for the fully developed turbulent flow, the Colebrook–White model in a closed channel was used. This model, originally developed to relate the friction factor to relative roughness and Reynolds number in turbulent pipe flow, represents turbulent flow resistance over a wide range of flow conditions [32]. To account for asymmetric boundary roughness, the channel was modeled as a closed rectangular duct, and a composite equivalent sand-roughness height was computed using a perimeter-weighted approach. The wetted perimeter was divided into the top wall (ice cover), bottom wall (bed), and two side walls. The channel had a width of $B = 0.20\,\text{m}$, a depth of $H = 0.06\,\text{m}$, resulting in a cross-sectional area of $A = 0.012\,\text{m}^2$ and a wetted perimeter of $P = 0.52\,\text{m}$. The corresponding hydraulic diameter was $D_h = 4A/P = 0.0923\,\text{m}$.

Roughness heights assigned to the surfaces were: $k_{s,\text{top}} = 1 \times 10^{-4}\,\text{m}$ for the smooth ice case and $5 \times 10^{-3}\,\text{m}$ for the rough ice case; and $k_{s,\text{bed}} = k_{s,\text{side}} = 3 \times 10^{-6}\,\text{m}$ for the plexiglass bed and sidewalls. The equivalent roughness height was computed as:

$$k_{s,\text{eq}} = \frac{k_{s,\text{top}}B + k_{s,\text{bed}}B + 2k_{s,\text{side}}H}{P} \tag{6.12}$$

This yielded $k_{s,\text{eq}} \approx 4.03 \times 10^{-5}\,\text{m}$ for the smooth-ice case and $k_{s,\text{eq}} \approx 1.92 \times 10^{-3}\,\text{m}$ for the rough-ice case, corresponding to relative roughness values of $k_{s,\text{eq}}/D_h \approx 4.37 \times 10^{-4}$ and 2.09×10^{-2}, respectively.

Assuming a bulk velocity of $U_b = 0.12\,\text{m/s}$ and a kinematic viscosity of $\nu = 1.0 \times 10^{-6}\,\text{m}^2/\text{s}$, the Reynolds number was approximately $Re \approx 1.1 \times 10^4$. The Darcy–Weisbach friction factor f was then computed by solving the Colebrook–White equation in Eq. 6.13, using the Swamee–Jain approximation for initial estimates and iterating to convergence.

$$\frac{1}{\sqrt{f}} = -2\log_{10}\left(\frac{k_s}{3.7D_h} + \frac{2.51}{Re\sqrt{f}}\right) \tag{6.13}$$

The resulting friction factors were $f \approx 0.031$ for the smooth-ice composite case

and $f \approx 0.053$ for the rough-ice case, indicating increased flow resistance due to the larger roughness elements introduced by the rough ice cover.

Under rough ice cover, the inner-bank cell (IBC, vortex 1 in Figure 6.5a) and the center vortex appear to merge and form a single primary vortex (vortex 1 in Figure 6.5b), which shifts closer to the inner bank. The total circulation in the ice layer decreases by 42%, from 4.83 to 2.78 $\times 10^3$ mm^2/s, under the rough ice cover. In contrast, the counter-rotating circulation in the bottom layer increases from 0.72 to 1.13 $\times 10^3$ mm^2/s under the rough ice cover. The height of the primary vortex's center in the ice layer shifts from 4.68 cm under smooth ice to 4.42 cm (a 5.6% reduction) under rough ice, extending the ice-influenced layer downward and compressing the bed layer. This lowers the height of bed vortices (vortex 2 in Figure 6.5b) by 4.9%, while increasing their strength by 57%. The increased circulation in the bed may be attributed to the enhanced momentum transfer downward to the bed vortices, which will be further analyzed.

Figures 6.6 and 6.7 jointly illustrate the lateral evolution of the transverse-flow structure under smooth and rough ice covers. Figure 6.6 presents a comparison of vertical profiles of the cross-stream velocity component at ten lateral positions across the channel width, ranging from 10% (near the inner bank) to 95% (near the outer bank), under both smooth and rough ice cover conditions. These profiles are derived directly from Particle Image Velocimetry (PIV) measurements, presented without filtering or curve fitting to preserve the true characteristics of the flow. The profiles of cross-stream velocity are similar across the channel and consistent with dual stacked counter-rotating primary cells, except near the inner-bank (Figure 3a-b) due to interactions between the inner bank cell and the primary cells.

In the upper layer of the flow, near the inner bank (Figures 6.6a–b), the transverse velocity under the smooth ice cover is either slightly higher or comparable to that under the rough ice. As the profiles progress toward the center and outer parts of the channel, the rough ice progressively exhibits higher cross-stream velocities in the mid-depth region, where the magnitude tends to peak. At one-third of the channel width from the inner bank (Figure 6.6c), cross-stream velocity is greater under the smooth ice condition than under the rough ice condition. This location approximately corresponds to the position of Vortex 2 under the smooth ice condition, where localized recirculation increases transverse velocity.

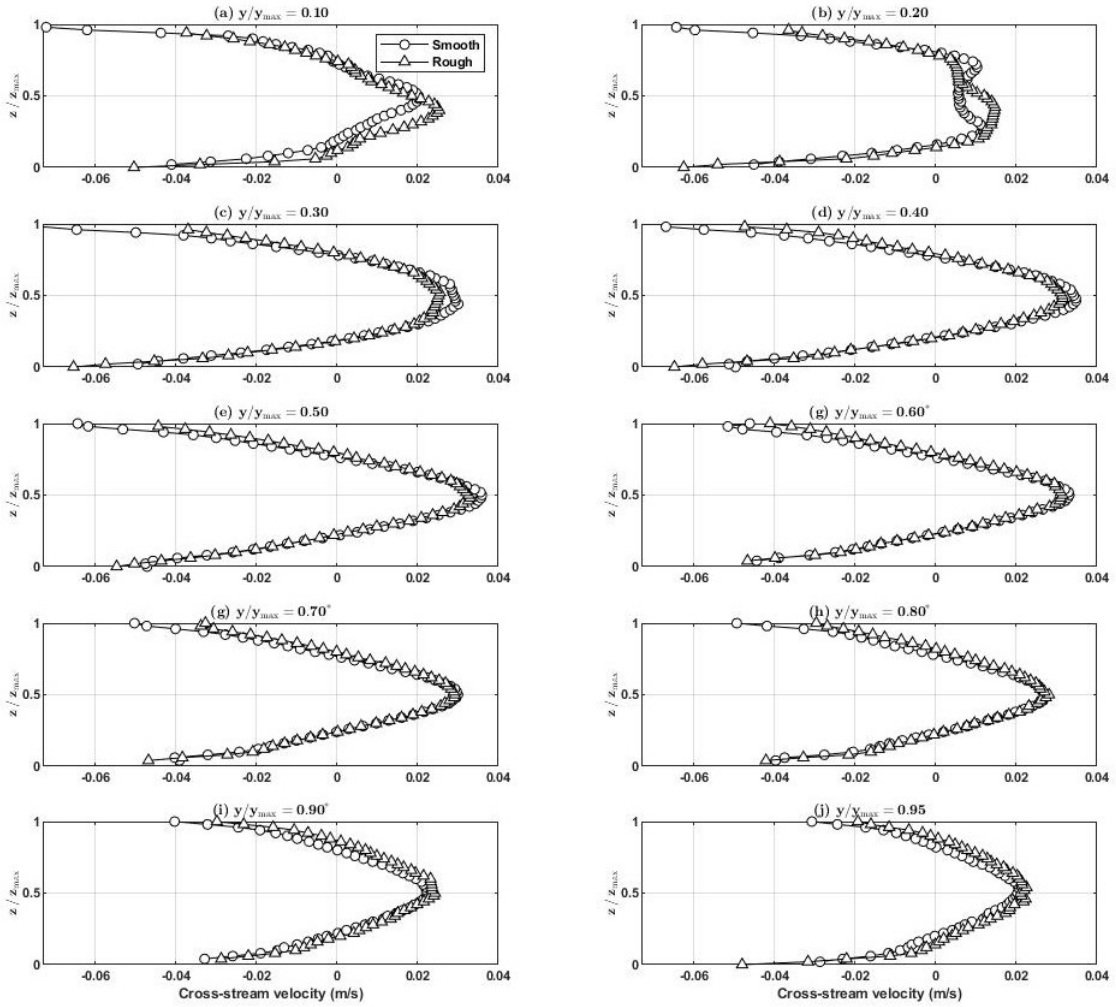


Figure 6.6. Vertical profiles of cross-stream velocity (V) at selected lateral positions across the channel width, ranging from 10% near the inner bank to 95% near the outer bank, under smooth (circle markers) and rough (triangle markers) ice cover conditions. Each subplot is labeled with the corresponding normalized lateral position, where y is the lateral distance from the inner bank and $y_{\max}$ is the total channel width. The vertical axis represents the dimensionless height $z/z_{\max}$, where $z_{\max}$ denotes the flow depth. No velocity filtering was applied. An asterisk (*) indicates profiles where near-bed data points were excluded due to high velocity uncertainty.

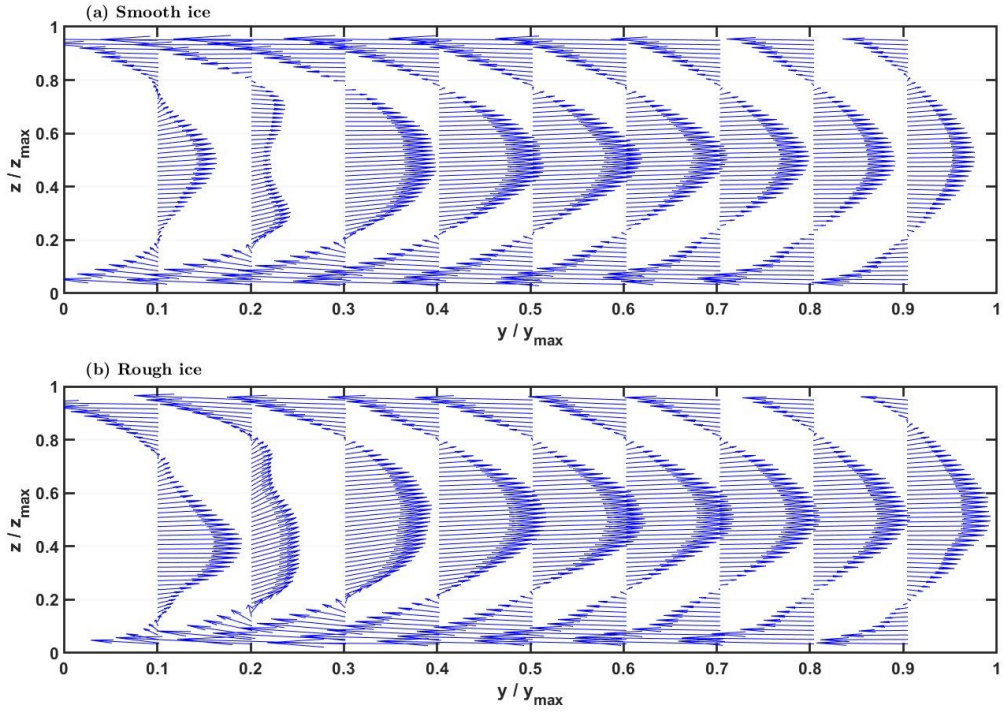


Figure 6.7. Vector fields of transverse circulation under (a) smooth and (b) rough ice covers, where arrows indicate the direction of secondary flow, and their lengths reflect local velocity magnitudes. The horizontal and vertical axes are normalized by the channel width and flow depth, respectively, where y denotes the lateral position, $y_{\max}$ the total channel width, z the vertical position, and $z_{\max}$ the total flow depth. White bands at the top and bottom of each panel represent masking applied to exclude near-ice and bed data.

While Figure 6.6 presents discrete vertical profiles at selected lateral stations, quantifying magnitude differences, Figure 6.7 provides a more continuous depiction of the flow field, showing differences in both the direction and relative strength of transverse motion across the full cross-section. Figure 6.7b for the rough ice condition illustrates a downward displacement of the maximum transverse velocity near the inner bank, which gradually bounces upward toward mid-depth around the channel center and outer bank. Taken together, Figures 6.6 and 6.7 show that the peak transverse velocity increases from the inner bank ($y/y_{\max} \approx 0.10$) to mid-channel (≈ 0.50) and then decreases toward the outer bank, with an overall trend of higher peaks under the rough-ice cover, demonstrating that surface roughness intensifies secondary circulation.

6.4.2 Directional influence of roughness on secondary flow and momentum distribution

Analyzing the momentum distribution across the channel plane provides a physically grounded and effective means of characterizing secondary flow structures [117]. While some ice-covered channel studies address momentum transport indirectly through shear stress analysis [130], the present study investigates the full three-dimensional momentum flux distribution. Using momentum is conceptually consistent with the governing equations of fluid mechanics and aligns with approaches adopted in prior literature. Moreover, it enables broader applicability to variable-density flows, where momentum distributions would convey additional insights.

Here, the 3D momentum is calculated in a 2D cross-sectional plane using a constant fluid density. Let ρ denote density (kg/m^3), and $U(y,z)$, $V(y,z)$, and $W(y,z)$ represent mean streamwise, cross-stream, and vertical velocity components (m/s), respectively. For example, the streamwise momentum flux, M_x, across a cross-sectional area A, is defined as:

$$M_x = \rho \iint_A \vec{U} \cdot \vec{n}\, U \, \mathrm{d}A \tag{6.14}$$

The cross-stream and vertical momenta, M_y and M_z, are calculated similarly. The total momentum magnitude $M_t(x,z)$ is then calculated as:

$$M_t(x,z) = \sqrt{M_x(x,z)^2 + M_y(x,z)^2 + M_z(x,z)^2} \tag{6.15}$$

Figure 6.8 shows the distribution map of directional momentum under both ice conditions. The data in regions near the channel boundaries, where velocity measurements are obscured by laser reflections (indicated by the white mask along the borders), were excluded from the analysis. The positive and negative values of the momentum components reflect the flow direction observed across the different components.

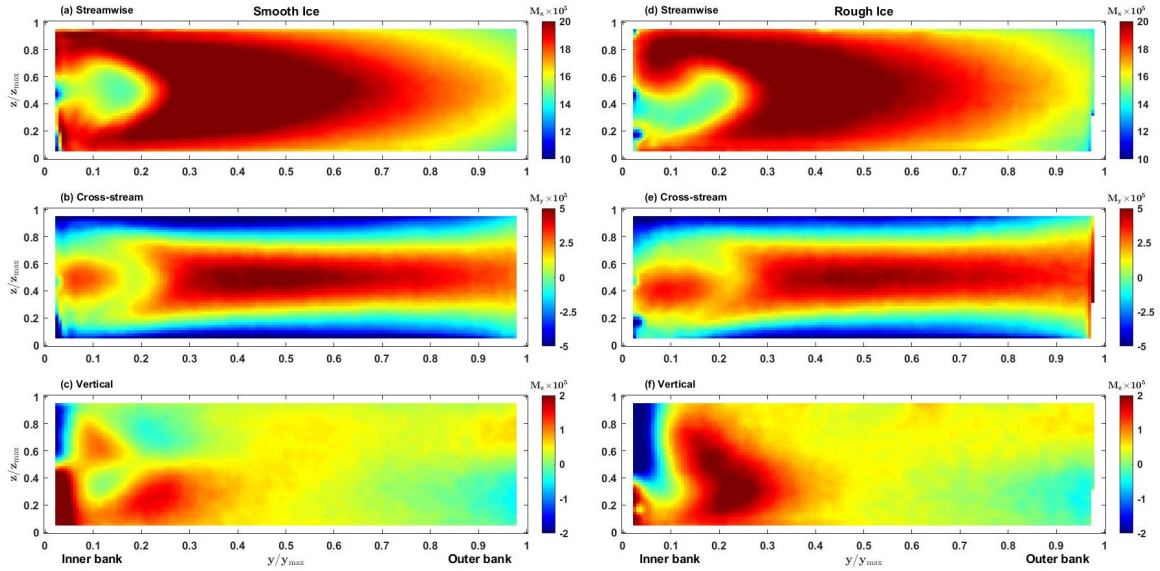


Figure 6.8. Momentum distribution for (a–c) smooth ice and (d–f) rough ice cover in the streamwise (a,d), cross-stream (b,e), and vertical (c,f) directions. All momentum components shown are time-averaged. The colorbar shows momentum magnitude and direction. The white areas near the edges indicate masked data.

Under smooth ice conditions, the streamwise momentum (M_x, Figure 6.8a) is all positive, consistent with downstream-directed primary flow. Its peak region, located centrally, aligns with the maximum streamwise velocity near the channel centerline. Moving laterally from the center toward the channel boundaries, M_x progressively decreases, forming regions of reduced momentum near both the ice surface and the bed. Cross-stream momentum (M_y, Figure 6.8b) shows a symmetrical reduction from its maximum in the channel's center toward the top and bottom boundaries. Positive M_y values indicate lateral momentum directed from the inner toward the outer bank, whereas negative values correspond to momentum directed from the outer toward the inner bank. An elevated band of M_y is observed stretching laterally across the section, spanning from the inner to the outer bank. Vertical momentum flux (M_z) demonstrates a similar general distribution trend from the channel center outward. In the vertical direction, positive values represent upward momentum, while negative values indicate downward-directed flow.

Under rough ice-cover (Figures 6.8d–f), momentum fluxes intensify at the channel center and particularly near the inner bank in all three directions, most notably in the streamwise and vertical directions. In the cross-stream direction (M_y, Figure 6.8e), both positive

(outer-bankward) and negative (inner-bankward) momentum regions descend downward toward the bed near the inner bank. The vertical momentum flux (M_z, Figure 6.8f) exhibits the greatest response to increased surface roughness, with the most pronounced enhancement near the inner bank throughout the vertical profile from the ice to the bed layer.

Layered momenta were calculated by dividing the vertical cross-section into two layers (top and bottom) at the mid-height of the flow. For each layer, directional (M_x, M_y, M_z) and total (M_t) momenta were integrated across all grid cells. Positive and negative contributions in the cross-stream (outward/inward) and vertical (upward/downward) directions were decomposed and summed separately. The percentage change in each momentum component from smooth to rough ice cover is also included in Table 6.3.

Table 6.3. Layered momentum comparison: M_x, M_y^+, M_y^-, M_z^+, M_z^-, and M_t represent streamwise, outward cross-stream, inward cross-stream, upward vertical, downward vertical, and total momentum sums, respectively. Units are in $\times 10^5$ kg·m/s.

Layer	M_x	M_y^+	M_y^-	M_z^+	M_z^-	M_t
Direction	downstream	outward	inward	upward	downward	–
Smooth Ice Cover						
Top Layer	0.661	0.047	0.068	0.0125	0.0033	0.680
Bottom Layer	0.664	0.055	0.053	0.0225	0.0011	0.680
Full Cross-section	1.320	0.102	0.121	0.0351	0.0044	1.360
Rough Ice Cover						
Top Layer	0.683	0.052	0.043	0.0203	0.0074	0.693
Bottom Layer	0.697	0.063	0.054	0.0252	0.0024	0.713
Full Cross-section	1.380	0.114	0.097	0.0454	0.0097	1.410
Percentage Change from Smooth to Rough Ice Cover (%)						
Top Layer	3.3	8.6	-36.8	62.4	120.1	1.90
Bottom Layer	5.0	14.4	1.9	12.0	121.7	4.90
Full Cross-section	4.5	11.8	-19.8	29.3	120.2	3.70

Compared to the smooth ice condition, the rough ice cover results in consistent increases in streamwise momentum (M_x) across both layers, with the top, bottom, and full cross-section increasing by 3.3%, 5.0%, and 4.5%, respectively. The positive cross-stream momentum (M_y^+) also increases noticeably, especially in the bottom layer (14.4%) and across the full cross-section (11.8%), while the negative component (M_y^-) shifts less uniformly, showing a 36.8% reduction in magnitude in the top layer and a 1.9% increase in magnitude in the bottom layer.

In the vertical direction, the positive momentum (M_z^+) shows strong amplification, with increases of 62.4% in the top layer and 12.0% in the bottom. Conversely, the negative vertical momentum (M_z^-) becomes more intense, with magnitudes increasing by 120.1% in the top and 121.7% in the bottom layer. Overall, the total momentum (M_t) increases modestly, with greater rise (4.8%) in the bottom layer, indicating that roughness enhances horizontal and vertical momentum transport. These patterns, observed from the Table 6.3 comparisons, suggest that roughness not only amplifies momentum exchange but also alters the spatial configuration of secondary circulation.

6.4.3 Statistical significance of momentum changes

To evaluate the statistical significance of the layered momentum differences reported in Table 6.3, the Mann–Whitney U test (also referred to as the Wilcoxon rank-sum test) was applied. This non-parametric method compares two independent groups based on an ordinal variable without assuming any particular distribution [81, 159]. This test was selected after inspection of the 3D velocity component histograms, which revealed the distributions were non-normal, asymmetric, and showed different degrees of skewness under both ice cover conditions (not shown). This test assesses whether two independent samples originate from the same distribution by comparing the sums of their ranks, rather than their means.

Layered directional momentum was computed across all 6000 timesteps. For each comparison, the momentum values under smooth ice were defined as sample 1, and those under rough ice as sample 2. MATLAB's built-in `ranksum()` function was used to perform the Mann–Whitney U test. This function returns the *p*-value, representing the probability of observing the test statistic under the null hypothesis, and the z-value, which is a standardized form of the U statistic.The U statistic itself is calculated based on the sum of the ranks for

each group and reflects the number of times a value from one sample precedes a value from the other sample when all observations are ranked together [81]. A lower U value indicates a greater difference between the two groups. For two independent samples of sizes n_1 and n_2, the $\boldsymbol{U}$ statistics for each group are calculated as:

$$U_1 = n_1 n_2 + \frac{n_1(n_1+1)}{2} - R_1, \quad U_2 = n_1 n_2 + \frac{n_2(n_2+1)}{2} - R_2, \tag{6.16}$$

where R_1 and R_2 are the sums of the ranks for sample 1 and sample 2, respectively. The Mann–Whitney $\boldsymbol{U}$ statistics is then taken as the smaller of the two:

$$\boldsymbol{U} = \min(U_1, U_2) \tag{6.17}$$

A standardized test statistic (z-value) was then calculated to determine the corresponding *p*-value. The z-value (or *z-score*) represents the standardized difference between the observed U statistic and its expected value under the null hypothesis, measured in units of standard deviation ($z = \frac{U-\mu_U}{\sigma_U}$, where σ_U is standard deviation). The null hypothesis, H_0, in this comparison states that the momentum distributions under smooth and rough ice conditions are identical. Rejecting the null implies a statistically significant difference between the two datasets. A z-score of zero implies no difference between the two groups, whereas $|z| > 1.96$ indicates significance at the 95% confidence level. Positive z-values (e.g., top-layer streamwise) suggest momentum is greater under smooth ice, while negative values (e.g., bottom-layer vertical) indicate enhanced momentum under rough ice.

The *p*-value represents the probability of obtaining a test statistic that is as far from the expected value under the null hypothesis as the one observed, assuming H_0 is true. Its range is $0 \leq p \leq 1$. The expected value, μ_U, of the $\boldsymbol{U}$ statistics under H_0 is given by $\mu_U = \frac{n_1 n_2}{2}$. A small p-value (e.g., < 0.05) provides strong evidence against H_0, whereas a larger p-value (≥ 0.05) indicates insufficient evidence to reject it. A p-value less than 0.001 indicates a highly significant difference between the properties of the smooth and rough ice cases. Table 6.4 summarizes the test results for each comparison.

Table 6.4. Results of the Mann–Whitney $\boldsymbol{U}$ test for momentum under smooth and rough ice conditions.

Comparison	**p-value**	**z-value**	**H_0 Rejected**
Top Layer M_{x}	<0.001	94.8	Yes (1)
Bottom Layer M_{x}	<0.001	-13.0	Yes (1)
Full Cross-section M_{x}	<0.001	92.7	Yes (1)
Top Layer M_{y}	<0.001	85.0	Yes (1)
Bottom Layer M_{y}	<0.001	-32.2	Yes (1)
Full Cross-section M_{y}	<0.001	54.9	Yes (1)
Top Layer M_{z}	<0.001	-35.3	Yes (1)
Bottom Layer M_{z}	<0.001	-63.0	Yes (1)
Full Cross-section M_{z}	<0.001	-61.8	Yes (1)

The H_0 was rejected in all cases with p-values less than 0.001. The large z-values observed (as expected for large samples, where the small σ_U inflates the z-value), particularly for the top layer transverse momentum ($z = 85.0$) and vertical momentum at full cross-section ($z = -61.8$), highlight regions where roughness-induced momentum differences are especially pronounced. The results for the z-values of the momentum components reveals clear trends; roughness generally decreases momentum in the top layer and increases it near the bed, aligning with the physical response of ice and bed layers to roughness in previous sections. These results firmly established the statistically significant differences in momentum values between smooth and rough ice conditions across all three directions (streamwise, cross-stream, and vertical) and across all vertical layers (top, bottom, and full depth). These findings confirmed the conclusion that ice roughness strongly influences momentum distribution within the flow.

6.4.4 Roughness-induced patterns of momentum changes

Ice roughness was found to influence all three components of momentum flux differently. This raises the question: how much change, relative to the smooth-ice momentum, occurs at each location due to roughness? While some conventional metrics such as ab-

solute difference, percentage change, and the ratio change were calculated to examine the influence of ice conditions, the absolute difference and the percentage change were found to be insufficient to capture the complexity of under-ice flow structures, where flow direction varies both vertically and horizontally across the top and bottom layers. Here we present only the results for the rough-to-smooth momentum ratio, which was simply defined at each grid point (i, j) as:

$$\text{ratio}_{i,j} = \frac{M_{\text{rough},\, i,j}}{M_{\text{smooth},\, i,j} + \varepsilon} \tag{6.18}$$

where $M_{\text{rough},\, i,j}$ and $M_{\text{smooth},\, i,j}$ represent the momentum components under rough and smooth ice conditions, respectively, and ε is a small threshold (here, 10^{-6}) introduced to avoid division by zero. The results are shown in Figure 6.9.

The streamwise ratio (Figure 6.9a) remains above zero across the cross-section, with values close to 1.0 in most regions, indicating minimal overall change in downstream momentum between cases. Ratios greater than 1.0 occur primarily near the inner bank under the ice cover, identifying zones where roughness locally enhances the streamwise flow relative to smooth ice. This zone coincides with the centre of the upper vortex where the smooth case has an inner-bank cell and falls below 1.0 near the bed. This pattern indicates a redistribution of streamwise momentum, with roughness shifting more flow to the upper ice region near the inner bank while slightly reducing it near the bed. However, the overall magnitude of these enhancements in the streamwise direction is modest compared to those in the cross-stream and vertical directions.

In the cross-stream momentum ratio plot (Figure 6.9b), both positive and negative values appear. Two narrow horizontal bands of negative ratio values are observed near $z/z_{\text{max}} \approx 0.2$ and 0.8, extending across the channel width. These indicate regions where the stratified cross-stream momentum pattern seen under smooth ice (Figure 6.8b) is displaced vertically downward in the rough-ice condition (Figure 6.8e), leading to a local reversal of momentum direction and thus a negative ratio.

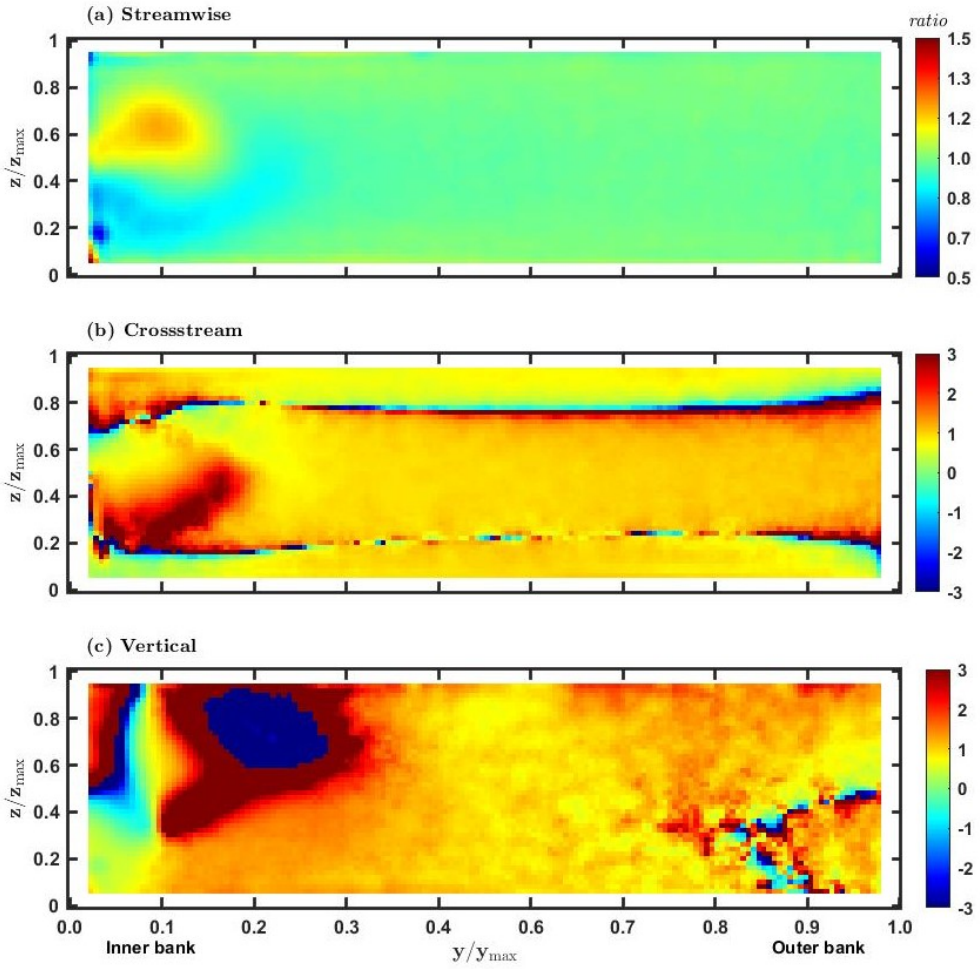


Figure 6.9. Distribution of rough to smooth momentum ratios in (a) streamwise, (b) cross-stream, and (c) vertical components. Note the lower colorbar range in plot (a) compared to plot (b) and (c). The white areas near the edges indicate masked data.

The remaining areas with positive ratios fall into two main categories. First, in regions near the top and bottom boundaries in Figure 6.8b and 6.8e where both smooth and rough ice flow generate momentum in the negative direction (inward motions), thus positive ratio. Second, strong positive ratios are also observed in the central zone (approximately $y/y_{\text{max}} = 0.25$ to 0.95 and $z/z_{\text{max}} = 0.25$ to 0.7 in Figure 6.8b and 6.8e), where roughness amplifies outward momentum.

Vertical momentum ratios indicate a mixed pattern of positive and negative values (Figure 6.9c). Zones with ratios exceeding 1.0 (deep red) extend downward from the inner bank past mid-depth, corresponding to the positions of vortices 1 and 2 identified under smooth ice conditions (Figure 6.5a). These high-positive-ratio regions indicate intensified vertical motion resulting from increased ice roughness, relative to smooth-ice conditions.

Conversely, negative ratios (dark blue and aqua) represent flow reversals, where vertical momentum under rough ice is opposite in direction to that under smooth ice. In the ice layer, this reversal is prominently observed in two distinct regions along the inner bank. First, a narrow vertical region of negative ratios indicates opposing momentum directions between rough- and smooth-ice conditions. This arises from the dominance of the strong downward (negative) vertical flow associated with vortex 1 under rough-ice conditions (Figure 6.5b), overwhelming the weaker upward (positive) motion of the vortex (IBC) under smooth ice (Figure 6.5a). Second, the clearly defined circular region of negative ratios (dark blue), prominently embedded within a surrounding zone of positive ratios (red) in the ice layer, signifies an important influence of roughness in a region corresponding to vortex 2 under smooth ice and vortex 1 under rough ice conditions. This localized reversal in vertical momentum direction highlights the stronger downward (negative) momentum associated with smooth-ice vortex 2 in comparison to the comparatively weaker upward vertical flow of rough-ice vortex 1.

In the bed layer, a distinct negative-ratio region border (dark blue and aqua) outlines a confined positive-ratio region near the outer bank corner, corresponding to the spatial extension of upward vertical momentum of the lower vortex layer induced by bed roughness (aqua zone in the lower layer outer bank corner, Figure 6.8c and 6.8f). Although upward (negative) vertical momentum flux under both smooth and rough ice cover flows, predominantly produces positive ratios (Figure 6.9c), implying consistency in flow direction near the outer bank, the clear negative border around this region uniquely indicates that rough ice cover enhanced and increased the spatial extent of upward flow near the bed.

6.5 Discussion

The opposing momentum directions in the upper and lower layers in the cross-stream direction (Figures 6.8b and 6.8e) reflect the characteristic two-cell structure of secondary circulation. The clear formation of a double-layer secondary flow structure that is also observed in Figures 6.5 and 6.7 is consistent with previous studies that have directly or indirectly examined the influence of ice cover on transverse flow [145, 138, 115, 77], although some studies have not consistently reported a two-layer structure [38, 69].

Under rough ice, cross-stream momentum (Figures 6.8b and 6.8e) near the inner bank increases, particularly in the lower half of the water column. Compared to the smooth ice case, the region of peak positive M_y (red circle) expands and shifts vertically downward, indicating stronger vortex-driven advection and a downward shift in momentum transfer toward the bed. The vertical momentum maps (Figures 6.8c and 6.8f) support this relationship while providing further insights. The expansion of negative vertical momentum from the ice downward (in the region where the IBC formed under smooth ice), combined with upward-directed momentum from the bed and along the inner bank in the rough ice section (Figure 6.8f), indicates an intensification of vertical shear across the flow depth. Such shear conditions disturb the upper-layer IBC region observed under smooth ice, as well as shift the main vortex (vortex 2 in Figure 6.5a), reinforcing the notion of roughness-induced flow structure reconfiguration.

The observed disproportionate amplification of vertical and lateral momentum components (M_z and M_y), as reported in Table 6.3, arises from the enhanced generation of secondary flows and turbulence under rough ice conditions. While streamwise momentum (M_x) remains largely controlled by the bulk pressure gradient and axial flow, the vertical and lateral components are more sensitive to local shear effects and secondary circulations, which are strongly modulated by surface roughness. In a curved channel, ice roughness distorts the near-surface velocity profile and intensifies the velocity gradient, particularly near the inner bank. This promotes stronger secondary currents and curvature-driven motions in the upper flow region. Increased surface drag redistributes energy away from the main axial flow, sustaining counter-rotating vortices and enhancing vertical exchanges. As a result, momentum transfer in the vertical and lateral directions is amplified more strongly than in the streamwise direction.

Furthermore, flow resistance was calculated (Eq. 6.13) as a proxy for the energy loss that must be overcome to maintain the flow structure. The higher Colebrook–White friction factor under rough ice conditions ($f_r = 0.053$) compared to the smooth ice case ($f_s = 0.031$), in line with previous studies on ice-covered river bends [145, 130, 41, 3], indicates increased flow resistance, leading to greater head loss and enhanced energy dissipation. The increased resistance destabilizes the vortex configuration observed under smooth ice and promotes a downward shift of the upper-layer vortices (Figure 6.5) as a compensatory mechanism for the increased resistance. This suggests that roughness influences both the strength and location of vortices across the channel (Table 6.2), with greater alterations occurring near the banks and in mid-channel regions.

While an expansion of the upper-layer circulation is observed under rough boundary conditions, albeit with lower total circulation in the top layer, the forcing responsible for the attenuation or merging of the IBC remains unclear. This raises two questions: Does rough ice increase turbulence-induced circulation everywhere in the cross-section? And how do the dominant vortex structures shift under rough versus smooth ice? To gain further insight, we examined the secondary flow and main flow magnitude averaged over depth (Figure 6.10), calculated as:

$$U_{\text{SF}} = \frac{1}{H} \int_0^H \sqrt{V^2(y,z) + W^2(y,z)}\, dz \tag{6.19}$$

and

$$U_{\text{mag}} = \frac{1}{H} \int_0^H \sqrt{U^2(y,z) + V^2(y,z) + W^2(y,z)}\, dz \tag{6.20}$$

The depth-averaged velocity patterns in Figure 6.10a indicate that the presence of a rough ice cover generally enhances secondary flow magnitude in two key regions of the bend cross-section. Near the inner bank ($0.02 < y_{\text{dir}} < 0.045$), the primary helical cell beneath the rough ice cover (vortex 1 in Figure 6.5b) exhibits greater intensity than the corresponding location vortex, IBC (vortex 1 in Figure 6.5a) observed under smooth ice. This results in a localized increase in secondary flow velocity (U_{SF}). Near the outer bank ($y_{\text{dir}} > 0.18$), the strengthening of near-bed helical cell (vortex 2 in Figure 6.5b) further contributes to

higher U_{SF} magnitudes. These observations demonstrate that increased surface roughness modifies the cross-sectional flow structure, amplifying secondary circulation both at the inner bank, primarily through enhanced upper-layer circulation, and at the outer bank, through intensification of near-bed vortices. Such modifications point to greater lateral and vertical momentum exchange, especially in bank-adjacent regions of the bend (cf. Figures 6.8e–f).

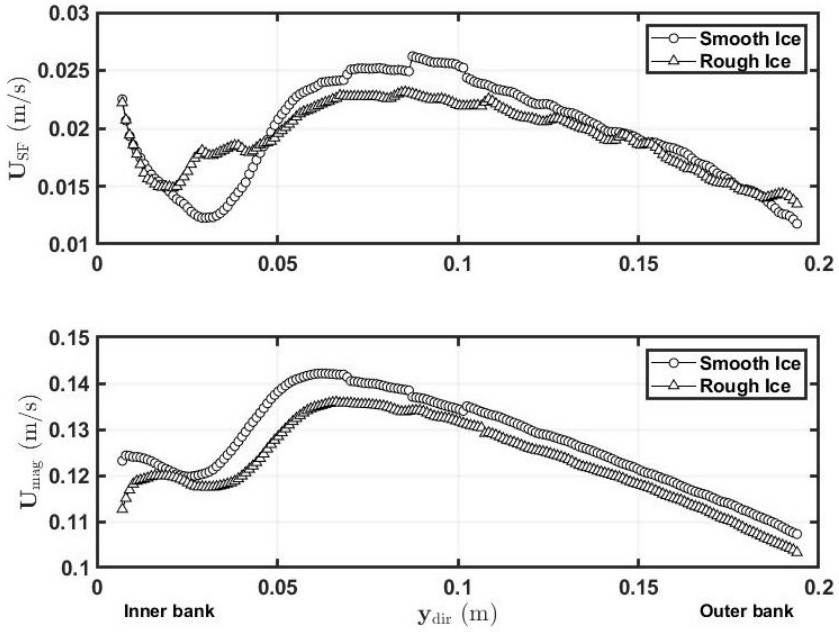


Figure 6.10. Lateral distribution of depth-averaged secondary flow magnitude (top panel) and total velocity magnitude (bottom panel) under smooth (○) and rough (△) ice-covered conditions. Profiles adjacent to the sidewalls are excluded due to PIV data obscured in those regions.

In Figure 6.10b, the total velocity magnitude (U_{mag}) remains consistently higher under smooth ice cover compared with rough ice. This elevation in U_{mag} increases the centrifugal force term $\left(U_{\mathrm{mag}}^2/R\right)$, thereby strengthening curvature-induced pressure gradients that sustain secondary circulation. Under rough ice, however, changes in the upper-layer flow structure and enhanced near-bed vortices appear to redistribute rather than increase secondary circulation energy. This redistribution suppresses large-scale transverse motions in the channel core, despite localized intensification near the banks. Overall, the depth-averaged results suggest that ice-cover roughness alters the balance between curvature-driven and turbulence-driven mechanisms in bend hydraulics, shifting the secondary flow

dominance from mid-channel toward near-bank regions.

Turbulent kinetic energy was computed (Figures 6.11a–b) using the following formula:

$$k = \frac{1}{2}\left(u'^2 + v'^2 + w'^2\right) = \frac{1}{2T}\int_0^T \left[(u-\bar{U})^2 + (v-\bar{V})^2 + (w-\bar{W})^2\right] dt \qquad (6.21)$$

here, $\vec{u} = \bar{\vec{U}} + \vec{u}'$, where u, v, and w are the instantaneous velocities; $\bar{U}$, $\bar{V}$, and $\bar{W}$ are the time-averaged velocity components; and the u', v', and w' are the velocity fluctuations from the mean. The resulting turbulent kinetic energy fields are normalized by $\frac{1}{2}U_b^2$ of each flow condition. Figure 6.11c presents the difference in normalized turbulent kinetic energy, calculated as:

$$\Delta k = k_{\text{rough, norm}} - k_{\text{smooth,norm}} \qquad (6.22)$$

The enhanced turbulence under rough ice conditions (Figure 6.11c) is clearly evident throughout the outer-bank region. Together with increased vertical momentum mixing (Figures 6.8e–f), this intensified turbulence redistributes circulation vertically, thereby reducing the influence of increased bed-layer vortex circulation on the depth-integrated transverse velocity field.

These findings are consistent with observations by Blanckaert *et al.* [21], who demonstrated that enhanced outer-bank roughness expands the outer-bank cell and intensifies turbulent kinetic energy, subsequently diminishing the imprint of near-bed vortices on the depth-averaged flow field. A similar redistribution of flow momentum near the ice boundary was also reported by Peters *et al.* [102], who observed increased shear stress near the edges of partial ice covers (Figure 9 in their paper), indicating intensified turbulence and vertical exchange in those regions. Although their study was conducted in a straight flume with partial ice cover, the elevated boundary shear they report near the ice edge reinforces the concept that surface roughness, in the form of ice boundaries, can induce localized turbulence amplification and momentum redistribution.

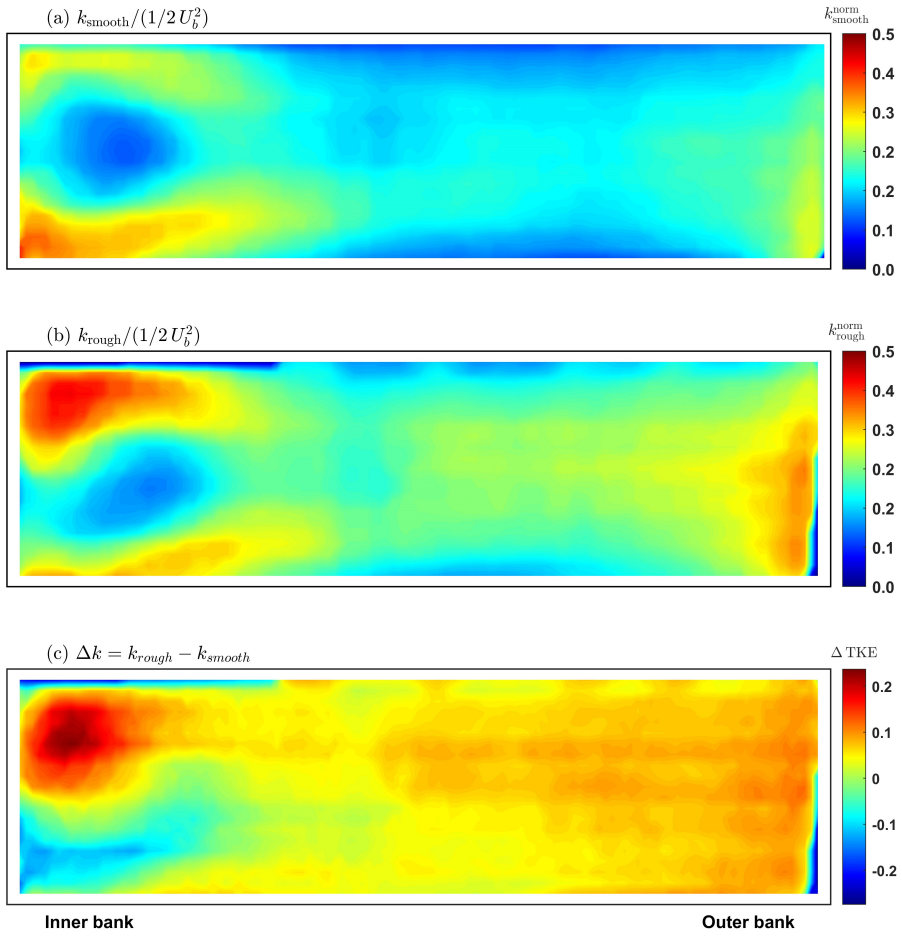


Figure 6.11. Comparison of normalized turbulent kinetic energy fields under (a) smooth and (b) rough ice conditions, and (c) their difference. The vertical axis represents flow depth (0-0.06 m, from bed to ice cover), and the horizontal axis represents channel width (0-0.20 m, from inner bank to outer bank. Note the lower colorbar range in plot (c) compared to plot (a) and (b). The white areas near the edges indicate masked data.

An important distinction between Blanckaert [21]'s open-channel experiments and the closed-channel conditions in the current study is, first, that while a displacement of peak turbulence away from the outer bank was observed under open-channel boundary conditions (Figures 12–13 in Blanckaert [21]), the closed-channel configuration in this study clearly demonstrates increased turbulence near both the inner and outer banks. Second, unlike bank roughness in open channels, roughness applied at the ice cover influences the turbulence structure across the entire flow domain. This reinforces the notion that ice roughness is not simply analogous to bank roughness; it has distinct implications for secondary circulation and energy distribution.

The streamwise momentum under rough ice (Figure 6.8d) exhibits a vertically and laterally expanded high-momentum core, indicating not only an intensified shear zone but a fundamental redistribution of momentum that directly perturbs the cross-sectional force balance. The existence and persistence of an inner-bank cell (IBC) in curved channels require a local equilibrium between outward centrifugal forcing ($\bar{U}^2/R$), inward-directed cross-stream pressure gradients (Figure 6.1), and turbulence-mediated vertical and lateral momentum fluxes.

Under rough ice, increased surface drag reduces the near-surface streamwise velocity, thus weakens the centrifugal forcing above the inner bank, as evidenced by the depressed $\bar{U}$ magnitudes in Figure 6.12. At the same time, turbulence-mediated momentum transport is reorganized: vertical momentum flux increases substantially across both layers, while the upper-layer lateral momentum flux directed toward the IBC region decreases. The combined effect of reduced centrifugal support and enhanced vertical coupling erodes the separatrix (i.e. an invisible boundary that separates two flow patterns) that previously isolated the IBC, allowing the primary vortex to expand laterally toward the inner bank. Consistent with this mechanism, the vector fields under rough ice (Figure 6.7b) display a broader outer-bank-directed motion within the first 20% of the channel width compared to the smooth-ice case (Figure 6.7a). The IBC therefore no longer persists as a dynamically distinct circulation, but is absorbed into the shear zone at the inner edge of the dominant secondary cell, yielding a reorganized single-cell secondary circulation under rough-ice conditions.

The increased turbulence under rough ice, extending from the outer bank toward the mid-channel and inner bank (Figure 6.11c), facilitates the merging of the inner-bank cell (IBC), observed in the smooth ice case, with the primary circulation cell, resulting in a single dominant vortex in the ice layer. Thus, rather than being entirely suppressed, the IBC undergoes a structural reorganization under rough ice conditions, integrating with the primary circulation cell.

While consistent in concept with the outer-bank cell behavior described in open-channel flow, the increased ice roughness in our results reshapes momentum distribution in all three directions, contributing to a reconfiguration of secondary circulation that is unique to ice-covered conditions. The directional sensitivity of momentum variation to increased ice roughness, evaluated using the signed ratio in Eq. 6.18, revealed intensified localized variations in the cross-stream and vertical directions (Figures 6.9b–c), while streamwise

changes (Figure 6.9a) remain comparatively diffuse. In contrast to open-channel conditions, where concave wall roughness primarily enhanced streamwise momentum redistribution and intensified secondary circulations across the cross-section [21], roughness at the ice cover substantially altered the vertical and transverse momentum flux distributions. This directional sensitivity to upper-boundary roughness has important implications for sediment transport processes and morphological evolution in ice-affected river systems [30, 116].

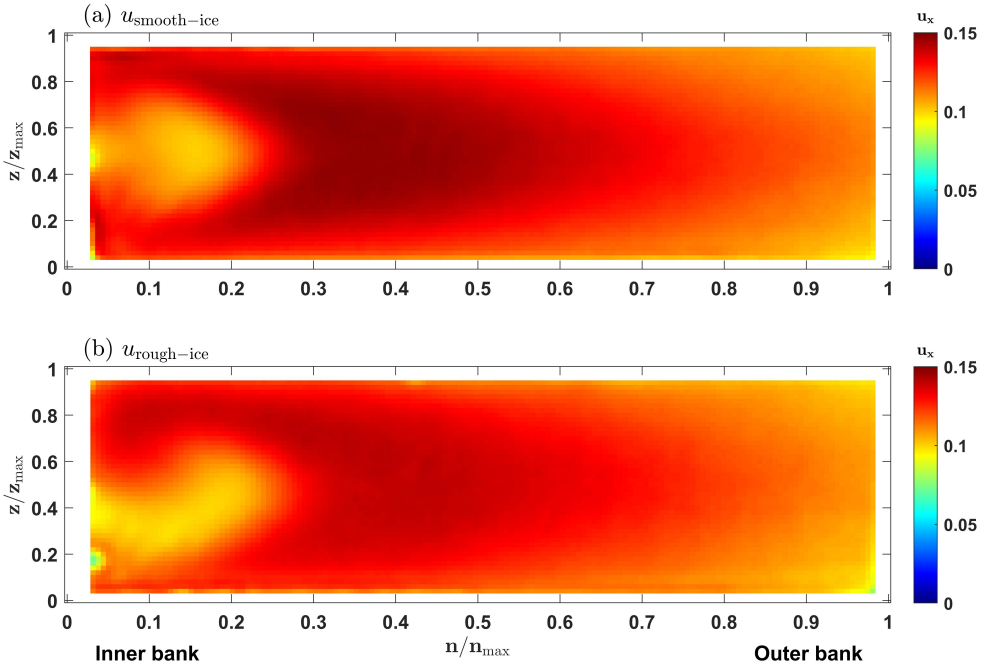


Figure 6.12. Mean streamwise velocity component under smooth and rough-ice conditions.

This study lays foundational groundwork for controlled investigations into boundary-induced turbulence and momentum redistribution in ice-covered river bends. Given the constraints of the PIV technique (such as optical alignment, calibration sensitivity, and wall reflections under simulated ice cover), the measurements in this study were limited to one section in the bend. Considering the critical role and inherent variability of channel curvature in natural rivers, future research could extend these findings to multiple cross-sections along curved channels. Such expanded investigations would provide a more comprehensive understanding of turbulent flow dynamics and secondary circulation under ice-covered conditions. Additionally, because the present study was conducted at a single flow rate, the

generality of the conclusions across different hydraulic regimes remains a limitation, which future work should address through multi-flow experiments.

6.6 Conclusions

Given the extended duration of sub-freezing temperatures during the cold season in many regions, understanding how an ice-cover influences transverse velocity characteristics and their controlling factors is essential for accurately predicting flow responses in cold conditions. Due to the limited availability of field data from ice-covered rivers, particularly regarding sub-ice roughness, laboratory experiments remain among the most effective methods to investigate turbulence and flow patterns. In this study, secondary flow structures in a curved channel were examined as functions of different ice-cover surface roughness. The measured data demonstrated a clear double-layer transverse flow structure under both ice conditions. Increasing ice roughness disrupted the turbulence distribution, affecting the formation, intensity, and position of vortices. The enhanced Darcy–Weisbach friction factor, used as a proxy for flow resistance, reflected greater energy loss under rough ice associated with heightened surface drag. The elevated drag led to increased turbulence, redistributing the momentum in different directions and spatially reconfiguring regional circulation structures, in both ice and bed layers.

In open-channel scenarios, such as Blanckaert's study [21], roughness along the concave bank primarily enhanced streamwise momentum redistribution and intensified secondary circulation, predominantly affecting the outer-bank flow regions. However, our experiments uniquely demonstrated that roughness at the ice boundary notably reshapes momentum flux distributions in all three directions. Additionally, a 3D analysis of momentum transfer revealed that the increased roughness has a stronger impact on the cross-stream and vertical components than on the streamwise momentum flux, which responded more moderately and diffusely. The directional sensitivity of momentum contributes to the merger and suppression of the inner bank cell secondary flow structure, the shifting of the primary cell within the ice layer, and the intensification of circulation near the bed. This heightened sensitivity underscores the importance of accounting for roughness effects in predicting flow distributions when managing resources in ice-covered rivers.

From a practical perspective, the strong sensitivity of cross-stream and vertical momentum fluxes to ice-cover roughness highlights important considerations for river engineering in cold regions. Increased roughness can elevate flow resistance and modify circulation patterns in ways that influence bank stability, local scour near structures, and overall flow conveyance. Accordingly, ice management strategies and engineering designs should account for roughness-induced momentum redistribution when predicting hydraulic performance and mitigating risks in ice-covered rivers.

Chapter 7

Secondary Flow and Aspect Ratio Change

Influence of Channel Aspect Ratio on Secondary Flow Circulation and Turbulence in an Ice Covered Rectangular Bend Channel

This chapter has been drafted as a journal paper for submission entitled: ***Influence of Channel Aspect Ratio on Secondary Flow Circulation and Turbulence in an Ice Covered Rectangular Section Bend Channel*****.**

7.1 Abstract

This study investigated the influence of channel aspect ratio (AR), defined as the ratio of channel width to flow depth, on secondary flow structure and turbulence dynamics in a sharp, ice-covered meander bend. Experiments were conducted using Particle Image Velocimetry (PIV) in a rectangular flume with a 135° bend under fixed bulk velocity and

full ice cover. Three flow depths were examined, corresponding to aspect ratios of 4.0, 2.9, and 2.5. Results showed that decreasing aspect ratio (i.e., increasing flow depth) drives a transition from weak, vertically compressed vortices in shallow flows (AR4.0) to larger, more coherent and stronger counter-rotating cells in deeper flows (AR2.5). In deeper flows, enhanced vertical–transverse Reynolds shear stresses and increased streamwise vorticity indicated stronger coupling between boundary layers and the interior flow, particularly near the bed. In contrast, shallow flows exhibited greater confinement effects, leading to disrupted vortex coherence and more localized turbulence due to overlapping boundary layers. Kinetic energy distributions further indicated a shift from turbulence-dominated dissipation toward more organized momentum transport with increasing flow depth. It is also found that aspect ratio regulates the structure and efficiency of momentum exchange across the flow depth. Higher aspect ratios were associated with boundary-localized interactions and vertically separated secondary cells, whereas lower aspect ratios promoted more depth-integrated redistribution. Together, these results underscored the controlling role of flow depth and confinement in shaping secondary motion and turbulent momentum transport in curved, ice-covered channels.

Keywords: Secondary flow, Aspect ratio, Turbulence, Ice cover, River Bend.

7.2 Introduction

Secondary flow refers to cross-stream circulation superimposed on the primary streamwise flow that develops in river bends. In curved open channels, centrifugal acceleration drives the flow toward the outer bank, while the resulting cross-stream pressure gradient acts in the opposite direction. This imbalance generates helical flow structures that play a crucial role in sediment transport, mixing, and bank erosion [19, 127, 132].

In an open-channel, secondary circulation typically forms a dominant vortex near the channel center, sometimes accompanied by a weaker counter-rotating cell near the outer bank. However, in ice-covered channels, the presence of a rigid upper boundary substantially modifies the flow dynamics. The ice-water interface introduces an additional shear layer, resulting in a pair of vertically stacked counter-rotating cells: a bed-driven lower vortex and an ice-driven upper vortex [166, 146, 145, 38]. This two-layered structure represents

a key departure from open-channel flow behavior and critically influences momentum exchange, sediment dynamics, and turbulence structure in cold-region rivers.

Previous studies have emphasized that ice cover imposes major changes on hydraulic resistance, sediment transport regimes, and channel morphology through its modulation of flow boundaries and shear stress distributions [47, 31]. Despite growing recognition of the importance of ice cover on flow structure, sub-ice turbulence remains poorly characterized due to the logistical and safety challenges of field measurements during winter [14, 95, 69]. Field observations have shown significant spatial variation in ice thickness across meandering river bends, which may further complicate secondary circulation and turbulence patterns [63]. To address these limitations, laboratory-scale physical models have been increasingly employed to simulate flow under controlled ice-covered conditions.

Aspect ratio ($AR = B/H$), defined as the ratio of channel width (B) to flow depth (H), is an important parameter governing flow confinement, turbulence production, and secondary circulation [92]. Numerous open-channel studies have highlighted how varying AR affects vortex development and momentum redistribution [19, 64, 86, 91, 139, 59, 71]. A complementary numerical investigation by [150] showed that in turbulent rectangular straight ducts, secondary flow topology and intensity vary systematically with increasing AR, revealing spanwise development constraints and the evolution of vortex structures that bear strong relevance to confined open-channel systems. However, their study was based on idealized direct numerical simulations (DNS) without geometric curvature, roughness, or ice cover, and therefore does not capture how these factors may interact or override AR-driven mechanisms in more complex natural or experimental settings.

While many studies are well established in open-channel contexts, the corresponding behavior under ice-covered conditions remains unclear. In particular, it is not known whether similar aspect-ratio-driven mechanisms operate when vertical confinement from the ice modifies the boundary shear and turbulence structure. This gap limits our understanding of flow dynamics and morphodynamic processes in seasonally ice-covered rivers. Given that more than half of Earth's rivers are subject to seasonal ice cover during winter months [163], improving our understanding of ice-affected river processes is of global importance.

The present study aims to address this gap by investigating how channel aspect ratio influences secondary circulation and turbulence characteristics under full ice cover repre-

senting smooth ice conditions. The specific objectives of this study are: (1) to quantify changes in secondary flow strength and structure across different aspect ratios; (2) to analyze the velocity distribution and shear layer interaction in relation to confinement effects; and (3) to examine the spatial patterns of turbulence intensity and Reynolds shear stresses across the bend cross-section. The findings enhance our understanding of curvature-induced flow dynamics in ice-covered rivers, with implications for sediment transport, pollutant dispersion, and channel evolution in cold regions.

7.3 Methodology

This study's experiments were conducted at the hydraulic laboratory of the University of Ottawa using a scaled physical model of a curved channel. A simulated ice cover with smooth underside roughness was installed to replicate an ice-covered flow condition observed in natural rivers. More details on the experimental setup, simulated ice cover, measurement procedures, and data processing methods are provided in the following sections.

7.3.1 Physical bend channel model

The physical model of river channel used in this study consisted of a transparent, plexiglass-walled bend flume with a rectangular cross-section. The flume comprised a 2.4 m long straight entrance section, followed by a 135° bend with a centerline radius of curvature (R) equal to 0.3 m, and a downstream straight exit section. The channel had a constant width of 0.2 m, while the flow depth varied between 0.05 and 0.08 m, depending on the experimental conditions. Flow depth was regulated using a tailgate installed at the downstream end of the flume, enabling the desired flow conditions to be achieved under a constant bed slope. A schematic representation of the channel geometry and experimental setup is provided in Figure 7.1.

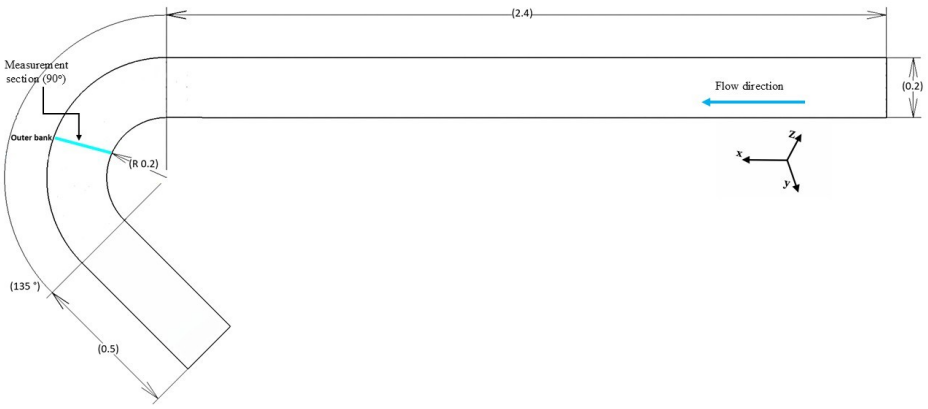


Figure 7.1. Schematic of the 135° bend physical model, including the dimensions of the main components expressed in metres. The blue arrow in the straight entrance indicates the flow direction, and the blue line in the curve shows the 90° measurement section in the bend.

7.3.2 Simulated ice-cover

The ice-covered was simulated using marine-grade mahogany plywood, cut in the shape of the channel bed, to represent a continuous, rigid ice cover. This material was selected due to its high resistance to moisture-induced deformation, ensuring minimal warping and maintaining geometric consistency throughout the experiments. The density of the plywood ($\approx$ 800 kg/m^3) is reasonably comparable to that of natural freshwater ice (917 kg/m^3), allowing for a representative approximation of the hydraulic loading at the ice–water interface without requiring additional weighting. This facilitates a reliable reproduction of flow confinement effects characteristic of ice-covered channels. To enhance the accuracy of PIV measurements, the underside of the simulated ice cover was fully coated with a matte black vinyl film. This treatment minimizes light reflection and glare, thereby improving image quality and reducing measurement noise during velocity field acquisition.

7.3.3 Flow conditions and scaling

The flow depths investigated in this study were selected as $H = 5$, 7, and 8 cm. The channel width was kept constant at $B = 0.20$ m, resulting in aspect ratios (B/H) ranging from 2.5 to 4.0. Maintaining a natural width-to-depth aspect ratio near 10 would require a flow depth of approximately 2 cm for the given channel width. However, such shallow flow conditions were not suitable for reliable velocity measurements using PIV, primarily due

to limitations in spatial resolution and optical access. The experimental range in this study enabled a systematic evaluation of the influence of flow depth and aspect ratio on the flow structure.

Among the available similarity criteria, the Reynolds number (Re) and the Froude number (Fr) are most commonly used in river flow studies. In the present experiments, full Reynolds similarity could not be achieved due to geometric and hydraulic constraints of the laboratory flume. Achieving Reynolds similarity would require either unrealistically high flow velocities or significantly larger model dimensions, which were not feasible. Consequently, Froude similarity was adopted as the primary scaling criterion to preserve the ratio of inertial to gravitational forces between the model and prototype. All experiments were conducted at sufficiently high Reynolds numbers ($Re \gtrsim 4{,}000$), ensuring fully turbulent flow conditions.

Froude number was calculated as $Fr = \frac{U_b}{\sqrt{gH}}$, where U_b is the bulk velocity and g is the gravitational acceleration. The resulting Froude numbers ranged between approximately 0.05 and 0.16, indicating subcritical flow conditions in all cases. The Reynolds number was computed based on the hydraulic diameter ($D_h = 4A/P$) as $Re = \frac{U_b D_h}{\nu}$, where ν is the kinematic viscosity of water. The corresponding Reynolds numbers ranged from approximately 8×10^3 to 1.1×10^4. Table 7.1 summarizes the hydraulic characteristics of the experimental cases considered in this study.

Table 7.1. Summary of test conditions and their hydraulic characteristics. In this table, H is the flow depth (cm), B/H is the aspect ratio for a constant channel width of $B = 20$ cm, U_b is the bulk velocity (m/s), Q is the discharge (L/s), $m = \frac{Q^2}{gA^3}$ is the momentum function, $Fr = \frac{U_b}{\sqrt{gH}}$ is the Froude number, and $Re = \frac{U_b D_h}{\nu}$ is the Reynolds number based on the hydraulic diameter $D_h = \frac{4A}{P}$.

Case	H (cm)	B/H (-)	U_b (m/s)	Q (L/s)	m (-)	Fr (-)	Re (-)
1	5	4.0	0.10	1.00	0.102	0.14	8000
2	7	2.9	0.10	1.40	0.073	0.12	10400
3	8	2.5	0.10	1.60	0.064	0.11	11400

7.3.4 Velocity measurement technique

Velocity measurements were conducted using a stereoscopic Particle Image Velocimetry (stereo-PIV) system to obtain high-resolution, three-component velocity fields (3C-2D) in the channel bend section. The system consisted of a dual-cavity Nd:YAG laser (Litron Nano L100-50; wavelength 532 nm, pulse energy up to 100 mJ per cavity, repetition rate 50 Hz), two LaVision Imager sCMOS cameras equipped with Nikon F-mount lenses, and a LaVision Programmable Timing Unit (PTU X). The PTU X provided precise synchronization of laser pulses and camera exposures with a timing resolution of 10 ns, ensuring accurate capture of instantaneous particle displacements.

The flow was seeded with neutrally buoyant hollow glass microspheres (mean diameter ~ 10 μm), which are commonly used in hydraulic PIV applications due to their good flow-following characteristics. The measurement plane was illuminated using a laser sheet introduced from underside of the transparent flume bed.

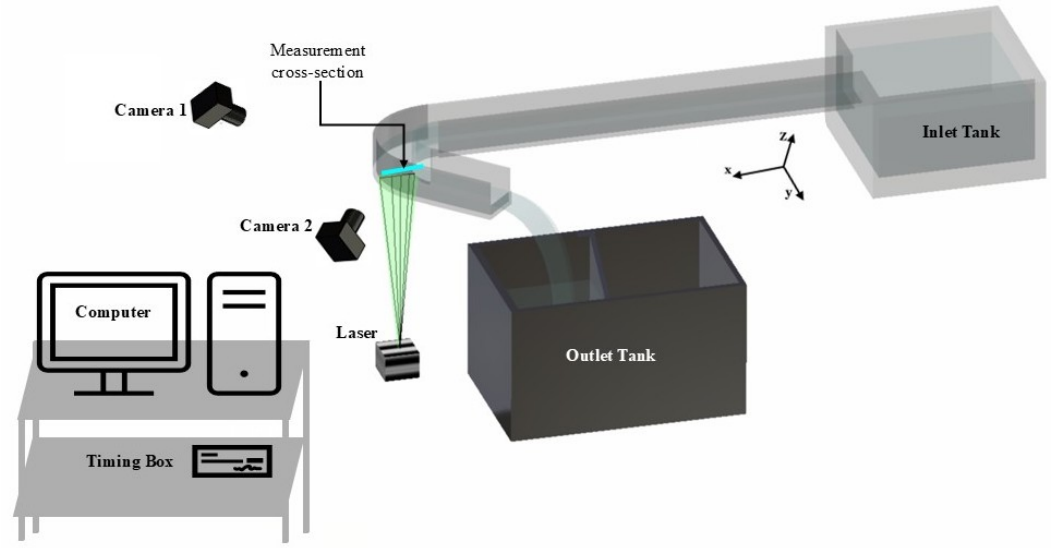


Figure 7.2. Schematic representation of the stereo-PIV system and experimental configuration (credit: Julien Pierrat). The coordinate axes (x, y, z) correspond to the streamwise, cross-stream, and vertical directions, respectively.

Velocity measurements were acquired at the 90° cross-section of the bend, where secondary circulation and turbulence structures are typically most pronounced in curved channel flows. A total of 6000 instantaneous velocity fields were recorded at a sampling frequency of 10 Hz over a duration of 600 s. This sampling strategy ensured statistical con-

vergence of time-averaged velocity components and turbulence quantities, which is essential for reliable characterization of flow structures relevant to river hydraulics and ice-covered flow dynamics [43].

The PIV processing parameters, including interrogation window size, overlap, and sub-pixel displacement estimation algorithms, were carefully configured to resolve the dominant turbulent scales while maintaining acceptable signal-to-noise ratios. A detailed description of the PIV calibration, resolution assessment, and uncertainty analysis is provided in [44, 43]. The resulting velocity fields were of sufficient accuracy to capture key hydraulic features, including secondary circulation cells, velocity redistribution due to ice cover, and turbulence statistics relevant to momentum transfer in ice-covered river systems.

7.3.5 Vortex identification algorithm

To identify coherent vortical structures within the measured velocity fields, the vortex identification method proposed by Graftieaux et al. (2001) was applied during post-processing of the PIV data. This approach is based on local geometric properties of the velocity field and defines two dimensionless scalar functions, Γ_1 and Γ_2, which enable the detection of vortex centers and their associated core regions.

The scalar function Γ_1 is used to locate vortex centers. For a given point P within the flow domain and a surrounding neighborhood S, Γ_1 is defined in continuous form as:

$$\Gamma_1(P) = \frac{1}{S} \int_{M \in S} \frac{(\vec{PM} \times \vec{U}_M) \cdot \vec{z}}{|\vec{PM}| \cdot |\vec{U}_M|} \, dS = \frac{1}{S} \int_S \sin(\theta_M) \, dS \tag{7.1}$$

where $\vec{PM}$ is the position vector from point P to a neighboring point M, $\vec{U}_M$ is the local velocity vector at M, $\vec{z}$ is the unit vector normal to the measurement plane, and θ_M is the angle between $\vec{PM}$ and $\vec{U}_M$. The value of Γ_1 ranges between -1 and 1, with values approaching $|\Gamma_1| \approx 1$ indicating the presence of a vortex center.

The vortex core boundary is identified using the second scalar function, Γ_2, defined

as:

$$\Gamma_2(P) = \frac{1}{S}\int_{M\in S} \frac{\left[\vec{PM} \times \left(\vec{U}_M - \tilde{\vec{U}}_P\right)\right] \cdot \vec{z}}{\|\vec{PM}\| \cdot \|\vec{U}_M - \tilde{\vec{U}}_P\|} dS \tag{7.2}$$

where $\tilde{\vec{U}}_P$ represents the local mean velocity within the neighborhood S centered at point P. A threshold value of $|\Gamma_2| \approx 2/\pi$ (≈ 0.636) is commonly used to delineate the vortex core. In the present study, a slightly higher threshold of 0.69 was adopted, within the accepted range of 0.6–0.7, to reduce the influence of background noise and improve the robustness of vortex detection. The vortex center is therefore identified at locations where Γ_1 attains local extrema, while the vortex boundary is defined by the contour corresponding to the selected Γ_2 threshold. These scalar fields were computed at each grid point using MATLAB. Owing to their independence from velocity magnitude, the Γ-criteria are particularly suitable for analyzing PIV data in turbulent flows with measurement noise, making them well suited for the present ice-covered flow conditions.

7.4 Results

The analysis focuses on the 90° bend section, where curvature-induced secondary circulation is most pronounced. Instantaneous PIV measurements are used to characterize transient flow characteristics, while time-averaged velocity fields identify the persistent flow structures governing the mean flow. To determine whether differences among the aspect-ratio configurations are statistically significant, the probability distributions of the instantaneous velocity components are compared, providing an analytical basis for understanding aspect-ratio effects across the tested flow conditions.

7.4.1 Statistical difference across the AR configurations

To enable a physically consistent comparison across flows with different depths, the velocity fields were first mapped onto a common normalized cross-section using the nondimensional coordinates x/B and z/H, where B is the channel width and H is the local flow depth for each case. The statistical analysis was then performed on interpolated velocity samples from this common normalized domain, to ensure the compared samples correspond to equivalent relative positions within the flow depth.

Table 7.2. Integrated summary of statistical outcomes for velocity components across aspect ratios based on the normalized-coordinate analysis. Results synthesize the distributional differences (Kruskal–Wallis and Kolmogorov–Smirnov tests), pairwise comparisons, effect sizes (Cliff's δ), and variance-based responses (Brown–Forsythe test).

Streamwise velocity (u)	
Omnibus distributional difference	Significant ($\chi^2 = 376.45$)
Pairwise distributional outcome	All AR pairs differ
Dominant pairwise effect size	Small separation ($\delta = 0.109$, AR2.9–AR2.5)
Variance response across ARs	Significant for AR4–AR2.9 and AR4–AR2.5; not significant for AR2.9–AR2.5
Transverse velocity (v)	
Omnibus distributional difference	Significant ($\chi^2 = 132.04$)
Pairwise distributional outcome	All AR pairs differ; weakest separation for AR2.9–AR2.5
Dominant pairwise effect size	Small separation overall ($\lvert\delta\rvert \leq 0.061$)
Variance response across ARs	Significant differences across all AR pairs
Vertical velocity (w)	
Omnibus distributional difference	Significant ($\chi^2 = 600.95$)
Pairwise distributional outcome	AR2.5 differs from both AR4 and AR2.9; AR4–AR2.9 not significant in rank-based post-hoc tests
Dominant pairwise effect size	Small but strongest for comparisons with AR2.5 ($\delta \approx 0.11$)
Variance response across ARs	Significant differences across all AR pairs

The omnibus Kruskal–Wallis tests indicated that all three velocity components exhibited statistically significant differences among the aspect-ratio cases at a conservative significance level ($\alpha = 0.001$). The strongest group separation was observed for the vertical velocity w ($\chi^2 = 600$), followed by the streamwise velocity u ($\chi^2 = 376$), while the transverse velocity v showed the weakest, yet still highly significant, separation ($\chi^2 = 132$). Here, χ^2 denotes the Kruskal–Wallis test statistic, which measures deviations of group-wise

rank sums from the expectation under identical distributions. Statistical significance of χ^2 is determined by comparing the associated p-value against the chosen significance level (here $\alpha = 0.001$). The governing equation and computational details are provided in Appendix 1. These results show that aspect ratio systematically modifies the statistical distributions of all three velocity components when compared on a common normalized cross-section.

Post-hoc pairwise comparisons revealed a component-dependent response to aspect-ratio variation. For the streamwise velocity u, all pairwise contrasts among AR4, AR2.9, and AR2.5 were statistically significant ($p < 0.001$), indicating that each configuration produced a distinct streamwise velocity distribution. The transverse velocity v also showed significant separation for all three pairs, although the AR2.9–AR2.5 contrast was weaker than the contrasts involving AR4. For the vertical velocity w, comparisons involving AR2.5 were strongly significant, whereas the AR4–AR2.9 contrast was not significant based on the rank-based post-hoc tests ($p_{\mathrm{Dunn–Sidak}} = 0.308$; $p_{\mathrm{Holm}} = 0.0618$). However, the corresponding Kolmogorov–Smirnov test for this pair remained highly significant ($p \ll 0.001$), indicating that although the central tendency of w was similar between AR4 and AR2.9, their overall distributional shapes still differed.

Effect-size analysis showed that the observed differences were systematic but generally small in magnitude. For u, the largest separation occurred between AR2.9 and AR2.5 (Cliff's $\delta = 0.109$), while the AR4–AR2.5 contrast was comparatively weak ($\delta = 0.020$). For v, all pairwise effect sizes were small ($|\delta| \leq 0.061$), consistent with the relatively weaker omnibus separation for this component. For w, the largest pairwise differences were associated with AR2.5, with $\delta = 0.111$ for AR4–AR2.5 and $\delta = 0.116$ for AR2.9–AR2.5, whereas the AR4–AR2.9 comparison showed negligible rank-based separation ($\delta = -0.010$).

Variance analysis based on the Brown–Forsythe test further demonstrated that aspect ratio influences not only the central tendency but also the spread of the velocity distributions. The omnibus Brown–Forsythe tests were significant for all three components ($p < 0.001$). For u, pairwise variance differences were significant for AR4–AR2.9 and AR4–AR2.5, but not for AR2.9–AR2.5, indicating that the variance structure of the streamwise velocity was primarily distinguished by the shallowest case. In contrast, all pairwise variance comparisons for both v and w were significant, showing that aspect ratio also systematically alters the variability of the transverse and vertical motions throughout the bend cross-section. Detailed statistical formulations and full test-result tables are provided in Appendix 1.

7.4.2 Effect of aspect ratio on secondary flow structure

Instantaneous velocity field

The raw instantaneous velocity fields exhibited substantial spatial variability associated with small-scale, intermittent turbulent motions. Several spatial filtering techniques, including median filtering, Gaussian smoothing, and spectral low-pass filtering, were examined to reduce small-scale fluctuations and improve visualization of the underlying secondary-flow motions. Such filtering approaches are commonly used in experimental fluid mechanics and signal processing to separate flow structures across spatial scales (e.g., [2, 103, 96]).

The filtered instantaneous fields revealed localized regions of directionally consistent vector curvature and rotation; however, these features remained weak and spatially fragmented. They indicate instantaneous signatures of secondary circulation but were superimposed on turbulent fluctuations and did not form a coherent large-scale circulation cell. Similar behavior was observed for all three aspect-ratio cases (figures not shown). Therefore, the instantaneous fields provide limited evidence of the persistent secondary-flow structure, which is more clearly resolved through time averaging.

Temporally averaged velocity fields

Secondary-circulation structures were identified from the temporally averaged velocity fields using the vortex-detection method of Graftieaux *et al.* [53]. Figure 7.3 compares the three ice-covered cases, each subjected to the same initial bulk velocity but with different flow depths. The detected vortex characteristics are summarized in Table 7.3, with vortex identification numbers corresponding to those in Figure 7.3. A distinct two-layer circulation pattern was observed for all three aspect ratios. Near the ice and bed boundaries, the cross-stream flow was directed from the outer bank toward the inner bank, whereas near the mid-depth it was directed from the inner bank toward the outer bank (blue arrows in Figure 7.3). However, the strength, number, and spatial distribution of the secondary-flow vortices varied with aspect ratio.

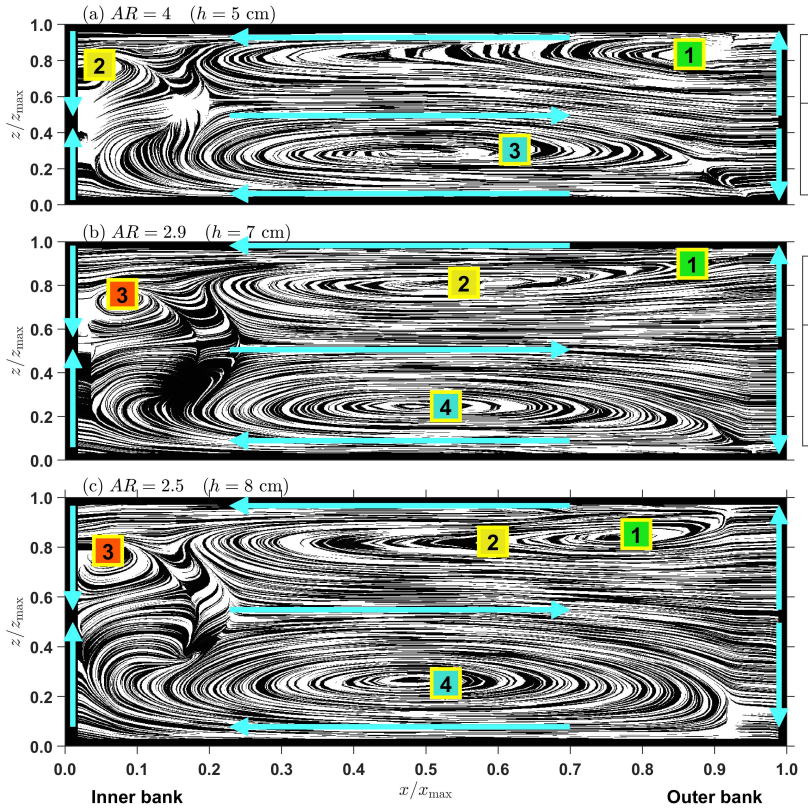


Figure 7.3. Secondary-flow vortex structures for different aspect ratios beneath a smooth ice cover. Colored rectangles shows the identified the detected vortices, and blue arrows indicate the direction of secondary flow. The horizontal axis represents the normalized channel width, $x/x_{\max}$, where $x_{\max} = 0.20$ m; $x/x_{\max} = 0$ and 1 correspond to the inner and outer banks, respectively. The vertical axis represents the normalized flow depth for (a) 0.05 m, (b) 0.07 m, and (c) 0.08 m, where 0 and 1 correspond to the channel bed and ice cover, respectively.

At the highest aspect ratio ($AR = 4.0$, $h = 5$ cm), three distinct vortices were identified. The main ice-layer vortex ($|\Gamma| = 0.71$ mm^2/s) was stronger than the inner-bank cell ($|\Gamma| = 0.21$ mm^2/s), while the bed-layer vortex exhibited a higher circulation magnitude ($|\Gamma| = 1.40$ mm^2/s) and extended across much of the channel width.

As the aspect ratio decreased to $AR = 2.9$ ($h = 7$ cm), the main ice-layer vortex separated into two cells, with the circulation near the inner bank increasing from $|\Gamma| = 0.21$ mm^2/s at $AR = 4.0$ to $|\Gamma| = 1.26$ mm^2/s at $AR = 2.9$. The total circulation of the main cell in the ice layer ($|\Gamma_{\text{total}}| = |\Gamma|\text{main} + |\Gamma|\text{separated}$), however, showed a slight decrease as the aspect ratio decreased (3% from AR4.0 to AR2.9). The bed-layer vortex strengthened and shifted toward the inner bank.

At the lowest aspect ratio, $AR = 2.5$ ($h = 8$ cm), the bed layer exhibited the strongest circulation, with Vortex 4 reaching $|\Gamma| = 6.11\ \mathrm{mm}^2/\mathrm{s}$. This vortex shifted further toward the inner bank and extended toward the channel center. In contrast, the positions and circulation magnitudes of the ice-layer vortices remained comparable to those at $AR = 2.9$, with only a slight reduction in circulation. Overall, the ice-layer vortices followed the same trend observed from $AR = 4.0$ to $AR = 2.9$, with an increase in the inner-bank vortex strength and a decrease in the total main-cell circulation as the aspect ratio decreased from $AR = 4.0$ to $AR = 2.5$.

Table 7.3. Properties of secondary-flow vortices identified at different aspect ratios. "AR" denotes the flow aspect ratio, and the vortex IDs correspond to the vortex labels shown in Figure 7.3.

Flow Type	Vortex ID	Circulation (mm^2/s)	x Location (m)	y Location (m)
AR4	1	0.71	0.17	0.04
AR4	2	0.21	0.01	0.04
AR4	3	-1.40	0.12	0.02
AR2.9	1	0.52	0.17	0.06
AR2.9	2	0.17	0.11	0.06
AR2.9	3	1.26	0.02	0.05
AR2.9	4	-3.73	0.11	0.02
AR2.5	1	0.44	0.16	0.07
AR2.5	2	0.20	0.12	0.07
AR2.5	3	1.22	0.01	0.06
AR2.5	4	-6.11	0.11	0.06

The overall trend showed that the total ice-layer circulation increased by approximately 112%, from $\Gamma_{\mathrm{ice}} = 0.92\ \mathrm{mm}^2/\mathrm{s}$ at $AR = 4.0$ to $\Gamma_{\mathrm{ice}} = 1.95\ \mathrm{mm}^2/\mathrm{s}$ at $AR = 2.9$, and then remained relatively stable, with a slight decrease of approximately 4.6% to $\Gamma_{\mathrm{ice}} = 1.86\ \mathrm{mm}^2/\mathrm{s}$ at $AR = 2.5$. In contrast, the magnitude of the counter-rotating bed-layer circulation increased progressively by approximately 166%, from $|\Gamma_{\mathrm{bed}}| = 1.40\ \mathrm{mm}^2/\mathrm{s}$ at $AR = 4.0$ to $|\Gamma_{\mathrm{bed}}| = 3.73\ \mathrm{mm}^2/\mathrm{s}$ at $AR = 2.9$, and by a further 64% to $|\Gamma_{\mathrm{bed}}| = 6.11\ \mathrm{mm}^2/\mathrm{s}$ at $AR = 2.5$. These results indicated that changes in aspect ratio modified the secondary-

circulation strength in both the ice and bed layers, with the substantially greater variation in the bed-layer circulation demonstrating a stronger sensitivity of the near-bed secondary circulation structure to channel aspect ratio. The transverse velocity profiles were compared next to provide a measure of the strength and vertical distribution of the cross-stream motion across the aspect-ratio cases $\mathrm{AR}4.0$, $\mathrm{AR}2.9$, and $\mathrm{AR}2.5$.

7.4.3 Analysis of some transverse velocity profiles

Figure 7.4 shows some cross-stream velocity profiles, normalized by the reference velocity for each case, defined as the maximum absolute cross-stream velocity (e.g., $U_{\mathrm{ref,AR4}} = \max(|v_{\mathrm{grid,AR4}}|)$). The general shape of the profiles was similar across all cases, with a characteristic velocity peak near the mid-height under the ice cover, indicating well-established counter-rotating circulation layers. However, the strength, vertical distribution, and asymmetry of the profiles changed noticeably as the aspect ratio decreased, reflecting the different evolution of the vortices in each layer across the aspect-ratio configurations.

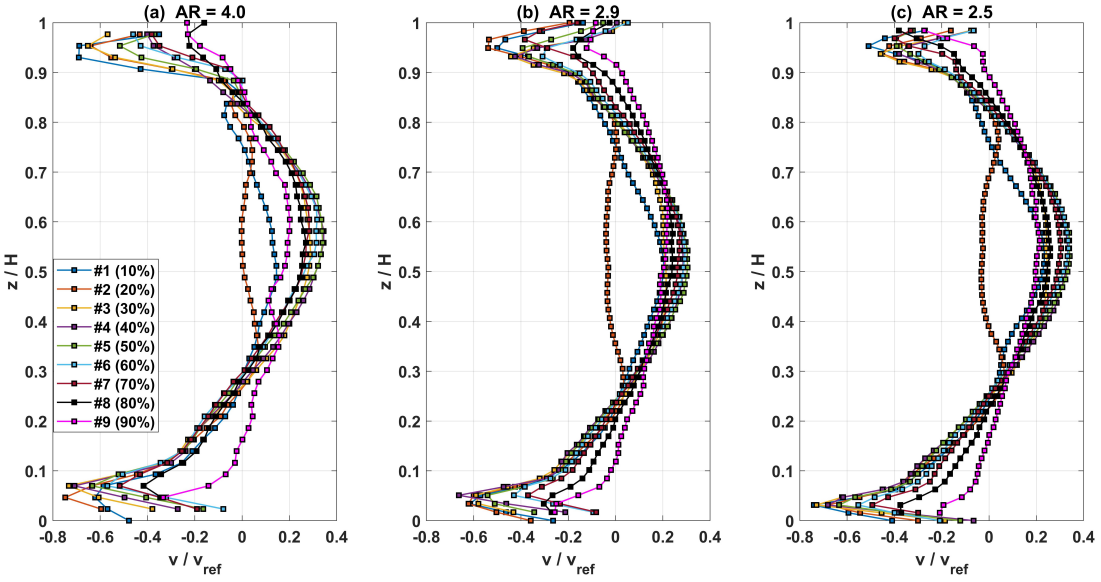


Figure 7.4. Normalized cross-stream velocity profiles at different width locations (10-90% from the inner bank) for three aspect-ratio cases. The horizontal axis shows the normalized cross-stream velocity component v/v_{ref}, where v_{ref} is the maximum absolute cross-stream velocity for each case. The vertical axis shows the normalized flow depth z/H, where z is the vertical location and H is the flow depth. The legend in all subplots is the same as in subplot (a).

At profile #2 (20% width from inner bank), the cross-stream velocity between $z/H \approx$

0.3–0.7 was $v/v_{\mathrm{ref}} \geq 0$ (directed toward the outer bank) for the highest aspect ratio AR4.0, but $v/v_{\mathrm{ref}} \leq 0$ (toward the inner bank) for the lower aspect ratios AR 2.9 and AR 2.5. This location coincides with the interface between the ice layer inner-bank vortex mean-centre and the bed layer cell. When examining the circulation ratio,$|\Gamma_{\mathrm{inner}}|/|\Gamma_{\mathrm{bed}}|$, the corresponding values were 0.15, 0.34, and 0.20 for aspect-ratio 4.0, 2.9, and 2.5, respectively, indicating that the inner-bank circulation becomes proportionally stronger relative to the bed-layer counter-rotating vortex.

At the mid-channel location (profile #5, 50% width), the positive (outer-bank-directed) cross-stream velocities extended deeper toward the bed as the aspect ratio decreased. This shift was consistent with the weakening of the main ice-layer circulation and the strengthening of the counter-rotating bed-layer circulation.

Near the outer bank (80% and 90% of the channel width), the upper portion of the normalized cross-stream velocity profiles ($z/H \approx 0.85$–0.95) showed a distinct shift in direction that varied with aspect ratio. In the $AR = 4.0$ case, the velocity profile reversed sign from positive to negative (toward the inner bank) at approximately $z/H \approx 0.83$. In contrast, this reversal occurred higher in the water column, at approximately $z/H \approx 0.88$, for the lower aspect-ratio cases ($AR = 2.9$ and $AR = 2.5$). Thus, the lower aspect ratios shifted the flow reversal closer to the ice cover, indicating a reduced vertical influence of the ice-layer circulation near the outer bank.

7.4.4 Streamwise velocity and energy structure

The spatial distribution of the time-averaged streamwise velocity (Figure 7.5), together with the corresponding mean and turbulent kinetic energy fields (Figure 7.6), provides insight into how aspect ratio governs the organization of momentum and turbulence in the cross-section.

Across all cases, the peak streamwise velocity was located near the upper part of the flow close to the inner bank, consistent with the vertical profiles of maximum velocity. A relatively low-velocity region (or "dead zone") was observed in the middle of the water column ($0.3 < z/z_{\max} < 0.75$) near the inner bank ($x/x_{\max} < 0.25$). This region corresponded to the interface between two vertically stacked circulation cells and therefore represented

a stagnation or weak-momentum zone generated by the interaction between ice-driven and bed-driven secondary flows.

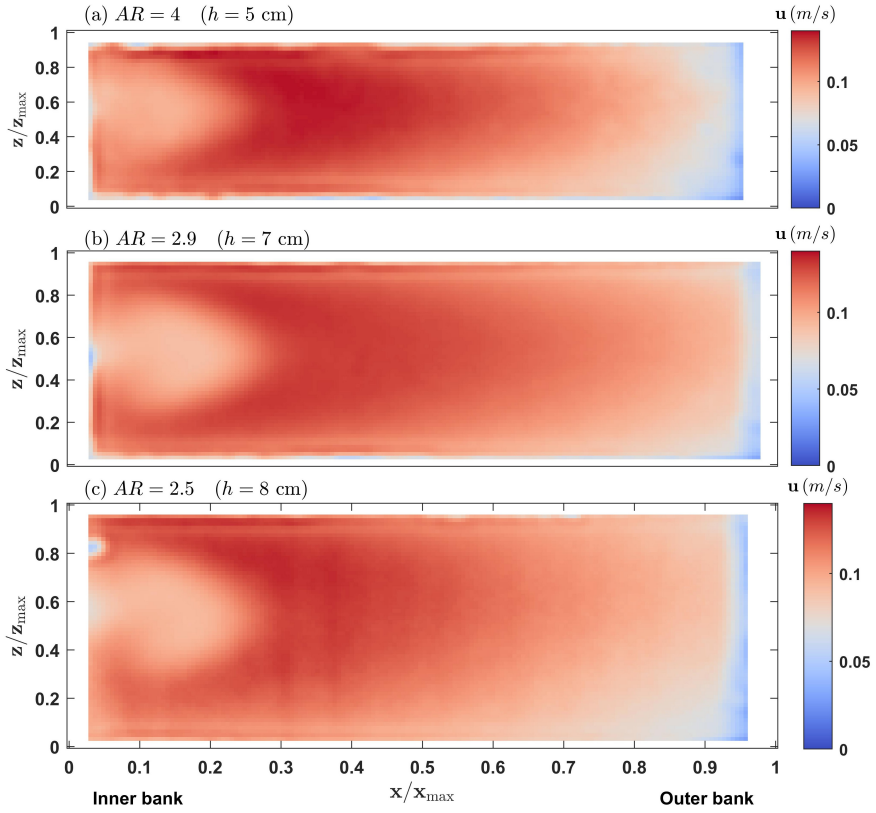


Figure 7.5. Time-averaged streamwise velocity distribution for (a) $AR = 4.0$, (b) $AR = 2.9$, and (c) $AR = 2.5$. The horizontal axis represents normalized channel width ($x/x_{\max}$), where 0 corresponds to inner bank and 1 to outer bank, while the vertical axis represents normalized flow depth ($z/z_{\max}$).

Comparison with the secondary-circulation patterns (Figure 7.3) indicated this low-velocity region coincided with where the two circulation cells diverged. In particular, the upper circulation cell associated with the ice cover and the lower circulation cell generated by bed shear separated near $x/x_{\max} \gtrsim 0.2$. As the bed-driven circulation strengthened, the core of high streamwise velocity was displaced downward from near-surface region toward mid-depth, indicating a redistribution of momentum across flow depth.

These velocity patterns were closely reflected in the mean kinetic energy fields (Figures 7.6a–c). As the aspect ratio decreased (increasing flow depth), the spatial extent of high-MKE regions increased significantly. In the lowest aspect-ratio case (AR2.5), elevated

MKE extended from the inner bank beneath the ice layer toward the central region of the cross-section, spanning a large portion of the flow depth. In contrast, for higher aspect ratios (AR2.9 and AR4.0), high-MKE regions were more confined and localized. The high-MKE regions were identified using the 90th percentile of the MKE distribution in each case, providing a consistent basis for comparison across different flow depths.

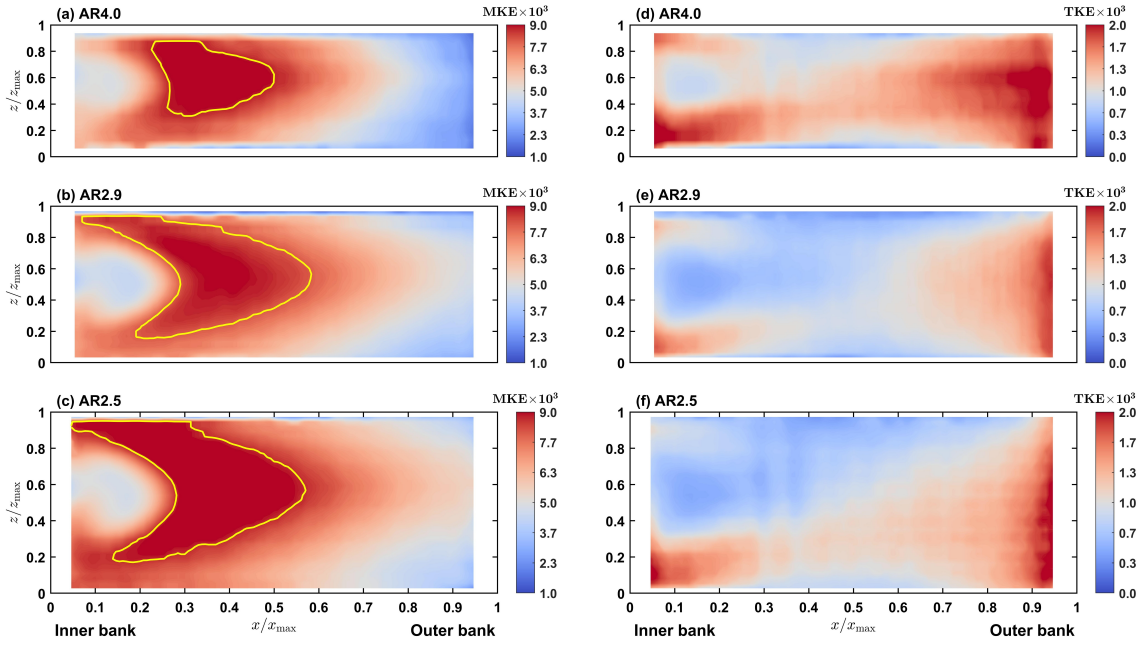


Figure 7.6. Mean flow kinetic energy (MKE) in (a–c) and turbulent kinetic energy (TKE) in (d–f) under high (AR4.0), medium (AR2.9), and low (AR2.5) aspect ratios. The yellow contour outlines the region corresponding to the upper 10% of mean kinetic energy values for each case.The vertical and horizontal axes of each plot represent the flow domain's normalized height and width, respectively.

The turbulent kinetic energy (TKE) fields (Figures 7.6d–f) exhibited a distinct spatial organization relative to the MKE distribution. While the highest aspect-ratio case (AR4.0) showed the largest local MKE values, these were confined to a smaller region, whereas the lower aspect-ratio cases exhibited a broader spatial distribution of energetic flow. In contrast, AR4.0 displayed elevated TKE over a larger portion of the cross-section. Across all cases, regions of high TKE were primarily located near the outer bank and along the bed and ice boundaries, particularly in zones where the mean flow decelerated or where secondary circulation interacted with boundary layers.

A clear spatial separation between MKE- and TKE-dominated regions was observed. Regions of strong mean secondary circulation did not coincide with maximum turbulence intensity, indicating a redistribution of energy between organized mean motion and turbulent fluctuations. This separation reflected the role of secondary circulation in transferring energy from coherent flow structures to turbulence, particularly in regions of strong shear and boundary interaction. Together Figure 7.5 and Figure 7.6 demonstrated that aspect ratio controls not only the vertical redistribution of momentum but also the partitioning between mean flow energy and turbulence. Lower aspect ratios promoted a more distributed and vertically integrated flow structure, characterized by broader regions of elevated MKE and enhanced interaction between circulation cells, whereas higher aspect ratios favored more localized velocity cores and stronger turbulence concentrations near boundaries.

While the streamline patterns, the velocity field, and kinetic energy distributions characterize the structure of the secondary circulation and the spatial organization of streamwise momentum and turbulence, they do not directly quantify the kinetic energy associated with the cross-sectional motion. This distinction is particularly important in an ice-covered bend because the mean kinetic energy is dominated by the streamwise velocity component and therefore does not provide a direct measure of secondary-flow intensity. The secondary-flow kinetic energy provides a complementary measure by isolating the energetic contribution of the organized transverse and vertical velocity components responsible for cross-sectional circulation, and is examined next.

7.4.5 Secondary-flow kinetic energy

To determine where the kinetic energy associated with the mean secondary flow was concentrated, the influence of aspect ratio on the energy distribution of the secondary flow was examined. The local secondary-flow kinetic energy was calculated from the time-averaged transverse and vertical velocity components as

$$k_{\mathrm{sec}} = \frac{1}{2}\left(v^2 + w^2\right), \tag{7.3}$$

where v and w are the time-averaged cross-stream and vertical velocities, respectively. To express the secondary-flow kinetic energy relative to the bulk-flow velocity scale,

the local values were normalized by the square of the bulk velocity,

$$k^*_{\mathrm{sec}} = \frac{k_{\mathrm{sec}}}{U_b^2} = \frac{v^2 + w^2}{2U_b^2}. \tag{7.4}$$

Because U_b was maintained at $0.1\ \mathrm{m\,s^{-1}}$ for all three experiments, this normalization provides a direct measure of the fraction of the characteristic bulk-flow kinetic-energy scale represented locally by organized secondary motion. The cross-sectional mean value was additionally calculated by area averaging as:

$$\bar{k}^*_{\mathrm{sec}} = \frac{1}{A}\int_A \frac{v^2 + w^2}{2U_b^2}\, dA, \tag{7.5}$$

where A represents the measured cross-sectional area. Figure 7.7 shows a systematic increase in the area-averaged normalized secondary-flow kinetic energy as aspect ratio decreases. The contour distributions describe where secondary-flow energy is concentrated, whereas $\bar{k}^*_{\mathrm{sec}}$ provides a single integrated measure of the overall secondary-flow intensity for each aspect-ratio configuration.

The spatial distribution of k^*_{sec} for AR4.0 shows most of the interior cross-section is characterized by relatively low k^*_{sec}, with the principal energetic region forming an elongated band around the middle of the flow depth, approximately between $n/B \approx 0.3$ and 0.8. In the shallowest configuration, the limited separation between the bed and ice cover constrains the vertical development of the circulations. The relatively low secondary-flow energy over much of the cross-section therefore indicates a smaller proportion of the mean-flow energy was expressed as organized cross-sectional motion.

As the aspect ratio decreases to AR2.9, the energetic region becomes both stronger and more spatially developed. Elevated k^*_{sec} occupies a broader portion of the central section, with the main energetic band concentrated around $z/H \approx 0.4$–0.6. A distinct energetic region is also evident near the inner bank around mid-depth. This spatial pattern is consistent with the changes identified from the secondary-flow streamlines, where the lower-aspect-ratio cases exhibit a stronger inner-bank circulation together with a substantially strengthened bed-layer vortex. The previously reported circulation magnitude of the

bed-layer vortex increases from $|\Gamma| = 1.40$ for AR4.0 to 3.73 for AR2.9, while the inner-bank circulation also becomes more prominent. The k^*_{sec} field therefore showed that these topological changes were accompanied by an increase in the magnitude of the organized transverse and vertical velocities.

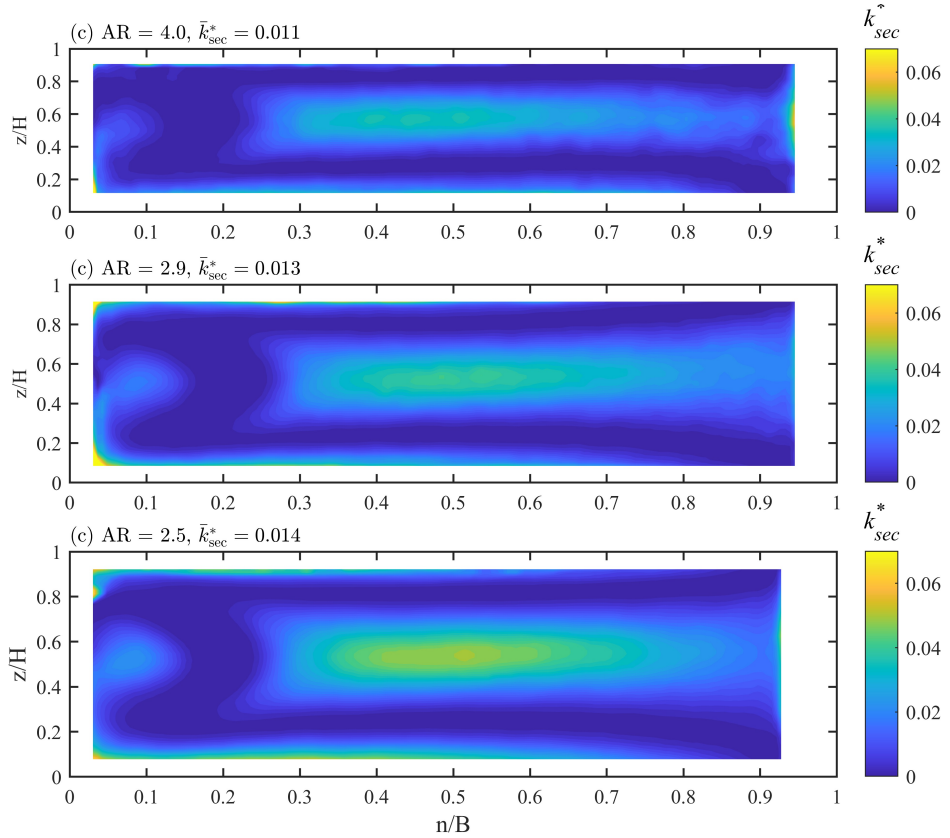


Figure 7.7. The normalized secondary flow kinetic energy under high (AR4.0), medium (AR2.9), and low (AR2.5) aspect ratios. The vertical and horizontal axes of each plot represent the flow domain's normalized height and width, respectively.

This tendency became most evident for AR2.5. The central region of elevated k^*_{sec} reached its largest magnitude and formed a broad, coherent band centered approximately around $z/H \approx 0.5$–0.6. Compared with AR4.0, the energetic region was less vertically compressed and extended over a greater fraction of the channel width. This behavior agrees with the substantial strengthening of the bed-layer circulation previously identified from the streamline analysis, for which the circulation magnitude reaches $|\Gamma| = 6.11$ in AR2.5.

An important feature of Figure 7.7 is the concentration of elevated secondary-flow energy around the central portion of the flow depth. The ice-covered configuration im-

poses shear at both the upper and lower boundaries, producing the vertically stacked circulation system. Near the interfaces between these circulation layers, cross-stream velocities change direction, while the return flows associated with the circulation can produce substantial transverse and vertical velocity magnitudes. Consequently, the energetic band around mid-depth represents an important pathway through which the vertically separated circulation cells redistribute momentum laterally across the section. The increasing magnitude and spatial continuity of this band from AR4.0 to AR2.5 indicate progressively stronger coupling of the cross-sectional motions as vertical confinement decreases.

The energetic region near the inner bank is also hydraulically significant. The previous transverse-velocity profiles showed substantial aspect-ratio-dependent changes near $n/B \approx 0.2$, where the direction of cross-stream velocity differed between AR4.0 and the two deeper cases. This location was interpreted as an interaction region between the inner-bank circulation and main circulation under the ice. The localized k^*_{sec} maximum near the inner bank in Figure 7.7 confirms that this region is not simply a geometric interface between vortices; it contains appreciable cross-sectional kinetic energy. The feature becomes particularly apparent for AR2.9 and AR2.5, providing further evidence that decreasing aspect ratio modifies the energetic importance of the inner-bank secondary-flow system.

The increase in $\bar{k^*_{\mathrm{sec}}}$ from 0.011 for AR4.0 to 0.013 for AR2.9 and 0.014 for AR2.5 corresponded to increases of approximately 18% and 27%, respectively, relative to AR4.0. This systematic increase with decreasing aspect ratio confirmed that the observed changes in secondary-flow structure were accompanied by a measurable increase in the kinetic energy of the mean cross-sectional motion. The concurrent expansion of the elevated-energy region indicated that this increase was not confined to localized circulation cells but was distributed over a larger portion of the cross-section. These results established secondary-flow kinetic energy as a complementary quantitative measure of the aspect-ratio effect, showing that increased flow depth enhanced both the intensity and cross-sectional extent of the organized secondary motion.

7.4.6 Reynolds shear stress distributions

While the preceding kinetic-energy analyses characterized the strength of the mean, turbulent, and secondary motions, the Reynolds shear stresses provided a measure of the

turbulent momentum fluxes associated with velocity fluctuations. Accordingly, the distributions of τ_{uw}, τ_{vw}, and τ_{uv} were examined across AR4.0, AR2.9, and AR2.5 to assess the influence of aspect ratio on cross-sectional momentum transport (Figure 7.8).

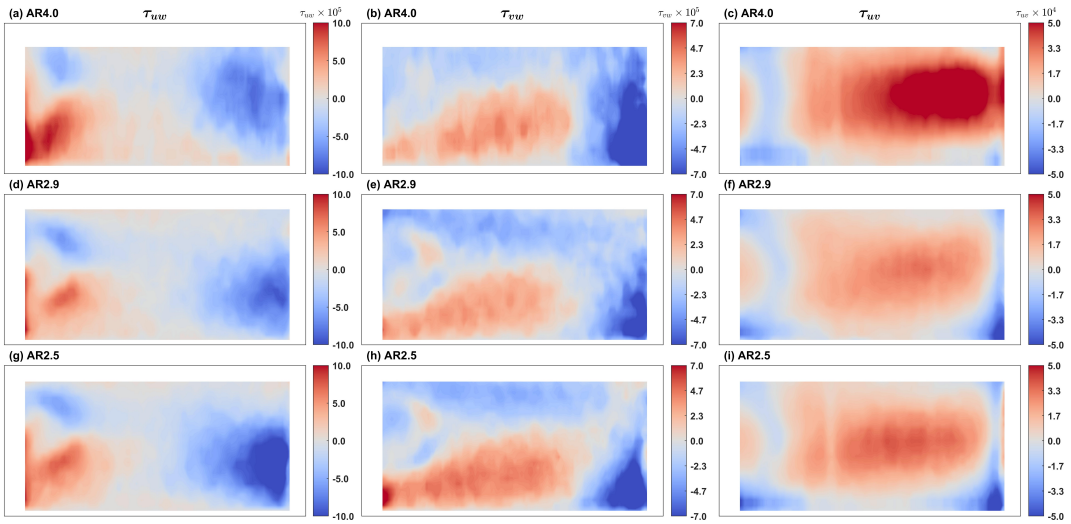


Figure 7.8. Spatial distributions of Reynolds shear stress components τ_{uw}, τ_{vw}, and τ_{uv}, for the three aspect-ratio configurations (AR4.0, AR2.9, AR2.5). Positive and negative values indicate the direction of turbulent momentum transfer between velocity components. The values are scaled by the order of magnitude indicated in the legend for visual enhancement.

The $\tau_{uw} = -\overline{u'w'}$ distributions (Figures 7.8a,d,g) represented the vertical transport of streamwise momentum. Positive values indicated upward transport of high-momentum fluid, while negative values corresponded to downward transport toward the bed. For all aspect ratios, strong τ_{uw} magnitudes were concentrated near the inner bank and close to the boundaries, particularly near the bed. As the aspect ratio decreased, the regions of intense τ_{uw} became more spatially extensive, reflecting enhanced vertical momentum exchange associated with stronger near-boundary shear and secondary-flow interactions in shallower configurations.

The $\tau_{vw} = -\overline{v'w'}$ component (Figures 7.8b,e,h) characterized the vertical transport of transverse momentum and was closely linked to the vertical structure of secondary circulation. Positive and negative regions indicated upward or downward transport of transverse velocity fluctuations, respectively. Across all cases, elevated τ_{vw} values were observed near the bed, where vertical motions associated with secondary vortices interacted with boundary layers. With decreasing aspect ratio, the magnitude and spatial coverage of τ_{vw} decreased,

indicating stronger coupling between vertical motions and cross-stream velocity fluctuations in shallower flows.

The $\tau_{uw} = -\overline{u'w'}$ distributions (Figures 7.8a,d,g) represented the vertical transport of streamwise momentum. Positive values indicated upward transport of high-momentum fluid, while negative values corresponded to downward transport toward the bed. For all aspect ratios, strong τ_{uw} magnitudes were concentrated near the inner bank and close to the boundaries, particularly near the bed. As the aspect ratio decreased, the regions of intense τ_{uw} became more spatially extensive, reflecting enhanced vertical momentum exchange associated with stronger near-boundary shear and secondary-flow interactions in shallower configurations.

The $\tau_{uv} = -\overline{u'v'}$ distributions (Figures 7.8c,f,i) described the lateral transport of streamwise momentum and were a key indicator of turbulence-induced cross-stream momentum exchange. Positive values corresponded to momentum transfer toward the outer bank, while negative values indicated transport toward the inner bank. For all aspect ratios, τ_{uv} exhibited broad regions of consistent sign across the central portion of the cross-section, aligning with the region between the main secondary circulation cells in the ice and bed layers. As the aspect ratio decreased, these regions became more spatially uniform and extended across a larger fraction of the flow depth, suggesting that turbulence increasingly contributed to redistributing streamwise momentum laterally in shallower configurations.

Overall, Figure 7.8 showed that aspect ratio altered the spatial organization of turbulent momentum transport across the channel cross-section. At AR4.0, the Reynolds shear stresses were more strongly localized near the boundaries, whereas decreasing aspect ratio produced broader regions of momentum exchange extending into the cross-sectional interior. This redistribution was consistent with the accompanying changes in secondary-flow structure and indicated increased interaction between boundary-generated turbulence and the interior flow as the flow depth increased. From a hydraulic perspective, the transition from localized to more spatially distributed Reynolds stresses may also modify the distribution of boundary forcing and, consequently, the spatial patterns of sediment entrainment and redistribution.

7.5 Discussion

The observed aspect-ratio dependence of the secondary circulation resulted from the interaction between curvature-induced forcing and the depth-dependent redistribution of streamwise momentum in the ice-covered cross-section. In a curved channel, the local centrifugal acceleration scales as

$$a_c = \frac{U^2}{R_c}, \tag{7.6}$$

where U is the local streamwise velocity and R_c is the local radius of curvature [117, 17, 15]. Although U_b and R_c were approximately unchanged among the experiments, the local velocity U was not spatially uniform and its cross-sectional distribution varied with aspect ratio. Consequently, a constant bulk velocity did not imply an invariant centrifugal forcing field. Rather, the redistribution of streamwise momentum with increasing flow depth modified the spatial distribution of U^2/R_c and, therefore, the local imbalance between centrifugal acceleration and the cross-stream pressure-gradient force that sustained the secondary circulation.

This distinction was important for a better understanding of the present results. The streamwise velocity and mean kinetic-energy fields (Figures 7.5 and 7.6) showed a progressive redistribution of the high-momentum core as the aspect ratio decreased from AR4.0 to AR2.5. At AR4.0, the streamwise momentum was comparatively confined in the vertical direction by the proximity of the bed and ice boundaries. Increasing the flow depth increased the separation between these opposing boundary layers and allowed the high-momentum region to occupy a larger fraction of the cross-section. The resulting change in the spatial distribution of U^2/R_c altered the forcing available to the cross-sectional circulation even though the externally imposed bulk velocity and bend curvature remained approximately constant. The aspect-ratio effect therefore arose primarily through modification of the internal momentum distribution rather than through a change in the bulk centrifugal forcing scale U_b^2/R_c.

The mean kinetic-energy (MKE) distributions provided an energetic representation of this aspect-ratio-dependent reorganization of the mean momentum field. As shown in

Figure 7.6a–c, the region of elevated MKE became progressively larger as the aspect ratio decreased. At AR4.0, the highest MKE was concentrated within a comparatively confined region in the upper-central portion of the cross-section. At AR2.9 and AR2.5, this region extended farther vertically and laterally, occupying a substantially larger fraction of the flow interior. This expansion was consistent with the streamwise velocity distributions (Figure 7.5) and indicated that increasing the bed–ice separation allowed the high-momentum region to develop over a greater portion of the cross-section. Because the local curvature-induced forcing depended on U^2/R_c, this broader redistribution of mean-flow energy was also consistent with a corresponding reorganization of the centrifugal forcing field.

The changes in MKE were accompanied by a pronounced development of the secondary circulation shown in Figure 7.3. In particular, the expansion of the high-MKE region from AR4.0 to AR2.9 and AR2.5 occurred concurrently with the strengthening and spatial development of the large lower-layer counter-rotating cell. Its circulation magnitude increased from $1.40\ \mathrm{mm}^2/\mathrm{s}$ at AR4.0 to $3.73\ \mathrm{mm}^2/\mathrm{s}$ at AR2.9 and $6.11\ \mathrm{mm}^2/\mathrm{s}$ at AR2.5 (Table 7.3). The inner-bank ice-layer cell also strengthened substantially, with its circulation increasing from $0.21\ \mathrm{mm}^2/\mathrm{s}$ at AR4.0 to 1.26 and $1.22\ \mathrm{mm}^2/\mathrm{s}$ at AR2.9 and AR2.5, respectively. These concurrent changes indicated that the redistribution of the mean momentum field was closely associated with the reorganization and strengthening of the secondary circulation as vertical confinement decreased.

The different spatial organization of MKE and TKE demonstrated that regions containing high mean-flow energy were not necessarily regions of strongest turbulent fluctuations. The MKE distributions characterized the aspect-ratio-dependent organization of the mean momentum field from which the curvature-induced forcing arose, whereas TKE identified regions of enhanced turbulent activity capable of participating in momentum redistribution. The strengthening of the secondary circulation with decreasing aspect ratio therefore cannot be attributed simply to an overall increase in turbulence intensity. Rather, the results indicate that increasing flow depth reorganized the mean momentum field while simultaneously modifying the spatial distribution of turbulent activity.

The corresponding response of the circulation was evident from the secondary-flow velocity and kinetic-energy fields. The increase in $\bar{k}^*_{\mathrm{sec}}$ with decreasing aspect ratio showed that a progressively larger fraction of the bulk-flow kinetic-energy scale was contained in the mean transverse and vertical motions. More importantly, the elevated k^*_{sec} region expanded

into the cross-sectional interior at lower aspect ratios. Thus, the effect of increasing flow depth was not limited to an increase in the local magnitude of the secondary velocity; it was accompanied by a spatial reorganization of the circulation over a larger portion of the cross-section. This behavior was consistent with the observed development of secondary-flow cells and with the accompanying redistribution of turbulent momentum fluxes. The rotational response to this redistribution was directly evident in the streamwise-vorticity field. The streamwise vorticity was calculated as

$$\omega_s = \frac{\partial w}{\partial x} - \frac{\partial v}{\partial z}, \tag{7.7}$$

where v and w are the time-averaged transverse and vertical velocity components, respectively, and x and z denote the cross-stream and vertical coordinates. Unlike the secondary-flow kinetic energy, which measures the magnitude of the cross-sectional motion, ω_s identifies regions of concentrated mean rotation and therefore provides a complementary measure of the spatial organization of the secondary circulation.

Figure 7.9 shows a marked change in the streamwise-vorticity field with aspect ratio. For AR4.0, the strongest positive and negative vorticity remained concentrated near the inner-bank region and occupied a relatively limited portion of the cross-section. At AR2.9 and AR2.5, the inner-bank vorticity developed into a more distinct adjacent positive–negative structure and extended farther into the flow interior. The persistence of opposite-signed ω_s regions was consistent with the counter-rotating secondary-flow structures identified from the mean cross-sectional velocity field. Their increased spatial extent at lower aspect ratio further indicated that the rotational influence of the inner-bank secondary circulation penetrated farther into the cross-section as the flow depth increased.

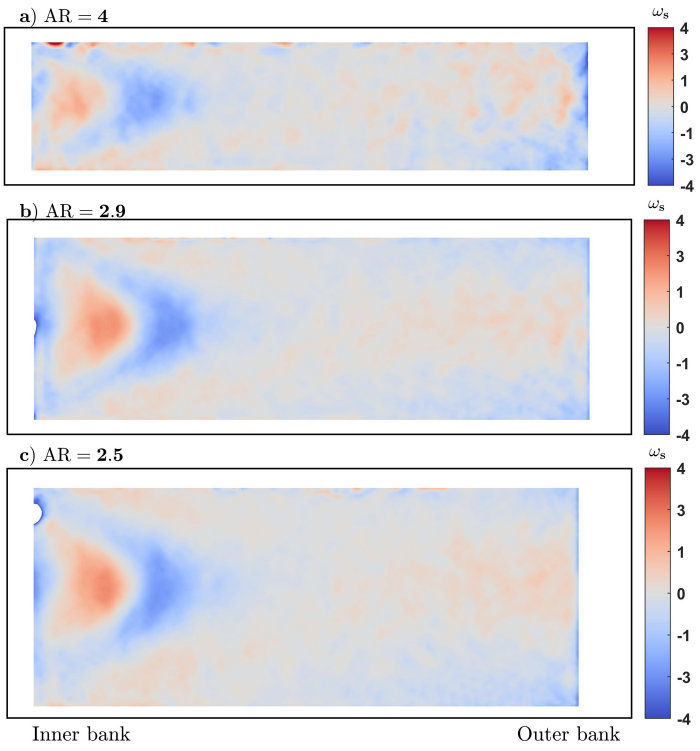


Figure 7.9. Spatial distributions of streamwise vorticity ω_s for the three aspect-ratio configurations: (a) AR4.0, (b) AR2.9, and (c) AR2.5. The horizontal direction extends from the inner bank (left) to the outer bank (right), and the vertical direction extends from the bed to the ice cover.

Figure 7.9 shows a marked change in the streamwise-vorticity field with aspect ratio. For AR4.0, the strongest positive and negative vorticity remained concentrated near the inner-bank region and occupied a relatively limited portion of the cross-section. At AR2.9 and AR2.5, the inner-bank vorticity developed into a more distinct adjacent positive–negative structure and extended farther into the flow interior. The persistence of opposite-signed ω_s regions was consistent with the counter-rotating secondary-flow structures identified from the mean cross-sectional velocity field. Their increased spatial extent at lower aspect ratio further indicated that the rotational influence of the inner-bank secondary circulation penetrated farther into the cross-section as the flow depth increased.

The strengthening of streamwise vorticity at lower aspect ratios was concentrated primarily near the inner bank (Figure 7.9), where a pronounced low-streamwise-momentum region was also observed (Figure 7.5). The reduced streamwise velocity in this region pro-

duced a strong spatial variation in the local centrifugal acceleration, u^2/R_c, relative to the surrounding higher-momentum flow. This spatial correspondence was accompanied by elevated magnitudes and strong spatial gradients of $\tau_{uw} = -\rho\overline{u'w'}$ (Figures 7.8a,d,g), indicating strong vertical turbulent transport of streamwise momentum near the low-momentum region. The coincidence of these features suggests a coupled response in which the redistribution of streamwise momentum modified the local centrifugal forcing, while turbulent momentum transport contributed to the maintenance and redistribution of the secondary circulation. The resulting momentum gradients were therefore consistent with the stronger and more spatially developed ω_s structures observed near the inner bank as the aspect ratio decreased.

The increase in magnitude and spatial extent of these vorticity regions from AR4.0 toward AR2.5 therefore demonstrated that the changes in momentum redistribution were accompanied by a stronger and more spatially developed rotational response. This ice-covered flow observations were consistent with the aspect-ratio dependence reported by [64] for an open-channel configuration with the same bend curvature, where secondary vortices at the bend apex became stronger and more vertically developed as aspect ratio decreased. The agreement suggests that the geometric control imposed by aspect ratio remained important under an ice cover. However, the present flow differed fundamentally from the open-channel case because the rigid ice boundary introduced an additional shear layer and eliminated the stress-free upper boundary. The resulting interaction between bed-generated and ice-generated shear constrained the vertical organization of the streamwise momentum field and produced the vertically stacked secondary-flow structure observed here. Thus, the response to aspect ratio under ice cover cannot be interpreted simply as an extension of open-channel behavior; it reflects the combined influence of curvature and two dynamically active vertical boundaries.

To further examine how the strength of secondary flow varied relative to the bulk velocity with aspect ratio, the normalized secondary-flow velocity magnitude was considered:

$$U^*_{\mathrm{sec}} = \frac{\sqrt{v^2 + w^2}}{U_b}, \qquad U_{\mathrm{sec}} = \sqrt{v^2 + w^2}. \tag{7.8}$$

This measure complemented the streamwise-vorticity distributions because regions of large streamwise vorticity were associated with strong spatial gradients of cross-sectional

velocity and did not necessarily coincide with regions of maximum secondary-flow velocity.

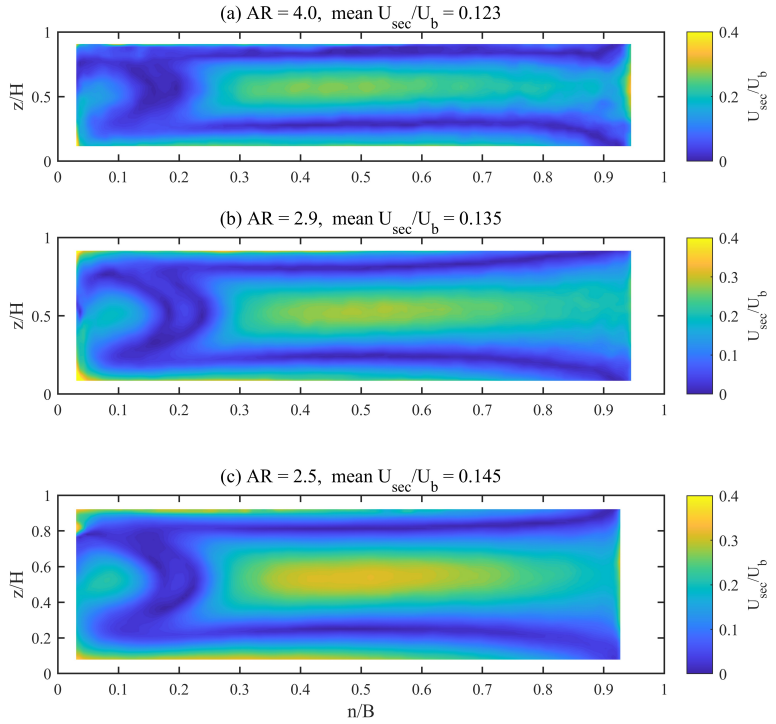


Figure 7.10. Spatial distributions of the normalized secondary-flow velocity magnitude, U^*_{sec}, for the three aspect-ratio configurations: (a) AR = 4.0, (b) AR = 2.9, and (c) AR = 2.5. The corresponding cross-sectionally averaged values, U^*_{sec}, are reported for each case. The lateral and vertical coordinates are normalized by the channel width, B, and flow depth, H, respectively.

The cross-sectional mean U^*_{sec} increased from 0.123 at AR4.0 to 0.135 at AR2.9 and 0.145 at AR2.5, corresponding to increases of approximately 10% and 18%, respectively, relative to AR4.0. Thus, the mean magnitude of the organized transverse and vertical motion represented approximately 12–15% of the bulk streamwise velocity over the investigated range.

The spatial distributions in Figure 7.10 showed that this strengthening was not uniform across the cross-section. At AR4.0, the elevated interior values of U^*_{sec} were concentrated primarily within the central portion of the cross-section, approximately between $n/B = 0.3$ and 0.7 and near mid-depth. As the aspect ratio decreased to AR2.9 and AR2.5, this region became progressively stronger and more spatially extensive, with local interior values approaching $U^*_{\text{sec}} \approx 0.3$ at AR2.5. A distinct region of elevated U^*_{sec} was also evident near the inner bank and became considerably more pronounced at the two lower aspect ra-

tios. These spatial changes corresponded closely to the reorganization and strengthening of the circulation cells identified from the patterns in Figure 7.3.

Near the inner bank, the increase in U^*_{sec} from AR4.0 to the lower-aspect-ratio cases coincided with the substantial strengthening of the ice-layer inner-bank vortex. The circulation of this cell increased from $0.21\ \text{mm}^2/\text{s}$ at AR4.0 to $1.26\ \text{mm}^2/\text{s}$ at AR2.9 and remained comparably strong at $1.22\ \text{mm}^2/\text{s}$ at AR2.5 (Table 7.3). The persistence of elevated U^*_{sec} in this region at AR2.9 and AR2.5 was therefore consistent with the stronger inner-bank circulation relative to AR4.0. This region also corresponded to the localized high-magnitude τ_{uw} structure near the inner bank in Figure 7.8. Since $\tau_{uw} = -\rho\overline{u'w'}$ represents the vertical turbulent flux of streamwise momentum, this spatial correspondence indicated that the strengthening of the inner-bank secondary motion occurred in a region of substantial vertical turbulent momentum exchange. The inner-bank circulation and the local turbulent redistribution of streamwise momentum were therefore dynamically coupled features of the aspect-ratio-dependent flow structure.

A stronger and more systematic correspondence was observed for the large lower circulation cell. Its circulation magnitude increased from $1.40\ \text{mm}^2/\text{s}$ at AR4.0 to $3.73\ \text{mm}^2/\text{s}$ at AR2.9 and $6.11\ \text{mm}^2/\text{s}$ at AR2.5 (Table 7.3). This progressive strengthening accompanied the increase and spatial expansion of the elevated-U^*_{sec} region across the central portion of the cross-section. The correspondence was particularly evident at AR2.5, where the strongest and broadest interior U^*_{sec} distribution occurred together with the largest circulation magnitude of the lower vortex. The increase in the cross-sectional mean U^*_{sec} therefore reflected not simply a uniform increase in transverse and vertical velocity, but the strengthening and spatial development of the dominant circulation structures.

The Reynolds-stress distributions provided further insight into this relationship. The central region of elevated U^*_{sec} associated with the large lower circulation cell overlapped substantially with the region of elevated τ_{uv} in Figure 7.8. Because $\tau_{uv} = -\rho\overline{u'v'}$ represents the lateral turbulent flux of streamwise momentum, its spatial organization indicated substantial turbulent redistribution of streamwise momentum across the channel in the same region occupied by the dominant secondary circulation. As the aspect ratio decreased, the persistence of this lateral momentum flux together with the increasing U^*_{sec} and circulation magnitude was consistent with stronger coupling between the streamwise momentum field and the cross-sectional circulation. Similarly, the correspondence between the inner-bank

cell and the localized τ_{uw} distribution indicated an important role of vertical momentum redistribution in the inner-bank region. These relationships suggest that the aspect-ratio dependence of the secondary flow involved changes in both vertical and lateral turbulent momentum transport rather than a purely geometric expansion of the circulation cells.

The spatial relation between U^*_{sec} and the secondary circulation cells patterns was also consistent with the kinematics of rotational flow. The largest values of U^*_{sec} were generally distributed around the circulation cells rather than being concentrated at their vortex centers, where the local cross-sectional velocity can be relatively small. Consequently, U^*_{sec} characterized the magnitude and spatial extent of the transverse and vertical motion associated with the circulation, whereas the circulation values quantified the integrated rotational strength of the individual cells. The streamwise-vorticity field provided a complementary measure by identifying regions of strong local velocity gradients and rotation. Considered together, these quantities showed that decreasing aspect ratio altered both the intensity and spatial organization of the secondary motion.

The energetic consequence of this strengthening was examined using the normalized secondary-flow kinetic energy. The progression toward stronger and more spatially extensive k^*_{sec} at lower aspect ratio therefore confirmed that the observed changes were not restricted to vortex geometry. A greater fraction of the cross-section participated energetically in the secondary motion as the flow became deeper.

However, a better understanding of these dynamics requires evaluating how the interaction between bed- and ice-generated shear layers shapes the distribution of flow energy, as well as how vertical confinement modulates the balance between mean and turbulent kinetic energy. The spatial expansion of high-MKE regions with decreasing AR in Figure 7.6a–c reflects a deepening of the flow, which intensifies the influence of vertical gradients in momentum and the generation of large-scale secondary flow structures. In the lowest aspect ratio case (AR2.5), the deeper water column promoted stronger vertical momentum exchanges, facilitating the development of a helical secondary circulation cell that transports high-momentum fluid from the outer bank toward the inner bank beneath the ice cover. This circulation redistributed momentum over a larger depth, leading to an expanded region of elevated MKE (cf. Figure 7.6c). Conversely, at the highest aspect ratio (AR4.0), the shallow flow depth restricts vertical shear development and confines secondary motions closer to the channel bed and surface, resulting in a more laterally confined MKE zone (Figure 7.6a).

This is consistent with earlier studies reporting that shallow channels (higher AR) suppress secondary circulation due to limited vertical room for vortex development ([17, 142]).

The corresponding TKE fields further highlight the dynamical role of flow depth in modulating turbulence production. In the AR4.0 case, high TKE concentrations near the outer bank and near-wall regions is attributed to stronger turbulence production and shear stress (Figure 7.8c) due to confined vortical structures and lateral gradients ([93]). The spatial decoupling between MKE and TKE suggests that regions with strong organized secondary motion are not necessarily zones of intense turbulence. Instead, in deeper flows (e.g., AR2.5), the vertical extent of secondary circulation may promote more coherent motion with less turbulent breakdown, shifting the energy budget toward organized transport rather than dissipation. This decoupling aligns with findings from compound channel and open-channel flow studies that show distinct energy partitioning between mean flow and turbulence depending on flow geometry and boundary constraints ([129, 126]). In particular, the enhanced vertical structure of flow in lower AR cases leads to broader zones of coherent momentum transport, while turbulence is more localized to boundary-layer interactions and recirculation zones.

7.6 Conclusion

The results demonstrated that decreasing the channel aspect ratio, corresponding to increasing flow depth, produced a systematic strengthening and reorganization of the secondary circulation. The deeper AR2.9 and AR2.5 configurations exhibited larger and more developed counter-rotating cells than the relatively shallow AR4.0 configuration, accompanied by an increase in the mean U^*_{sec} from 0.123 to 0.145. This strengthening was particularly evident in the ice-layer inner-bank vortex, whose circulation increased from $0.21\ \mathrm{mm}^2/\mathrm{s}$ at AR4.0 to 1.26 and $1.22\ \mathrm{mm}^2/\mathrm{s}$ at AR2.9 and AR2.5, respectively, and in the lower-layer vortex, whose circulation magnitude increased more substantially from 1.40 to 3.73 and $6.11\ \mathrm{mm}^2/\mathrm{s}$. The concurrent expansion of elevated U^*_{sec} and k^*_{sec} and strengthening of the corresponding ω_s structures confirmed that decreasing aspect ratio affected not only the topology of the circulation cells, but also the magnitude, spatial extent, and energy of the associated secondary motion.

The observed aspect-ratio dependence reflected the combined effects of reduced vertical confinement and redistribution of streamwise momentum. At AR4.0, the smaller bed–ice separation constrained the vertical development of the secondary circulation, whereas increasing the flow depth allowed the circulation structures to develop over a larger vertical extent. Concurrent changes in the streamwise velocity distribution, including the inner-bank low-momentum region, modified the spatial distribution of the local centrifugal forcing, u^2/R_c, despite the approximately constant bulk velocity and bend curvature. The correspondence among the streamwise velocity, MKE, ω_s, and secondary-flow distributions therefore indicated that the reorganization of the primary momentum field was closely coupled to the development and strengthening of the cross-sectional circulation.

The Reynolds shear-stress distributions provided the physical connection between this mean-flow reorganization and turbulent momentum transport. Near the inner bank, the localized high-magnitude τ_{uw} region coincided with elevated U^*_{sec}, stronger ω_s, and the substantial increase in inner-bank vortex circulation, indicating that its development occurred in a region of strong vertical turbulent transport of streamwise momentum. Similarly, the broader τ_{uv} distribution across the central portion of the cross-section corresponded to the expanding U^*_{sec} and k^*_{sec} regions and the pronounced strengthening of the lower circulation cell, indicating substantial lateral redistribution of streamwise momentum. The aspect-ratio-dependent organization of τ_{vw} further demonstrated concurrent changes in turbulent momentum exchange between the transverse and vertical directions.

Taken together, the circulation strength, streamwise velocity and MKE, Reynolds stresses, ω_s, U^*_{sec}, and k^*_{sec} fields provided a consistent physical description of the aspect-ratio effect. Increasing flow depth reduced vertical confinement and reorganized the streamwise momentum field and its associated local centrifugal forcing, while concurrent changes in turbulent momentum transport redistributed momentum vertically and laterally across the section. These changes were accompanied by stronger and more spatially developed rotational motion, ultimately producing the larger and stronger secondary-flow cells observed at lower aspect ratios. The aspect-ratio effect was therefore expressed as a coupled reorganization of primary-flow momentum, turbulent momentum transport, and secondary circulation rather than simply as a geometric change in vortex topology.

Appendices

A.1 Statistical difference across the AR configurations

To evaluate the statistical significance of the observed differences in flow patterns, the distributions of the instantaneous velocity components (u, v, w) were first examined. The corresponding histograms (not shown) exhibited notable skewness; therefore, a non-parametric statistical approach was adopted. As a first step, the Kruskal–Wallis H-test was applied to each velocity component to determine whether their distributions differed significantly among the aspect-ratio groups. This method evaluates group-level differences without assuming normality, making it suitable for skewed and potentially heteroscedastic data.

A.1.1 Kruskal–Wallis H-test

For each velocity component $c \in \{u, v, w\}$, three groups, (i), were considered: $\mathrm{AR}4$ $(i = 1)$, $\mathrm{AR}2.9$ $(i = 2)$, and $\mathrm{AR}2.5$ $(i = 3)$. Let $X_c^{(i)} = \{X_{c,1}^{(i)}, \ldots, X_{c,n_i}^{(i)}\}$ denote the data for group i, with n_i the sample size and $N = \sum_{i=1}^{3} n_i$ the total size. For each component, the samples from all groups are combined and ranked jointly in ascending order. The Kruskal–Wallis test statistic was then computed from the group-wise sums of the pooled ranks. The hypotheses, applied separately for each component, were:

$$H_{0,c}: \quad F_c^{(1)}(x) = F_c^{(2)}(x) = F_c^{(3)}(x) \ \text{ for all } x \quad \text{(all group distributions are equal)}, \tag{A.1}$$

$$H_{1,c}: \quad \exists\, i \neq j \text{ such that } F_c^{(i)}(x) \neq F_c^{(j)}(x) \text{ for some } x \quad \text{(at least one group distribution differs)}. \tag{A.2}$$

At a given significance level α, the null hypothesis $H_{0,c}$ of equal distributions across aspect ratios is rejected whenever the Kruskal–Wallis p-value is less than α. In such cases, there is sufficient statistical evidence in favor of the alternative hypothesis $H_{1,c}$, indicating that at least one aspect ratio yields velocity values that differ significantly from those of another group.

The Kruskal–Wallis test statistic H (reported as χ^2) quantifies the extent to which the rank sums of the groups deviate from what would be expected if all groups originated from the same distribution. It is defined as

$$H \;=\; \frac{12}{N(N+1)} \sum_{i=1}^{k} \frac{R_i^2}{n_i} \;-\; 3(N+1), \tag{A.3}$$

where $R_i = \sum_{k=1}^{n_i} r_{ik}$ denotes the sum of pooled ranks for group i, with r_{ik} representing the rank of the k-th observation $X_{c,k}^{(i)}$ among all $N = \sum_{i=1}^{3} n_i$ datasets. To account for ties (identical values within the pooled dataset), MATLAB applies the standard tie correction internally. Under the null hypothesis H_0, the tie-corrected statistic H_c follows approximately a chi-squared distribution with $k-1$ degrees of freedom. For the present analysis with three groups, this corresponds to $\mathrm{df} = 2$.

The results of the Kruskal–Wallis tests indicate statistically significant differences in the distributions of all three velocity components across the aspect-ratio configurations. Specifically, the streamwise velocity exhibits a test statistic of $\chi^2 = 376$ with an associated p-value of 1.80×10^{-82}, while the transverse velocity yields $\chi^2 = 132$ with $p = 2.13\times10^{-29}$. The vertical velocity shows the strongest distributional separation, with $\chi^2 = 600$ and $p = 3.20 \times 10^{-131}$. In all cases, the p-values are substantially smaller than the significance threshold $\alpha = 0.001$, leading to rejection of the null hypothesis $H_{0,c}$ for each component.

These results demonstrate that the velocity distributions are strongly dependent on aspect ratio for all components, with the most pronounced differences observed in the vertical velocity. Where the Kruskal–Wallis test indicated statistical significance, post-hoc analyses were subsequently conducted to identify the specific pairwise differences between aspect-ratio configurations.

A.1.2 Post-hoc pairwise comparisons

Two complementary post-hoc analyses were used: Dunn–Šidák adjusted contrasts based on the Kruskal–Wallis ranks, and Wilcoxon rank–sum tests with Holm-adjusted p-values. This two-step approach first determines whether differences exist globally and then isolates the specific pairwise contrasts responsible, thereby reducing the likelihood of false positives due to multiple comparisons. The primary advantage of this method is its robustness to non-normal distributions and unequal variances, conditions common in experimental hydraulic data where flow turbulence, boundary effects, and measurement uncertainties can produce skewed velocity distributions.

In addition, the two-sample Kolmogorov–Smirnov (KS) test was applied as a complementary nonparametric check, as it is sensitive to both location and shape differences in the empirical distributions. Including the KS test ensures that not only central tendency shifts but also broader distributional differences are identified, thereby strengthening the reliability of the pairwise comparisons. Given the distributional characteristics of the present datasets, this approach provides a statistically robust and conservative assessment of group differences. The results for velocity components across aspect ratios are summarized in Table A.1.

The omnibus test results in Table A.1 show that, for all velocity components, the null hypothesis of equal group distributions across aspect ratios is strongly rejected at the significance level $\alpha = 0.001$. Among the components, the vertical velocity exhibits the strongest evidence of group differences ($\chi^2 = 600$), followed by the streamwise component ($\chi^2 = 376$), while the transverse component ($\chi^2 = 132$) shows comparatively smaller, though still highly significant, separation across aspect ratios.

Given these significant omnibus results, post hoc pairwise comparisons were performed to identify the specific differences between aspect-ratio configurations.

The pairwise comparisons for the streamwise (u) and transverse (v) velocity components show that all three aspect-ratio pairs differ significantly across all applied tests, indicating that both components are consistently sensitive to aspect-ratio variations.

Table A.1. Kruskal–Wallis tests for each velocity component across aspect ratios (AR4, AR2.9, AR2.5), and post hoc pairwise comparisons. Omnibus KW reports χ^2 statistic, p, and call at $\alpha = 0.001$; pairwise tests report Dunn–Šidák (DS), Holm-adjusted Wilcoxon (H), and Kolmogorov–Smirnov (KS) p-values. "S" denotes significant and "NS" denotes non-significant.

Omnibus (Kruskal–Wallis)

Component	Comparison	χ^2	p_{KW}	Call
u	All AR groups	376	$p < 0.001$	S
v	All AR groups	132	$p < 0.001$	S
w	All AR groups	600	$p < 0.001$	S

Pairwise comparisons (post hoc)

Component	AR Pair	p_{DS}	DS	p_{H}	H	p_{KS}	KS
u	4 vs 2.9	$p < 0.001$	S	$p < 0.001$	S	$p < 0.001$	S
u	4 vs 2.5	$p < 0.001$	S	$p < 0.001$	S	$p < 0.001$	S
u	2.9 vs 2.5	$p < 0.001$	S	$p < 0.001$	S	$p < 0.001$	S
v	4 vs 2.9	$p < 0.001$	S	$p < 0.001$	S	$p < 0.001$	S
v	4 vs 2.5	$p < 0.001$	S	$p < 0.001$	S	$p < 0.001$	S
v	2.9 vs 2.5	$p < 0.001$	S	$p < 0.001$	S	$p < 0.001$	S
$\boldsymbol{w}^*$	4 vs 2.9	0.308	NS	0.0618	NS	$p < 0.001$	S
w	4 vs 2.5	$p < 0.001$	S	$p < 0.001$	S	$p < 0.001$	S
w	2.9 vs 2.5	$p < 0.001$	S	$p < 0.001$	S	$p < 0.001$	S

In contrast, the vertical velocity (w) exhibits a distinct behavior: the comparison between AR4 and AR2.9 is not significant based on rank-based tests (Dunn–Šidák and Holm), while both AR4–AR2.5 and AR2.9–AR2.5 pairs show strong statistical significance. Notably, the Kolmogorov–Smirnov test indicates a significant difference even for the AR4–

AR2.9 pair, suggesting that although central tendencies are similar, differences in distributional shape persist. This pattern suggests a component-dependent response of velocity field to AR variation. While the streamwise and transverse components exhibit systematic and consistent differences across all configurations, the vertical component shows selective sensitivity, primarily driven by contrasts involving the smallest aspect ratio (AR2.5). To complement these significance-based findings, effect size measures were computed to assess the magnitude and practical relevance of the observed differences.

A.1.3 Pairwise effect size comparisons

In addition to significance testing, effect sizes were computed to quantify the magnitude and direction of pairwise differences between aspect-ratio groups. For each pair of aspect ratios, Cliff's δ was calculated as a nonparametric measure of stochastic dominance, defined by

$$\delta \;=\; \frac{n_{>} - n_{<}}{n_1 n_2}, \tag{A.4}$$

where $n_{>}$ and $n_{<}$ denote the number of all possible pairwise comparisons between the two groups in which one observation is greater or smaller than the other, respectively, and n_1 and n_2 are the sample sizes of the two groups. Values of δ range from -1 to $+1$, with $\delta = 0$ indicating substantial overlap between the two distributions and larger absolute magnitudes indicating stronger separation. The sign of δ indicates the direction of stochastic dominance between the compared aspect-ratio groups.

In parallel, the difference in group medians, $\Delta\tilde{x} = \tilde{x}_i - \tilde{x}_j$, where $\tilde{x}_i$ and $\tilde{x}_j$ denote the sample medians of groups i and j, respectively, was reported to provide an interpretable effect size in physical units $[\mathrm{m\,s^{-1}}]$. Together, Cliff's δ and median differences complement the hypothesis tests by distinguishing between effects that are statistically detectable and those that are also practically meaningful for flow dynamics. The computed values of Cliff's δ and median differences for all pairwise aspect-ratio comparisons are summarized in Table A.2.

The pairwise effect-size results indicate that all observed differences remain small in

magnitude, despite the strong statistical significance identified by the nonparametric tests. For the streamwise velocity component (u), the largest effect is observed for the AR2.9 vs AR2.5 comparison ($\delta = 0.109$, $\Delta\tilde{x} = 0.0058\ \mathrm{m\,s^{-1}}$), while the contrasts involving AR4 exhibit smaller effect sizes ($\delta = -0.064$ and $\Delta\tilde{x} = -0.0045\ \mathrm{m\,s^{-1}}$ for AR4 vs AR2.9, and $\delta = 0.020$ and $\Delta\tilde{x} = 0.0013\ \mathrm{m\,s^{-1}}$ for AR4 vs AR2.5), indicating relatively modest but consistent differences. This pattern suggests that the most pronounced shift in the streamwise-velocity distribution occurs between the two smaller aspect-ratio cases, although the magnitude of separation remains limited.

Table A.2. Effect sizes for pairwise comparisons across aspect ratios, reported as Cliff's δ, which indicates the direction and magnitude of stochastic dominance between the compared groups, and the median difference $\Delta\tilde{x}$, reported in physical units.

Component	Pair	Cliff's δ	$\Delta\tilde{x}\,[\mathrm{m\,s^{-1}}]$
u	AR4 vs AR2.9	-0.064	-0.0045
u	AR4 vs AR2.5	$+0.020$	$+0.0013$
u	AR2.9 vs AR2.5	$+0.109$	$+0.0058$
v	AR4 vs AR2.9	-0.039	-0.0012
v	AR4 vs AR2.5	-0.061	-0.0018
v	AR2.9 vs AR2.5	-0.023	-0.0006
w	AR4 vs AR2.9	-0.010	-0.0001
w	AR4 vs AR2.5	$+0.111$	$+0.0003$
w	AR2.9 vs AR2.5	$+0.116$	$+0.0004$

For the transverse velocity component (v), all pairwise comparisons also yield small effect sizes, with negative values for all three contrasts. The largest magnitude occurs for AR4 vs AR2.5 ($\delta = -0.061$, $\Delta\tilde{x} = -0.0018\ \mathrm{m\,s^{-1}}$), followed by AR4 vs AR2.9

($\delta = -0.039$, $\Delta\tilde{x} = -0.0012\ \mathrm{m\,s^{-1}}$), whereas the comparison between AR2.9 and AR2.5 yields only a very small effect ($\delta = -0.023$, $\Delta\tilde{x} = -0.0006\ \mathrm{m\,s^{-1}}$). This indicates that, although statistically significant differences are detected across all pairs, the practical separation between AR2.9 and AR2.5 remains minimal, consistent with the relatively small magnitude of both stochastic dominance and median shift.

For the vertical velocity component (w), the AR4 vs AR2.9 comparison produces an almost negligible effect size ($\delta = -0.010$, $\Delta\tilde{x} = -0.0001\ \mathrm{m\,s^{-1}}$), which is consistent with the non-significant rank-based post-hoc comparisons reported earlier. In contrast, the AR4 vs AR2.5 and AR2.9 vs AR2.5 comparisons yield the largest effect sizes among the w-component contrasts, with $\delta = 0.111$ and $\Delta\tilde{x} = 0.0003\ \mathrm{m\,s^{-1}}$, and $\delta = 0.116$ and $\Delta\tilde{x} = 0.0004\ \mathrm{m\,s^{-1}}$, respectively. Although still small in absolute magnitude, these results indicate that the vertical-velocity differences are primarily associated with contrasts involving the smallest aspect ratio, AR2.5.

The effect-size analysis confirms that the influence of aspect ratio is component-dependent. The streamwise and vertical components show their strongest pairwise separation in comparisons involving AR2.5, whereas the transverse component exhibits uniformly small but statistically detectable differences across all aspect-ratio pairs. More broadly, the small magnitudes of Cliff's δ and the small median differences indicate that statistical significance here is driven mainly by subtle but systematic distributional shifts rather than by large pairwise separation. Since effect sizes primarily characterize location-related differences, an additional Brown–Forsythe analysis was conducted to evaluate whether the observed aspect-ratio effects were also associated with differences in distributional spread.

A.1.4 Brown–Forsythe variance test

The Brown–Forsythe variance test is a robust modification of Levene's test, using the absolute deviations of each observation from its group median to assess differences in variance across groups. The test is applied as an omnibus comparison across all aspect-ratio groups, with hypotheses given by

$$H_0: \quad \sigma^2_{\mathrm{AR4}} = \sigma^2_{\mathrm{AR2.9}} = \sigma^2_{\mathrm{AR2.5}} \quad \text{(equal variances across groups)}, \tag{A.5}$$

$$H_1 : \ \exists\, i \neq j \ \text{ such that } \ \sigma_i^2 \neq \sigma_j^2 \quad \text{(at least one group variance differs).} \tag{A.6}$$

The Brown–Forsythe test statistic is based on a one-way ANOVA applied to the transformed values

$$Z_{ik} \ = \ \left|X_{ik} - \tilde{X}_i\right|, \tag{A.7}$$

where X_{ik} is the k-th observation in group i, and $\tilde{X}_i$ is the median of group i. The resulting p-values (p_{BF}) test the null hypothesis of equal variances across aspect-ratio groups (Table A.3).

Beyond the omnibus test, pairwise Brown–Forsythe comparisons were conducted to identify which specific aspect-ratio groups differ in variance. This approach applies the same procedure to each group pair, allowing direct contrasts of dispersion between two aspect ratios at a time. For each comparison, the test statistic is evaluated along with its associated p-value (p_{BF}), and Holm-adjusted values are reported to control for multiple testing. The omnibus Brown–Forsythe results in Table A.3 indicate that the null hypothesis of equal variances is strongly rejected for all velocity components (u, v, and w) at $\alpha = 0.001$. This demonstrates that the variability (spread) of the velocity distributions differs significantly across aspect ratios for all components.

The pairwise comparisons further reveal component-dependent patterns of variance response. For the streamwise component (u), significant variance differences are observed between AR4 and both AR2.9 and AR2.5, whereas the AR2.9 vs. AR2.5 comparison is not significant. This indicates that variance changes in u are primarily associated with the largest aspect ratio (AR4), while the two smaller aspect ratios exhibit similar dispersion. For the transverse component (v), all pairwise comparisons are significant, indicating consistent variance differences across all aspect-ratio combinations. This suggests that the spread of transverse velocity responds sensitively and progressively to changes in aspect ratio. For the vertical component (w), all pairwise comparisons are also significant, with particularly strong contrasts involving AR2.5. This indicates that vertical velocity variability is strongly

influenced by aspect-ratio changes, especially when comparing the smallest aspect ratio to the others. Omnibus and pairwise tests together confirm both global and localized variance heterogeneity driven by aspect ratio under ice cover.

Table A.3. Brown–Forsythe variance test results for velocity components across aspect ratios (AR4, AR2.9, AR2.5). Reported are omnibus p-values and pairwise F-statistics with raw and Holm-adjusted p-values. Significance is evaluated at $\alpha = 0.001$. "S" denotes significant and "NS" denotes non-significant.

Omnibus (Brown–Forsythe)

Component	Comparison	p_{BF}	Call
u	All AR groups	$p < 0.001$	S
v	All AR groups	$p < 0.001$	S
w	All AR groups	$p < 0.001$	S

Pairwise comparisons

Component	AR Pair	F_{BF}	p_{BF}	$p_{\mathrm{BF,H}}$	Call
u	4 vs 2.9	1125	$p < 0.001$	$p < 0.001$	S
u	4 vs 2.5	1314	$p < 0.001$	$p < 0.001$	S
u^*	2.9 vs 2	≈ 0	0.9	0.9	NS
v	4 vs 2.9	27	$p < 0.001$	$p < 0.001$	S
v	4 vs 2.5	142	$p < 0.001$	$p < 0.001$	S
v	2.9 vs 2.5	41	$p < 0.001$	$p < 0.001$	S
w	4 vs 2.9	22	$p < 0.001$	$p < 0.001$	S
w	4 vs 2.5	452	$p < 0.001$	$p < 0.001$	S
w	2.9 vs 2.5	239	$p < 0.001$	$p < 0.001$	S

The pairwise comparisons further reveal component-dependent patterns of variance response. For the streamwise component (u), significant variance differences are observed between AR4 and both AR2.9 and AR2.5, whereas the AR2.9 vs. AR2.5 comparison is not significant. This indicates that variance changes in u are primarily associated with the largest aspect ratio (AR4), while the two smaller aspect ratios exhibit similar dispersion. For the transverse component (v), all pairwise comparisons are significant, indicating consistent variance differences across all aspect-ratio combinations. This suggests that the spread of transverse velocity responds sensitively and progressively to changes in aspect ratio. For the vertical component (w), all pairwise comparisons are also significant, with particularly strong contrasts involving AR2.5. This indicates that vertical velocity variability is strongly influenced by aspect-ratio changes, especially when comparing the smallest aspect ratio to the others. Omnibus and pairwise tests together confirm both global and localized variance heterogeneity driven by aspect ratio under ice cover.

Together, the convergence of evidence from multiple statistical approaches, distributional (Kruskal–Wallis, KS), central tendency (Cliff's δ, medians), and spread (Brown–Forsythe tests), indicates that modifications in aspect ratio induce statistically significant and component-specific changes in the statistical properties of turbulence. In particular, the w component appears most consistently responsive across all metrics, while the v component exhibits more selective sensitivity, and the u component shows pronounced spread-based differentiation. Although the magnitudes of these effects remain small, this pattern suggests a multidimensional alteration of turbulence structure in response to geometrical changes in the flow domain.

Chapter 8

Conclusions and Future Works

8.1 Study Summary and Remarks

Understanding secondary flow dynamics is fundamental for interpreting the processes governing riverine hydrodynamics and for predicting channel response to natural and anthropogenic changes. This is particularly critical in cold-region environments, where the presence of an ice cover fundamentally alters boundary conditions, turbulence structure, and sediment transport mechanisms. Despite its importance, the study of ice-covered flows remains limited due to the significant logistical challenges associated with field measurements during winter conditions, as well as the complexity of reproducing realistic ice-water interactions in controlled environments.

Traditional theoretical approaches, often adapted from open-channel flow assumptions, are insufficient to fully describe the hydrodynamics of ice-covered rivers. In particular, the assumption of a shear-free upper boundary fails under ice-covered conditions, where the ice layer introduces additional roughness and shear stresses that substantially modify velocity distributions and turbulence characteristics. Consequently, both field observations and laboratory experiments have been used to investigate ice-covered river hydraulics. While field studies provide valuable insight into natural river behaviour, laboratory flume experiments offer a controlled environment in which individual hydraulic parameters can be sys-

tematically varied, enabling the underlying physical mechanisms governing flow structure to be isolated and examined.

However, many previous experimental studies have focused on straight-channel configurations, which are suited for investigating flow in straight river reaches but do not capture the curvature-induced three-dimensional flow structures that develop in natural river bends. Secondary currents, which are strongly influenced by channel curvature, play a dominant role in sediment transport, momentum redistribution, and morphological evolution. Their behavior under ice-covered conditions cannot be reliably inferred from straight-channel analogues.

Furthermore, while Acoustic Doppler Velocimetry (ADV/ADVP) techniques are commonly employed due to their relative simplicity and cost-effectiveness, they are inherently limited to point-based or profile-based measurements. Such approaches are insufficient for resolving fully three-dimensional, spatially coherent flow structures such as secondary circulation cells that evolve across both space and time. In contrast, Particle Image Velocimetry (PIV) enables high-resolution, spatially distributed measurements of velocity fields, providing a continuum representation of flow behavior. This allows for a more reliable characterization of turbulence structures, vortex dynamics, and momentum transport processes, which are essential for understanding ice-covered river systems.

The present study addresses these limitations by systematically investigating the physics of secondary flow in an ice-covered meander bend using high-resolution PIV measurements. By isolating key governing parameters and examining their interactions, this research provides new insights into the mechanisms driving flow structure under combined effects of curvature and ice cover.

The main outcomes of this research and their contributions to the understanding of ice-covered river hydraulics are summarized as follows:

1. **High-resolution turbulence characterization in an ice-covered channel bend:** A detailed characterization of turbulence at the bend apex cross-section was conducted using high-frequency PIV measurements over extended sampling durations. This enabled reliable statistical convergence of mean and fluctuating flow quantities, including velocity components, Reynolds stresses, and turbulent ki-

netic energy distributions.

2. **Characterization of secondary circulation structure and vortex strength:** The study provides a detailed characterization of the secondary circulation structure in an ice-covered channel bend, revealing the organization, relative strength, and circulation characteristics of vortices in the ice-dominated and bed-influenced layers. These findings improve the understanding of how secondary circulation develops under different ice-covered conditions.

3. **Layer-wise analysis of flow structure and controls:** The study presents a comprehensive analysis of flow behavior within the dual-layer system formed by the bed and ice boundaries. The relative contributions of Reynolds stresses, turbulent kinetic energy, and mean flow curvature to the development of secondary currents are examined, providing a framework for estimating flow structure in the absence of detailed in situ measurements or high-fidelity numerical models.

4. **Momentum redistribution and boundary sensitivity analysis:** A systematic investigation of the sensitivity of momentum components (streamwise, transverse, and vertical) to boundary conditions and ice surface roughness was conducted, with emphasis on characterizing the role of these factors in governing momentum redistribution and the resulting organization of secondary flow structures.

5. **Development of a momentum ratio difference framework:** A simple momentum ratio difference approach was introduced to quantify the relative dominance of competing momentum transport mechanisms under varying boundary conditions. This framework provides a physically interpretable metric for assessing how ice cover modifies flow structure and energy redistribution.

6. **Assessment of flow parameter effects (Froude number, aspect ratio, and roughness):** The study systematically evaluated the influence of key flow and boundary parameters on turbulence distribution and secondary circulation. This analysis provides a framework for assessing how variations in flow conditions and boundary characteristics influence the development of secondary flow structures.

7. **Advancement of experimental methodologies for ice-covered flows:** This research demonstrated the effectiveness of PIV-based approaches for resolving

complex three-dimensional flow structures in ice-covered channels. The dataset generated represents one of the most detailed experimental investigations of secondary flow in ice-covered meander bends, addressing a critical gap in the literature.

Collectively, these contributions advance the current understanding of secondary flow processes in ice-covered river bends by explicitly linking variations in turbulence structure, momentum transport, and boundary condition effects. Because these factors govern the detailed physics of secondary flow processes, they provide a powerful framework for examining the controls on river flow and how these may vary temporally and spatially at a given site.

8.2 Key Findings

The analytical frameworks developed in this study provide a strong foundation for clarifying flow dynamics in cold-region river systems. By integrating high-resolution experimental measurements with turbulence energy analyses, this research contributes to a more comprehensive understanding of flow behavior under ice-covered conditions. The key findings are summarized below, followed by recommendations for future research.

8.2.1 Effect of Flow Rate (Froude Number)

This study examined the impact of varying flow rate conditions at the same apex cross-section of a fixed channel bend, with particular emphasis on bulk velocity variations under a constant flow depth. All experimental conditions were maintained within the turbulent flow regime, as laminar conditions do not adequately represent riverine processes and fail to capture the turbulence-driven mechanisms responsible for secondary flow formation. In laminar flow, momentum transfer is governed by molecular viscosity, resulting in smooth, layered motion with limited cross-sectional interaction. In contrast, turbulent flow enables momentum redistribution through Reynolds stresses, which is essential for the development of secondary circulation structures.

The key findings are as follows:

1. A distinct two-layer structure, with the top layer linked to the ice cover and the bottom layer associated with the bed, was evident under all flow conditions, with the secondary circulation moving from the inner to the outer bank at mid-depth, and in the opposite direction near the top and bottom walls.

2. At the highest flow rate, the bed-layer circulation represented the dominant vortex within the cross-section and is the strongest among all tested conditions. Within the ice layer, two vortices of comparable strength were observed, with the inner-bank vortex slightly exceeding the central vortex.

3. At the intermediate flow rate (25% reduction in discharge), the bed-layer circulation decreased significantly, exhibiting a reduction exceeding 80%. In the ice layer, the inner-bank vortex weakened by more than 50%, whereas the central circulation cell remained comparable to its magnitude under high-flow conditions, becoming the dominant structure in this regime.

4. At the lowest flow rate (greater than 50% reduction in Froude number), the bed-layer circulation weakened further by more than 58%. Additionally, a secondary, weaker vortex emerged, indicating the onset of flow structure fragmentation within the bed region.

5. The number and spatial distribution of high vorticity cores (HVCs) varied systematically with changes in secondary flow structure, reflecting the strong coupling between circulation intensity and localized rotational features.

6. The normalized mean kinetic energy (MKE), evaluated using the 90th percentile values across each flow condition, increased as flow rate decreased. Peak values rised from $\mathrm{MKE} = 1.7$ under high-flow conditions to $\mathrm{MKE} = 2.72$ in the low-flow case, indicating a relative intensification of organized flow structures at lower velocities.

7. Despite exhibiting the lowest absolute turbulent kinetic energy (TKE), the low-flow case showed the highest relative TKE distribution across the cross-section, suggesting more spatially coherent and dynamically significant turbulence relative to the mean flow under reduced discharge conditions.

8. Analysis of Reynolds stresses revealed that τ_{uw} in the bed layer consistently exhibited strong positive values, indicating upward momentum transfer from the bed toward the ice cover. In contrast, the ice layer showed weaker and often negative values, corresponding to downward momentum flux.

9. The distribution of τ_{vw} demonstrated an expansion of regions characterized by negative (downward) lateral–vertical momentum flux as flow rate decreased. This indicates an enhanced transfer of lateral momentum from the ice layer toward the bed, coinciding with a reduction in the effectiveness of bed-layer circulation in sustaining transverse momentum transport.

10. The turbulent structure parameter a_1 exhibited its highest values under high-flow conditions. As flow rate decreased, both the magnitude and spatial extent of elevated a_1 values diminished, indicating a reduction in turbulence anisotropy and structural intensity.

Collectively, these findings demonstrate that reductions in flow rate lead to significant reorganization of both turbulence structure and secondary circulation. In particular, weaker bed-layer circulation, enhanced relative turbulence intensity, and altered momentum exchange mechanisms contribute to a fundamentally different flow structure under lower Froude number conditions.

8.2.2 Effect of Ice Roughness (Boundary Conditions)

Secondly, the influence of ice cover roughness on velocity and momentum distribution at the bend apex cross-section of the channel was examined. Surface roughness significantly alters velocity profiles and turbulence intensity beneath the ice covered flow, and the relative roughness between the bed and ice changes turbulence structure and secondary currents. The sensitivity of momentum components in different directions within both the ice and bed layers to the changes in ice cover roughness was investigated. The flow rate was kept constant to isolate the response solely due to roughness variation.

The key findings were as follows:

1. Under the smooth ice cover, two vortices formed in the upper layer: a primary vortex

and a strong inner-bank cell. However, with increasing ice roughness, the inner-bank cell and the center vortex merged to form a single primary vortex that shifted closer to the inner bank, and the total circulation in the ice layer decreased by 42% under rough ice conditions.

2. In contrast, the counter-rotating circulation in the bottom layer increased from the smooth- to the rough-case. The vertical position of the primary vortex center in the ice layer shifted downward, with a 5.6% reduction in height, extending the ice-influenced layer and compressing the bed layer. This resulted in a 4.9% reduction in the height of bed vortices and a 57% increase in its strength.

3. To account for asymmetric boundary roughness, the channel was modeled as a closed rectangular duct, and a composite equivalent sand-roughness height was computed using a perimeter-weighted approach. The equivalent roughness height yielded $k_{s,eq} \approx 4.03\times10^{-5}\ \mathrm{m}$ for the smooth-ice case and $k_{s,eq} \approx 1.92\times10^{-3}\ \mathrm{m}$ for the rough-ice case, corresponding to relative roughness values of $k_{s,eq}/D_h \approx 4.37\times10^{-4}$ and 2.09×10^{-2}, respectively. The resulting friction factors were $f \approx 0.031$ for the smooth-ice case and $f \approx 0.053$ for the rough-ice case, indicating increased flow resistance due to larger roughness elements.

4. Vector fields of transverse circulation under smooth and rough ice covers illustrated a downward displacement of the maximum transverse velocity near the inner bank, which gradually shifted upward toward mid-depth around the channel center and outer bank.

5. Vertical profiles of cross-stream velocity (V) at selected lateral positions, together with transverse circulation vector fields, showed that the peak transverse velocity increased from the inner bank ($y/y_{max} \approx 0.10$) to mid-channel (≈ 0.50) and then decreased toward the outer bank. Higher peak values were consistently observed under rough ice conditions, indicating that surface roughness intensifies secondary circulation.

6. Momentum distribution under each ice cover showed that, under rough ice conditions, momentum fluxes intensified at the channel center and particularly near the inner bank in all three directions, most notably in the streamwise and vertical directions. In the cross-stream direction (M_y), both positive (outer-bankward) and negative (inner-bankward) momentum regions extended downward toward the bed near the inner bank.

7. Layered momentum comparisons indicated that rough ice cover led to consistent increases in streamwise momentum (M_x) across both layers.

8. The positive cross-stream layered momentum (M_y^+) increased significantly for rough ice cover, particularly in the bottom layer (14.4%) and across the full cross-section (11.8%). The negative component (M_y^-) showed less uniform behavior, with a 36.8% reduction in magnitude in the top layer and a 1.9% increase in magnitude in the bottom layer.

9. In the vertical direction, the positive momentum (M_z^+) increased substantially (62.4% in the top layer and 12.0% in the bottom layer), while the negative vertical momentum (M_z^-) intensified in magnitude by 120.1% and 121.7% in the top and bottom layers, respectively.

10. The total momentum (M_t) increased modestly, with a greater increase (4.8%) in the bottom layer, indicating that roughness enhances both horizontal and vertical momentum transport; a pattern suggesting that roughness not only amplifies momentum exchange but also modifies the spatial configuration of secondary circulation.

11. To evaluate the statistical significance of layered momentum differences, the Mann-Whitney U test (Wilcoxon rank-sum test) was applied. The results confirmed statistically significant differences in momentum distributions between smooth and rough ice conditions across all directions (streamwise, cross-stream, and vertical) and across all vertical layers (top, bottom, and full depth), reinforcing the strong influence of ice roughness on flow structure.

12. The rough-to-smooth momentum ratio analysis showed that the streamwise ratio remains close to unity across most of the cross-section, indicating minimal change in downstream momentum.

13. In contrast, the cross-stream momentum ratio exhibited both positive and negative regions. Two narrow horizontal bands of negative ratios appeared near $z/z_{max} \approx 0.2$ and 0.8, while the remaining regions showed positive ratios. These patterns indicated zones where both smooth and rough conditions generate inward momentum, as well as regions where roughness amplified outward momentum, particularly in the central zone ($0.25 < y/y_{max} < 0.95$ and $0.25 < z/z_{max} < 0.7$).

14. Vertical momentum ratios displayed a mixed distribution, with regions exceeding unity extending downward from the inner bank, corresponding to vortex locations

identified under smooth ice conditions. These regions indicated enhanced vertical motion under rough ice, while negative ratios represented local reversals in vertical momentum direction.

The directional sensitivity of momentum highlights the critical role of ice-cover roughness in governing momentum redistribution and flow structure in ice-covered channels. This behavior reinforces the need to explicitly incorporate roughness-driven turbulence effects when analyzing and modeling secondary flow dynamics under ice-covered conditions.

8.2.3 Effect of Aspect Ratio (flow width-to-hight)

The same analytical approach was used to examine different width-to-height aspect ratio scenarios for the ice-covered bend channel based on the PIV data. The flow cases were conducted under identical ice-cover and bulk velocity conditions, with variations only in flow depth. This analysis aimed to evaluate changes in secondary flow strength and structure across different aspect ratios by analyzing velocity distribution, shear-layer interactions related to confinement effects, and spatial patterns of turbulence intensity and Reynolds shear stresses across the bend cross-section.

The key findings were as follows:

1. While the omnibus Kruskal–Wallis tests indicated that all three velocity components exhibited statistically significant differences among aspect ratios at a conservative significance level ($\alpha = 0.001$), post-hoc pairwise comparisons revealed a component-dependent response to aspect-ratio variation. For the streamwise (u) and vertical (w) velocities, all pairwise contrasts between AR4, AR2.9, and AR2.5 were statistically significant ($p < 0.001$). In contrast, the transverse velocity (v) showed significant differences between AR4 and both smaller aspect ratios, while the AR2.9–AR2.5 comparison was not statistically significant, suggesting convergence of transverse flow behavior at lower ratios.

2. The application of several spatial filtering techniques (i.e., median filtering, Gaussian smoothing, and spectral low-pass filtering) to the instantaneous velocity fields

revealed only weak and fragmented features associated with secondary flow, without coherent large-scale vortices. This indicated that secondary flow structures were largely obscured by turbulence in instantaneous snapshots.

3. Using a vortex-detection method, secondary circulation structures were identified from the temporally averaged velocity fields, with a distinct two-layer circulation pattern observed in all cases.

4. The strength, number, and distribution of secondary flow vortices varied with flow height, with increased circulation observed at lower aspect ratios.

5. Analysis of the temporally averaged transverse velocity profiles showed that, although the general shape of the profiles remained consistent across all cases, the strength, vertical distribution, and asymmetry of the profiles changed noticeably as the aspect ratio decreased. This reflected the evolving balance between the ice-layer secondary circulation and the bed-layer counter-rotating vortex.

6. Examination of the vertical position of maximum streamwise velocity demonstrated that, for all aspect ratios, the peak velocity occurred near the upper region of the flow close to the inner bank and remained near or above mid-depth toward the outer bank.

7. The time-averaged streamwise velocity distribution showed that the peak velocity was located near the upper portion of the flow close to the inner bank, while a relatively low-velocity region (or "dead zone") was observed within the mid-depth range ($0.3 < z/z_{max} < 0.75$) near the inner bank ($n/n_{max} < 0.25$). This region corresponded to the interface between two vertically stacked circulation cells.

8. With decreasing aspect ratio, the spatial extent of regions with elevated mean kinetic energy (MKE) increased. Although the highest aspect-ratio case (AR4.0) exhibited the largest local MKE values, these were confined to a smaller region, whereas lower aspect-ratio cases showed a broader distribution of elevated MKE.

9. In contrast, the AR4.0 case exhibited the highest turbulent kinetic energy (TKE) across much of the cross-section.

10. A general spatial separation between MKE- and TKE-dominated regions was observed, indicating that zones of strong mean secondary circulation did not necessarily coincide with regions of maximum turbulence intensity. This suggested a redistribution of energy between organized mean motion and turbulent fluctuations as secondary flow structures interacted with the bed and ice boundaries.

11. Reynolds shear stress components exhibited a clear dependence on aspect ratio in both magnitude and spatial organization. Higher aspect ratios showed more localized shear stress concentrations near the boundaries, whereas lower aspect ratios exhibited more distributed momentum transport across the cross-section.

12. These trends indicated that, as flow depth decreased, turbulent momentum exchange played an increasingly important role in mediating interactions between secondary circulation, boundary layers, and the mean flow.

These results demonstrated that aspect ratio plays a fundamental role in controlling the spatial organization of secondary vortices, their circulation strength, turbulence distribution, and momentum exchange within ice-covered channel bends. This is particularly important as river flow depth can vary due to seasonal changes, ice formation, or hydraulic regulation, thereby exerting a strong influence on flow structure, sediment transport processes, and channel stability under confined conditions.

8.3 Recommendations for Future Work

While this study provides detailed and important insights into the behavior of ice-covered flow in bend channels, river turbulence remains a highly complex phenomenon with many interacting processes that extend beyond the scope of this study. Building on the findings presented herein, there remain several meaningful opportunities for further research to expand and refine the understanding of these systems.

The following areas are identified as primary directions for future work:

1. Investigation of transient and unsteady flow conditions is recommended to better represent the temporal variability inherent in natural river systems, including fluctuations in discharge and flow acceleration effects.

2. Inclusion of ice formation and breakup processes would provide a more complete representation of seasonal river ice dynamics, particularly in capturing evolving boundary conditions and their impact on flow structure.

3. Inclusion of ice cover roughness variations in concert with changes in bed and sidewall roughness would enable a more comprehensive representation of seasonal river ice dynamics in both space and time, particularly by capturing evolving boundary conditions and their influence on flow structure.

4. Extension of the experimental framework to mobile-bed conditions is necessary to evaluate the coupling between secondary flow structures and sediment transport processes, including erosion, deposition, and bedform evolution.

5. Investigation of the influence of channel curvature (e.g., varying bend radius and curvature ratios) is recommended to further isolate the interaction between geometric forcing and ice-induced boundary effects on secondary flow development.

6. Analysis of multiple cross-sections along the bend is recommended to capture the spatial evolution of flow structures and to better understand the development and interaction of secondary circulation mechanisms throughout the channel.

7. Further development of momentum-based analytical frameworks, incorporating different cross-sectional geometries and boundary configurations, would enhance predictive modeling capabilities for ice-covered river systems, particularly under varying roughness and confinement conditions.

8. Examination of larger-scale laboratory setups and field-based measurements is required to assess the scalability of the present findings and to account for natural variability in channel geometry, roughness, and ice conditions.

9. Integration of high-resolution experimental data with advanced numerical modeling approaches (e.g., RANS, LES, or DNS) would allow for deeper investigation of turbulence anisotropy, vortex dynamics, and momentum transfer mechanisms across scales.

Advancing these areas will not only improve the fundamental understanding of secondary flow processes under ice-covered conditions but will also enhance the reliability of predictive tools used in cold-region hydraulic engineering. Ultimately, such efforts will contribute to more informed management and design of river systems in environments where ice plays a dominant role in shaping flow behavior.

Bibliography

[1] R. J. Adrian. Particle-imaging techniques for experimental fluid mechanics. *Annual Review of Fluid Mechanics*, 23:261–304, 1991.

[2] Ronald J. Adrian and Jerry Westerweel. *Particle Image Velocimetry: A Practical Guide*. Cambridge University Press, Cambridge, UK, 2nd edition, 2011.

[3] S. G. Aghaji Zare, S. A. Moore, C. D. Rennie, O. Seidou, H. Ahmari, and J. Malenchak. Boundary shear stress in an ice-covered river during breakup. *J. Hydraul. Eng.*, 142:04015065, 2016.

[4] M. Amir, V. Nikora, and M. Stewart. Pressure forces on sediment particles in turbulent open-channel flow: A laboratory study. *Journal of Fluid Mechanics*, 2014.

[5] G. D. Ashton. River ice. *Annual Review of Fluid Mechanics*, 10(1):369–392, 1978.

[6] G. D. Ashton. *River and lake ice engineering*. Water Resources Publication, 1986.

[7] H. T. Barnes. The science of ice engineering. *The Scientific Monthly*, 29(4):289–297, 1929.

[8] S. Beltaos. A conceptual model of river ice breakup. *Canadian Journal of Civil Engineering*, 11(3):516–529, 1984.

[9] S. Beltaos. Hydraulic roughness of breakup ice jams. *Journal of Hydraulic Engineering*, 127(8):650–656, 2001.

[10] Spyros Beltaos. *River Ice Breakup*. Water Resources Publications, 2008.

[11] Spyros Beltaos, editor. *River Ice Formation*. Committee on River Ice Processes and the Environment, Canadian Geophysical Union Hydrology Section, Edmonton, Alberta, Canada, 2013.

[12] K. E. Bennett and T. D. Prowse. Northern hemisphere geography of ice-covered rivers. *Hydrological Processes*, 24(2):235–240, 2010.

[13] S. J. Beresh. Time-resolved particle image velocimetry. *Measurement Science and Technology*, 2021.

[14] P. M. Biron, T. Buffin-Bélanger, and N. Martel. Three-dimensional turbulent structures at a medium-sized confluence with and without an ice cover. *Earth Surface Processes and Landforms*, 44(15):3042–3056, 2019.

[15] K. Blanckaert. Saturation of curvature-induced secondary flow, energy losses, and turbulence in sharp open-channel bends. *Journal of Geophysical Research: Earth Surface*, 114, 2009.

[16] K. Blanckaert. Flow separation at convex banks in open channels. *Journal of Fluid Mechanics*, 779:432–467, 2015.

[17] K. Blanckaert and H. J. de Vriend. Nonlinear modeling of mean flow redistribution in curved open channels. *Water Resources Research*, 39(12):1345, 2003.

[18] K. Blanckaert and H. J. De Vriend. Secondary flow in sharp open-channel bends. *Journal of Fluid Mechanics*, 498:353–380, 2004.

[19] K. Blanckaert and H. J. De Vriend. Turbulence characteristics in sharp open-channel bends. *Physics of Fluids*, 17(5), 2005.

[20] K. Blanckaert and H. J. De Vriend. Meander dynamics: A nonlinear model without curvature restrictions for flow in open-channel bends. *Journal of Geophysical Research: Earth Surface*, 115(F4), 2010.

[21] K. Blanckaert, A. Duarte, Q. Chen, and A. J. Schleiss. Flow processes near smooth and rough (concave) outer banks in curved open channels. *Journal of Geophysical Research: Earth Surface*, 117(F4), 2012.

[22] K. Blanckaert and W. H. Graf. Momentum transport in sharp open-channel bends. *Journal of Hydraulic Engineering*, 130(3):186–198, 2004.

[23] K. Blanckaert, M. G. Kleinhans, S. J. McLelland, W. S. J. Uijttewaal, B. J. Murphy, A. van de Kruijs, D. R. Parsons, and Q. Chen. Flow separation at the inner (convex) and outer (concave) banks of constant-width and widening open-channel bends. *Earth Surface Processes and Landforms*, 38(7):696–716, 2013.

[24] Koen Blanckaert. Saturation of curvature-induced secondary flow, energy losses, and turbulence in sharp open-channel bends: Laboratory experiments, analysis, and modeling. *Journal of Geophysical Research: Earth Surface*, 114(F3), 2009.

[25] Koen Blanckaert and Walter H. Graf. Mean flow and turbulence in open-channel bend. *Journal of Hydraulic Engineering*, 127(10):835–847, 2001.

[26] S. Bolton and J. Schellberg. Ecological issues in floodplains and riparian corridors. Technical report, University of Washington, 2001.

[27] D. I. Bray and K. S. Davar. Resistance to flow in gravel-bed rivers. *Canadian Journal of Civil Engineering*, 14(1):77–86, 1987.

[28] S. M. Cameron. Theoretical description of piv measurement errors. *Acta Geophysica*, 70(5):2379–2387, 2022.

[29] T. Carstens. Hydraulics of river ice. *La Houille Blanche*, 54(4):271–284, 1968.

[30] W. Y. Chang, G. Constantinescu, W. F. Tsai, and H. C. Lien. Coherent structure dynamics and sediment erosion mechanisms around an in-stream rectangular cylinder at low and moderate angles of attack. *Water Resources Research*, 47(12), 2011.

[31] T. Cheng, J. Wei, J. Ni, J. Wang, H. Lu, K. Cheng, and H. Fu. The impact of ice on river morphology and hydraulic structures: A review. *Water*, 17(4):480, 2025.

[32] Cyril Frank Colebrook, T. Blench, H. Chatley, E. H. Essex, J. R. Finniecome, G. Lacey, J. Williamson, and G. G. Macdonald. Correspondence. turbulent flow in pipes, with particular reference to the transition region between the smooth and rough pipe laws (includes plates). *Journal of the Institution of Civil Engineers*, 12(8):393–422, 1939.

[33] G. Constantinescu, S. Kashyap, T. Tokyay, C. D. Rennie, and R. D. Townsend. Hydrodynamic processes and sediment erosion mechanisms in an open channel bend of strong curvature with deformed bathymetry. *Journal of Geophysical Research: Earth Surface*, 118(2):480–496, 2013.

[34] M. J. Crance and Kelly M. Frothingham. The impact of ice cover roughness on stream hydrology. In *Proceedings of the 65th Eastern Snow Conference*, 2008.

[35] T. R. Davies and A. J. Sutherland. Extremal hypotheses for river behavior. *Water Resources Research*, 19(1):141–148, 1983.

[36] H. J. De Vriend. Velocity redistribution in curved rectangular channels. *Journal of Fluid Mechanics*, 107:423–439, 1981.

[37] W. R. Dean and J. M. Hurst. Note on the motion of fluid in a curved pipe. *Mathematika*, 6(1):77–85, 1959.

[38] S. Demers, T. Buffin-Bélanger, and A. G. Roy. Helical cell motions in a small ice-covered meander river reach. *River Research and Applications*, 27(9):1118–1125, 2011.

[39] S. L. Dingman. Analytical derivation of at-a-station hydraulic–geometry relations. *Journal of Hydrology*, 334(1–2):17–27, 2007.

[40] S. L. Dingman and S. Afshari. Field verification of analytical at-a-station hydraulic–geometry relations. *Journal of Hydrology*, 564:859–872, 2018.

[41] E. N. Dolgopolova. Energy losses and hydraulic friction of open and ice-covered river flow. *Power Technology and Engineering*, 45(1):17–24, 2011.

[42] Franz Durst. Turbulent flows. In *Fluid Mechanics*, Graduate Texts in Physics, chapter 19. Springer, Berlin, Heidelberg, 2022.

[43] S. Ebrahimi, A. Mohammadian, and C. D. Rennie. Roughness influence on secondary circulation and momentum distribution in an ice-covered river bend. *Physics of Fluids*, 38(2), 2026.

[44] S. Ebrahimi, C. D. Rennie, A. Mohammadian, and H. K. Schreiner. Secondary flow dynamics and turbulence in an ice-covered sharp bend channel at different subcritical froude numbers. *Environmental Fluid Mechanics*, 26(2):13, 2026.

[45] F. Engelund. Flow and bed topography in channel bends. *Journal of the Hydraulics Division*, 100:1631–1648, 1974.

[46] E. O. Engmann. Turbulent diffusion in channels with a surface cover. *Journal of Hydraulic Research*, 15(4):327–335, 1977.

[47] R. Ettema. Review of alluvial-channel responses to river ice. *Journal of Cold Regions Engineering*, 16(4):191–217, 2002.

[48] R. Ettema and H. P. Huang. Ice formation in frequently transited navigation channels. Technical Report CRRELSB9040, Cold Regions Research and Engineering Laboratory (CRREL), 1990.

[49] R. I. Ferguson. Flow resistance equations for gravel- and boulder-bed streams. *Water Resources Research*, 43(5):W05427, 2007.

[50] Robert W. Fox, Alan T. McDonald, and John W. Mitchell. *Fox and McDonald's Introduction to Fluid Mechanics*. John Wiley & Sons, 2020.

[51] A. H. Frazier. Effects of ice on the flow of the upper mississippi river. *Eos, Transactions American Geophysical Union*, 15(2):421–427, 1934.

[52] I. Fujita, M. Muste, and A. Kruger. Large-scale particle image velocimetry for flow analysis in hydraulic engineering applications. *Journal of Hydraulic Research*, 36(3):397–414, 1998.

[53] L. Graftieaux, M. Michard, and N. Grosjean. Combining piv, pod and vortex identification algorithms for the study of unsteady turbulent swirling flows. *Measurement Science and Technology*, 12(9):1422, 2001.

[54] F.R. Hauer, H. Locke, V.J. Dreitz, et al. Gravel-bed river floodplains are the ecological nexus of glaciated mountain landscapes. *Science Advances*, 2(6), 2016.

[55] Valentin Heller. Self-similarity and reynolds number invariance in froude modelling. *Journal of Hydraulic Research*, 2017.

[56] R. D. Hey. Geometry of river meanders. *Nature*, 262(5568):482–484, 1976.

[57] Faye Hicks and Spyros Beltaos. River ice. In *Cold Region Atmospheric and Hydrologic Studies. The Mackenzie GEWEX Experience: Volume 2: Hydrologic Processes*, pages 281–305. Springer Berlin Heidelberg, Berlin, Heidelberg, 2008.

[58] W. G. Hoyt. The effects of ice on stream flow. Technical Report Water-Supply Paper 337, U.S. Geological Survey, Washington, DC, 1913.

[59] P. Hu and M. Yu. Experimental study of secondary flow in narrow and sharp open-channel bends. *Journal of Applied Fluid Mechanics*, 16(9):1767–1777, 2023.

[60] S. Ikeda, G. Parker, and K. Sawai. Self-formed straight channels in sandy beds. *Journal of Fluid Mechanics*, 112:363–377, 1981.

[61] Monica Ionita, Lena M. Tallaksen, Daniel G. Kingston, James H. Stagge, Gregor Laaha, Henny A. J. Van Lanen, Patrick Scholz, Silvia M. Chelcea, and Klaus Haslinger. The european 2015 drought from a climatological perspective. *Hydrology and Earth System Sciences*, 21(3):1397–1419, 2017.

[62] E. C. Jamieson, C. D. Rennie, and R. D. Townsend. Turbulence and vorticity in a laboratory channel bend at equilibrium clear-water scour with and without stream barbs. *Journal of Hydraulic Engineering*, 139(3):259–268, 2013.

[63] Maria Kämäri, O. lotsberg, J. Lindgren, J. Turunen, T. Hölttä, and J. Räisänen. Spatial variation of river-ice thickness in a meandering river. *Cold Regions Science and Technology*, 137:17–29, 2017.

[64] S. Kashyap, G. Constantinescu, C. D. Rennie, G. Post, and R. Townsend. Influence of channel aspect ratio and curvature on flow, secondary circulation, and bed shear stress in a rectangular channel bend. *Journal of Hydraulic Engineering*, 138(12):1045–1059, 2012.

[65] D. W. Knight and K. Shiono. Turbulence measurements in a shear layer region of a compound channel. *Journal of Hydraulic Research*, 28(2):175–196, 1990.

[66] Nikolay I. Kolev. Solubility of o_2, n_2, h_2 and co_2 in water. In *Multiphase Flow Dynamics 3: Turbulence, Gas Absorption and Release, Diesel Fuel Properties*, pages 185–214. Springer Berlin Heidelberg, Berlin, Heidelberg, 2007.

[67] A. N. Kolmogorov. The local structure of turbulence in incompressible viscous fluid for very large reynolds numbers. *Proceedings of the Royal Society of London. Series A: Mathematical and Physical Sciences*, 434(1890):9–13, 1991.

[68] N. E. Kotsovinos. Secondary currents in straight wide channels. *Applied Mathematical Modelling*, 12(1):22–24, 1988.

[69] B. Koyuncu and T. B. Le. On the impacts of ice cover on flow profiles in a bend. *Water Resources Research*, 58(9):e2021WR031742, 2022.

[70] B. Koyuncu and T. B. Le. Modelling shear stress distribution in ice-covered streams. *Geological Society, London, Special Publications*, 540(1):SP540–2022, 2024.

[71] Sedem Kumahor and Mark F. Tachie. Effects of streamwise aspect ratio on the spatio-temporal characteristics of flow around rectangular cylinders. *International Journal of Heat and Fluid Flow*, 101:109133, 2023.

[72] M. R. Leeder and P. H. Bridges. Flow separation in meander bends. *Nature*, 253(5490):338–339, 1975.

[73] L. B. Leopold and M. G. Wolman. River channel patterns. In *Rivers and River Terraces*, pages 197–237. Palgrave Macmillan UK, London, 1970.

[74] L.B. Leopold, M.G. Wolman, and J.P. Miller. *Fluvial Processes in Geomorphology*. W.H. Freeman, 1964.

[75] G. Li, J. Sui, and S. Sediqi. Hydrodynamic characteristics in pools with leafless vegetation under ice-covered flow conditions—an experimental study and numerical simulation. *Journal of Hydrology*, 657:133135, 2025.

[76] Samuel Li. Field estimates of hydraulic resistance of ice-covered rivers. *Advanced Materials Research*, 250:3880–3883, 2011.

[77] Y. Li, X. Wang, B. Zhou, S. Yuan, and S. K. Tan. Dean instability and secondary flow structure in curved rectangular ducts. *International Journal of Heat and Fluid Flow*, 68:189–202, 2017.

[78] Q. Liu, W. Chen, L. Hu, H. Xie, and X. Fu. Experimental investigation of cavity stability for a gas-jet penetrating into a liquid sheet. *Physics of Fluids*, 27(8):082106, 2015.

[79] Y. Liu, C. Wang, Y. Qian, and X. Sun. Uncertainty analysis of PIV measurements in bubbly flows considering sampling and bubble effects with ray optics modeling. *Nuclear Engineering and Design*, 364:110677, 2020.

[80] F. Lopez and M. H. García. Wall similarity in turbulent open-channel flow. *Journal of Engineering Mechanics*, 125(7):789–796, 1999.

[81] Henry B. Mann and Donald R. Whitney. On a test of whether one of two random variables is stochastically larger than the other. *The Annals of Mathematical Statistics*, 18(1):50–60, 1947.

[82] A. Masullo and R. Theunissen. On dealing with multiple correlation peaks in PIV. *Experiments in Fluids*, 59(5):89, 2018.

[83] B. McFee. *Digital Signals Theory*. Chapman and Hall/CRC, 2023.

[84] Q. Mei, P. Zhang, Y. Wang, S. Liu, and J. Hu. Evolution of turbulent-structure scale distribution in decelerating open-channel flow. *Water*, 18(7):815, 2026.

[85] B. Michel and R. O. Ramseier. Classification of river and lake ice. *Canadian Geotechnical Journal*, 8(1):36–45, 1971.

[86] Emmanuel Mignot, Wei Cai, and Nicolas Riviere. Analysis of the transitions between flow patterns in open-channel lateral cavities with increasing aspect ratio. *Environmental Fluid Mechanics*, 19(1):231–253, 2019.

[87] M. Muste, F. Braileanu, and R. Ettema. Flow and sediment transport measurements in a simulated ice-covered channel. *Water Resources Research*, 36(9):2711–2720, 2000.

[88] M. Muste, F. Braileanu, and R. Ettema. Flow and sediment transport measurements in a simulated ice-covered channel. *Water Resources Research*, 36(9):2711–2720, 2000.

[89] M. Muste, D. A. Lyn, D. Admiraal, R. Ettema, V. Nikora, and M. H. Garcia. *Experimental Hydraulics: Methods, Instrumentation, Data Processing and Management: Volume I: Fundamentals and Methods*. CRC Press, 2017.

[90] D. Naot. Response of channel flow to roughness heterogeneity. *Journal of Hydraulic Engineering*, 110(11):1568–1587, 1984.

[91] G. Nasif, R. Balachandar, and R. M. Barron. Supercritical flow characteristics in smooth open channels with different aspect ratios. *Physics of Fluids*, 32(10), 2020.

[92] I. Nezu and H. Nakagawa. *Turbulence in Open Channels*. IAHR/AIRH Monograph, Balkema, Rotterdam, The Netherlands, 1993.

[93] I. Nezu, A. Tominaga, and H. Nakagawa. Field measurements of secondary currents in straight rivers. *Journal of Hydraulic Engineering*, 119(5):598–614, 1993.

[94] Iehisa Nezu. Open-channel flow turbulence and its research prospect in the 21st century. *Journal of Hydraulic Engineering*, 131(4):229–246, 2005.

[95] B. Nyantekyi-Kwakye, E. E. Essel, K. Dow, S. P. Clark, and M. F. Tachie. Hydraulic and turbulent flow characteristics beneath a simulated partial ice-cover. *Journal of Hydraulic Research*, 59(3):392–403, 2021.

[96] Alan V. Oppenheim and Ronald W. Schafer. *Discrete-Time Signal Processing*. Prentice Hall, Upper Saddle River, NJ, 3rd edition, 2009.

[97] J.J. Opperman, P.B. Moyle, E.W. Larsen, and J.L. Florsheim. *Floodplains: Processes and Management for Ecosystem Services*. University of California Press, 2017.

[98] S.W. Park and J. Ahn. Experimental and numerical investigations of primary flow patterns and mixing in laboratory meandering channel. *Smart Water*, 4, 2019.

[99] G. Parker. On river meanders. *Journal of Fluid Mechanics*, 52:513–529, 1971.

[100] H. J. Perkins. The formation of streamwise vorticity in turbulent flow. *Journal of Fluid Mechanics*, 44(4):721–740, 1970.

[101] M. Peters, S. P. Clark, K. Dow, J. Malenchak, and D. Danielson. Flow characteristics beneath a simulated partial ice cover: Effects of ice and bed roughness. *Journal of Cold Regions Engineering*, 32(1):04017017, 2018.

[102] Mitchel Peters, Mark Loewen, Tyler Heisel, and Faye Hicks. Experimental investigation of the flow characteristics beneath partial ice covers. *Cold Regions Science and Technology*, 142:69–78, 2017.

[103] Stephen B. Pope. *Turbulent Flows*. Cambridge University Press, Cambridge, UK, 2000.

[104] Stephen B. Pope. Turbulent flows. *Measurement Science and Technology*, 12(11):2020–2021, 2001.

[105] B. Pradhan, S. Pradhan, and K. Khatua. Experimental investigation of three-dimensional flow dynamics in a laboratory-scale meandering channel. *Ocean Engineering*, 2024.

[106] L. Prandtl. *Essentials of Fluid Dynamics: Authorized Translations*. Blackie & Son, 1949.

[107] A. K. Prasad. Stereoscopic particle image velocimetry. *Experiments in Fluids*, 29:103–116, 2000.

[108] P. Prinos, R. Townsend, and S. Tavoularis. Structure of turbulence in compound channel flows. *Journal of Hydraulic Engineering*, 111(9):1246–1261, 1985.

[109] T. D. Prowse and S. Beltaos. Climatic control of river-ice hydrology: A review. *Hydrological Processes*, 16(4):805–822, 2002.

[110] T. D. Prowse, B. R. Bonsal, C. R. Duguay, and M. P. Lacroix. River-ice break-up/freeze-up: a review of climatic drivers, historical trends and future predictions. *Annals of Glaciology*, 46:443–451, 2007.

[111] M. S. Quraishy. The origin of curves in rivers. *Current Science*, 13(2):36–39, 1944.

[112] M. Raffel, C. E. Willert, S. T. Wereley, and J. Kompenhans. *Particle Image Velocimetry: A Practical Guide*. Springer Berlin Heidelberg, 2007.

[113] Markus Raffel, Christian E. Willert, Fulvio Scarano, Christian J. Kähler, Steven T. Wereley, and Jürgen Kompenhans. *Particle Image Velocimetry: A Practical Guide*. Springer, 3rd edition, 2018.

[114] S. E. Rantz. *Measurement and Computation of Streamflow, Volume 1: Measurement of Stage and Discharge*. U.S. Geological Survey, 1981.

[115] A. Robert and T. Tran. Mean and turbulent flow fields in a simulated ice-covered channel with a gravel bed: Some laboratory observations. *Earth Surface Processes and Landforms*, 37(9):951–956, 2012.

[116] S. Roy, K. Barman, V. K. Das, K. Debnath, and B. S. Mazumder. Experimental investigation of undercut mechanisms of river bank erosion based on 3d turbulence characteristics. *Environmental Processes*, 7:341–366, 2020.

[117] I. L. Rozovskii. *Flow of water in bends of open channels*. Academy of Sciences of the Ukrainian SSR, 1957. Israel Program for Scientific Translations, Trans., 1961.

[118] Fulvio Scarano. Tomographic piv: principles and practice. *Measurement Science and Technology*, 24(1), 2013.

[119] H. Schlichting and K. Gersten. *Boundary-Layer Theory*. McGraw-Hill, New York, 7 edition, 1979. Chapters 14 and 20; edited by J. Kestin.

[120] H. K. Schreiner, A. Mohammadian, and C. D. Rennie. Machine learning and parametrisation of multi-cell structures of secondary circulation in a tight open channel bend using les. *Engineering Applications of Computational Fluid Mechanics*, 18(1):2302559, 2024.

[121] H. K. Schreiner, C. D. Rennie, and A. Mohammadian. Insights into secondary flow structure from clusters of instantaneous vortices. *Environmental Fluid Mechanics*, 23(1):89–101, 2023.

[122] H. K. Schreiner, C. D. Rennie, and A. Mohammadian. Effect of a nonbuoyant submerged transverse jet on bend secondary circulation. *Journal of Hydro-environment Research*, page 100671, 2025.

[123] W. R. Schwarz and P. Bradshaw. Turbulence structural changes for a three-dimensional turbulent boundary layer in a 30 bend. *Journal of Fluid Mechanics*, 272:183–210, 1994.

[124] A. Sciacchitano and B. Wieneke. Piv uncertainty propagation. *Measurement Science and Technology*, 27(8):084006, 2016.

[125] Sanaz Sediqi, Jueyi Sui, Guowei Li, and Mauricio Dziedzic. Characteristics of turbulent flow around bridge abutments in the presence of vegetation in channel bed under ice-covered flow conditions. *Cold Regions Science and Technology*, 221:104172, 2024.

[126] R. H. J. Sellin, D. A. Ervine, and B. B. Willetts. Behaviour of meandering two-stage channels. *Proceedings of the Institution of Civil Engineers: Water, Maritime and Energy*, 101(2):99–111, 1993.

[127] Eitan Shelef. Channel profile and plan-view controls on the aspect ratio of river basins. *Geophysical Research Letters*, 45(21):11712–11720, 2018.

[128] H. T. Shen and P. D. Yapa. Flow resistance of river ice cover. *Journal of Hydraulic Engineering*, 112(2):142–156, 1986.

[129] Koji Shiono and Donald W. Knight. Turbulent open-channel flows with variable depth across the channel. *Journal of Fluid Mechanics*, 222:617–646, 1991.

[130] B. T. Smith and R. Ettema. Flow resistance in ice-covered alluvial channels. *Journal of Hydraulic Engineering*, 123(7):592–599, 1997.

[131] K. Smith, J. Cockburn, and P. V. Villard. The effect of ice cover on velocity and shear stress in a riffle-pool sequence. *Earth Surface Processes and Landforms*, 48(7):1414–1427, 2023.

[132] K. Somsook, M. A. Duka, N. A. Olap, J. C. C. Casila, and K. Yokoyama. Direct measurement of secondary circulation in a meandering macrotidal estuary. *Science of the Total Environment*, 739:139503, 2020.

[133] S. Song, B. Schmalz, G. Hörmann, and N. Fohrer. Accuracy, reproducibility and sensitivity of acoustic doppler technology for velocity and discharge measurements in medium-sized rivers. *Hydrological Sciences Journal*, 57(8):1626–1641, 2012.

[134] John Southard. *Introduction to Fluid Motions and Sediment Transport*. LibreTexts, 2019.

[135] K. R. Sreenivasan and G. Stolovitzky. Statistical dependence of inertial range properties on large scales in a high-reynolds-number shear flow. *Physical Review Letters*, 77(11):2218–2221, 1996.

[136] T. Stoesser, N. Ruether, and N. R. B. Olsen. Calculation of primary and secondary flow and boundary shear stresses in a meandering channel. *Advances in Water Resources*, 33(2):158–170, 2010.

[137] J. Sui, J. Wang, R. Balachandar, Z. Sun, and D. Wang. Accumulation of frazil ice along a river bend. *Canadian Journal of Civil Engineering*, 35(2):158–169, 2008.

[138] A. Sukhodolov, M. Thiele, H. Bungartz, and C. Engelhardt. Turbulence structure in an ice-covered, sand-bed river. *Water Resources Research*, 35(3):889–894, 1999.

[139] Y. Takakuwa and S. Fukuoka. Three-dimensional flow structures of straight rough-bed channels with different aspect ratios. In W. S. J. et al. Uijttewaal, editor, *River Flow*, 2020.

[140] M. J. Teal, R. Ettema, and J. F. Walker. Estimation of mean flow velocity in ice-covered channels. *Journal of Hydraulic Engineering*, 120(12):1385–1400, 1994.

[141] D. Termini. Experimental observations of flow and bed processes in large-amplitude meandering flume. *Journal of Hydraulic Engineering*, 135(10):1123–1133, 2009.

[142] D. Termini and M. Piraino. Experimental analysis of cross-sectional flow motion in a large amplitude meandering bend. *Earth Surface Processes and Landforms*, 36(2):244–256, 2011.

[143] Donatella Termini. Momentum transport and bed shear stress distribution in a meandering bend: Experimental analysis in a laboratory flume. *Advances in Water Resources*, 81:128–141, 2015.

[144] D. R. Townsend. An investigation of turbulence characteristics in a river model of complex cross section. *Proceedings of the Institution of Civil Engineers*, 40(2):155–175, 1968.

[145] W. F. Tsai and R. Ettema. Ice cover influence on transverse bed slopes in a curved alluvial channel. *Journal of Hydraulic Research*, 32(4):561–581, 1994.

[146] G. E. Urroz and R. Ettema. Application of two-layer hypothesis to fully developed flow in ice-covered curved channels. *Canadian Journal of Civil Engineering*, 21(1):101–110, 1994.

[147] T. Utami and T. Ueno. Visualization and picture processing of turbulent flow. *Experiments in Fluids*, 2(1):25–32, 1984.

[148] Wouter Van Balen, Koen Blanckaert, and Wim S. J. Uijttewaal. Analysis of the role of turbulence in curved open-channel flow at different water depths by means of experiments, les and rans. *Journal of Turbulence*, 11:N12, 2010.

[149] J. C. Vassilicos. Dissipation in turbulent flows. *Annual Review of Fluid Mechanics*, 47(1):95–114, 2015.

[150] Ricardo Vinuesa, Philipp Schlatter, and H. M. Nagib. Secondary flow in turbulent ducts with increasing aspect ratio. *Physical Review Fluids*, 3(5):054606, 2018.

[151] F. Wang, W. Huai, Y. Guo, and M. Liu. Turbulence structure and momentum exchange in compound channel flows with shore ice covered on the floodplains. *Water Resources Research*, 57(4):e2020WR028621, 2021.

[152] F. Wang, W. Huai, M. Liu, and X. Fu. Modeling depth-averaged streamwise velocity in straight trapezoidal compound channels with ice cover. *Journal of Hydrology*, 585:124336, 2020.

[153] J. Wang, J. Y. Sui, and B. W. Karney. Incipient motion of non-cohesive sediment under ice cover-an experimental study. *Journal of Hydrodynamics*, 20(1):117–124, 2008.

[154] Jun Wang. Progress in studies on ice accumulation in river bends. *Journal of Hydrodynamics, Ser. B*, 23(6):737–744, 2011.

[155] J.V. Ward, K. Tockner, D.B. Arscott, and C. Claret. Riverine landscape diversity. *Freshwater Biology*, 47(4):517–539, 2002.

[156] G. Webel and M. Schatzmann. Transverse mixing in open channel flow. *Journal of Hydraulic Engineering*, 110(4):423–435, 1984.

[157] M. Wei, K. Blanckaert, J. Heyman, D. Li, and A. J. Schleiss. A parametrical study on secondary flow in sharp open-channel bends: Experiments and theoretical modelling. *Journal of Hydro-Environment Research*, 13:1–13, 2016.

[158] Jerry Westerweel. Fundamentals of digital particle image velocimetry. *Measurement Science and Technology*, 8(12):1379–1392, 1997.

[159] Frank Wilcoxon. Individual comparisons by ranking methods. *Biometrics Bulletin*, 1(6):80–83, 1945.

[160] E. Wohl. An integrative conceptualization of floodplain storage. *Reviews of Geophysics*, 59, 2021.

[161] M. G. Wolman and L. B. Leopold. River flood plains: Some observations on their formation. Technical report, U.S. Government Printing Office, Washington, DC, 1957.

[162] S. Q. Yang, S. K. Tan, and X. K. Wang. Mechanism of secondary currents in open channel flows. *Journal of Geophysical Research: Earth Surface*, 117(F4), 2012.

[163] Xiao Yang, Tamlin M. Pavelsky, and George H. Allen. The past and future of global river ice. *Nature*, 577(7788):69–73, 2020.

[164] S. Yokosi. The structure of river turbulence. *Bulletin of the Disaster Prevention Research Institute, Kyoto University*, 17(2):1–29, 1967.

[165] Ya Zhong, Wenxin Huai, and Gang Chen. Analytical model for lateral depth-averaged velocity distributions in rectangular ice-covered channels. *Journal of Hydraulic Engineering*, 145(1):04018080, 2019.

[166] J. Zufelt and Z. Sun. A laboratory study of transverse velocities and ice jamming in a river bend. In *Proceedings of the IAHR Symposium on Ice Problems, Sapporo, Japan*, pages 23–27, August 1988.